Velocity and Attenuation Structure of the Mantle: Constraints from Differential Properties of Shear Waves

by

Fiona Jane Louise Reid



Thesis submitted for the Degree of
Doctor of Philosophy
to the University of Oxford

Exeter College &
The Department of Earth Sciences

Hilary Term
March 1999

For my mother...

Velocity and Attenuation Structure of the Mantle: Constraints from Differential Properties of Shear Waves

Fiona Jane Louise Reid

Exeter College & Department of Earth Sciences

Thesis submitted for the degree of Doctor of Philosophy

to the University of Oxford

Hilary Term, 1999

Abstract

Although much progress has been made in determining the three dimensional distribution of seismic wave velocities in the Earth, substantially less is known about the three dimensional distribution of intrinsic attenuation. In this study variations in attenuation and shear velocity of the Earth's mantle are constrained using measurements of differential travel time and attenuation.

The data are broadband displacement SH seismograms filtered to have energy in the period range 8 to 20 s. Broadband data are used as they should allow a more accurate estimation of body wave attenuation to be made. The seismograms are obtained from over 600 globally distributed earthquakes of magnitude, M_w, 5.5 or greater.

Two new methods for determining differential travel times and differential t^* values from multiple S phases are presented. The first of these, referred to as the "waveform fitting method" is used to analyse approximately 4300 SS and S waveforms and around 1000 SSS and SS waveforms resulting in differential $SS-S$ and $SSS-SS$ travel times, and corresponding values of differential attenuation represented by t^*. The second method, referred to as the "spectral ratio method" is used to analyse approximately 3200 SS and S and around 900 SSS and SS waveforms.

The differential travel times and t^* values are inverted to obtain models of the lateral variation of shear velocity and lateral variation of q_μ where $q_\mu = \frac{1}{Q_\mu}$. The models explain the data well but have limited depth resolution. The velocity models show good correlation with previous studies, in particular, low velocities are observed underlying spreading ridges and convergent margins and high velocities are observed under continental regions. The q_μ model shows shield regions to be less attenuating than PREM, with ridges appearing as highly attenuating features.

Models of shear velocity and attenuation are also obtained by combining the body wave dataset of this study with the surface wave datasets of Van Heijst (1997) and Selby (1998).

Velocity and Attenuation Structure of the Mantle: Constraints from Differential Properties of Shear Waves

Fiona Jane Louise Reid

Exeter College & Department of Earth Sciences

Thesis submitted for the degree of Doctor of Philosophy

to the University of Oxford

Hilary Term, 1999

Extended abstract

Seismology is one of the few tools that can be used to study the deep interior of the Earth. An understanding of the distribution of the elastic and anelastic properties and density of the Earth's interior is of importance for a wide variety of geophysical, geochemical and astronomical studies. The technique of seismic tomography provides a method for investigating Earth structure.

Since the late 1970's seismic tomography has been used to construct models of the three dimensional structure of the interior of the Earth. Over the last two decades there has been a dramatic increase in both the quantity and quality of data available. This, along with advances in computation have allowed increasingly more detailed models of Earth structure to be constructed. The velocity structure of the Earth is now quite well known, although some areas such as the transition zone and some sections of the lower mantle lack adequate resolution. However, substantially less is known about the three dimensional distribution of intrinsic attenuation. Only a very limited number of studies have investigated the lateral variation of attenuation within the Earth. Studies of the attenuation structure are of interest for several reasons:

- Attenuation can provide additional constraints on Earth properties such as the temperature and state of the material through which a wave has travelled.
- Attenuation affects the amplitude of a seismic wave, and therefore an understanding of it is important for the assessment of the seismic risk in a particular area, the design of earthquake resistant structures and both the detectability and yield determination of underground nuclear explosions.
- Improved models of seismic wave velocity should be possible if the effects of attenuation are taken into account.

In this study variations in attenuation and shear velocity of the Earth's mantle are constrained from differential measurements of travel time and attenuation made from multiple S phases.

The data used for this study are broadband displacement SH seismograms recorded over the time period 1989-1996. The use of broadband records prevents the use of data from events prior to 1989.

The data are filtered to have energy in the period range 8 to 20 s. Broadband data are used as they contain more high frequency information and therefore should allow a more accurate estimation of body wave attenuation to be made. The seismograms are obtained from over 600 globally distributed earthquakes of magnitude, M_w, 5.5 or greater. The seismograms lie in the epicentral distance ranges $50° - 105°$ and $90° - 179°$ for $SS - S$ and $SSS - SS$ datasets respectively. For the $SS - S$ dataset this distance range is selected so as to avoid the core shadow region for shear waves and also, for epicentral distances greater than 50° both the direct and reflected phases sample the source and receiver regions in a similar manner. For the $SSS - SS$ dataset, the distance range is chosen so as to ensure the rays remain in the lower mantle as much as possible, and to avoid rays turning in the transition zone.

Two new methods for determining differential travel times and t^* values from multiple S phases are presented. The attenuation parameter, t^* is defined as the time integral of inverse quality factor Q^{-1} along the ray path i.e. $t^* = \int_{ray} Q^{-1} d\tau$. The first of these methods, referred to as the "waveform fitting method" is used to analyse approximately 4300 SS and S waveforms and around 1000 SSS and SS waveforms resulting in differential $SS - S$ and $SSS - SS$ travel times, and corresponding values of differential attenuation represented by t^*. The waveform fitting method is applied to waveforms obtained from filtered real and synthetic seismograms. The synthetic seismograms are calculated by summation of over 20,000 normal modes.

The second method, referred to as the "spectral ratio method" is used to analyse approximately 3200 SS and S and around 900 SSS and SS waveforms resulting in measurements of $SS - S$ and $SSS - SS$ differential attenuation. The spectral ratio method is applied only to waveforms selected from raw unfiltered seismograms. Unfiltered data are used as the spectral method relies on the frequency content of the data and filtering would alter this.

The measurements of differential travel time and t^* are inverted using the method of damped weighted least squares to obtain models of the lateral variation of shear velocity, $\frac{\delta v_s}{v_s}$, and the lateral variation of attenuation represented by q_μ where $q_\mu = \frac{1}{Q_\mu}$. The models are parameterised using the spherical harmonic basis functions to describe lateral variations and spline functions for the depth dependence. The velocity models are constructed using harmonics of degree and order 12 and splines over 6 knots spanning the depth interval Moho to 380 km. The models of attenuation are constructed using harmonics of degree and order 8 and a similar spline representation with depth. This results in a total of 1014 and 486 unknowns for the models of velocity and attenuation respectively. Before inversion of the travel time residuals, corrections for the effects of the crust and the Earth's ellipticity are applied. The crustal model used is model CRUST 5.1 of Mooney *et al.* (1998).

The models explain the data well but have limited depth resolution. The velocity models show good correlation with previous studies, in particular, low velocities are observed underlying mid oceanic ridges and convergent margins and high velocities are observed under continental regions. The q_μ model shows shield regions to be less attenuating than PREM, with mid oceanic ridges appearing as highly attenuating features. Comparison of the velocity and attenuation models shows correlation between

regions of low velocity and high attenuation. Regions of high velocity and low attenuation are also observed to correlate.

The velocity models are compared with existing three dimensional models of shear velocity heterogeneity. Overall the agreement is good, although the resolution degrades at depth.

The attenuation models are also compared with previously published models. Comparison with the only other global body wave study of lateral variation of q_μ shows little similarity. However comparison with model QMU3b of Selby (1998), derived from surface wave data, shows many regions of similarity.

Finally, the body wave datasets of this study are combined with the surface wave datasets of Van Heijst (1997) and Selby (1998) to obtain combined models of shear velocity and attenuation respectively. The velocity model is parameterised by spherical harmonics up to degree and order 20 using 21 depth splines, the deepest of which corresponds to the core mantle boundary. The combined velocity model is capable of explaining both the body wave and surface wave data extremely well. The model has good depth resolution to around 1500 km depth, due the inclusion of the surface wave data. Some sensitivity is also observed in the deep mantle from the turning of the deepest S rays.

Comparison with existing models of whole mantle shear velocity show good agreement. In the upper mantle the model correlates with known tectonic features: low velocities are observed underlying ridges and convergent margins, high velocities are observed underlying continental regions. In the lowermost mantle, the model is characterised by a ring of high velocities surrounding the Pacific with a region of low velocity in the central Pacific. These features are consistent with many other existing models of shear velocity.

The combined attenuation model is parameterised by spherical harmonics up to degree and order 8 over the depth range Moho to 380 km. In constructing this model it is demonstrated that it is possible to obtain a model of the three dimensional variations in q_μ which is capable of fitting both the body wave and surface wave datasets. The vertical resolution of the model is not sufficient to allow discussion of changes in attenuation with depth. The model shows a pattern of attenuation which correlates with the ocean-continent pattern and with some tectonic features. High attenuation is observed to correlate with the ridges and oceans, low attenuation correlates with continental regions.

Acknowledgements

First and foremost, I would like to thank my supervisor, John Woodhouse. I enjoyed working with him a great deal, his extensive knowledge of seismology and the ability to derive any expression from first principles has never failed to amaze me. I thank him for his patience in explaining things, however trivial, for his enthusiasm and for his encouragement. I would also like to thank the other seismologists here at Oxford. I feel I benefited greatly from our weekly discussions.

I would like to thank Neil Selby and Hendrik Jan van Heijst for allowing the use of their surface wave datasets, mentioned in chapter 7.

During my time in Oxford I have formed many new friendships both at Exeter college and within the department. These people have made the time I have spent here a most enjoyable experience, without them I'm sure I would not have survived. I would like to thank, in no particular order, Gretta, Nathan, Arwen, Margaret, Teresa, Yvonne, Paola, Jason, Pete, Hans, Tim, Jenny, Santo and many others. I would also like to thank my friends from Edinburgh for staying in touch and for visiting me in England.

Thanks also go to the secretarial, technical and computing staff for their assistance, particularly in the final stages.

My mother is one of the reasons this thesis exists, without her encouragement and support I would most likely have given up long ago. I thank her for her support and reassurance that I was not wasting my time. I also thank my brother for his phone calls and e-mails, however infrequent, they were often a source of great amusement.

Finally I thank Mike, his visits have been extremely important to me. It has been very difficult spending the last 3.5 years at different ends of the country and I am very grateful that we are still together.

The figures in this thesis are constructed using the Generic Mapping Tools software (GMT), Wessel & Smith (1991, 1995).

Contents

Abstract i
Extended abstract ii
Acknowledgements v
Table of Contents vi
List of Figures ix
List of Tables xvii

1 Introduction **1**
1.1 Introduction to seismic attenuation 3
1.2 Definition of the attenuation parameters 3
1.3 Mechanisms of attenuation 4
1.4 The stress-strain relationship 7
1.5 The frequency dependence of attenuation 8
1.6 The seismic absorption band model of attenuation 8
1.7 Earth models and studies of attenuation 11
1.7.1 Background and motivation 11
1.7.2 Spherical Earth models and attenuation 13
1.7.3 Aspherical Earth models 15
1.8 Regional studies 17
1.9 Seismic velocity tomography 20

2 Data **24**
2.1 Event selection 25
2.2 Filters applied to the data 26

3 Methodology: waveform fitting **33**
3.1 Introduction 33
3.2 Motivation for using differential measurements 33
3.3 The theory behind the waveform fitting method 35
3.4 The processing stage 39

3.4.1 The fit parameter . . . 44
3.4.2 Waveform fitting: an example . . . 45
3.5 Summary . . . 48

4 Spectral ratio method for determining Δt^* values 49
4.1 Introduction . . . 49
4.2 Theory of the spectral ratio method . . . 49
4.3 Data processing . . . 51
4.3.1 A matter of weighting . . . 55
4.3.2 Consequences for the errors . . . 57
4.4 Example results from the spectral ratio method . . . 59
4.5 Summary . . . 59

5 Preliminary results: examining the residuals 61
5.1 Introduction . . . 61
5.2 Results from the waveform fitting method . . . 61
5.2.1 Travel time residuals . . . 61
5.2.2 t^* residuals . . . 64
5.2.3 What are the errors ? . . . 66
5.3 Results from the spectral ratio method . . . 67
5.3.1 What are the errors ? . . . 68
5.4 Comparison with other studies . . . 68
5.5 Preliminary discussion of results . . . 69

6 Three dimensional modelling of the data 94
6.1 Introduction . . . 94
6.2 Formulation of the problem . . . 94
6.3 Model parameterisation . . . 95
6.4 Modelling of seismic parameters using weighted damped least squares . . . 96
6.5 Data selection . . . 97
6.6 Damping . . . 98
6.7 Data weighting . . . 99
6.8 Corrections to the travel time residuals . . . 99
6.8.1 Crustal corrections using CRUST 5.1 . . . 99
6.8.2 Ellipticity corrections . . . 101
6.9 Velocity models . . . 102
6.9.1 $SS - S$ models . . . 102
6.9.2 $SSS - SS$ models . . . 103

6.9.3 Combining the $SS-S$ and $SSS-SS$ models . . . 104
6.10 Attenuation models . . . 106
6.10.1 Attenuation models obtained from the results of the waveform fitting method . . 106
6.10.2 Attenuation models obtained from the results of the spectral ratio method 108
6.11 Resolution tests . . . 108

7 Combining body wave and surface wave measurements **161**
7.1 Attenuation model from body wave and surface wave data . . . 161
7.2 Velocity model from body wave and surface wave data . . . 163

8 Discussion **171**
8.1 Discussion of the velocity models . . . 171
8.2 Discussion of the q_μ models . . . 172
8.3 Comparison of the velocity and attenuation models . . . 173
8.4 Discussion of the combined body wave and surface wave models . . . 174
8.4.1 Model MVBS . . . 174
8.4.2 Model MQBS . . . 175
8.5 Comparisons with existing work . . . 175
8.5.1 Velocity models . . . 175
8.5.2 q_μ models . . . 177
8.6 Geophysical implications . . . 178

9 Conclusions **197**

A Inverse Theory **208**
A.1 The spherical harmonics . . . 208
A.2 Inverse theory: some further details . . . 208
A.2.1 Introduction . . . 208
A.2.2 Weighted damped least squares . . . 209
A.3 Resolution . . . 211
A.4 Variance Ratio . . . 212

B Additional figures **213**

C Testing the methodologies employed in this study **216**
C.1 Synthetic testing of the waveform fitting method . . . 216
C.2 Testing of the spectral ratio method . . . 219

List of Figures

1.1 The stress-strain relation for loading and unloading of an anelastic solid 7
1.2 Debye function of $Q^{-1}(\omega)$ for an anelastic solid having a single characteristic relaxation time of τ. 9
1.3 Attenuation in an anelastic solid possessing a range of characteristic relaxation times distributed continuously between τ_1 and τ_2. 10
1.4 Schematic illustration of the absorption band (Anderson & Given, 1982). Q_{min} is the shear wave attenuation in the mantle, τ_1 is calculated as a function of depth from seismic data and α and τ_2/τ_1 are fixed. 11
1.5 Absorption band model of attenuation in the Earth at various depths where Q is the quality factor for shear waves. Reproduced from Anderson (1989). 12
1.6 The PREM model, plotted using the coefficients given in Dziewonski & Anderson (1981). 14
1.7 PREM upper mantle velocity structure. Note that the upper mantle is defined as the region from the base of the crust to a depth of 670 km. 15
1.8 Model S16B30 reproduced from Masters *et al.* (1996) 23

2.1 Source locations for 597 events used with the waveform fitting method for the $SS-S$ study. 27
2.2 Source locations for 260 events used with the waveform fitting method for the $SSS-SS$ study. 27
2.3 Station locations for 95 stations used with the waveform fitting method for the $SS-S$ study. 28
2.4 Station locations for 82 stations used with the waveform fitting method for the $SSS-SS$ study. 28
2.5 Event depth distribution for the $SS-S$ study, all epicentral depths are obtained from the CMT solutions. 29
2.6 Event depth distribution for the $SSS-SS$ study, all epicentral depths are obtained from the CMT solutions. 29
2.7 Magnitude distribution for the $SS-S$ study. 30
2.8 Magnitude distribution for the $SSS-SS$ study. 30

2.9 Amplitude versus frequency for each of the filters applied to the data. 31
2.10 Example of filtered and non filtered $SS - S$ data for 4 stations from event 960305B. . . 32

3.1 Schematic of the S and SS ray paths 34
3.2 Showing the relationship between q and $\ln \omega$ obtained from having a constant Q over a particular frequency band. 37
3.3 Showing p against $\ln \omega$ 38
3.4 Seismograms showing an example of windowed out data 41
3.5 Graph showing the PREM values of $(t^*_{SS} - t^*_S)$ for a range of source depths. 43
3.6 Final output from the fitting algorithm showing an example of good quality and poor quality fits 44
3.7 Seismograms from station DGR of event 960507F. The black trace shows the real data, the blue trace shows the synthetic data. The S and SS waveforms are marked out by the "a" and "b" intervals respectively. 45
3.8 Example of waveforms obtained from fitting the synthetic data. 46
3.9 Example of waveforms obtained from fitting the real data. 47

4.1 Example of data used with the spectral method 52
4.2 Rotated, unfiltered segments of the seismogram from station AAK event 960502F. . . . 53
4.3 Cosine bell window function used to smooth the end points of the waveform segments. . 54
4.4 Rotated unfiltered segments of the seismogram from station AAK event 960502F with the smoothing function applied. 55
4.5 Amplitude spectra for the S (left) and SS (right) phases. 56
4.6 Amplitude spectra for the S (left) and SS (right) phases after application of a cosine taper between 0-0.04 Hz. 57
4.7 Logarithm of the amplitude spectra for the S (left) and SS (right) phases from station AAK of event 960502F. 58
4.8 Spectral ratio for $SS - S$ plotted against frequency. The red line shows the resulting straight line fit to the data over the range 0-0.25 Hz. The gradient and intercept of this line are -6.31 and -0.31 respectively. 60

5.1 Distribution of travel time residuals for the $SS - S$ data obtained from the waveform fitting method. 71
5.2 Distribution of travel time residuals for the $SSS - SS$ data obtained from the waveform fitting method. 71
5.3 Distribution of $SS - S$ travel time residuals for different epicentral distance ranges using data obtained from the waveform fitting method. 72

5.4 Distribution of $SSS - SS$ travel time residuals for different epicentral distance ranges using data obtained from the waveform fitting method. 73
5.5 Distance dependence of $SS - S$ travel time residuals plotted as the means of 2° bins for epicentral distances between $50° - 102°$. The numbers directly below each point give the total number of residuals for that 2° bin. 74
5.6 Distance dependence of $SSS - SS$ travel time residuals plotted as the means of 4° bins for epicentral distances between $90° - 180°$. The numbers directly below each point give the total number of residuals for that 4° bin. 74
5.7 Travel time residuals for the $SS - S$ data plotted at the SS bounce point. Note that many residuals plot on top of each other making the map difficult to interpret. 75
5.8 Travel time residuals for the $SS - S$ data in 5° spherical caps - 1 point or more per cap. 75
5.9 Travel time residuals for the $SS - S$ data in 5° spherical caps - 3 points or more per cap. 76
5.10 Travel time residuals for the $SS - S$ data in 5° spherical caps - 5 points or more per cap. 76
5.11 Density of measurements for the waveform fitting method plotted in 5° spherical caps. . 77
5.12 Distribution of Δt^* residuals for the $SS - S$ data obtained from the waveform fitting method. The Δt^* values are plotted relative to PREM. 78
5.13 Distribution of Δt^* residuals for the $SSS - SS$ data obtained from the waveform fitting method. The Δt^* residuals are plotted relative to PREM. 78
5.14 Distribution of $SS - S$ Δt^* residuals for different epicentral distance ranges using data obtained from the waveform fitting method. 79
5.15 Distribution of $SSS - SS$ Δt^* residuals for different epicentral distance ranges using data obtained from the waveform fitting method. 80
5.16 Distance dependence of $SS - S$ t^* residuals plotted as the means of 2° bins for epicentral distances between $50° - 102°$. The numbers directly below each point give the total number of residuals for that 2° bin. 81
5.17 Distance dependence of $SSS - SS$ t^* residuals plotted as the means of 4° bins for epicentral distances between $90° - 180°$. The numbers directly below each point give the total number of residuals for that 4° bin. 81
5.18 Δt^* residuals, plotted relative to PREM at the SS bounce point for the $SS - S$ data . . 82
5.19 Δt^* residuals, plotted relative to PREM, for the $SS - S$ data in 5° spherical caps - 1 point or more per cap. 82
5.20 Δt^* residuals, plotted relative to PREM, for the $SS - S$ data in 5° spherical caps - 3 points or more per cap. 83
5.21 Δt^* residuals, plotted relative to PREM, for the $SS - S$ data in 5° spherical caps - 5 points or more per cap. 83
5.22 Distribution of the errors in the $SS - S$ differential travel time measurements obtained from the waveform fitting method. 84

5.23 Distribution of the errors in the $SS - S$ differential t^* measurements obtained from the waveform fitting method. 84
5.24 Distribution of the errors in the $SSS-SS$ differential travel time measurements obtained from the waveform fitting method. 85
5.25 Distribution of the errors in the $SSS - SS$ differential t^* measurements obtained from the waveform fitting method. 85
5.26 Distribution of Δt^* residuals for the $SS - S$ data obtained from the spectral method. The Δt^* residuals are plotted relative to the PREM values. 86
5.27 Distribution of Δt^* residuals for the $SSS-SS$ data obtained from the spectral method. The Δt^* residuals are plotted relative to the PREM values. 86
5.28 Distribution of $SS - S$ Δt^* residuals for different epicentral distance ranges using data obtained from the spectral ratio method. 87
5.29 Distribution of $SSS - SS$ Δt^* residuals for different epicentral distance ranges using data obtained from the spectral ratio method. 88
5.30 Distance dependence of $SS - S$ t^* residuals obtained from the spectral ratio method, plotted as the means of 2° bins for epicentral distances between $50° - 102°$. The numbers directly below each point give the total number of residuals for that 2° bin. 89
5.31 Distance dependence of $SSS - SS$ t^* residuals obtained from the spectral ratio method, plotted as the means of 4° bins for epicentral distances between $90° - 180°$. The numbers directly below each point give the total number of residuals for that 4° bin. 89
5.32 Density of measurements for the spectral ratio method plotted in 5° spherical caps. . . . 90
5.33 Distribution of the errors in $SS - S$ differential t^* measurements obtained from the spectral ratio method. 91
5.34 Distribution of the errors in $SSS - SS$ differential t^* measurements obtained from the spectral ratio method. 91
5.35 Map showing the smoothed $SS - S$ travel time residuals. Reproduced from Woodward & Masters (1991a) 92
5.36 Map of cap-averaged t^* values reproduced from Bhattacharyya *et al.* (1996) 93

6.1 Depth splines, $f_k(r)$, for $k = 1, 2 \ldots 20$. 110
6.2 Depth splines for $k = 1, 2 \ldots 6$ along with the depth at which the maximum of each spline occurs. 111
6.3 Distribution of travel time residuals with fit parameters of 0.2 or less obtained from the waveform fitting method. The left hand plot shows the distribution for the $SS - S$ dataset, the right hand plot shows the distribution for the $SSS - SS$ dataset. 112
6.4 Distribution of t^* residuals with fit parameters of 0.2 or less obtained from the waveform fitting method. The left hand plot shows the distribution for the $SS - S$ dataset, the right hand plot shows the distribution for the $SSS - SS$ dataset. 112

6.5 Relationship between model size and the number of effective eigenvalues used. The number beside each data point gives the value of η used for the inversion. For reference, a degree 8, 6 spline inversion for q_μ was used to obtain the results shown here. 113
6.6 Relationship between the variance ratio and the number of effective eigenvalues used. The number beside each data point gives the value of η used for the inversion. For reference, a degree 8, 6 spline inversion for q_μ was used to obtain the results shown here. 113
6.7 Crustal types from CRUST 5.1, reproduced from Mooney *et al.* (1998). The crustal structure in unmeasured regions has been extrapolated using statistical averages of regions of similar tectonic setting. 114
6.8 Global crustal thickness, including topography above sea level but not bathymetry of CRUST 5.1 (reproduced from Mooney *et al.* (1998)). 114
6.9 Crustal corrections for $SS-S$ calculated for a grid of hypothetical bounce points in 5° intervals. The oceans exhibit negative corrections, whereas the continents show positive corrections. 115
6.10 Schematic showing how a SSS ray may be split into two legs denoted by 1 and 2. The first leg is an S ray over the distance Δ_1, the second leg is an SS ray over the distance Δ_2. 115
6.11(a) Model MVSSa: $SS-S$ velocity model with no corrections applied for depths 50-129 km 116
6.11(b) Model MVSSa: $SS-S$ velocity model with no corrections applied for depths 190-329 km 117
6.12(a) Model MVSSb: $SS-S$ velocity model with only crustal corrections applied for depths 50-129 km 118
6.12(b) Model MVSSb: $SS-S$ velocity model with only crustal corrections applied for depths 190-329 km 119
6.13(a) Model MVSSc: $SS-S$ velocity model with crustal and ellipticity corrections applied for depths 50-129km 120
6.13(b) Model MVSSc: $SS-S$ velocity model with crustal and ellipticity corrections applied for depths 190-329 km 121
6.14(a) Model MVSSSa: $SSS-SS$ velocity model with no corrections applied for depths 50-129 km 122
6.14(b) Model MVSSSa: $SSS-SS$ velocity model with no corrections applied for depths 190-329 km 123
6.15(a) Model MVSSSb: $SSS-SS$ velocity model with only crustal corrections applied for depths 50-129 km 124
6.15(b) Model MVSSSb: $SSS-SS$ velocity model with only crustal corrections applied for depths 190-329 km 125

6.16(a) Model MVSSSc: $SSS - SS$ velocity model with crustal and ellipticity corrections applied for depths 50-129 km . . . 126
6.16(b) Model MVSSSc: $SSS - SS$ velocity model with crustal and ellipticity corrections applied for depths 190-329 km . . . 127
6.17 Variance ratio of $SSS - SS$ data against variance ratio of $SS - S$ data for the combined model. Point A shows the point of equal weighting and point B shows the point of equal improvement of the $SSS - SS$ and $SS - S$ variance ratios. . . . 128
6.18(a) Model MVCOMB1: Combined velocity model with crustal and ellipticity corrections applied for depths 50-129 km . . . 129
6.18(b) Model MVCOMB1: Combined velocity model with crustal and ellipticity corrections applied for depths 190-329 km . . . 130
6.19(a) Model MVCOMB2: Combined velocity model with crustal and ellipticity corrections applied for depths 50-129 km. The weightings used are $w_1 = \frac{1}{2.5}$ and $w_2 = 1.0$ . . . 131
6.19(b) Model MVCOMB2: Combined velocity model with crustal and ellipticity corrections applied for depths 190-329 km. The weightings used are $w_1 = \frac{1}{2.5}$ and $w_2 = 1.0$ . . . 132
6.20(a) Model MQSS: $SS - S$ attenuation model for depths 50-129 km . . . 133
6.20(b) Model MQSS: $SS - S$ attenuation model for depths 190-329 km . . . 134
6.21(a) Model MQSSS: $SSS - SS$ attenuation model for depths 50-129 km . . . 135
6.21(b) Model MQSSS: $SSS - SS$ attenuation model for depths 190-329 km . . . 136
6.22(a) MQCOMB1: Combined attenuation model for depths 50-129 km . . . 137
6.22(b) MQCOMB1: Combined attenuation model for depths 190-329 km . . . 138
6.23 Variance ratio of $SS - S$ data against variance ratio of $SSS - SS$ data for the combined model for different weightings. Point A is the point of equal weighting. Point B is the point of equal improvement of the $SS - S$ and $SSS - SS$ variance ratios. . . . 139
6.24(a) MQCOMB2: Combined attenuation model for depths 50-129 km. The weightings used are $w_1 = \frac{1}{2.5}$ and $w_2 = 1.0$ . . . 140
6.24(b) MQCOMB2: Combined attenuation model for depths 190-329 km. The weightings used are $w_1 = \frac{1}{2.5}$ and $w_2 = 1.0$ . . . 141
6.25(a) MQSRMSS: $SS - S$ attenuation model from spectral ratio measurements for depths 50-129 km . . . 142
6.25(b) MQSRMSS: $SS - S$ attenuation model from spectral ratio measurements for depths 190-329 km . . . 143
6.26(a) MQSRMSSS: $SSS - SS$ attenuation model from spectral ratio measurements for depths 50-129 km . . . 144
6.26(b) MQSRMSSS: $SSS - SS$ attenuation model from spectral ratio measurements for depths 190-329 km . . . 145

6.27(a) MQSRMCOMB1: Combined attenuation model from spectral ratio measurements for depths 50-129 km . . . 146
6.27(b) MQSRMCOMB1: Combined attenuation model from spectral ratio measurements for depths 190-329 km . . . 147
6.28 Variance ratio of $SSS-SS$ data against variance ratio of $SS-S$ data for the combined model. Point A indicates equal weighting of the two datasets. Point B indicates the point of equal improvement for the variance ratios of the $SS-S$ and $SSS-SS$ datasets. 148
6.29(a) MQSRMCOMB2: Combined attenuation model from spectral ratio measurements for 50-129 km. The weightings used are $w_1 = \frac{1}{2.0}$ and $w_2 = 1.0$ . . . 149
6.29(b) MQSRMCOMB2: Combined attenuation model from spectral ratio measurements for 50-129 km. The weightings used are $w_1 = \frac{1}{2.0}$ and $w_2 = 1.0$ . . . 150
6.30(a) Input checkerboard pattern at 74 km for depths 25-129 km . . . 151
6.30(b) Input checkerboard pattern at 74 km for depths 190-329 km . . . 152
6.31(a) Output for $SS-S$ dataset for depths 25-129 km . . . 153
6.31(b) Output for $SS-S$ dataset for depths 190-329 km . . . 154
6.32(a) Output for $SSS-SS$ dataset for depths 25-129 km . . . 155
6.32(b) Output for $SSS-SS$ dataset for depths 190-329 km . . . 156
6.33(a) Output for combined dataset for depths 25-129 km . . . 157
6.33(b) Output for combined dataset for depths 190-329 km . . . 158
6.34 Input checkerboard at 256km for depths 30-329 km . . . 159
6.35 Output for combined dataset for depths 30-329 km . . . 160

7.1 Surface wave against body wave variance ratios for the combined model, degree zero term included. . . . 165
7.2 Surface wave against body wave variance ratios for the combined model with the degree zero term removed. . . . 165
7.3 q_μ model constructed from combination of the $SS-S$ and $SSS-SS$ datasets with the surface wave data of Selby (1998) using the "best" model from Figure 7.1. . . . 166
7.4 Model MQBS: q_μ model constructed from combining the $SS-S$ and $SSS-SS$ datasets with the surface wave data of Selby (1998) using the "best" model from Figure 7.2. . . . 167
7.5(a) Velocity model MVBS for depths 50 - 498 km . . . 168
7.5(b) Velocity model MVBS for depths 596 - 1614 km . . . 169
7.5(c) Velocity model MVBS for depths 1823 - 2891 km . . . 170

8.1 Density of measurements for the $SS-S$ dataset, plotted in 5° spherical caps . . . 181
8.2 Density of measurements for the $SSS-SS$ dataset, plotted in 5° spherical caps. . . . 181
8.3(a) Velocity model from Su *et al.* (1994) for 12 different depths . . . 182
8.3(b) Velocity model from Su *et al.* (1994) for 12 different depths . . . 183

8.4(a) Reprint of Plate 1 from Li & Romanowicz (1996), depths 150 - 750 km 184
8.4(b) Reprint of Plate 1 from Li & Romanowicz (1996), depths 850 - 2800 km 185
8.5 Model S16B30 reproduced from Masters *et al.* (1996). Note that the scale bar is in variation of $\frac{\delta v}{v}$ and not percent. 186
8.6 Model MVBS for depths 1823 - 2891 km, displayed for degrees 1-12 only. 187
8.7 Model S12_WM13 for depths 1823 - 2891 km, displayed for degrees 1-12 only. 188
8.8 Model MVBS for depths 1823 - 2891 km, displayed for degrees 1-8 only. 189
8.9 Model U84L85/SH for depths 1823 - 2891 km, displayed for degrees 1-8 only. 190
8.10 Q model, QR19, from Romanowicz (1995). 191
8.11 Model QMU3b from Selby (1998). 192
8.12 Upper mantle combined body wave and surface wave q_μ model from Bhattacharyya (1996). 193
8.13 q_μ model from Bhattacharyya *et al.* (1996). 194
8.14 Model MVBS for depths 25-329 km showing the hotspot distribution. Hotspots are plotted as green circles. 195
8.15 Values of Δt calculated at the hotspot locations for model MVBS at a depth of 129 km. 12 hotspots correspond to regions of high velocity and 35 correspond to regions of low velocity. 195
8.16 Model MQBS showing the hotspot distribution. Hotspots are plotted as green circles. . 196
8.17 Values of Δt^* calculated at the hotspot locations for model MQBS at a depth of 129 km. 27 hotspots correspond to regions of high attenuation and 20 correspond to regions of low attenuation. 196

B.1(a) Model S20RMC18 of Van Heijst (1997) for depths 50-400 km 214
B.1(b) Model S20RMC18 of Van Heijst (1997) for depths 500-1200 km 215

C.1 Synthetic traces for 4 stations from event 950712B. For each station pair, the top trace shows the synthetic seismogram with the usual filters applied (see Section 2.2). The lower trace shows the synthetic seismogram with an additional t^* filter of 3.0 seconds applied. The "a" and "b" intervals show the windows selected for the S and SS phases respectively. The S and SS ticks mark the PREM travel times for the S and SS phases. 218
C.2 Seismograms for 4 stations from event 950629D. For each station pair, the top trace shows the raw unfiltered seismogram, the lower trace shows the same seismogram with an additional t^* filter of 3.0 seconds applied. The "a" and "b" intervals show the windows selected for the S and SS phases respectively. The S and SS ticks mark the PREM travel times for the S and SS phases. 220

List of Tables

1.1 Summary of the effect of scattering for different length scales. 6

2.1 A summary of the filters applied to the $SS - S$ dataset and their effects. 26

3.1 Take-off angle for S, SS and SSS rays over the distance range of this study. 35

4.1 Results from the spectral ratio method for event 960502F. Δt^* is the $SS-S$ differential attenuation and $\frac{\sigma_a}{\pi}$ is its standard deviation. Δt_P^* is the PREM value of $SS - S$ differential attenuation computed from the PREM tables. 59

6.1 Summary of the different $SS - S$ velocity models. N is the total number of data points used and λ_e is the number of effective eigenvalues. 102

6.2 Summary of the different $SSS - SS$ velocity models. N is the total number of data points used and λ_e is the number of effective eigenvalues. 103

6.3 Summary of the different velocity models obtained from the combined $SS - S$ and $SSS - SS$ datasets. N is the total number of data points used and λ_e is the number of effective eigenvalues. 105

6.4 Summary of the different attenuation models obtained using residuals from the waveform fitting method. N is the total number of data points used, λ_e is the number of effective eigenvalues. 107

6.5 Summary of the different attenuation models obtained using residuals from the spectral ratio method. N is the total number of data points used, λ_e is the number of effective eigenvalues. 108

8.1 Correlation coefficient between models MVCOMB2 and MQCOMB2 for various depths. The probability value gives the probability that the correlation could have arisen by chance. 174

8.2 Correlation coefficient between models MVBS and MQBS for various depths. The probability value gives the probability that the correlation could have arisen by chance. . . . 179

C.1 Results of synthetic testing of the waveform fitting method for event 950712B. The value of Δt^* corresponds to the difference between the differential t^* values obtained with and without the additional t^* filter of 3 seconds applied. Δ is the epicentral distance in degrees, $\sigma_{\Delta t^*}$ is the error in Δt^* as obtained from the waveform fitting method, the fit parameter is also given for reference. 217

C.2 Results from testing of the spectral ratio method for event 950629D using real seismograms. The value of Δt^* corresponds to the difference between the differential t^* values obtained with and without the additional t^* filter of 3 seconds applied. Δ is the epicentral distance in degrees, $\sigma_{\Delta t^*}$ is the error in the differential value of Δt^* as obtained from the spectral ratio method. 219

Chapter 1

Introduction

Seismology is one of the only tools available for studying the deep interior of the Earth. An understanding of the magnitude and distribution of the elastic and anelastic properties and density in the Earth's interior is important for a wide variety of geophysical, geochemical and astronomical studies. The technique of seismic tomography provides a method for investigating Earth structure. In tomography the aim is to provide as accurate a map of the three dimensional distribution of the seismic parameters within the Earth as is possible.

Seismic parameters may be separated into two main categories: elastic and anelastic. Elastic processes are those in which no energy is lost as a seismic wave passes through a region. Anelastic processes are those in which energy loss occurs i.e. the seismic waves are attenuated. Consequently maps of the anelastic structure of the Earth contain information about seismic attenuation, whereas models of elastic structure do not.

Models of the spherically symmetric component of Earth structure have existed for almost 60 years (Jeffreys & Bullen, 1940). Over time these models have become increasing more accurate (Gilbert & Dziewonski, 1975; Dziewonski & Anderson, 1981; Kennett & Engdahl, 1991).

Seismic tomography has been used to construct models of the three dimensional Earth structure since the late 1970's. Over the past two decades there has been a dramatic increase in both the quantity and quality of data available. These factors, in addition to the technological advances in computation have allowed increasingly more detailed models of Earth structure to be constructed. The velocity structure in many regions of the Earth is now quite well known, although some areas lack adequate resolution such as the transition zone and some parts of the the lower mantle. However, substantially less is known about the distribution of intrinsic attenuation. Only a very limited number of studies have been carried out to investigate the lateral variation of attenuation within the Earth, a problem this thesis attempts to address.

In this thesis, two new techniques for making differential travel time and attenuation measurements from shear waves are presented. Using these measurements models of the variations in shear wave

velocity and intrinsic attenuation q_μ in the upper mantle are constructed. The outline of this thesis is as follows:

- In chapter 1, Sections 1.1 - 1.8 present a detailed review of seismic attenuation including a discussion of some of the current three dimensional models of intrinsic shear attenuation. Section 1.9 presents a short review of seismic velocity tomography with specific reference to global models of shear velocity.

- Chapter 2 describes the types of data used, the event selection procedure and the filters applied to the data. Maps showing the source and station locations, and histograms giving the source depth and magnitude distributions are also provided.

- In chapter 3, we present a new method, subsequently referred to as the "waveform fitting method", for determining both differential travel times and t^* values from multiple S phases.

- In chapter 4, a second method for determining differential t^* values is presented. This method, referred to as the "spectral ratio method", uses only real unfiltered waveforms.

- Chapter 5 presents the results from the waveform fitting and spectral ratio methods. The range and distribution of the residuals, their behaviour with epicentral distance, the geographical distribution of the residuals, the density of residuals and the distribution of errors are amongst the topics discussed.

- In chapter 6 the travel time and t^* residuals are inverted to obtain three dimensional models of shear velocity and attenuation. The method used is that of damped weighted least squares. Before inversion, corrections are made to the travel time residuals for the effects of the Earth's crust and ellipticity. Models are constructed for the $SS - S$, $SSS - SS$ and for the combined $SS - S$ and $SSS - SS$ datasets. Resolution tests are also presented.

- In chapter 7 we combine the body wave data of this study with surface wave datasets of Van Heijst (1997) and Selby (1998) to obtain combined models of velocity and attenuation respectively.

- Chapter 8 discusses the models presented by chapters 6 and 7. The velocity and attenuation models are compared with each other and with existing models. The geophysical implications of the models are also discussed.

- In chapter 9 the conclusions of this study are presented.

1.1 Introduction to seismic attenuation

Attenuation is the loss of energy that occurs as a wave propagates through the Earth. This energy loss occurs because the Earth does not behave as a truly elastic solid. Measuring the amount of attenuation and its variation with location can provide information about the material properties of the rocks and minerals through which a particular seismic wave has travelled. An understanding of attenuation is also important for assessment of the seismic risk in a particular area, the design of earthquake resistant structures and the detectability and yield determination of underground nuclear explosions.

The amplitude of a propagating seismic wave is affected by three factors: geometric spreading, anelastic attenuation and scattering. Of these only anelastic attenuation involves true energy loss related to the intrinsic physical properties of the medium. Although scattering does not involve loss of energy, the energy of the original wave is reduced and the effects of scattering are often difficult to distinguish from those of attenuation. Scattering may provide information on the spatial characteristics and dimensions of possible heterogeneities of the medium.

If the results of measurements of seismic attenuation are to be fully interpreted it is essential to have a good understanding of the different attenuation mechanisms. With such understanding it is then possible to compensate for individual effects. Some fundamental definitions commonly used in attenuation studies are presented in Section 1.2. The different mechanisms of attenuation are summarised in Section 1.3. The stress-strain relationship for attenuation in an anelastic solid is described in Section 1.4. The frequency dependence of seismic attenuation is discussed in Section 1.5. The absorption band model for seismic attenuation is described in Section 1.6. For a more comprehensive review of seismic attenuation, both nomenclature and mechanisms, the reader is referred to Cormier (1989) and Anderson (1989). Equally important is how attenuation varies both regionally and globally within the Earth. Various studies of seismic attenuation are discussed on a broad scale, ranging from global studies in Section 1.7 to regional studies in Section 1.8.

1.2 Definition of the attenuation parameters

The most commonly used measure of seismic attenuation is the quality factor, Q. Q is an *intrinsic* property of the rock and can be defined in terms of the ratio of wave energy to its rate of decay:

$$Q = \frac{\omega E}{-dE/dt} \tag{1.1}$$

where E is the instantaneous energy, dE/dt is the rate of energy loss and ω is the angular frequency. Equation (1.1) can also be written as (Anderson, 1989):

$$Q = \frac{2\pi E_{max}}{\Delta E} \tag{1.2}$$

where E_{max} is the total stored energy and ΔE is the amount of energy lost in one cycle of harmonic excitation. If a wave loses a large amount of energy per cycle, i.e. it passes through a highly attenuating region then the value of Q will be low. Hence, it follows that a wave passing through a weakly attenuating medium will lose a small amount of energy per cycle and thus Q will be large. It is often useful to instead use the reciprocal of the quality factor, Q^{-1}. This is because the attenuation of a seismic wave travelling through regions with different properties can be written as a linear sum of terms in $1/Q$ instead of Q. From this it is now possible to define the attenuation parameter. The attenuation parameter, t^* is defined as the time integral of the inverse quality factor $(1/Q)$ along the ray path (Der *et al.*, 1982):

$$t^* = \int_{ray} \frac{1}{Q} dt \tag{1.3}$$

This expression can also be written as:

$$t^* = T\overline{Q^{-1}} \tag{1.4}$$

where T is the total travel time along the path and $\overline{Q^{-1}}$ is the mean inverse quality factor along the path. If the travel time does not vary, then an increase in t^* implies a decrease in attenuation and vice-versa. Thus t^* can be used as a direct measure of body wave attenuation. t^* itself is path-dependent since it is a function of the Q variation in the Earth. Thus if a seismic wave travels through a series of n different regions, t^* can be written as a linear sum of the contribution due to each region:

$$t^* = \sum_{i=1}^{n} t_i^* = t_1^* + t_2^* + t_3^* + \cdots + t_n^* \tag{1.5}$$

and

$$t_i^* = \frac{T_i}{Q_i} \tag{1.6}$$

where T_i is the travel time due to the region i and Q_i is the quality factor for region i. This additive property makes t^* a convenient parameter for the measurement of body wave attenuation.

1.3 Mechanisms of attenuation

Geometric spreading

The reduction in wave amplitude caused by geometrical spreading arises from the decrease in energy density that occurs as an elastic wavefront expands. As a wave propagates the surface area of the wavefront increases. This spreading out of the wavefront results in a decrease in the seismic energy or energy density with no loss of elastic energy. For a homogeneous Earth of constant velocity and density, the geometric spreading of a seismic body wave is proportional to the distance between source and receiver. Within the real Earth however, velocity and density vary more strongly with depth than laterally and thus the spreading is more complex. However given a model of this variation the

geometrical spreading can easily be calculated. An example can be found in Aki & Richards (1980a).

Scattering

Scattering is not a true energy loss; instead it involves the redistribution of elastic energy. Scattering occurs by reflection, refraction and mode conversions (i.e. P to S) of elastic energy by irregularities in the medium. These irregularities may be discontinuous or rapid variations in the velocity or density of the medium. In the Earth the most important discontinuities are the approximately planar layers in the crust and the spherically symmetric boundaries such as the core-mantle boundary (CMB) and the Mohorovičić discontinuity (Moho) between the crust and the mantle. In addition to these discontinuities rapid variations in velocity and density occur over variable length scales, the distribution of which are poorly understood and may vary strongly with depth. Different scales of heterogeneity affect seismic waves in different ways. Large-scale (global) heterogeneities have the effect of splitting the normal modes of the Earth which implies that the Earth is spherically asymmetric, whereas small scale (local) heterogeneities tend to generate coda especially at high frequencies (Wu, 1989).

The reduction in amplitude due to multiple scattering from such heterogeneities can be identified on a seismogram as the coda prior to the main arrival. High frequency energy is preferentially transferred out of the main arrival and into the coda. Scattering effects are most easily corrected for at low frequencies. Wu (1989) states that at the higher frequencies (> 1 Hz) scattering can cause apparent elastic attenuation making the two difficult to distinguish.

The scattering of seismic waves depends on both the wavelength of the travelling wave and the length scale of the heterogeneities. The type of scattering which occurs depends on P, which is the ratio of the scale length of heterogeneity, L to the wavelength of seismic energy, λ. For body waves with frequencies low enough so that the wavelength is much larger than the scale length of heterogeneity (i.e. $L << \lambda/100$ or $P << 0.01$) the effects of scattering can often be neglected. This is because the individual heterogeneities are too small to be *seen* by the waves. The medium can then be treated as if it were homogeneous and the effect of the heterogeneity is observed as some mean property of the medium, such as a lower effective wave speed or anisotropy. At very low frequencies, where the wavelength is very much greater than the scale length of the heterogeneities (i.e. $\lambda >> L$) the domain of Rayleigh scattering is reached. In this case the energy loss in the forward direction is inversely proportional to the frequency raised to the power four, f^4. Scattering in this domain may cause significant apparent attenuation.

For wavelengths that are significantly smaller than the scale length of heterogeneity small angle scattering occurs (i.e. $\lambda << L$). The effect of small angle scattering can be calculated using ray theory providing both the distribution and shape of the scatters is known.

Large angle scattering occurs for higher frequencies in which the wavelength is of the same order of magnitude as the scale length of heterogeneity (i.e. $\lambda \approx L$). The presence of such heterogeneities can significantly alter the propagation of the seismic wave, in this domain calculations are complex.

Parameter $P = L/\lambda$	Description
$P << 0.01\ L << \lambda/100$	Homogeneous medium with properties equivalent to the mean of the heterogeneities
$P << 0.1\ L << \lambda$	Rayleigh Scattering: scattered power proportional to f^{-4} i.e. λ^{-4}; may cause apparent attenuation
$P \approx 1\ L \approx \lambda$	Large Angle Scattering: Incident power scattered in lots of different directions at large angles to the incident direction; main component of the coda generation; can cause severe apparent attenuation
$P >> 1\ L >> \lambda$	Small Angle Scattering: effects can be calculated providing the distribution and shape of the scatters is known

Table 1.1: Summary of the effect of scattering for different length scales where L is the scale length of heterogeneity and λ is the wavelength of seismic energy.

Fully numerical calculations such as finite-difference solutions of the elastic wave equation are often the only method for predicting the effects of scattering on the wave field. This type of scattering is thought to be the main component in the coda wave generation and can cause severe apparent anelastic attenuation.

The effect of scattering for different scale lengths and wavelengths is summarised in Table 1.1. A more detailed description is provided by Wu (1989).

Anelastic attenuation

Anelastic or intrinsic attenuation is the energy lost to heat and internal friction during the passage of a seismic wave through a specific medium. It is best illustrated by examining the behaviour of the stress-strain relation (see Section 1.4). Stress is the normal force per unit area applied to a solid. Strain is a non-dimensional measure of the deformation of the solid due to the applied stress. In a perfectly elastic body the stress σ is directly proportional to the strain ϵ by a constant of proportionality M (the elastic modulus) such that:

$$\sigma = M\epsilon \tag{1.7}$$

In such an ideal elastic body the application of a stress results in no loss of energy since there is no permanent deformation or strain. However in an anelastic body application of such a stress results in some permanent deformation and loss in energy. The Earth behaves anelastically as indicated by the absorption of body waves and decay of free oscillations, therefore seismic waves lose energy as they travel through the Earth.

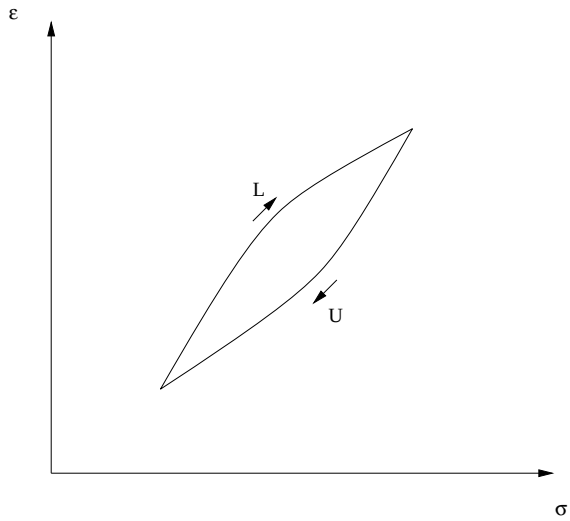


Figure 1.1: The stress-strain relation for loading and unloading of an anelastic solid after Wu (1989): The solid is loaded (line L) and unloaded (line U) resulting in energy loss to heat and internal friction. The amount of energy lost is proportional to the area enclosed by the hysteresis curve (i.e. the area enclosed between lines L and U).

1.4 The stress-strain relationship

All real solids are to some extent anelastic (i.e. attenuative). Therefore a cycle of increasing and decreasing stress does not produce a perfectly proportional increase and decrease in strain. Instead hysteresis results, in which the strain lags behind the stress (see Figure 1.1). The area enclosed between the loading, (line L) and unloading, (line U) curve is proportional to the energy lost to heat and internal friction in a single cycle. In the case of the stress cycle associated with the passage of a seismic wave, the energy loss to such internal friction within the region through which the wave is passing, is then not available to deform adjacent regions of the solid just ahead of the wavefront.

On examination of the hysteresis curve (Figure 1.1), it is clear that the stress-strain relationship for an anelastic material can no longer be described by a simple constant of proportionality as in the case of an elastic solid. A more complex relationship is required which must incorporate both the time lag of strain and the time history of the applied stress. If it is assumed that there is a linear dependence of stress on strain history then the general theory of viscoelasticity results. In this case it is possible to obtain a simpler form of this relationship by Fourier transform to the frequency domain. In this domain and for a given frequency, the Fourier transform of the stress will be proportional to the Fourier transform of the strain by an elastic modulus $M(\omega)$. The phase lag, δ, of strain means the modulus must be a complex number. It must also be frequency dependent since the phase lag of strain is dependent on the time history of the stress. This frequency dependence means that the propagation of a stress pulse will be dispersive, where higher frequencies travel faster than lower frequencies. For

a nearly elastic, low loss, i.e. high Q solid, Q is related to $M(\omega)$ by (Anderson, 1967; Cormier, 1989):

$$Q^{-1} = \frac{M_I}{M_R} = \tan\delta \approx \delta \tag{1.8}$$

where M_R and M_I are the real and imaginary parts respectively of the elastic modulus such that: $M = M_R + iM_I$, δ is the phase lag of the stress behind the strain and Q is the quality factor as defined previously. From this it is clear that since M is frequency dependent then Q also depends on frequency. This frequency dependence of Q and the resulting absorption band model are discussed in sections 1.5 and 1.6.

1.5 The frequency dependence of attenuation

The frequency dependence of attenuation did not begin to be fully understood until the comparison of studies conducted in widely separated frequency bands, e.g. body waves and free oscillations. One of the earliest observations was made by Gutenberg (1958) who noted that if the phase $PKPPKP$ was to be observed then its t_P^* must be inversely proportional to ω. Subsequent studies, comparing free oscillation and body wave measurements in the range 0.0001-0.1 Hz with body wave studies in the 1-10 Hz band also required an increase in Q with frequency to explain the amplitude spectra in the 1-10 Hz band (Cormier, 1989).

Many studies of the frequency dependence of seismic attenuation over specific bandwidths have been performed (e.g. Anderson *et al.* (1977); Der & Lees (1985) and Bulter (1987)). For frequencies less than approximately 1 Hz, it appears that Q is effectively independent of frequency. Bulter (1987) compares surface waves with oceanic S-waves and suggests that for frequencies greater than approximately 1 Hz, seismic attenuation is strongly dependent on frequency. Der & Lees (1985) suggest that attenuation is frequency dependent in the band 0.3-2.0 Hz. Anderson *et al.* (1977) present an absorption band model (ABM) of Q in which attenuation is proposed to be independent of frequency over a broad frequency range. This absorption band model is discussed in Section 1.6.

1.6 The seismic absorption band model of attenuation

Background information

The physical mechanism for attenuation in the mantle is uncertain, but is most likely due to relaxation processes such as thermoelasticity, grain boundary effects and, possibly, phase changes. For a review of possible mechanisms of attenuation the reader is referred to Anderson (1967). Consider a solid having a single relaxation time, τ, for which the dissipation of energy as a function of frequency,

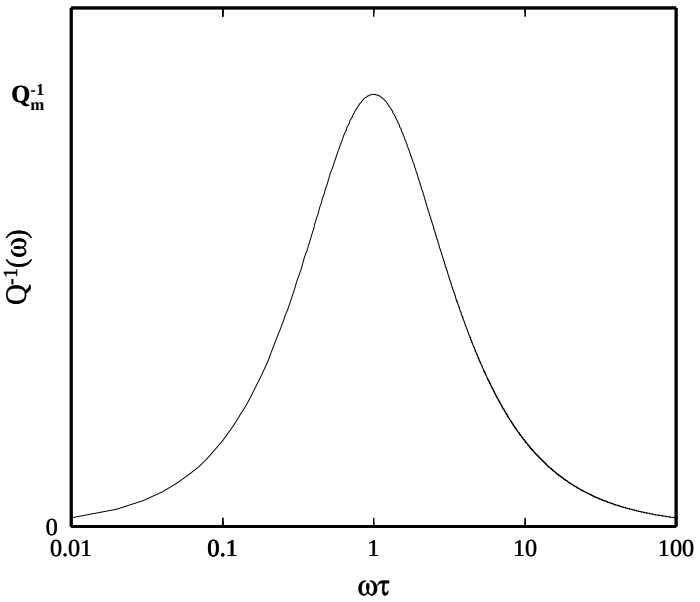


Figure 1.2: Debye function of $Q^{-1}(\omega)$ for an anelastic solid having a single characteristic relaxation time of τ.

$Q^{-1}(\omega)$ is given by a Debye function of frequency:

$$Q^{-1}(\omega) = 2Q_m^{-1}\frac{\omega\tau}{1+\omega^2\tau^2} \tag{1.9}$$

where Q_m^{-1} is the maximum or peak absorption occurring when $\omega\tau = 1$ as shown in Figure 1.2. The high and low frequency asymptotes of Q^{-1} are, respectively:

$$Q^{-1}(\omega) = 2Q_m^{-1}\omega\tau \qquad \omega\tau \ll 1 \tag{1.10}$$

$$Q^{-1}(\omega) = 2Q_m^{-1}(\omega\tau)^{-1} \qquad \omega\tau \gg 1 \tag{1.11}$$

However, in general solids and particularly mantle silicates are not characterised by a single relaxation time and a single Debye peak. Instead they are described by a distribution of relaxation times which results in a broadening of the peak shown in Figure 1.2, giving rise to an absorption band. It is possible that Q may depend weakly on frequency over such a band. However seismic values for Q^{-1} are roughly independent of frequency suggesting that seismic frequencies must lie within such a broad absorption band (Anderson *et al.*, 1977). It is possible to produce a nearly constant Q^{-1} by superposition of elementary relaxation peaks with τ distributed continuously between τ_1 and τ_2 (Anderson *et al.*, 1977). Such a distribution of relaxation times gives:

$$Q^{-1}(\omega) = \frac{2Q_m^{-1}}{\pi}\tan^{-1}\left[\frac{\omega(\tau_1-\tau_2)}{(1+\omega^2\tau_1\tau_2)}\right] \tag{1.12}$$

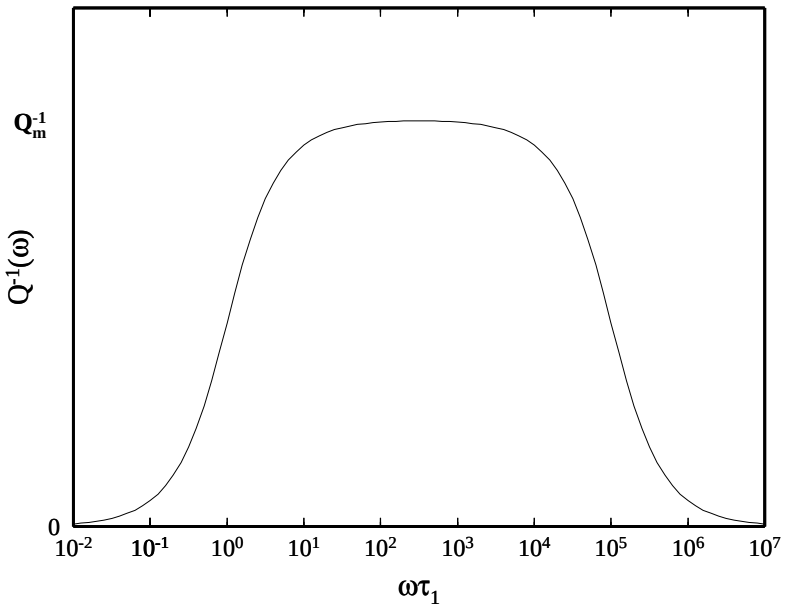


Figure 1.3: Attenuation in an anelastic solid possessing a range of characteristic relaxation times distributed continuously between τ_1 and τ_2.

as shown in Figure 1.3.

For $\tau_2^{-1} < \omega < \tau_1^{-1}$ the value of Q^{-1} is constant and equal to Q_m^{-1}, implying that the attenuation is largely independent of frequency over a broad band. Within the Earth such a distribution of relaxation times is used to describe the absorption band model discussed subsequently.

Absorption-band Q model for the Earth

The concept of an absorption band model is now taken a step further. Given a polycrystalline solid having a variety of grain sizes, orientations and activation energies, the absorption band as illustrated in Figure 1.3 can be many decades in width. The assumption that attenuation in the mantle is due mainly to thermally activated processes means that the relaxation times will be strongly dependent on both temperature and pressure. Therefore the location of the absorption band may change with depth since the temperature and pressure of the Earth are depth dependent.

If the solid has a non-zero elastic modulus at low frequency and a finite elastic modulus at high frequency then there must exist low and high frequency cut-offs in the relaxation spectrum. Therefore, physically the relaxation times cannot assume arbitrarily low and high values. Anderson & Given (1982) approximate the absorption band according to:

$$\begin{aligned} Q &= Q_{min}(f\tau_2)^{-1} && f < 1/\tau_2 \\ Q &= Q_{min}(f\tau_2)^{\alpha} && 1/\tau_2 < f < 1/\tau_1 \\ Q &= Q_{min}(\tau_1/\tau_2)^{\alpha}(f\tau_1) && f > 1/\tau_1 \end{aligned}$$

where $f = \omega/2\pi$ is the frequency, τ_1 and τ_2 are the short and long period cut-offs respectively and

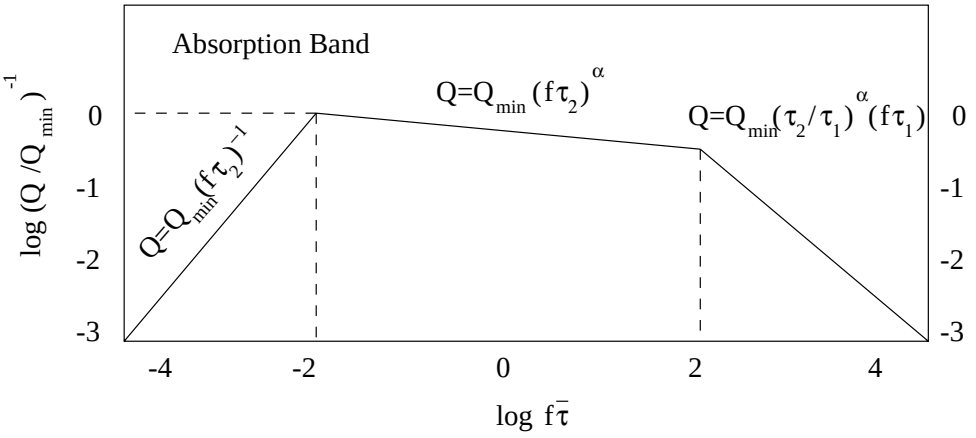


Figure 1.4: Schematic illustration of the absorption band (Anderson & Given, 1982). Q_{min} is the shear wave attenuation in the mantle, τ_1 is calculated as a function of depth from seismic data and α and τ_2/τ_1 are fixed.

Q_{min} is the minimum Q which occurs when $f = 1/\tau_2$, provided $\alpha > 0$. Anderson & Given (1982) used this approximation to model the attenuation in the mantle and core of the Earth (see Figure 1.4). The resulting model reproduced from Anderson (1989) is shown in Figure 1.5. This ABM is a globally-averaged model of the attenuation structure of the Earth. The value of Q_{min} is obtained by examining the minimum Q modes i.e. the mantle Rayleigh and Love waves and is assumed to remain constant with depth. The values of α and τ_1 are found using data which samples the mid-mantle at various frequencies. The parameter τ_2 is found using normal modes ${}_0S_2$ through to ${}_0S_5$. α and Q_{min} are the fixed parameters and are found using the procedure outlined above to be $\alpha = 0.15$ and $Q_{min} = 80$.

This ABM model of Q has been widely used in studies of the frequency-dependence of seismic attenuation (Anderson & Given, 1982; Der *et al.*, 1982; Der & Lees, 1985; Sharrock *et al.*, 1995) which have resulted in better constraints than in previous absorption band models.

Although we use broadband data, the period range extends only between $\approx 5 - 25s$. As a result, Q is assumed to be frequency independent throughout this study.

1.7 Earth models and studies of attenuation

1.7.1 Background and motivation

The study of seismic attenuation can provide a clearer understanding of the intrinsic properties of the materials within the Earth. Since attenuation is potentially a direct measure of anelasticity, it can yield information about the composition, state and temperature of the Earth's deep interior and how such parameters vary with depth. Most of the early work investigating Earth structure ignored attenuation



Figure 1.5: Absorption band model of attenuation in the Earth at various depths where Q is the quality factor for shear waves. Reproduced from Anderson (1989).

and concentrated on studying the variations of wave speed within the Earth. This was because, given the quality of data in the past, it was much easier to accurately measure arrival times than waveform amplitudes. Waveform amplitudes have consistently been notoriously difficult to interpret as they are subject to effects such as focusing, site amplification and instrument miscalibration. The advent of large quantities of high quality, broad-band digital data in recent years has made measurement of waveform amplitudes substantially more reliable and therefore the frequency of attenuation studies has increased accordingly.

The study of global Earth structure has involved the use of large datasets from the bulletins of the International Seismology Centre (ISC) and World Wide Standardised Seismic Network (WWSSN). In addition the increase in long period data from both the Global Digital Seismic Network (GDSN)

and the International Deployment of Accelerometers (IDA) has also contributed. These large datasets can be analysed to obtain three dimensional Earth structure, a process known as *seismic tomography* (Anderson & Dziewonski, 1984). With the increase in both the quantity and quality of data and advances in computational power global seismology has progressed rapidly in recent years.

Until recently most studies of Earth structure have been directed at obtaining global or regional velocity structure. [1] However, on realising the importance of anelasticity and dispersion when inverting for a reference Earth model, some researchers also made attempts to retrieve global and regional attenuation structure.

Models of Earth structure can be separated into two main types: spherical and aspherical. Spherical models describe radial variations of seismic parameters within the Earth. They are spherically symmetric and parameterised with respect to the radius only. Aspherical models are used to describe lateral variations of seismic parameters within the Earth. Spherical models will be described first followed by aspherical models, with specific reference to models of seismic attenuation in each case.

1.7.2 Spherical Earth models and attenuation

By the early 1980's many spherical whole Earth models had been proposed to describe Earth structure. The majority of these models made estimates for the bulk properties of the Earth such as density, P wave speed and S wave speed, with some making attempts to describe the anelasticity as a function of depth. The main problem with the latter is that values of Q were not particularly well determined then (Dziewonski & Anderson, 1981). Many such whole Earth models have been published for example 1066A and 1066B (Gilbert & Dziewonski, 1975), PEM (Parametric Earth Models) Dziewonski *et al.* (1975) and PREM (Preliminary Reference Earth Model) (Dziewonski & Anderson, 1981). Gilbert & Dziewonski (1975) used normal mode data and both the mass and moment of inertia of the Earth to create their Earth models 1066A and 1066B. The essential difference between these two models is in how the upper mantle structure is represented. Model A has continuous velocity and density variations from the Moho to the CMB, whereas model B has sharp discontinuities in the upper mantle at 420 and 670 km. In contrast the PREM model was formulated from a combination of normal mode periods, travel time data and Q values obtained from normal modes and both the mass and moment of inertia of the Earth. This model has discontinuities located at 220, 400 and 670 km depth with a continuous variation of velocity and density between these discontinuities. Figure 1.6 shows the variation in isotropic (1 Hz) compressional and shear velocity for the PREM model as a function of depth from the surface of the Earth (0 km) to the centre of the Earth (6371 km). The PREM model has an ocean layer of depth 3 km overlying the crust which extends to 24.4 km depth. The upper mantle extends to a depth of 670 km and is separated from the lower mantle by the transition zone (400 - 670

[1] In literature *velocity* is often used in place of *wave speed* with references made to velocity studies or velocity tomography. The use of velocity here is technically incorrect since velocity implies a vector quantity is being measured where in reality it is the scalar wave speed that is being measured.

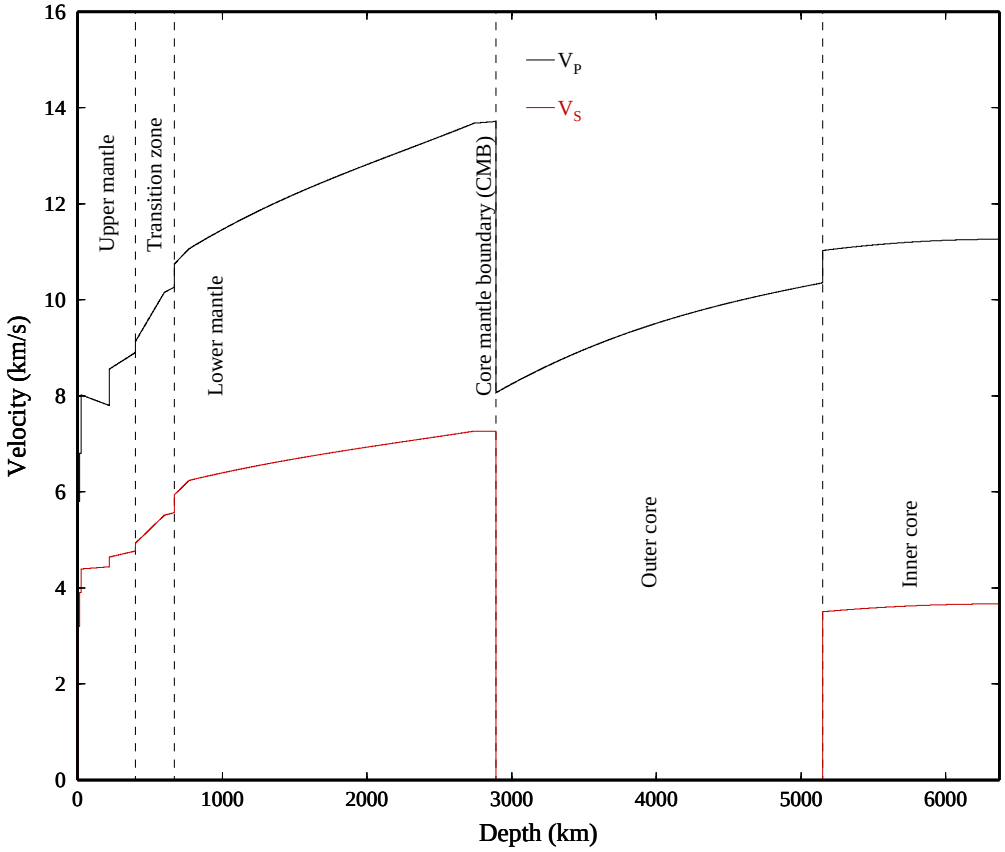


Figure 1.6: The PREM model, plotted using the coefficients given in Dziewonski & Anderson (1981).

km). The lower mantle is separated from the core by the core mantle boundary (CMB) at a depth of 2891 km. The inner core/outer core boundary occurs at a depth of 5149.5 km. Figure 1.7 shows the PREM upper mantle to illustrate the low velocity zone. In the PREM model, the low velocity zone is defined as the region between 80 - 220 km depth which is marked by a decrease in seismic velocities with depth.

Gilbert & Dziewonski (1975), Anderson & Hart (1978), Sailor & Dziewonski (1978), Dziewonski & Anderson (1981), Widmer *et al.* (1991) and Durek & Ekström (1996) have all published one-dimensional (radial) attenuation models for the average Earth which are primarily based on free oscillation and/or surface wave data. Although the modelling methods (strategies) and amount of detail included differs from one model to another, the average behaviour of shear attenuation, Q_μ as a function of radius obtained by each model is similar and they all have the following large-scale features in common:

1. A low Q region in the shallow mantle.

2. An intermediate Q transition region between the upper and lower mantle.

3. A high Q lower mantle, where Q_μ is found not to exceed 400 in any of the models listed.

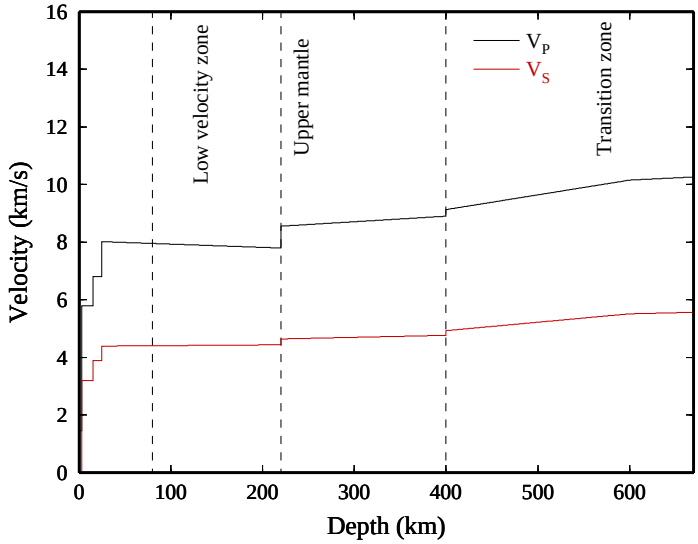


Figure 1.7: PREM upper mantle velocity structure. Note that the upper mantle is defined as the region from the base of the crust to a depth of 670 km.

4. Some finite amount of bulk attenuation, Q_κ.

Although the large-scale radial features appear to agree, appreciable differences in Q_μ and Q_κ do exist from one model to another. However, they all agree that the region of highest attenuation is located in the upper mantle which incidentally is where the largest lateral variation would be expected to occur.

One of the main problems in constructing Q models in the past has been that Q measurements could only be obtained for a relatively small number of modes due to problems with noise; only data lying above the noise level of individual recordings could be used. The development of the method of phase equalisation or "stacking" dramatically improved the signal to noise ratio allowing data from many recordings to be used simultaneously provided the source mechanism is known (Gilbert & Dziewonski, 1975). This technique has subsequently been used in studies of free oscillation (Sailor & Dziewonski, 1978) and body wave attenuation (Sipkin & Revenaugh, 1994).

1.7.3 Aspherical Earth models

The lateral variation of shear attenuation in the upper mantle has been investigated by the inversion of fundamental mode frequencies and apparent attenuation rates (Smith & Masters, 1989; Roult *et al.*, 1990; Suda *et al.*, 1991). These studies could only map structures of even harmonic degree and had limited success in explaining observations. Surface waves with periods > 150 seconds have been used to obtain maps of the lateral variation in Q_μ, (e.g. Romanowicz (1990); Durek *et al.* (1993)). Romanowicz (1990) used combinations of multiple surface wave orbits to eliminate the effects of focusing and defocusing and sought to constrain the degree 2 component of global Rayleigh wave attenuation. Durek *et al.* (1993) constrained spherical harmonic degrees up to 6, concluding that most of the data

could be explained by a model in which lateral variations in Q_μ^{-1} are concentrated in the low velocity zone. A variation on this technique was devised by Romanowicz (1994), which used both major and minor arc surface wave orbits to obtain information about odd degree attenuation structure. Subsequently this method was applied to low frequency (100-300 s) Rayleigh waves to obtain a large-scale three dimensional model of the upper mantle attenuation structure (Romanowicz, 1995). The model produced revealed lateral variations in shear attenuation limited to depths of less than 400 km.

Body wave measurements have also been used to study the attenuation in the mantle. These measurements are frequently complicated by the effects of waveform interference, scattering, source and receiver structure, multi-pathing and frequency dependent attenuation occurring when the corner of the mantle absorption band lies close to the body wave frequencies (Anderson & Given, 1982). Many regional body wave studies have been performed to obtain the attenuation structure of the mantle under specific regions (see Section 1.8 for more details). The differences between regions suggest that there are considerable variations in shear attenuation throughout the mantle.

Recently Bhattacharyya *et al.* (1996) obtained maps of global attenuation in the mantle from studies of body waves. They used differential $SS-S$ waveforms from long-period transverse component seismograms recorded at the Global Seismic Network (GSN) to constrain the lateral variation of shear attenuation in the upper mantle. They utilise a frequency domain measurement technique to measure both the amplitude and phase spectra of the S and SS waveforms. The differential amplitudes, and to some extent broadening of the pulse are used to constrain lateral variations in the shear attenuation of the mantle.

Of the studies mentioned so far only those performed by Romanowicz (1995) and Bhattacharyya *et al.* (1996) can be considered truly three dimensional, in the sense that both even and odd order harmonics are included in the resulting models. The main features of these two models are now discussed in more detail.

Model QR19 of Romanowicz (1995)

Model QR19 is given at six depth layers (100, 200, 310, 370, 466, 555 km), see Figure 8.10 for details. Depths 100-200 km are very similar: areas of high attenuation are observed along the mid Atlantic Ridge, across south east Asia, the eastern Pacific and western Europe with areas of low attenuation observed across North America, Australia, Antarctica and parts of South America and Africa. Depths 310-370 km are characterised by areas of high attenuation across most of the eastern Pacific, North America and the northern Africa/Red Sea area. Areas of low attenuation are observed in a belt from Europe across south east Asia and Australia to Antarctica with another region of low attenuation occurring in the Atlantic Ocean. Depths 466-555 km are similar to layers directly above except that the amplitude of the anomalies decreases. There is an additional area of low attenuation observed in South America for this depth range.

Q_β model of Bhattacharyya *et al.* (1996)

The Q_β model of Bhattacharyya *et al.* (1996) is presented at three different depths, (120, 310, 530 km) see Figure 8.13 for details. The top two layers are quite similar and show areas of high attenuation in the south east Pacific, across most of Africa and western Europe. Low attenuation features are observed across eastern Asia, Australia, the central Pacific, along the west coast of North America and across a large region of the central Atlantic. At 530 km depth the pattern is quite different, some of the areas of high and low attenuation have swapped over indicating that perhaps the stability of the model with depth is poor. For example along the west coast of North America the region of low attenuation observed in the layer above has changed to that of high attenuation. This also occurs in a band stretching from eastern Eurasia to the North of Australia. At 530 km depth areas of high attenuation are observed over much of Asia, Australia, the central Pacific and the west coast of North America. Areas of low attenuation are observed across the south Atlantic, the north central Pacific, the eastern Pacific, northern Africa and the Antarctic.

The models of Romanowicz (1995) and Bhattacharyya *et al.* (1996) both suggest some degree of correlation of attenuation with tectonic features. However, there seems to be little similarity between the two models and therefore it still remains to be seen if there is a Q model capable of fitting both surface wave and body wave data. This problem will be addressed in Section 7.1 where body wave and surface wave data are combined to produce a model compatible with both datasets.

1.8 Regional studies

Regional studies are important because they provide higher resolution information about a specific geographical area than can be obtained from global studies. Attenuation studies on regional length scales (e.g. across a continent) have been performed over many different geographical regions. These studies are useful because they provide higher resolution information over a particular geographic region than can be obtained from global studies. By incorporating results from regional models into global models it should be possible to obtain more refined and better constrained global models. Usually long period body wave (dominant period 20 s) data have been used. This is because the signal levels are typically high and effects such as scattering and multi-pathing are greatly reduced when using this type of data (Bhattacharyya *et al.*, 1996). However some studies have been performed using short period body waves or surface waves with varying degrees of success.

Der *et al.* (1982) used short-period, teleseismic P and S wave data to examine the frequency dependence and variation of anelastic attenuation in the mantle under the United States in the 0.5-4 Hz frequency range. They used P and S wave amplitude and spectral data to show that large variations in attenuation exist in the mantle beneath the United States. Their findings showed attenuation to be greatest in the south-western United States and lowest in the north and central shield regions. They also found that regional changes in $\bar{t}^*_S$ (the average attenuation factor for S waves) is around 3-4 times that of $\bar{t}^*_P$ (the average attenuation factor for P waves) and therefore the attenuation in the

mantle under the United States is predominantly due to shear losses. This work was subsequently extended by Der & Lees (1985), who used short-period body waves to study the frequency dependence of attenuation in the south-western United States. They found for short-period data with frequencies above 1 or 2 Hz that only an average t^* is obtainable and not a frequency dependent t^*.

Both these studies found that when using short period waves to investigate Q variations it is necessary to combine both amplitude and spectral measurements. Amplitude measurements can be unstable due to near source and near receiver structure, to the effects of focusing and the unknown crustal response which leads to the suggestion that more weight should be placed on spectral methods which have less sensitivity to these factors. Due to the strong variability in amplitude data, large quantities of information from many stations and azimuths must be used if reliable results are to be obtained using amplitude measurements from short-period body wave data. In an attempt to circumvent this problem Der *et al.* (1986) used teleseismic P and S waves recorded over a broad frequency range to describe both the depth and frequency dependence of Q under the northern shield areas of Eurasia. They used data in the range 0.02 - 8 Hz (i.e. long period through to short period) to make numerous t^* estimates from which a Q model of the Eurasian shield was constructed. The best fit model obtained required a minimum Q between 100 km and 200 km depth and higher Q values in the deeper mantle. The Q values obtained across the shield were found to be higher than the global average meaning that the amount of attenuation experienced by waves under the shield is less than that of the global average. Preliminary results from this study suggest that for frequencies in the range 0.02 to 8 Hz t^* is higher under tectonic regions than under shield regions suggesting that Q varies regionally as well as with frequency and depth.

Surface waves and oceanic S waves were used by Bulter (1987) to estimate the seismic attenuation in the western Pacific lithosphere. He found that Q remains fairly constant with frequency until about 1Hz after which it increases quite strongly with frequency.

A large number of studies have used multiple ScS body wave phases to obtain the whole mantle averaged shear attenuation under a particular region (Sipkin & Jordan (1980), Lay & Wallace (1983), Lay & Wallace (1988), Chan & Der (1988) and Sipkin & Revenaugh (1994)).

Frequency domain methods and the technique of phase equalisation and stacking were used by Sipkin & Jordan (1980), Lay & Wallace (1983) and Lay & Wallace (1988). Sipkin & Jordan (1980) obtained values of Q_{ScS} for a variety of regions including the Pacific, South America and China. Lay & Wallace (1983) and Lay & Wallace (1988) determined both ScS travel time and attenuation values beneath Mexico and Central America and the western United States respectively. A time domain method of obtaining Q_{ScS} was developed by Chan & Der (1988). They used a waveform and amplitude matching scheme to examine the regional variation of Q_{ScS} using data in the frequency band 0.02 to 0.1 Hz. The areas covered by their study included the Pacific, South America, Eurasia and North America. More recently Sipkin & Revenaugh (1994) used a combination of time (waveform inversion) and frequency (phase equalisation and stacking) domain techniques to estimate both differential travel

times and the multiple ScS attenuation operator under China.

All of these studies of Q_{ScS} found large variations of attenuation across regions implying large lateral variation in mantle attenuation. A good correlation with present day levels of tectonic activity was again found (active tectonic regions producing high values of attenuation, shield regions producing low values of attenuation).

The surface reflections of S and ScS can also be utilised to investigate regional variations in attenuation. Flanagan & Wiens (1990) use teleseismic sS and $sScS$ waveforms to provide constraints on the attenuation structure above deep seismic zones. The use both time and frequency domain techniques to estimate the average Q_β along sS and $sScS$ paths beneath the active Lau back arc spreading centre by comparison with S and ScS waveforms. They find low Q_β values which increase with depth suggesting high attenuation in the upper mantle with a rapid decrease in attenuation below 200-300 km. They also find lateral variations in Q_β indicated by very high attenuation near the active spreading centres and lower attenuation to the west of the Lau Ridge. Subsequently Flanagan & Wiens (1994) extended this work to examine the radial variation of attenuation in the upper mantle beneath inactive back basins. They use a spectral ratio technique to measure the differential attenuation between $sS - S$ and $sScS - ScS$ phase pairs to investigate the variation of attenuation with depth in the upper mantle of five inactive back arc basins: the Kuril Basin, Sea of Japan, Banda Sea, the Celebes and Sulu Seas, and the Shikoku Basin. In this study they employ two algorithms to compute the vertically averaged attenuation structure: a spectral stacking procedure and a least squares inversion. They find that the results obtained from the two algorithms are in good agreement. The Q_β models obtained for each region are found to be similar to each other within the uncertainties of the models. They find that attenuation does exist beneath inactive back arc basins, but that it is confined to depths shallower than 160 km. Their average radial model attenuation is consistent with the earlier study of Flanagan & Wiens (1990): low Q_β in the uppermost mantle with an increase in Q_β with depth.

1.9 Seismic velocity tomography

Since the late 1970's global three dimensional models of the mantle have been constructed using a variety of different data and techniques (e.g. Dziewonski *et al.* (1977); Masters *et al.* (1982); Woodhouse & Dziewonski (1984); Dziewonski (1984); Woodhouse & Dziewonski (1986); Giardini *et al.* (1987); Woodhouse & Dziewonski (1989); Inoue *et al.* (1990); Tanimoto (1990); Su *et al.* (1994); Grand (1994); Masters *et al.* (1996); Li & Romanowicz (1996); Grand *et al.* (1997); van der Hilst *et al.* (1997)). Reviews of various aspects of three dimensional imaging are provided by Dziewonski & Woodhouse (1987); Woodhouse & Dziewonski (1989); Ritzwoller & Lavely (1995).

Some of the first three dimensional models were constructed by Dziewonski *et al.* (1977) and Masters *et al.* (1982). Dziewonski *et al.* (1977) used P wave travel time residuals from data compiled by the ISC (International Seismology Centre) to obtain lower mantle P wave velocity heterogeneity. Masters *et al.* (1982) used free oscillation (normal mode) data to investigate heterogeneity in the Earth's upper mantle. Subsequent to the pioneering work of Dziewonski *et al.* (1977) many other studies have been carried out to refine the three dimensional images of Earth structure. These studies can be broadly classified depending on the types of data used. Examples of the data types used include:

1. Large collections of P, PKP, $PKIKP$ travel times, (e.g. Dziewonski (1984); Inoue *et al.* (1990); Morelli & Dziewonski (1991); Robertson & Woodhouse (1995); van der Hilst *et al.* (1997)).

2. Measurements of the locations of spectral peaks of surface wave modes and measurements of the phase and group velocity of surface waves, (e.g. Roult *et al.* (1990); Trampert & Woodhouse (1995, 1996); Van Heijst (1997); Ekström *et al.* (1997)).

3. Complete waveforms of mantle waves used in a least squares inversion, (e.g. Woodhouse & Dziewonski (1984); Tanimoto (1990)).

4. Waveforms of long-period body waves, (e.g. Woodhouse & Dziewonski (1986, 1989); Tanimoto (1990); Su *et al.* (1994)).

5. Complete spectra of split multiplets in the normal mode spectrum, (e.g. Giardini *et al.* (1987); Ritzwoller *et al.* (1988)).

6. Differential and absolute S wave travel time measurements, (e.g. Woodward & Masters (1991c,b); Su *et al.* (1992); Grand (1994); Robertson & Woodhouse (1995)).

7. Measurements of surface wave amplitude anomalies to constrain elastic and anelastic structures in the upper mantle, (e.g. Romanowicz (1990); Durek *et al.* (1993); Romanowicz (1995); Selby (1998)).

Studies of type 1 have yielded information about the lower mantle P velocity structure. Types 2 and 3 have resulted in models of upper mantle S velocity structure. Studies of types 4,5,6 have

provided constraints on the lower mantle S velocity structure. Studies such as those mentioned in type 7 have yielded information about the anelasticity in the mantle (see Section 1.7 for more details).

Many of the earliest models included data of one type only e.g. Dziewonski (1984) used body wave data alone to constrain lateral variations of P velocity in the lower mantle. Woodhouse & Dziewonski (1984) used complete mantle waveforms to obtain a model for shear wave velocity in the upper mantle. More recent studies have incorporated many types of data. For example Woodhouse & Dziewonski (1986, 1989) used a combination of 6600 mantle waveforms and 8500 body wave records to estimate the shear velocity structure of the mantle. Tanimoto (1990) used a combination of approximately 6000 long period (40-100 s) SH and 1100 long period (100-500 s) Love waves to obtain a model of the long wavelength S velocity anomalies in the mantle. Su *et al.* (1994) used a combination of long period differential $ScS - S$, $SS - S$ measurements, absolute S and SS measurements, long period body wave ($>$ 45 s) and mantle waveforms (surface waves of frequency 3-7 mHz) to obtain a three dimensional model for the variation in shear velocity over the whole mantle. Li & Romanowicz (1996) used a combination body wave and surface wave SH waveform data to produce a whole mantle three dimensional model of shear velocity. Grand (1994) constructed a model of the shear velocity structure beneath the Americas and surrounding oceans using a combination S, ScS and multibounce SS, SSS and $SSSS$ SH waves. Robertson & Woodhouse (1995) used P and S travel time data obtained from the ISC catalogue to obtain global models of the P and S velocity heterogeneity in the lower mantle. Masters *et al.* (1996) used a combination of absolute and differential travel times, surface wave phase velocities and normal mode structure coefficients to construct a model of the shear velocity in the mantle.

There have also been several recent studies utilising large volumes of P wave travel time data. For example, Inoue *et al.* (1990) used over 2 million P arrival times from the ISC catalogue to obtain a whole mantle model of P velocity heterogeneity, using a block based parameterisation. Subsequently van der Hilst *et al.* (1997) have used P wave travel time residuals to construct a model of P velocity in the lower mantle, again using a block parameterisation instead of the spherical harmonic basis functions. Their model is not well resolved in the upper mantle but they claim to be able to resolve the features in the lower mantle with unprecedented detail.

Although the resolution of the models has increased with the addition of more types of data and improved computing power many of the large scale features of the models have remained the same. For example, in the uppermost mantle (50-250 km) all models which have sensitivity in this region observe correlation of high and low velocities with known tectonic features. Spreading ridges and convergent margins are observed to be seismically slow whereas continents are seen as high velocity anomalies. The features common to most models of shear velocity (e.g. Woodhouse & Dziewonski (1984, 1989); Su *et al.* (1994); Li & Romanowicz (1996); Masters *et al.* (1996)) are summarised below:

- Surface - 400 km: In the upper most mantle the large scale structure conforms to that expected from plate tectonics: high velocities underlying continental shields and platforms, low velocities

underlying spreading ridges. These features are seen to extend to depths of 350 km Woodhouse & Dziewonski (1984), 300 km (Su *et al.*, 1994), 300-400 km (Masters *et al.*, 1996), 320-400 km (Grand, 1994) and possibly as deep as 450 km Li & Romanowicz (1996).

- Transition zone 400-670 km: In the transition zone between the upper and lower mantle the higher velocities observed in the upper mantle often seem to penetrate down through this zone, whereas the low velocities do not seem to do so. There is less correlation between the shear velocity models in this region because surface wave and body wave measurements are less sensitive to the structure there (Resovsky & Ritzwoller, 1998). Model S20RMC18 of Van Heijst (1997) provides greatly improved resolution in this region as it was constructed using measurements of surface wave overtones which have particularly high sensitivity over this depth range. Over the depth range 400-700 km model S20RMC18 is dominated by high velocity anomalies associated with subduction whilst the Pacific remains slower than average.

- Lower mantle (670-2000 km): The magnitude of the heterogeneity is smaller than that observed in the upper mantle. The top of the lower mantle is dominated by high velocities which are thought to be the projection of subducted slabs from the upper mantle. At around 1000 km there is sharp change in the pattern of heterogeneity. The pattern changes from one dominated by a few long wavelength structures to one dominated by many shorter wavelength features which corresponds to a "white" power spectrum in the spherical harmonics. These short wavelength features continue to around 1700 km where another abrupt change occurs (Su *et al.*, 1994). Masters *et al.* (1996) observe this change at closer to 2000 km. At these depths the power spectrum is observed to change from one which is nearly white to one dominated by degrees 2 and 3.

- Lowermost mantle (2000 km - CMB): The pattern of heterogeneity is dominated by spherical harmonics of degrees degree 2 and 3 which continues to the CMB. This part of the mantle is characterised by a ring of high velocities circumscribing the Pacific Ocean and regions of low velocity are observed in the Central Pacific and beneath Africa. The size of the heterogeneity is observed to increase with depth rising to a maximum close the CMB in the D'' region (depths 2741-2891 km).

To illustrate many of these features see Figure 1.8 which shows model S16B30 of Masters *et al.* (1996). Red areas correspond to areas of lower than average velocity and blue areas correspond to areas of higher than average velocity. Note that the scale of this plot is in $\frac{\delta v}{v}$ and not percent. Further discussion of models of shear velocity variations within the mantle is provided in Chapter 8 where various existing models are compared with those obtained in this study.



Figure 1.8: Model S16B30 reproduced from Masters *et al.* (1996)

Chapter 2

Data

All the data used in this study are obtained from the optical jukebox located within the Department of Earth Sciences at Oxford University. The jukebox contains digitally recorded seismograms from the IRIS, GSDN and GEOSCOPE networks over the period 1977 - 1997. The data used for the studies in this thesis are digital, broadband, long period displacement SH seismograms recorded over the time period 1989 - 1996. The data are sampled at 1 second intervals. Only data recorded on broadband instruments are used as they record more high frequencies than the older long period instruments. These data should allow a more accurate estimation of body wave attenuation to be made. This means the dataset is restricted to only events from 1989 onwards as prior to this date very few stations were recording broadband signals. Long period data are used because the wavelengths involved allow large scale structure to be studied and also because the effect of fine scale structure is averaged out (Woodward & Masters, 1991a). Seismograms within the epicentral ranges $50^\circ - 105^\circ$ and $90^\circ - 180^\circ$ are used for the $SS - S$ and $SSS - SS$ studies respectively. For the $SS - S$ data this distance range is chosen so as to avoid the core shadow region for shear waves and for epicentral distances greater than 50° both the direct and reflected phases sample the source and receiver regions in a similar manner. For the $SSS - SS$ data the distance range is chosen to keep the ray paths in the lower mantle as much as possible and to avoid rays turning in the transition zone.

Only events of magnitude, M_w, in excess of 5.5 are used for the $SS - S$ study. For the $SSS - SS$ study only events with magnitude greater than 5.8 are used. The higher limit is used for the $SSS - SS$ study as for magnitudes less than 5.8 it becomes difficult to distinguish the SSS phase from noise.

The horizontal component seismograms are rotated to obtain longitudinal and transverse component seismograms. Throughout this study only transverse component seismograms are considered. These have two advantages over horizontal component traces: they help minimise the effects of $S - P$ phase conversions and they eliminate the effects of possible interference of SKS near 80° (Woodward & Masters, 1991a). Also SH reflections from the ocean floor are simpler.

2.1 Event selection

The procedures for selecting events suitable for use with the waveform fitting and spectral ratio methods are very similar. For the waveform fitting method the event suitability is determined using filtered seismograms whereas for the spectral ratio method the event suitability is determined from raw, unfiltered seismograms. The following discussion describes the event selection for the waveform fitting method. The event selection procedure is identical for the spectral ratio method except that the filtering stage is removed.

For the $SS - S$ study, the seismograms from events with magnitude $M_w > 5.5$, during the period 1989-1996 are retrieved from the jukebox. These seismograms are rotated to obtain transverse component seismograms. The transverse component seismograms are filtered using the suite of filters described in Section 2.2. After filtering, the traces from each event are examined visually to determine which are suitable for further processing. Those events where both the S and SS phases can be clearly distinguished from noise are selected for processing, i.e. only events having a high signal-noise ratio are undergo further processing. From around 2900 events examined only 597 are selected for any further processing. The locations of the events used for the $SS - S$ study are given in Figure 2.1. For the $SSS - SS$ study the same procedure is used except that the lower magnitude limit is set to 5.8 instead of 5.5. The $SSS - SS$ dataset consists of a total of 260 events, the locations of which are shown in Figure 2.2. The locations of the recording stations for the $SS - S$ and $SSS - SS$ studies are shown in Figures 2.3 and 2.4 respectively.

The events used for the two studies cover a wide range of epicentral depths. The distribution of source depth is depicted in Figure 2.5 for the $SS - S$ study and Figure 2.6 for the $SSS - SS$ study. The vast majority of the events used are shallow (< 50 km), a few are intermediate ($50 - 300$ km) and deep (> 300 km) events. There are very few events in the depth range $300 - 525$ km, consistent with the general pattern of global seismicity. The magnitude of the events used for the $SS - S$ and $SSS - SS$ studies varies between 5.50 - 7.86 and 6.0 - 7.98 respectively. Figures 2.7 and 2.8 show the magnitude distribution of the $SS - S$ and $SSS - SS$ events.

For the spectral ratio method it transpires that the distribution of sources and stations is almost identical to those selected for use with the waveform fitting method (Figures 2.1 - 2.4). For the $SS - S$ study a total of 548 events recorded on 122 stations are used. For the $SSS - SS$ study a total of 212 events recorded on 106 stations are used. Since the source and station distributions are so similar no additional figures are included.

It should be noted that throughout this study the CMT (Centroid Moment Tensor) depths and source locations are used. There is no particular advantage in using the CMT values as opposed to any other set of source parameters provided the system used is the same for all the measurements.

Filter applied	**Effect of filter**
Deconvolve instrument response	Deconvolves instrument
Cosine low pass filter between 6.0-7.0 s (= 0.1429-0.1667 Hz)	Removes high frequency noise, specifically microseisms
Pendulum high pass at 0.01Hz with $\eta = 1$ and $n = 2$	Removes low frequency noise
Butterworth low pass at 0.0833Hz and $n = 10$	Removes high frequency noise

Table 2.1: A summary of the filters applied to the $SS - S$ dataset and their effects.

2.2 Filters applied to the data

In order to make the windowing of individual phases easier, a series of filters are applied to the seismograms. A number of different filter combinations were tested before deciding on the final suite of 4 filters. The filters used and the effects they have on the data are summarised briefly in Table 2.1. Figure 2.9 gives the amplitude versus frequency curves for each of the filters used. Note that the cosine low pass filter is effectively redundant due to the application of the Butterworth low pass filter at 12 seconds. The same suite of filters is applied to both the $SS - S$ and $SSS - SS$ datasets. By using the same filters for all the seismograms we hope that any possible biasing effects caused by the filtering will be cancelled out or at least will be the same for all data. This combination of filters is chosen as it provides generally clean seismograms for the S, SS and SSS phases for both real and synthetic data. The filtering provides us with data filtered to have energy in the period range 8-20 s. It should be noted that this choice of filters is in no way unique, there are many alternative filter combinations that may produce similar effects. To illustrate the advantages of filtering the data, consider Figure 2.10 which shows filtered and unfiltered data from event 960305B. The seismograms from 4 stations are shown, each is denoted by the 3 or 4 letter station code (e.g. COR, GSC etc.) on the left hand side of the figure. The upper trace of each station pair shows the raw seismogram with no filters applied to it. The lower trace shows the same seismogram after the suite of filters previously discussed have been applied. From Figure 2.10 it is clear that filtering makes both the S and SS phases substantially more visible from noise and thus makes it much easier to window/pick these phases.

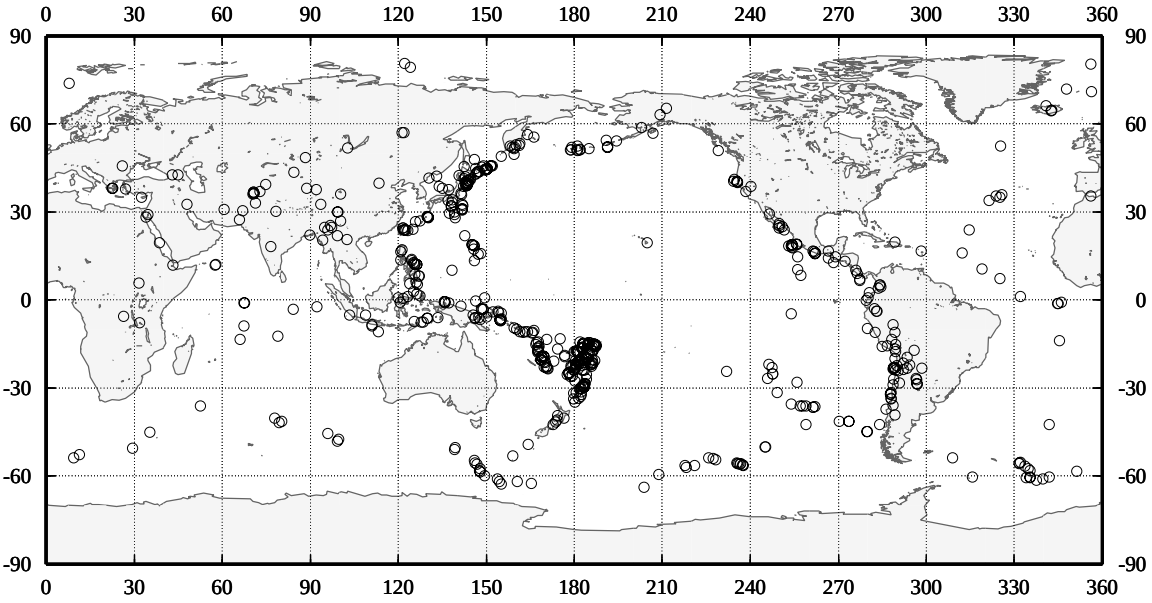


Figure 2.1: Source locations for 597 events used with the waveform fitting method for the $SS - S$ study.

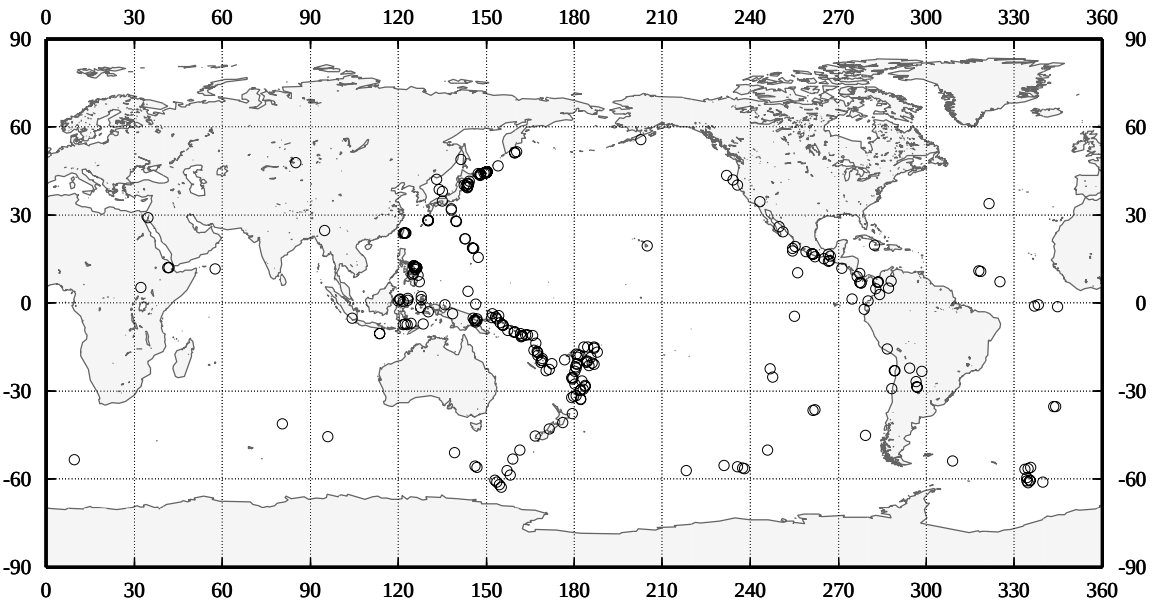


Figure 2.2: Source locations for 260 events used with the waveform fitting method for the $SSS - SS$ study.

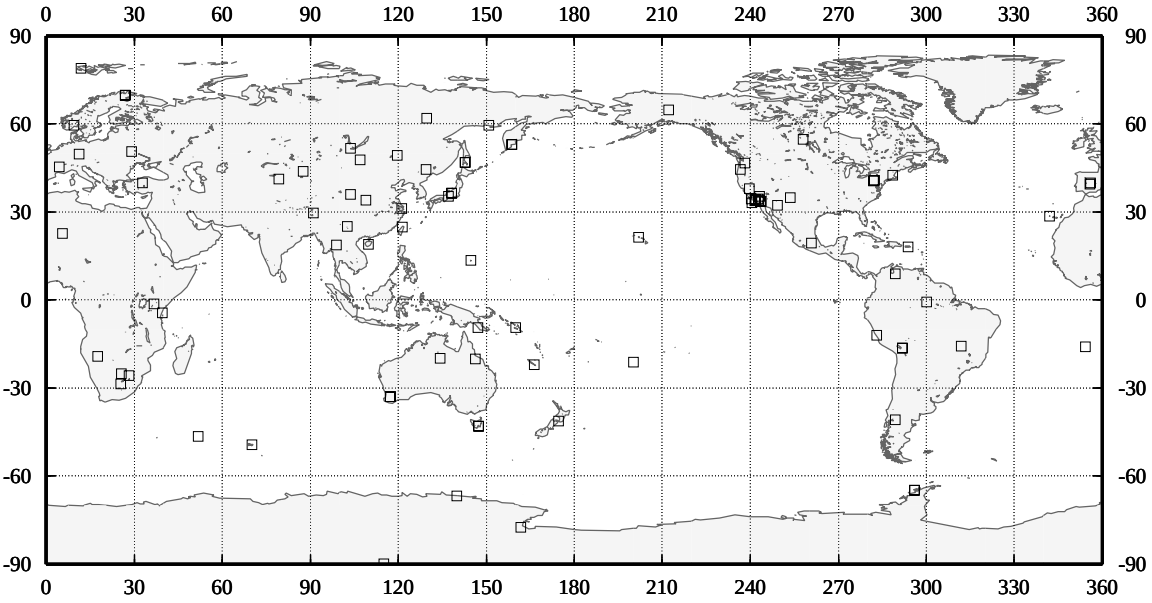


Figure 2.3: Station locations for 95 stations used with the waveform fitting method for the $SS - S$ study.

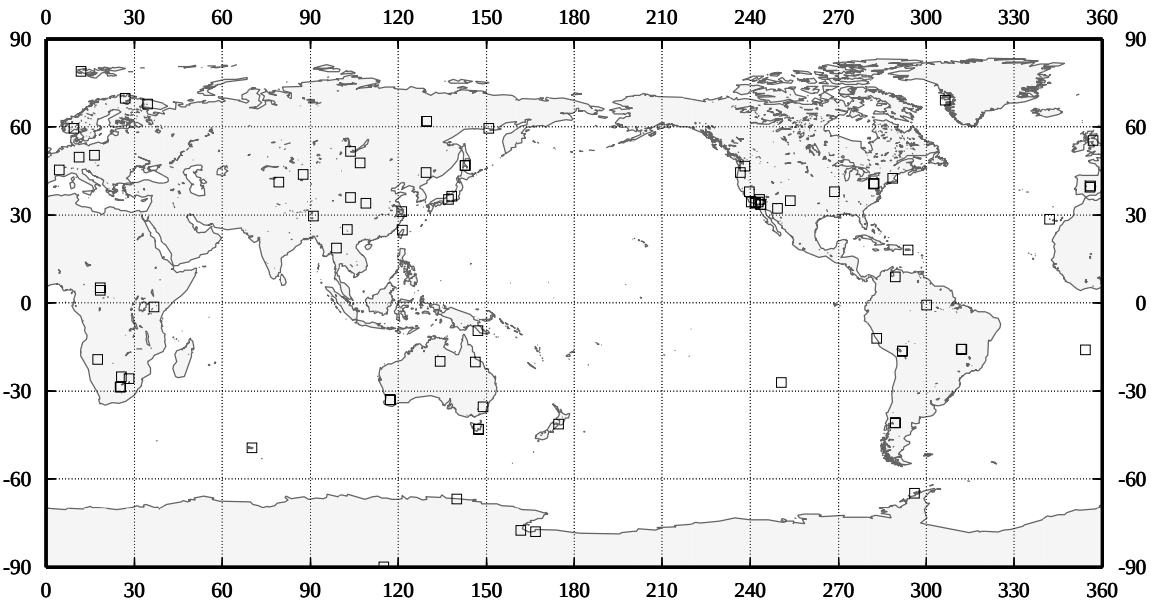


Figure 2.4: Station locations for 82 stations used with the waveform fitting method for the $SSS - SS$ study.

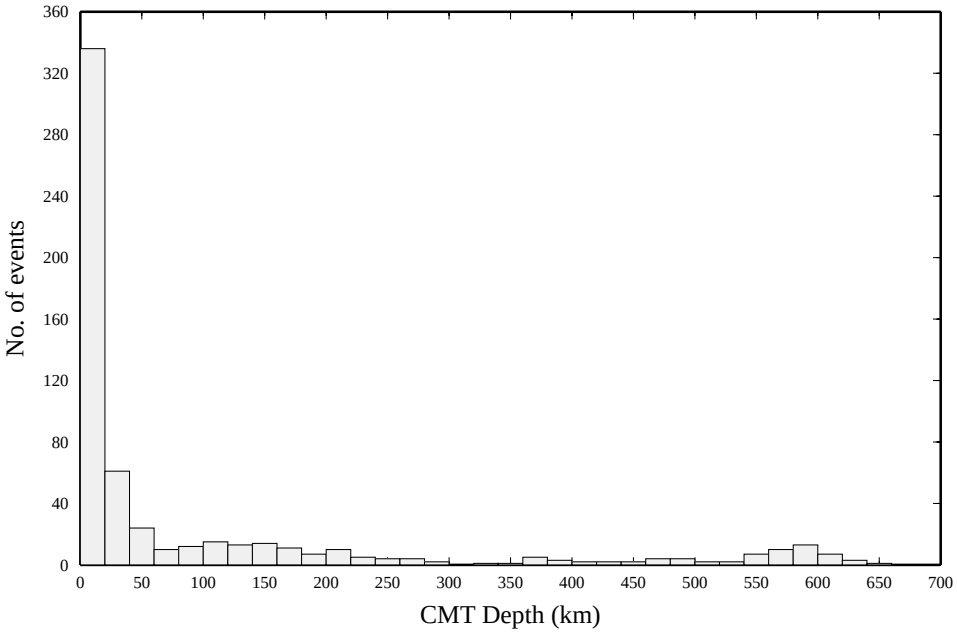


Figure 2.5: Event depth distribution for the $SS - S$ study, all epicentral depths are obtained from the CMT solutions.

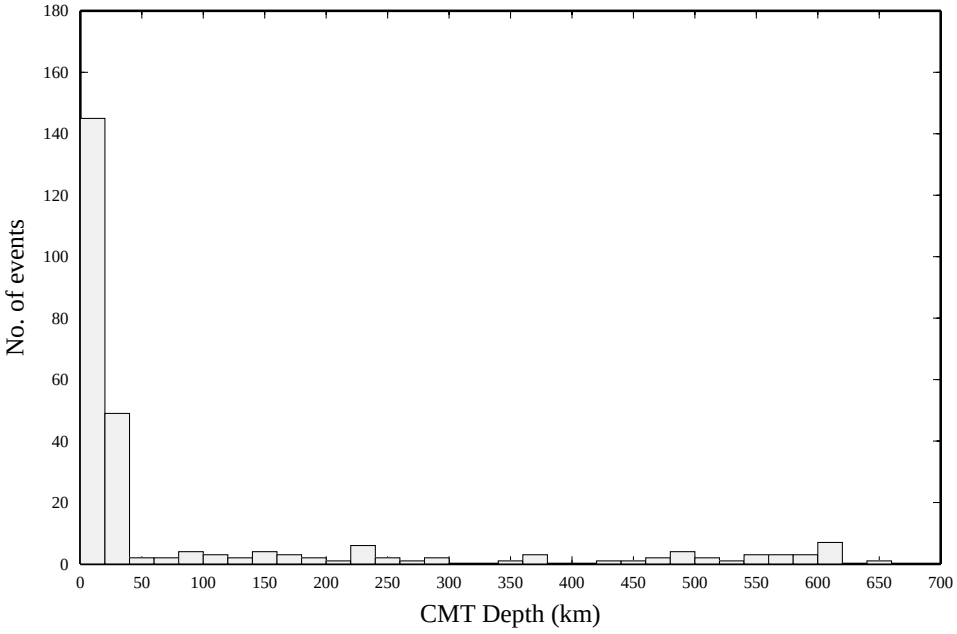


Figure 2.6: Event depth distribution for the $SSS - SS$ study, all epicentral depths are obtained from the CMT solutions.

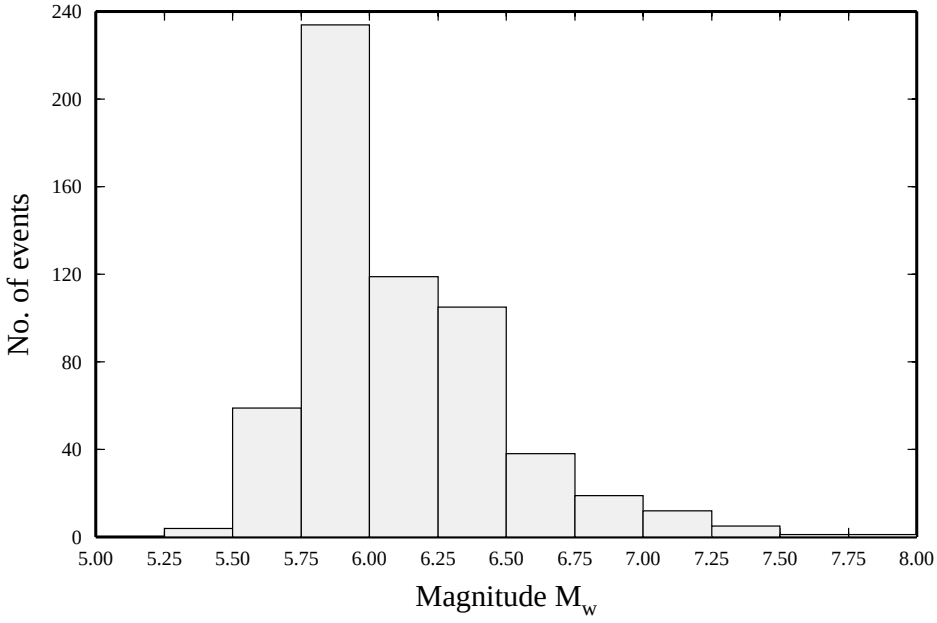


Figure 2.7: Magnitude distribution for the $SS - S$ study.

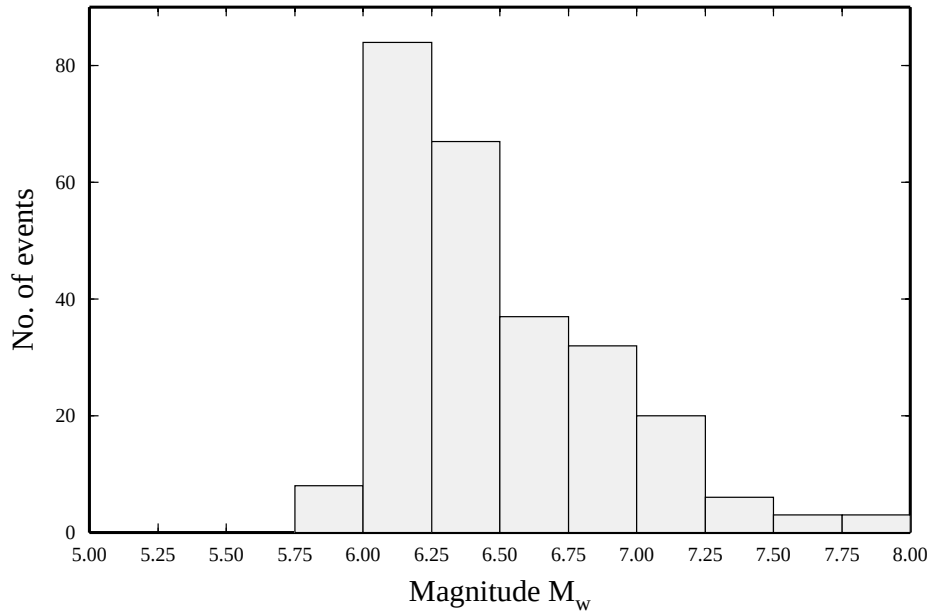


Figure 2.8: Magnitude distribution for the $SSS - SS$ study.

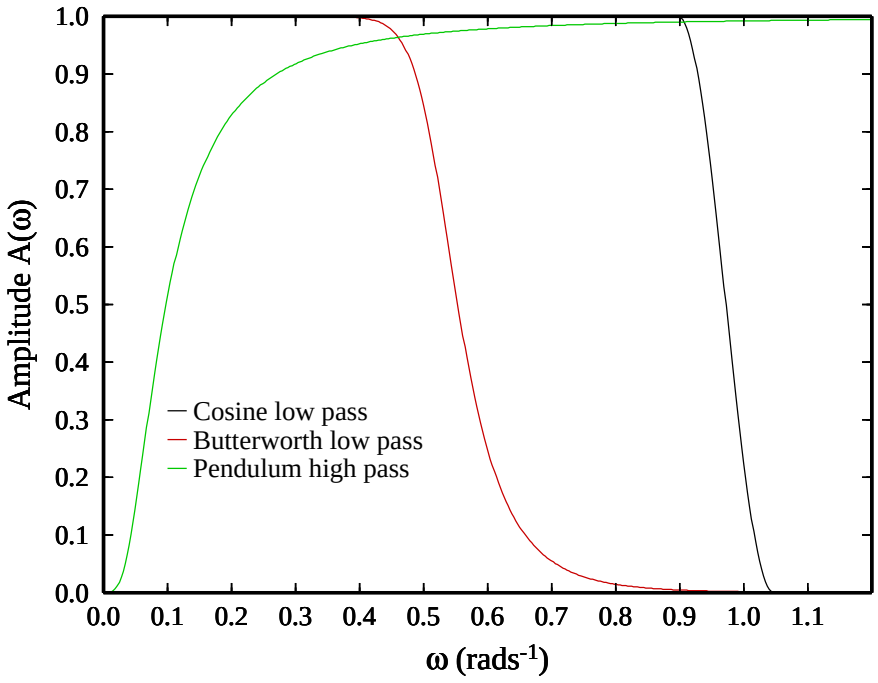


Figure 2.9: Amplitude versus frequency for each of the filters applied to the data.

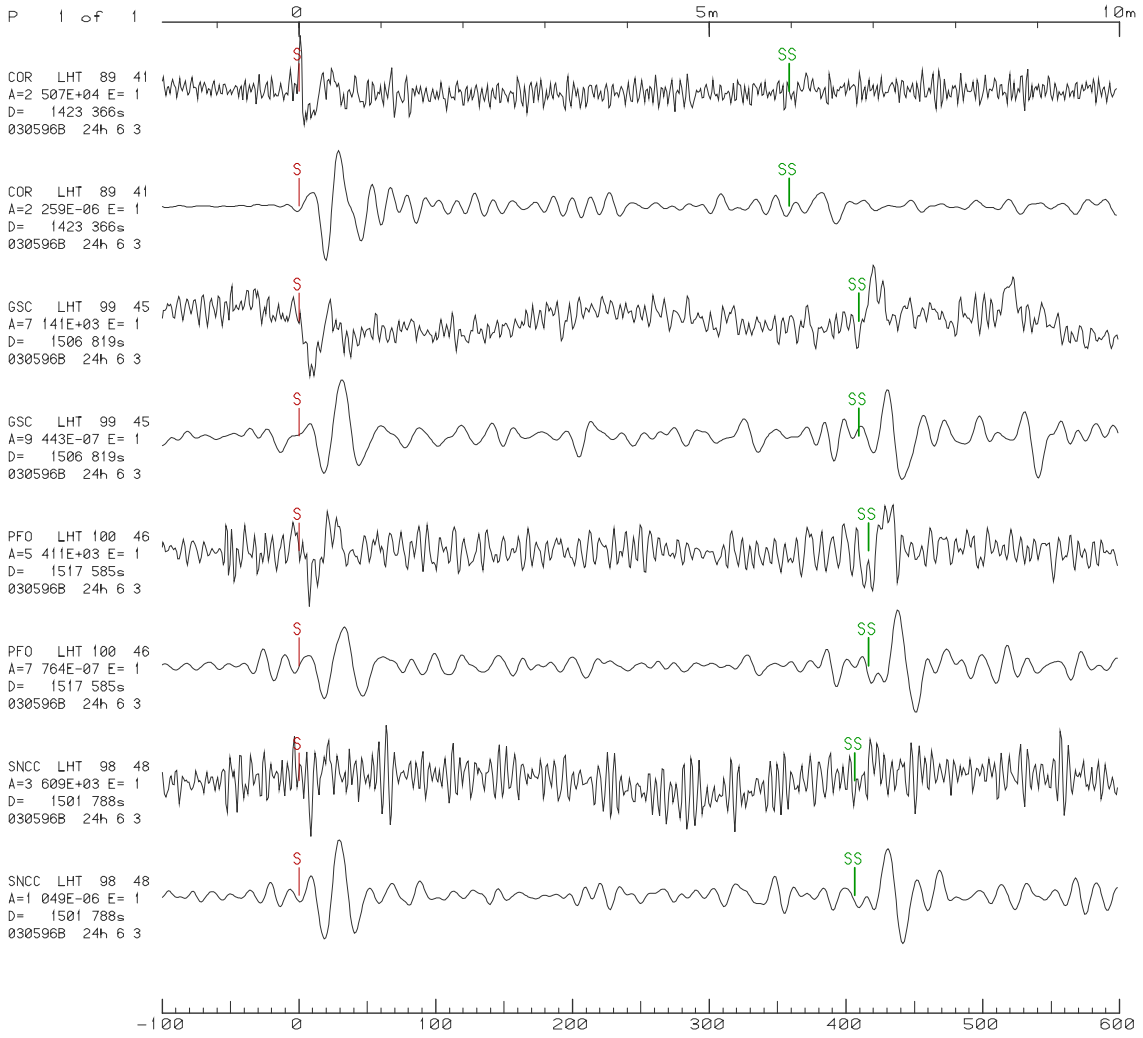


Figure 2.10: Example of filtered and non filtered $SS - S$ data for 4 stations from event 960305B.

Chapter 3

Methodology: waveform fitting

3.1 Introduction

The measurement of seismic attenuation within the Earth has been attempted using many different types of data with varying degrees of success. To date very few models of global attenuation structure have been obtained from body wave studies. A new method is presented in this chapter which enables body wave attenuation measurements and travel time values to be obtained from differential waveform measurements.

Differential measurements have been employed in a number of earlier studies. For example Woodward & Masters (1991a) used differential $PP - P$ and $SS - S$ measurements to obtain travel time measurements and Bhattacharyya *et al.* (1996) used differential $SS - S$ waveforms to obtain measurements of shear attenuation. Woodward & Masters (1991a) fitted waveforms using cross correlation techniques in the time domain whereas Bhattacharyya *et al.* (1996) used a multitaper frequency domain technique to fit waveforms. The technique described in this chapter is performed wholly in the time domain.

This chapter will explain why differential measurements are used instead of absolute measurements (see Section 3.2), and the basic theory behind the waveform fitting process (see Section 3.3). The actual data processing applied will be described in Section 3.4. An example of this processing is shown in Section 3.4.2. The results from this chapter are summarised in Section 3.5. The results of synthetic tests on the waveform fitting method are presented in Section C.1.

3.2 Motivation for using differential measurements

When using long period data, the measurement of absolute travel times or attenuation values can often be problematic. This is due to both the often emergent[1] nature of the pulses and to the fact that later

[1]Emergent means that the start of a particular phase rises slowly i.e. with a small gradient making determination of an absolute travel time difficult.

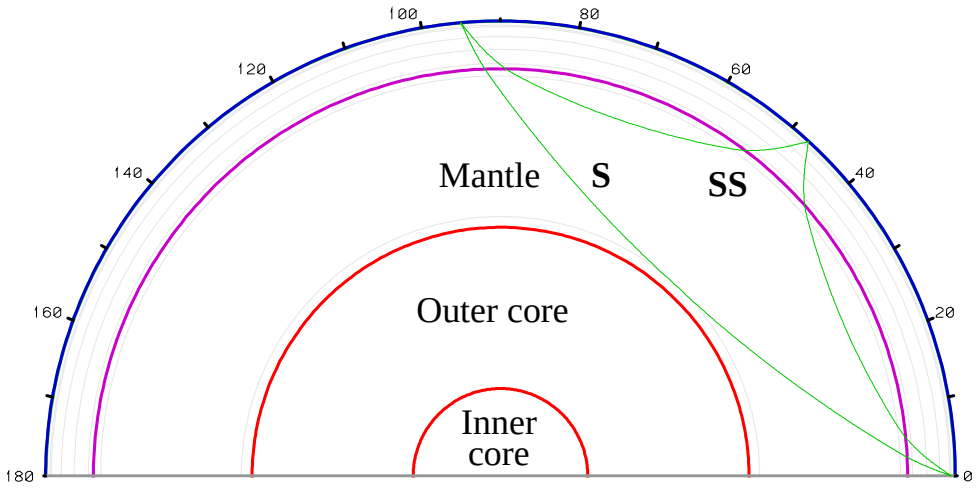


Figure 3.1: Schematic of the S and SS ray paths produced by a single earthquake recorded at the same seismic station. The earthquake source is at 0° and the station at 95°. The S and SS paths are shown in green. The blue line denotes the crust, the magenta line denotes the 670 km discontinuity and the two red lines denote the inner and outer core boundaries.

phases (e.g. S and SS) become distorted by the coda (tails) of earlier arrivals. A solution to this problem is to use differential measurements of travel time and attenuation. Differential measurements have several advantages over absolute measurements. They are less sensitive to the source location, independent of source origin time and less sensitive to structure in the source and receiver region. This can be explained by considering the total travel time of an S and SS wave travelling from a single source to the same recording station (see Figure 3.1).

The total travel time for each phase can be split up into contributions from different parts of the path. For example, consider the S phase, for which the total travel time, T_S from the earthquake source to recording station is composed of a contribution, $T_{Ssource}$ due to the source region a contribution, T_{Spath} due to the path and a contribution, $T_{Sreceiver}$ due to the receiver region. T_{Spath} is simply the travel time from the S ray path not in close proximity to the source or receiver region. Thus the total travel time for the S phase is:

$$T_S = T_{Ssource} + T_{Spath} + T_{Sreceiver} \tag{3.1}$$

similarly the total travel time for the SS phase is given by:

$$T_{SS} = T_{SSsource} + T_{SSpath} + T_{SSreceiver} \tag{3.2}$$

Hence the differential travel between SS and S phases is:

$$T_{SS} - T_S = T_{SSsource} + T_{SSpath} + T_{SSreceiver} - (T_{Ssource} + T_{Spath} + T_{Sreceiver}) \tag{3.3}$$

For epicentral distances, $\Delta = 50^\circ - 105^\circ$, the S and SS phases sample the source and receiver regions in a similar manner since their take-off and incident angles are similar and close to vertical. Table 3.1 summarises the range of take-off angles for the S, SS and SSS phases. The take-off angles are calculated from (Aki & Richards, 1980a)

$$\sin i = \frac{pv_0}{R_0} \tag{3.4}$$

where i is the take-off angle, v_0 is the PREM shear wave velocity at the source, R_0 is the source depth and p is the ray parameter.

Phase	Distance range	Take-off angle in degrees	
		mean	range
S	$50^\circ - 105^\circ$	24.27	17.18-45.90
SS	$50^\circ - 105^\circ$	35.63	29.10-58.22
SS	$90^\circ - 179^\circ$	28.83	20.24-50.39
SSS	$90^\circ - 179^\circ$	34.33	27.65-57.22

Table 3.1: Take-off angle for S, SS and SSS rays over the distance range of this study.

Therefore it is possible to write $T_{Ssource} \approx T_{SSsource}$ and $T_{Sreceiver} \approx T_{SSreceiver}$. Hence the $SS - S$ differential travel time becomes:

$$T_{SS} - T_S = T_{SSpath} - T_{Spath} \tag{3.5}$$

eliminating the effects of source and receiver structure. Similar arguments can be used to explain why differential measurements are less sensitive to source location and origin time. The same reasoning also applies to differential measurements of attenuation.

A feature specific to $SS-S$ differential measurements is that they can be used to sample regions of the Earth containing no sources or receivers. This is because in the case of differential measurements made between SS and S, the residuals can be plotted at the SS phase's bounce point instead of either the source or receiver location.

3.3 The theory behind the waveform fitting method

We seek expressions to relate the S phase to the SS phase and the SS phase to the SSS phase. The seismogram is a combination of many different components, one of which is the wave equation. Consider a monochromatic shear wave travelling in the x-direction, for which the particle displacement, $u(x,t)$, can be written as:

$$u(x,t) = e^{i(\omega t - kx)} = e^{i\omega(t - x/v_s)} \tag{3.6}$$

where k is the wave number, t is time, x is distance, ω is the angular frequency and v_s is the shear velocity. Defining the slowness, s as the reciprocal of velocity, $s = \frac{1}{v_s}$, we can say:

$$u(x,t) = e^{i\omega(t-sx)} \tag{3.7}$$

In an attenuating medium, slowness must be considered to have a small imaginary part, and a slight frequency dependence, so:

$$s(\omega) = s_0 \left(1 - \frac{1}{2} iq(\omega) - p(\omega)\right) \tag{3.8}$$

This means that the bracketed term's modulus on the RHS of Equation (3.8) is close to 1 and therefore s is approximately equal to s_0 where s_0 is defined as the real part of $s(\omega)$ evaluated at some reference frequency ω_0:

$$s_0 = \mathrm{Re}(s(\omega_0)) \tag{3.9}$$

The weak frequency dependence of $s(\omega)$ also means that both p and q must be small such that $p \ll 1$ and $q \ll 1$. Explicitly they are defined by:

$$p(\omega) = -\mathrm{Re}\left(\frac{s(\omega)}{s_0} - 1\right) \tag{3.10}$$

$$q(\omega) = -2\mathrm{Im}\left(\frac{s(\omega)}{s_0}\right) \tag{3.11}$$

Physically p is related to the dispersion and q is the reciprocal of the quality factor for shear waves such that $q = 1/Q_\mu$. An expression for the dispersion is derived as follows: If Q is constant over a certain band of frequencies then a graph of $q = 1/Q$ will take the form shown in Figure 3.2. The part of this graph in which q is constant results in a linear relationship between p and $\ln(\omega)$ as shown in Figure 3.3. These two graphs are related via the equation (Anderson *et al.*, 1977):

$$\frac{dp}{d\ln\omega} = \frac{q}{\pi} \tag{3.12}$$

If we choose a reference frequency ω_0 and define the dispersion p such that the dispersion at the reference frequency is zero i.e. $p(\omega_0) = 0$. Equation (3.12) can now be integrated as follows:

$$\int dp = \tfrac{q}{\pi} \int d\ln\omega$$

which implies

$$p = \tfrac{q}{\pi} \ln\omega + C$$

using the initial condition that if $\omega = \omega_0$ when $p = 0$ then

$$C = -\tfrac{q}{\pi} \ln\omega_0$$

thus

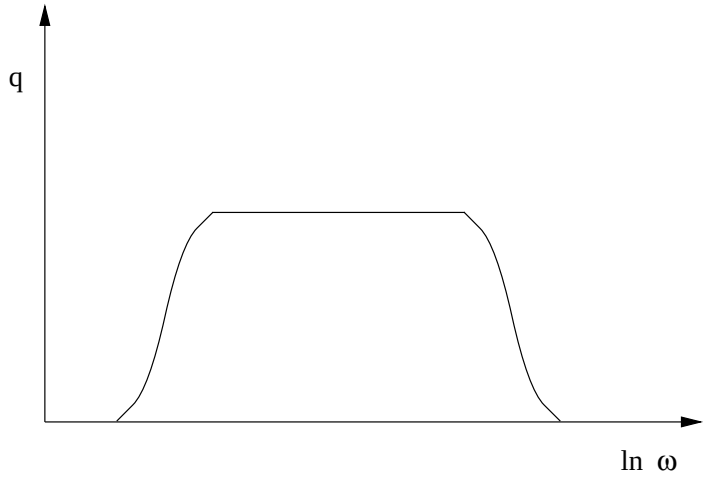


Figure 3.2: Showing the relationship between q and $\ln\omega$ obtained from having a constant Q over a particular frequency band.

$$p = (\ln\omega - \ln\omega_0)\frac{q}{\pi}$$

which implies

$$p(\omega) = \ln\left(\frac{\omega}{\omega_0}\right)\frac{q}{\pi} \tag{3.13}$$

Equation (3.13) is identical to that obtained by Kanamori & Anderson (1977) if the dispersion p is expressed as $p(\omega) = (C(\omega) - C(\omega_0))/C(\omega_0)$. $C(\omega)$ is the phase velocity at frequency ω and $C(\omega_0)$ is the phase velocity at the reference frequency ω_0.

The expression for slowness, Equation (3.8), and the expression for p, Equation (3.13), are now substituted into Equation (3.7) to obtain:

$$u(x,t) = e^{i\omega(t-s_0x)}e^{-\frac{1}{2}qs_0x\omega}e^{i\omega s_0x\ln(\frac{\omega}{\omega_0})\frac{q}{\pi}} \tag{3.14}$$

Now define the attenuation parameter, t^*, as $t^* = qs_0x$ so that:

$$u(x,t) = e^{i\omega(t-s_0x)}e^{(\frac{i\omega t^*}{\pi})(\ln\frac{\omega}{\omega_0}+i\frac{\pi}{2})} \tag{3.15}$$

The first exponential term in this expression is the equation of a plane wave travelling in a truly elastic, non-dispersive medium. The second exponential term describes the anelastic and dispersive behaviour of the wave. Equation (3.15) can also be expressed:

$$u(x,t) = e^{i\omega(t-s_0x)}e^{(\frac{i\omega t^*}{\pi})(\ln\frac{i\omega}{\omega_0})} \tag{3.16}$$

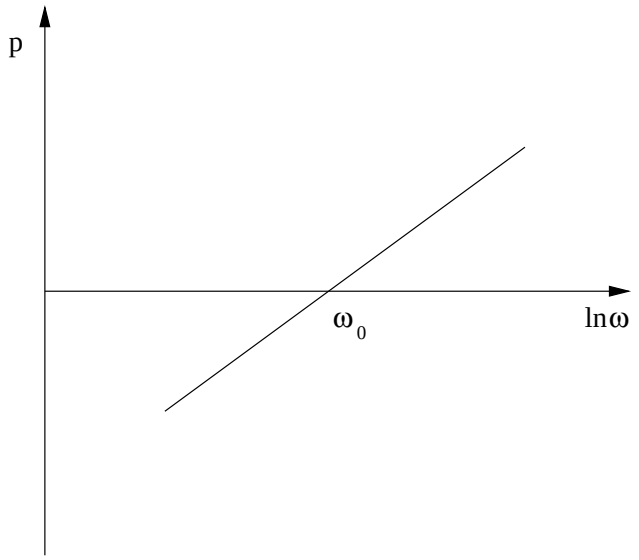


Figure 3.3: Showing p against $\ln\omega$

We define an attenuation and dispersion operator, $T(\omega, t^*)$:

$$T(\omega, t^*) = e^{\frac{i\omega t^*}{\pi}\ln(\frac{i\omega}{\omega_0})} = \left(e^{\ln(\frac{i\omega}{\omega_0})}\right)^{\frac{i\omega t^*}{\pi}} = \left(\frac{i\omega}{\omega_0}\right)^{\frac{i\omega t^*}{\pi}} \tag{3.17}$$

Equation (3.15) now becomes:

$$u(x,t) = e^{i\omega(t-s_0 x)}T(\omega, t^*) \tag{3.18}$$

The seismogram is a combination of many different components: source time function, instrument response, geometric spreading factor, amplitude factor and wave equation etc. In the frequency domain the S and SS phases of the seismogram can now be represented as the product of these components:

$$S(\omega) = \Omega(\omega)I(\omega)T(\omega, t_S^*)G_S(\omega)a_S e^{-i\omega t_S} \tag{3.19}$$

$$SS(\omega) = \Omega(\omega)I(\omega)T(\omega, t_{SS}^*)G_{SS}(\omega)a_{SS} e^{-i\omega t_{SS}} \tag{3.20}$$

where $\Omega(\omega)$ is the source time function, $I(\omega)$ is the instrument response function, $G_S(\omega)$ and $G_{SS}(\omega)$ are the geometrical spreading factors for the S and SS phases, a_S and a_{SS} describe the amplitude of the S and SS phases respectively, $T(\omega, t_S^*)$ and $T(\omega, t_{SS}^*)$ describe the attenuation experienced over the S and SS paths respectively and $e^{-i\omega t_S}$ and $e^{-i\omega t_{SS}}$ describe the travel time delay. Re-arranging the expression for $S(\omega)$, Equation (3.19), and substituting into the expression for $SS(\omega)$, Equation (3.20), the following expression is obtained:

$$SS(\omega) = \frac{S(\omega)T(\omega, t_{SS}^*)a_{SS}e^{-i\omega t_{SS}}}{T(\omega, t_S^*)a_S e^{-i\omega t_S}} \tag{3.21}$$

where $t_S = (t - s_{S,0}x)$ and $t_{SS} = (t - s_{SS,0}x)$. Equation (3.21) now simplifies to:

$$SS(\omega) = S(\omega)T(\omega, (t^*_{SS} - t^*_S))\frac{a_{SS}}{a_S}e^{-i\omega(t_{SS}-t_S)} \tag{3.22}$$

Now setting $t^*_{SS} - t^*_S = \Delta t^*$, $\frac{a_{SS}}{a_S} = a$ and $t_{SS} - t_S = \Delta t$ and introducing a Hilbert transform due to a caustic encountered by SS (Aki & Richards, 1980a,b) the following expression relating the S and SS phases is obtained:

$$SS(\omega) = S(\omega)e^{-i\omega\Delta t}iT(\omega, \Delta t^*)a \tag{3.23}$$

where Δt is related to the differential travel time between the SS and S phases, Δt^* is related to the differential attenuation and a is an amplitude factor related to the geometrical spreading between the SS and S phases. Multiplication by i indicates that the SS undergoes a Hilbert transform relative to the S phase (Choy & Richards, 1975). Equation (3.23) allows the SS phase to be re-written in terms of the S phase and vice versa. If the S and SS phase information are known then values for Δt, Δt^* and a can be obtained, the method for which will be described in section 3.4.

For the $SSS - SS$ differential measurements the corresponding expression is:

$$SSS(\omega) = SS(\omega)e^{i\omega\Delta t_1}iT(\omega, \Delta t^*_1)a_1 \tag{3.24}$$

Again the i corresponds to a Hilbert transform at the SS bounce point. Δt_1 is related to the $SSS-SS$ differential travel time, $\Delta t^*_1 = t^*_{SSS} - t^*_{SS}$ is related to the $SSS - SS$ differential attenuation and a_1 is the amplitude factor relating the SSS and SS phases.

3.4 The processing stage

A relationship between the S and SS waveforms is provided by Equation (3.23). If the S and SS phase information is known then the only unknowns left in Equation (3.23) are Δt, Δt^*, a and ω_0. The parameter ω_0 is set to be $\frac{2\pi}{15}$, where 15 seconds is the typical period of the data. These unknowns are found using a non-linear parameter estimation algorithm called "CURFIT". The Fortran code and the method used by the algorithm are described by Bevington (1969)(pp 235-240). The algorithm performs a least-squares fit to a function, where the function itself need not be linear. It then combines a gradient search with an analytical solution developed by linearising the fitting function. The fitting function used for the $SS - S$ study is given by Equation (3.23). We try to find the best possible fit of the true SS phase obtained from the seismogram with the SS phase obtained from Equation (3.23).

The parameters Δt^* and a trade off against one another i.e. increasing the amplitude factor a causes a decrease in the value of Δt^* and vice versa. Therefore simultaneously fitting both a and Δt^* is not ideal. As a result of this trade off between parameters it is necessary to use a two step procedure to fit the waveforms. The first step uses synthetic seismograms to fix a value of a and then this value

of a is used to fit the real data.

A variety of procedures need to be carried out before the fitting algorithm can be applied to the data. First data are extracted from the juke box (≈ 100 events at a time). Synthetic seismograms are then computed for each event. The synthetic seismograms are calculated by summation of over 20000 normal modes, the theory of which is beyond the scope of this study. For each event both the real and synthetic seismograms are rotated to obtain the transverse components. Each event is then examined visually to determine whether it is suitable for further processing (Section 2.1 details the criterion for event selection). After selecting appropriate events the S, SS and SSS phases are windowed out. The windowing is performed manually by selecting the required region with the mouse pointer. For each event the phase windows (or picks) are made subject to the following criteria:

- For a given seismic station, the real and synthetic seismograms must be similar.
- Both the S and SS or SS and SSS phases must be clearly visible, i.e. they must have a high signal to noise ratio.

The first of these criteria is to ensure the fitting program receives reasonable input parameters. The real and synthetic seismograms need to be similar as the amplitude ratio obtained from fitting the synthetic data is used to fit the real data. If the real and synthetic seismograms are not similar then the two step fitting procedure provides no advantage. The second criterion ensures that the true S and SS waveforms are fitted rather than noise. Figure 3.4 gives an example of seismograms for which windows are selected along with an example of seismograms which are not considered of high enough quality for windowing. Stations ADK and COL show examples of data which satisfy the criteria for windowing described above. For these two stations the real and synthetic traces are similar and the S and SS phases can be clearly distinguished from noise. Stations KBS and KIV show data which do not satisfy the windowing criteria. For these stations the signal to noise ratio is poor and it is difficult to determine where the S or SS phase begins, making the selection of a phase window extremely problematic.

Once all the high quality S, SS, and SSS phases have been windowed they are passed into the waveform fitting algorithm. As mentioned previously this is a two step procedure: The first step fits the synthetic data to obtain a value for the amplitude ratio between the SS and S or SSS and SS phases. The second step uses this amplitude ratio to fit the real data and thus to obtain values for the differential travel time and attenuation. We denote the input parameters to a particular run of the waveform fitting algorithm as α_1, α_2 and α_3 and the output parameters as β_1, β_2 and β_3. The subscript 1 is assigned to the time-shift parameter, subscript 2 is assigned to the attenuation parameter and subscript 3 is assigned to the amplitude parameter. Essentially the procedure is as follows:-

1. Determine an initial value for α_1.
2. Apply the fitting algorithm to the synthetic data with the input parameters:

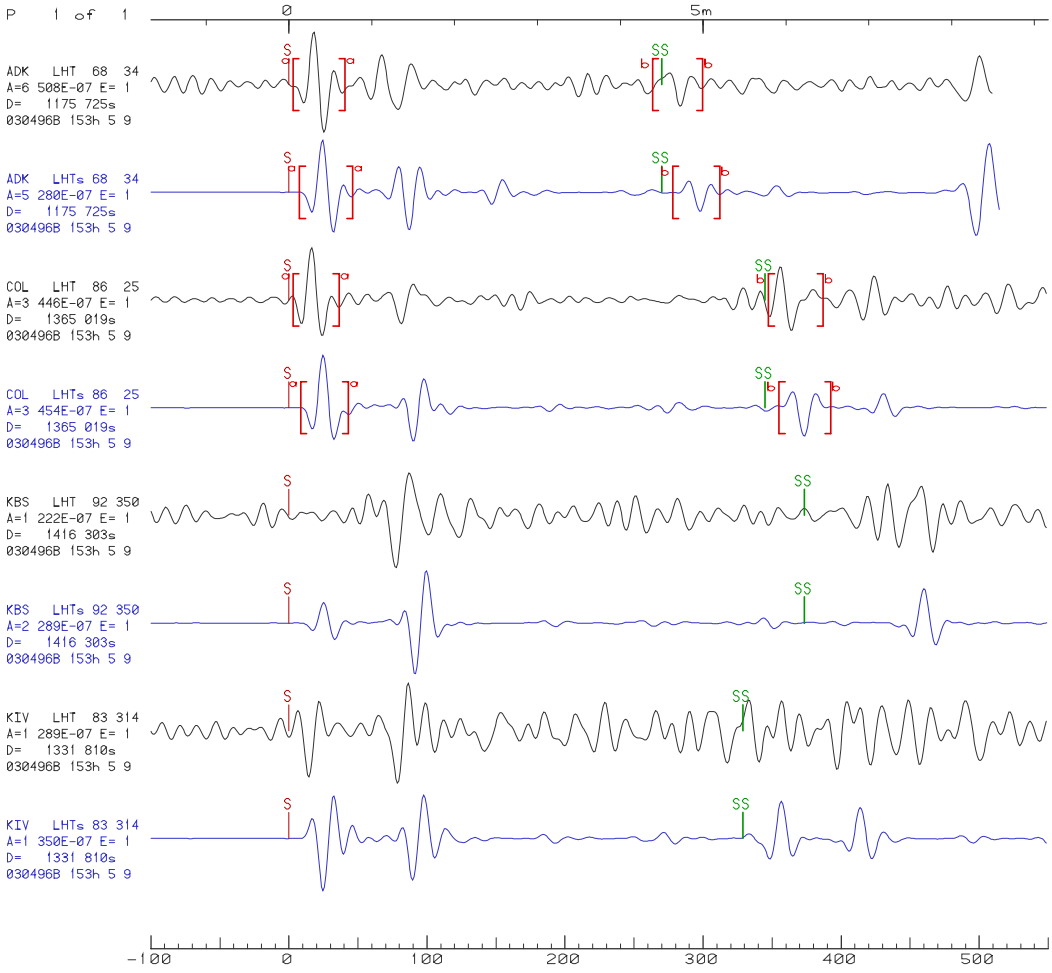


Figure 3.4: Seismograms from 4 stations from event 960306B. Black traces show the real data whereas blue traces are synthetics. The "a" and "b" intervals show the windows selected for the S and SS phases respectively. The S (in red) and SS (in green) marks show the PREM travel times for the phases. The seismograms have been filtered using the suite of filters described in Section 2.2.

- α_1 as obtained from stage 1.
- $\alpha_2 = 3.0$ s - *Held fixed*
- $\alpha_3 = 0.5$

The output parameters from the synthetic fit are:

- $\beta_1 = \Delta t_{syn}$
- $\beta_2 = \alpha_2 = \Delta t^*_{syn} = 3.0$ s
- $\beta_3 = a$

Where Δt_{syn} is the time shift required to fit the synthetic S (or SS) phase to the synthetic SS (or SSS) phase. Δt^*_{syn} is the assumed value of $SS - S$ (or $SSS - SS$) differential attenuation

for the synthetic data and a is the amplitude ratio between the synthetic SS and S or SSS and SS phases.

3. Now apply the fitting algorithm to the real data with the input parameters $\alpha_1, \alpha_2, \alpha_3$ being the results obtained from stage 2 i.e. use the input parameters $\alpha_1 = \Delta t_{syn}$, $\alpha_2 = \Delta t^*_{syn} = 3.0$ s and $\alpha_3 = a$. For this fit the amplitude factor, $\alpha_3 = a$, is held constant. The final output values after applying the waveform fitting algorithm to the real data are

   - $\beta_1 = \Delta t_{syn} + \Delta t_{real}$
   - $\beta_2 = \Delta t^*_{syn} + \Delta t^*_{real}$
   - $\beta_3 = a$

   Where Δt_{real} is the additional time shift required to fit the real S (or SS) phase to the real SS (or SSS) phase. Δt^*_{real} is the value of $SS - S$ differential attenuation relative to a value of 3.0 s.

These final output parameters, β_1, β_2 and β_3 allow values for the differential travel time and attenuation relative to the PREM model to be obtained. Explicitly the value of differential attenuation relative to PREM, Δt^*, is given by:

$$\Delta t^* = \beta_2 - \Delta t^*_{PREM} \tag{3.25}$$

where Δt^*_{PREM} is the value of $SS - S$ differential attenuation obtained from the PREM tables. The value of differential travel time between the two phases, Δt_{SS-S}, is given by $\Delta t_{SS-S} = \Delta t_{syn} + \Delta t_{real} + T_1$. T_1 is defined as the time interval between the start of the S and SS or SS and SSS intervals. For example in Figure 3.4, T_1 is the time interval between the start of the S phase window (the first "a" pick) and the start of the SS phase window (the first "b" pick). The differential travel time *residual* relative to PREM is then given by $\Delta t_{SS-S} - t_{PREM}$ where t_{PREM} is the $SS - S$ or $SSS - SS$ travel time as calculated from the PREM tables. If the travel time residual is defined in this way, then a positive residual will be obtained when the actual travel time is *greater* than that predicted by the PREM model and a negative residual will be obtained when the actual travel time is *less* than that predicted by the PREM model.

Stage 1 is used to ensure that the SS and SS' [2] waveforms have a good degree of correlation before attempting to execute the fitting algorithm. This is achieved by testing a series of different starting values for α_1 until a good correlation between SS and SS' is obtained. This stage is included because the convergence of the fitting algorithm is found to be most sensitive to the time-shift factor. Providing the two waveforms are relatively close (within 5-10 s of each other), in general few problems are encountered.

In stage 2 the value of α_2 is held fixed at 3 s, for which an explanation now follows. Consider Figure 3.5, which shows the $SS - S$ differential t^* values calculated from the PREM model for a range

[2] SS' denotes the SS waveform as obtained from Equation (3.23) with a given set of input parameters.

of epicentral distances and source depths. As the epicentral distance increases the value of $t^*_{SS} - t^*_S$ also increases. There is also a dependence on source depth: the deeper the event, the smaller the value of $t^*_{SS} - t^*_S$. The majority of events used in the $SS - S$ study are shallower than 100km and therefore for the epicentral range, $\Delta = 50° - 105°$, the PREM value of $t^*_{SS} - t^*_S$ varies between approximately 2.7 - 3.2 s (see Figure 3.5). The highest density of $SS - S$ data points occurs at epicentral distances of $80° - 90°$ corresponding to a PREM $t^*_{SS} - t^*_S$ of approximately 3.0 s which explains the use of 3.0 s in stage 2 of the processing.

In stage 3 we fit the real data in order to obtain values of differential travel time and attenuation. In doing so we make the assumption that the amplitude ratio between the two phases determined from the synthetic data is equal to the amplitude ratio for the real data with the exception of the contribution to the amplitude from attenuation. This assumption relies on the PREM amplitudes for shear body waves being close to the observed amplitudes. By fixing this amplitude ratio the trade off between amplitude and attenuation is removed and therefore it is thought that a more realistic value of differential attenuation will be obtained.

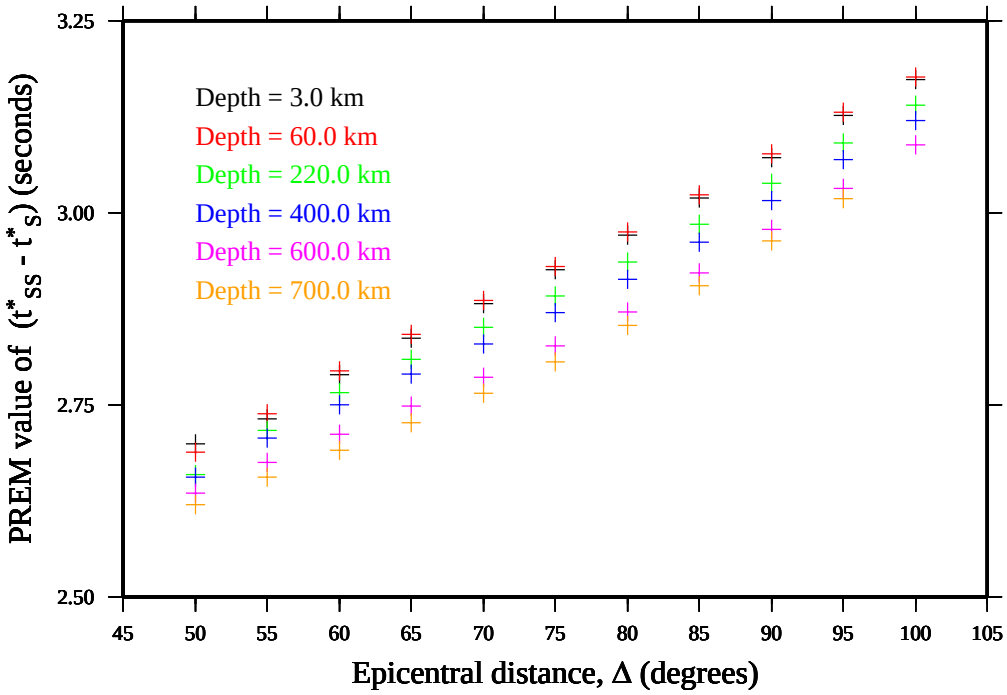


Figure 3.5: Graph showing the PREM values of $(t^*_{SS} - t^*_S)$ for a range of source depths.

In the preceding discussion no mention of how well the waveforms fit one another is made. This issue is addressed in Section 3.4.1.

3.4.1 The fit parameter

The fitting algorithm produces standard deviations for each of the parameters Δt, Δt^* and a. If a large error is obtained for one of the parameters, this suggests that the fit between the waveforms may have been less than ideal. We find that although the standard deviations provide a measure of the reliability of a particular parameter they provide no information on how well the entire waveforms fit each other. As a result the *fit parameter* is defined. The fit parameter provides a measure of how well two waveforms fit each other and is defined as follows:

$$\text{fit parameter} = \frac{\sum_{t=1}^{N} \left[SS(t) - SS_{fit}(t)\right]^2}{\sum_{t=1}^{N} \left[SS(t)\right]^2} \tag{3.26}$$

Where $SS(t)$ denotes the true SS phase time series, $SS_{fit}(t)$ denotes the time series for SS obtained from the waveform fitting algorithm using Equation (3.23), N is the total number of data points in the $SS(t)$ and $SS_{fit}(t)$ waveforms and t denotes the time in 1 second intervals from the start of the SS phase. A perfect fit will be obtained if the fit parameter $\equiv 0$ i.e. the case where the true SS phase is identical to the fitted SS phase such that $SS(t) \equiv SS_{fit}(t)$. The larger the fit parameter, the worse the fit between the two waveforms will be. For example, Figure 3.6 shows an example of two sets of waveforms one with a fit parameter of 0.09 (the left hand plot) and the other with a fit parameter of 0.58 (the right hand plot). The larger value of fit parameter quantifies the significantly poorer fit. The inversions discussed in Chapter 6 only use data with fit parameters less than 0.2. The threshold of 0.2 was selected subsequent to extensive visual examination of the waveform fits.

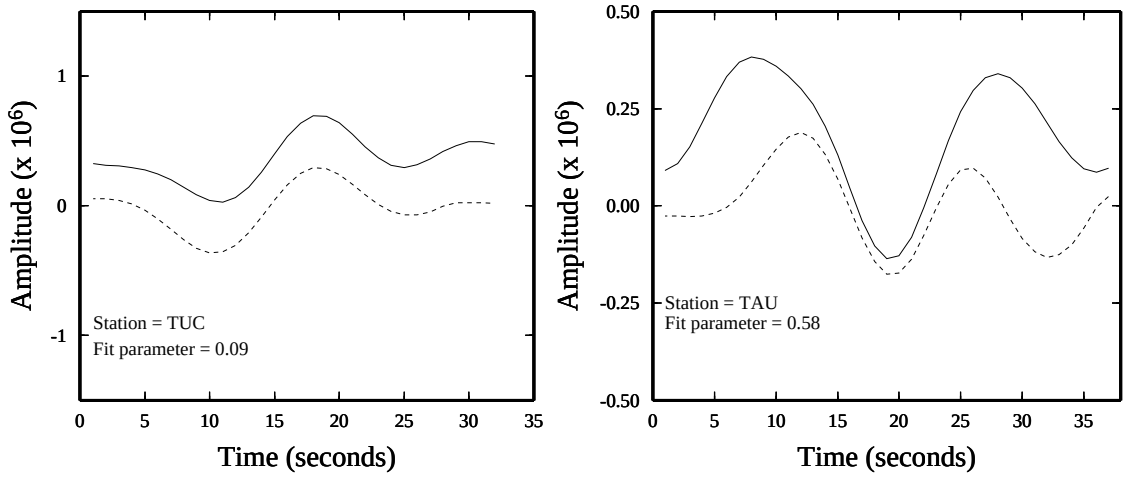


Figure 3.6: Final output from the fitting algorithm for two stations from event 960507F. In each plot the solid trace shows the $SS(t)$ time series whereas the bottom trace (dashed line) shows the SS waveform obtained from fitting, i.e. the $SS_{fit}(t)$. The left hand plot shows an example of a good quality fit from station TUC with fit parameter = 0.09. The right hand plot shows an example of a poor quality fit from station TAU with fit parameter = 0.58.

3.4.2 Waveform fitting: an example

The best method of illustrating how the waveform fitting process works is by considering an example. The seismograms used for this purpose are taken from station DGR of event 960507F. Figure 3.7 shows the filtered real and synthetic seismograms for station DGR with the S and SS waveforms shown in the red "a" and "b" intervals respectively. These seismograms have been filtered using the filters described in section Section 2.2.

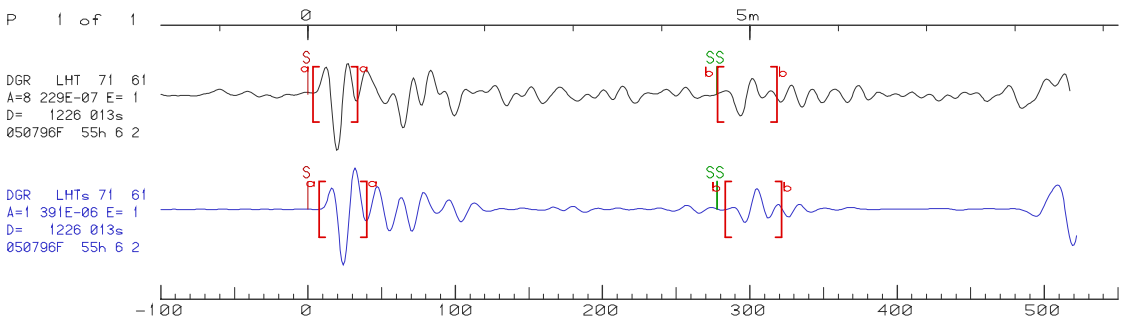


Figure 3.7: Seismograms from station DGR of event 960507F. The black trace shows the real data, the blue trace shows the synthetic data. The S and SS waveforms are marked out by the "a" and "b" intervals respectively.

The fitting algorithm is applied as described in Section 3.4. For the synthetic fit the input parameters to the fitting algorithm are $\alpha_1 = 1.0$, $\alpha_2 = 3.0$ and $\alpha_3 = 0.5$. The left hand side of Figure 3.8 shows the synthetic SS phases before the fitting algorithm has been executed. The right hand side of Figure 3.8 shows the resulting waveforms after running the fitting algorithm. The output parameters from the fitting algorithm are $\beta_1 = 0.66$, $\beta_2 = 3.0$ and $\beta_3 = 0.59$. By visual examination of the left hand plot of Figure 3.8 it is obvious that the original SS phase and the SS phase approximation given by $SS = Se^{-i\omega\alpha_1} iT(\alpha_2, \omega)\alpha_3$ are very similar. In fact after running the fitting algorithm, the output parameters, β_1 and β_3 are usually close to the original input values, α_1 and α_3. This means that the correlation between the two waveforms is good even before running the fitting algorithm. It turns out that this is very often the case when fitting the synthetic data. This is partly because in stage 1 of the fitting procedure the time-shift is set to a good starting value but also because in general the synthetic waveforms provide higher quality fits than the real data. This is to be expected as the synthetic data contain no noise unlike the real data, so the fits obtained are generally of higher quality than those obtained from fitting the real waveforms.

The values of β_1, β_2 and β_3 obtained from the synthetic fit are then used as the input parameters for fitting the real waveforms i.e. the input parameters for the real fit are $\alpha_1 = 0.66$, $\alpha_2 = 3.0$ and $\alpha_3 = 0.59$. When fitting the real waveforms the parameter α_3, relating the amplitudes of the SS and S waveforms is held fixed as described in the previous section. Figure 3.9 shows the real SS

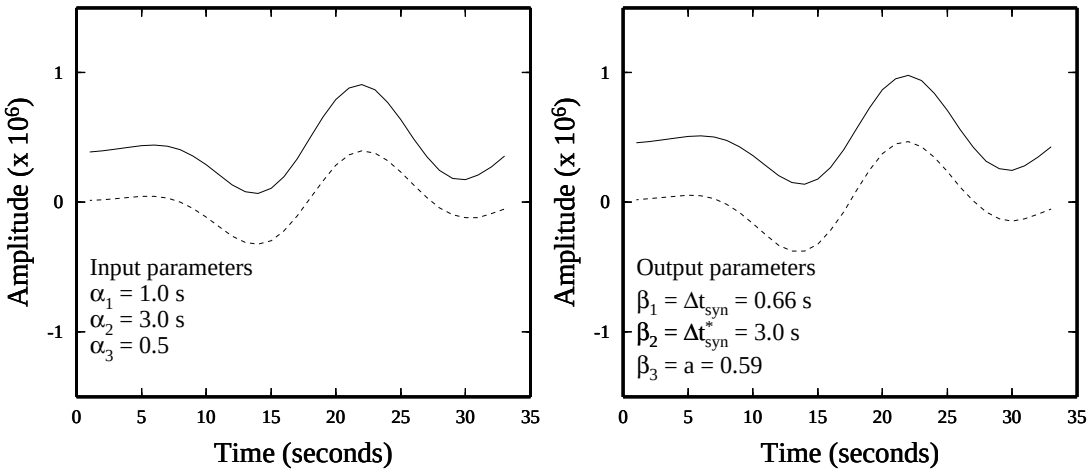


Figure 3.8: Example of waveforms obtained from fitting the synthetic data. The top trace (solid line) in each plot shows the synthetic SS phase as obtained from the seismogram. The bottom trace (dashed line) in each plot shows the SS phase as obtained from the fitting algorithm. The left hand plot shows the traces before running the fitting algorithm, the right hand plot shows the resulting traces after running the fitting algorithm. The synthetic seismograms are taken from station DGR of event 960507F.

phases both before and after execution of the fitting algorithm. The left hand diagram shows the real SS phase as obtained from the seismogram (solid line) along with the approximation to it obtained from $SS = Se^{-i\omega\alpha_1} iT(\alpha_2, \omega)\alpha_3$ (dashed line). As with the synthetic waveforms, the two waveforms are quite similar before running the fitting algorithm. The dashed trace is shifted slightly to the left relative to the solid trace. If a fit is to be obtained between these two waveforms, the value of the parameter $\alpha_1 = \Delta t_{syn}$ must increase so that the dashed trace is shifted to the right which will align it with the real SS phase. As expected the value of β_1 is indeed greater than the value of α_1

After running the fitting algorithm with the real data the final output parameters are $\beta_1 = 2.99$, $\beta_2 = 2.28$ and $\beta_3 = 0.59$. The fit parameter for the real data is 0.02 which is a good quality fit as can be seen by visual examination of the right hand plot in Figure 3.9. The values of β_1, β_2 and β_3 can now be used to obtain the $SS - S$ differential travel time and t^*. As mentioned in Section 3.4 the differential travel time residual relative to PREM is given by:

$$\Delta t = \Delta t_{syn} + \Delta t_{real} + T_1 - t_{PREM} \tag{3.27}$$

Now $\Delta t_{syn} = 0.66$ s, and $\Delta t_{real} = 2.33$ s. The value of T_1 is 275 s and the value of PREM $SS - S$ travel time is $t_{PREM} = 277.63$. Substituting these values into Equation (3.27) the $SS - S$ travel time residual relative to PREM, Δt, is equal to $0.66 + 2.33 + 275 - 277.63 = 0.36$ s. The $SS - S$ differential t^* residual relative to PREM, Δt^*, is given by Equation (3.25). Now substituting $\beta_2 = 2.28$ s and $\Delta t^*_{PREM} = 2.89$ s into Equation (3.25) the value of differential t^* relative to PREM (i.e. Δt^*) is given by $2.28 - 2.89 = -0.61$ s.

The values of Δt and Δt^* are relative to the PREM model. If Δt is positive this means the differential travel time obtained from the real data is greater than that predicted by PREM. i.e. the velocity is slower than in PREM. If Δt is negative this means that the travel time obtained from the real data is less than that predicted by PREM. i.e. the velocity is higher than in PREM. Similar arguments apply to the values of Δt^*. Positive values of Δt^* correspond to areas more attenuating than PREM and negative values correspond to areas less attenuating than PREM.

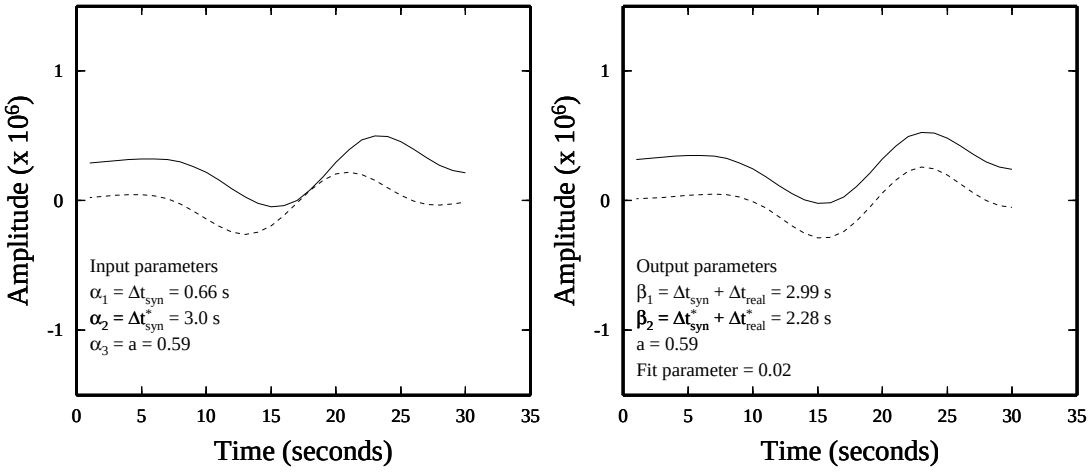


Figure 3.9: Example of the waveforms obtained from fitting the real data. The top trace (solid line) in each plot shows the real SS phase as obtained from the seismogram. The bottom trace (dashed line) in each plot shows the SS phase as obtained from the fitting algorithm. The left hand plot shows the traces before running the fitting algorithm, the right hand plots show the resulting traces after running the fitting algorithm. The real seismograms are taken from station DGR of event 960507F.

3.5 Summary

A method for obtaining travel times and attenuation values from differential waveform measurements is presented. Key points include:

- The assumption that the amplitude ratio between the real SS and S (or SSS and SS) phases is the same as that obtained from synthetic data.
- The assumption that the PREM value of $\Delta t^* = 3.0$ s, for both $SS - S$ and $SSS - SS$ differential measurements.

Chapter 4

Spectral ratio method for determining Δt^* values

4.1 Introduction

A method for determining values of differential travel time and attenuation using measurements made in the time domain is presented in Chapter 3. In this chapter an alternative method for obtaining differential t^* values using a frequency domain measurement technique is presented. This technique has the advantage that it requires only real data thus any bias from using the synthetic data is removed. This method obtains Δt^* independently i.e. it finds Δt^* without having to also find the differential travel time and amplitude factor as in the waveform fitting method. As a result, it may turn out to be a more reliable means of finding Δt^* values. The use of raw unfiltered data may however pose some problems: with no filtering of the seismograms it is likely to be more difficult to window out the phases as illustrated previously by Figure 2.10. As a result it is expected that fewer seismograms will be suitable for application of this method.

The theory behind the method is presented in Section 4.2. A description of how the data are handled including an example are discussed in Sections 4.3 and 4.4. The main results of this chapter are summarised in Section 4.5. The results of synthetic testing of the spectral ratio method are presented in Section C.2.

4.2 Theory of the spectral ratio method

It is possible to obtain differential t^* values using an alternative method which utilises only the real seismograms so neglecting the synthetic seismograms. The method presented in this section provides values for Δt^* only. Only raw unfiltered seismograms are used and since the calculations are performed in the frequency domain this method is referred to as the "spectral method" or "spectral ratio method".

Unfiltered data are used as the spectral method relies on the frequency content of the data and any filtering would alter this.

We use spectral ratio between two seismic phases to obtain differential t^* values. The amplitude, of a seismic wave can be written as (e.g. Bath, 1974):

$$|A(\omega,x)| = |S(\omega)||B(\theta)||C_s(\omega)||M(\omega,x)||G(x)||C_r(\omega,x)||I(\omega)| \tag{4.1}$$

where the parameters are defined as follows:

$|A(\omega,x)|$ = the amplitude of the seismic wave at a distance x

$S(\omega)$ = the source spectrum corresponding to the source time function

$B(\theta)$ = the source space function, where θ is the direction from the source

$C_s(\omega)$ = the source crustal effect on the spectrum

$M(\omega,x)$ = the mantle effect on the spectrum

$G(x)$ = geometrical spreading

$C_r(\omega,x)$ = the receiver crustal effect on the spectrum

$I(\omega)$ = the instrument response function

Therefore the amplitude ratio between two waves labelled 1 and 2 is:

$$\frac{|A_1(\omega,x)|}{|A_2(\omega,x)|} = \frac{|S_1(\omega)||B_1(\theta)||C_{s1}(\omega)||M_1(\omega,x)||G_1(x)||C_{r1}(\omega,x)||I_1(\omega)|}{|S_2(\omega)||B_2(\theta)||C_{s2}(\omega)||M_2(\omega,x)||G_2(x)||C_{r2}(\omega,x)||I_2(\omega)|} \tag{4.2}$$

Now if the mantle effect M is assumed to consist only of attenuation then $M(\omega,x)$ can be replaced with $e^{\frac{-\omega t^*}{2}}$ and thus Equation (4.2) becomes:

$$\frac{|A_1(\omega,x)|}{|A_2(\omega,x)|} = \frac{|S_1(\omega)||B_1(\theta)||C_{s1}(\omega)||G_1(x)||C_{r1}(\omega,x)||I_1(\omega)|\exp(-\frac{\omega t_1^*}{2})}{|S_2(\omega)||B_2(\theta)||C_{s2}(\omega)||G_2(x)||C_{r2}(\omega,x)||I_2(\omega)|\exp(-\frac{\omega t_2^*}{2})} \tag{4.3}$$

This expression is almost identical to Equation (16) of Matheney & Nowack (1995) except that they write the geometrical spreading term as $G(\omega,x)$ and then subsequently assume it to be independent of frequency so that it reduces to $G(x)$.

Since we are concerned only with differential measurements, both waves have the same source and are recorded on the same instrument and as a result the $S(\omega)$, $B(\theta)$ and $I(\omega)$ terms cancel. We also make the assumption that the source and receiver crustal terms $C_s(\omega)$ and $C_r(\omega)$ cancel. This assumption is valid because the take-off angles for S, SS and SSS are close to vertical over the epicentral ranges used in this study. Noting that the geometrical spreading is independent of frequency and taking the logarithm of both sides of Equation (4.3) the following expression is obtained:

$$\ln\frac{|A_1(\omega)|}{|A_2(\omega)|} = \ln\frac{G_1}{G_2} - \frac{\omega}{2}(t_1^* - t_2^*) \tag{4.4}$$

Equation (4.4) relates the amplitude spectra of two phases to the geometrical spreading and t^*. This

expression is the equation of a straight line with slope given by $-\frac{(t_2^*-t_1^*)}{2}$ and intercept given by $\ln\frac{G_1}{G_2}$. The value of differential attenuation between the two phases is then given by -2 times the slope. The slope and intercept are found by fitting a least squares line through a graph of $\ln\frac{|A_1(\omega)|}{|A_2(\omega)|}$ against ω.

Specifically this study is concerned with measurements of differential t^* between the $SS-S$ and $SSS-SS$ seismic phases so we re-write Equation (4.4) as:

$$\ln\frac{|A_{SS}(\omega)|}{|A_S(\omega)|} = \ln\frac{G_{SS}}{G_S} - \frac{\omega}{2}(t_{SS}^* - t_S^*) \tag{4.5}$$

for $SS-S$ measurements, and

$$\ln\frac{|A_{SSS}(\omega)|}{|A_{SS}(\omega)|} = \ln\frac{G_{SSS}}{G_{SS}} - \frac{\omega}{2}(t_{SSS}^* - t_{SS}^*) \tag{4.6}$$

for $SSS-SS$ measurements. $|A_S(\omega)|$, $|A_{SS}(\omega)|$ and $|A_{SSS}(\omega)|$ are the S, SS and SSS amplitude spectra respectively obtained by Fourier transforming the time domain waveforms into the frequency domain. The differential attenuation between $SS-S$ and $SSS-SS$ is given by $t_{SS}^*-t_S^*$ and $t_{SS}^*-t_S^*$ respectively.

Equation (4.5) and Equation (4.6) provide expressions relating the spectral ratio between two seismic phases to the differential t^* between the phases. Section 4.3 details the data processing involved including an example.

4.3 Data processing

As described in Section 4.2 values of differential t^* can be found from the spectral ratio between two seismic phases. For $SS-S$ differential t^* measurements the spectral ratio between the SS phase and S phase is used. For $SSS-SS$ differential t^* measurements the spectral ratio between the SSS phase and the SS phase is used.

The spectral ratio method utilises only real, unfiltered seismograms. The S, SS and SSS phases are windowed out as described in Section 3.4 providing 3246 seismograms for the $SS-S$ study and 885 seismograms for the $SSS-SS$ study. Again, only data where both the S and SS or SSS and SS phases can be clearly distinguished from noise are used. Figure 4.1 gives an illustration of two seismograms which are considered suitable for processing, along with for comparison, two which are considered unsuitable. Because no filtering is applied the total number of viable seismograms is significantly fewer than the number used in the waveform fitting method. This is essentially because it is more difficult to pick out the individual phases from raw data than from filtered data as discussed in Section 2.2.

The record length l of data segment used for each phase is typically between 25-50 s. The lower frequency limit in the Fourier transform is defined by the record length where the lowest usable frequency is given by $\frac{1}{l}$. This means that periods greater than 25-50 s, i.e. frequencies less than 0.02-0.05 Hz, should not be considered in the spectrum as they contain no useful information. These

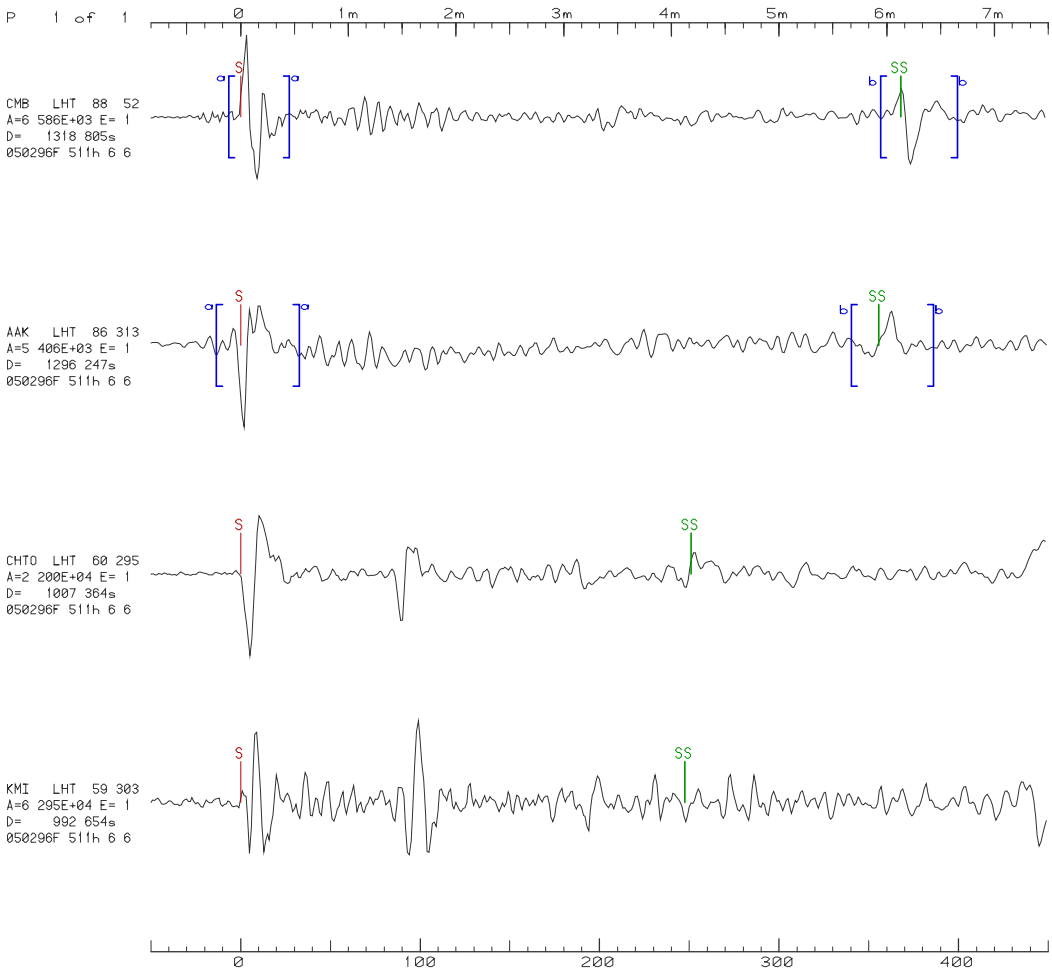


Figure 4.1: Rotated unfiltered seismograms from event 960502F. The top two traces (stations CMB, AAK) show seismograms of high enough quality for picking, the bottom two traces (stations CHTO, KMI) show seismograms for which the quality is not good enough for picks to be made. The intervals "a" and "b" show the regions used in the spectral fitting. The S and SS marks show the arrival time of S or SS as predicted by PREM.

frequencies are produced because the Fourier transform is an infinite sum and thus generates values at all frequencies between zero and the Nyquist frequency.

In general, the amplitude at the end points of each wave segment is non zero (see Figure 4.2 for an example). Although the S and SS wave segments in Figure 4.2 end close to zero this is not good enough. In order to reduce spikiness of the resulting frequency spectra the mean is removed from the data and each wave segment is multiplied by a cosine bell window function $C(t)$ in the time domain prior to applying the Fourier transform. The cosine bell function is shown in Figure 4.3 and is defined as follows:

$$C(t) = \frac{1}{2}\left[1 + \cos\left(\frac{2\pi t}{l} - \pi\right)\right] \qquad 0 \leq t \leq l \tag{4.7}$$

where t is the time in seconds measured from the start of the wave segment and l is the length of the

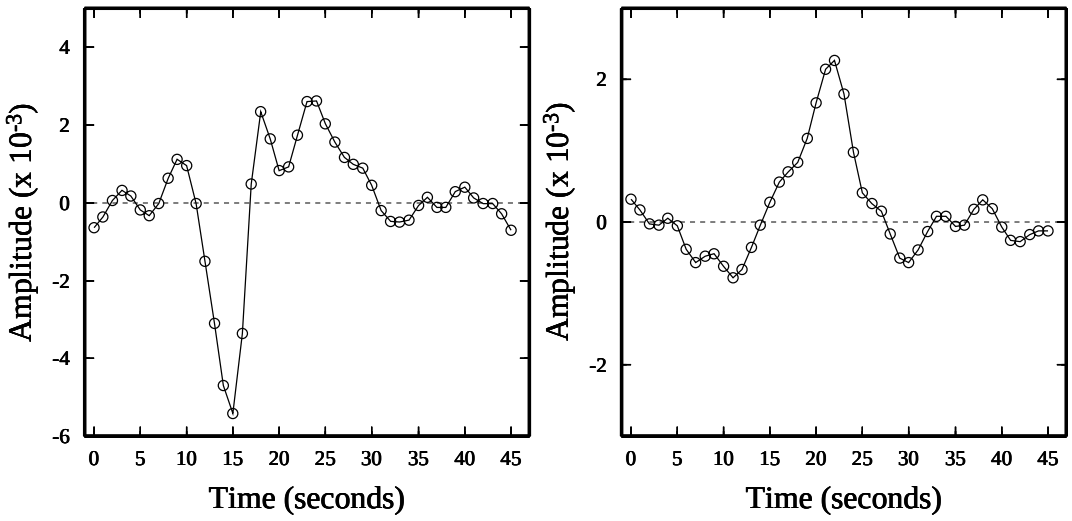


Figure 4.2: Rotated, unfiltered segments of the seismogram from station AAK event 960502F. The left hand plot shows the S phase segment and the right hand plot shows the SS phase segment. The open circles show the data points and the dashed line shows the zero line. Note that the end points of the S and SS traces do not fall exactly on the zero line.

wave segment being used. Multiplication of the wave segment by the cosine bell function has the effect of smoothing the sharp end points so that they finish on zero. It minimises any discontinuity between the start and end of the windowed pulse whilst having minimal effect on the overall shape of the pulse (Matheney & Nowack, 1995). Figure 4.4 shows the S and SS phases after application of the cosine bell function. The overall shape of the waveforms in Figure 4.4 are preserved. However, the start and end points of the waveforms now fall on the zero line unlike in Figure 4.2. After the smoothing is performed the data segments are padded out with zeros to a length of 256 points so that a Fast Fourier transform (FFT) routine can be used. The padded segments are then Fourier transformed into the frequency domain to obtain the amplitude spectra for the S and SS phases. For the forward calculation the transform is defined as follows:

$$F(\omega) = \int_{-\infty}^{\infty} f(t)e^{-i\omega t}dt \tag{4.8}$$

where $f(t)$ is the padded time domain segment and $F(\omega)$ is the resulting spectrum after applying the Fourier transform. This $F(\omega)$ is equivalent to the amplitude spectrum of the phase segment and the amplitude is given by $|A(\omega)| = |F(\omega)|$.

Figure 4.5 shows the amplitude spectra of the S and SS phases from station AAK of event 960502F. Previously, we noted that any frequencies less than 0.02-0.04 Hz should be rejected due to the length of the original data segment. As a result a cosine taper over the range 0.0-0.04 Hz is applied to the frequency domain data. The taper takes the values of 0 and 1 at 0.0 Hz and 0.04 Hz respectively. Figure 4.6 shows the resulting S and SS amplitude spectra after application of the cosine taper. The

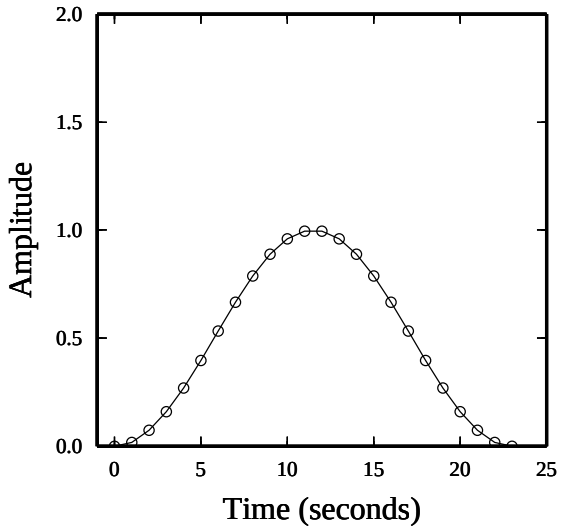


Figure 4.3: Cosine bell window function used to smooth the end points of the waveform segments. The cosine bell shown here is for a waveform segment containing 24 data points so that the length of segment, $l = 23$ units. The bell function is defined by $C(t) = \frac{1}{2}\left[1 + \cos\left(\frac{2\pi t}{l} - \pi\right)\right]$ for $0 \leq t \leq l$.

taper has the effect of greatly reducing the spikiness of the resulting spectral ratio and also helps to ensure that the relevant part of the frequency spectrum is used in the subsequent fitting routine. Figure 4.7 shows the logarithm of the amplitude spectra of the S and SS phases from station AAK of event 960502F after application of the cosine taper.

As mentioned in Section 4.2 the $SS-S$ differential t^* can be obtained from the gradient of a graph of $\ln \frac{|A_{SS}(\omega)|}{|A_S(\omega)|}$ against ω. Equation (4.5) takes the form of a straight line $y(x) = ax + b$ with intercept $\ln \frac{G_{SS}}{G_S}$ and gradient $-\frac{1}{2}(t^*_{SS} - t^*_S)$. The gradient and intercept are found using the method of linear regression as described by Press *et al.* (1986). This method makes a least squares fit to the line given by plotting the spectral ratio against ω. Essentially we seek to minimise the chi-square merit function, χ^2:

$$\chi^2 = \sum_{i=1}^{N} \frac{[y_i - (ax_i + b)]^2}{\sigma_i^2} \tag{4.9}$$

For the spectral data this expression is re-written replacing the i's with ω's and setting:

$y_i = \ln \frac{|A_{SS}(\omega)|}{|A_S(\omega)|}$

$x_i = \omega$

$a = -\frac{1}{2}\omega\Delta t^*$

$b = \ln \frac{G_{SS}}{G_S}$

$\sigma_i^2 = \sigma^2(\omega)$

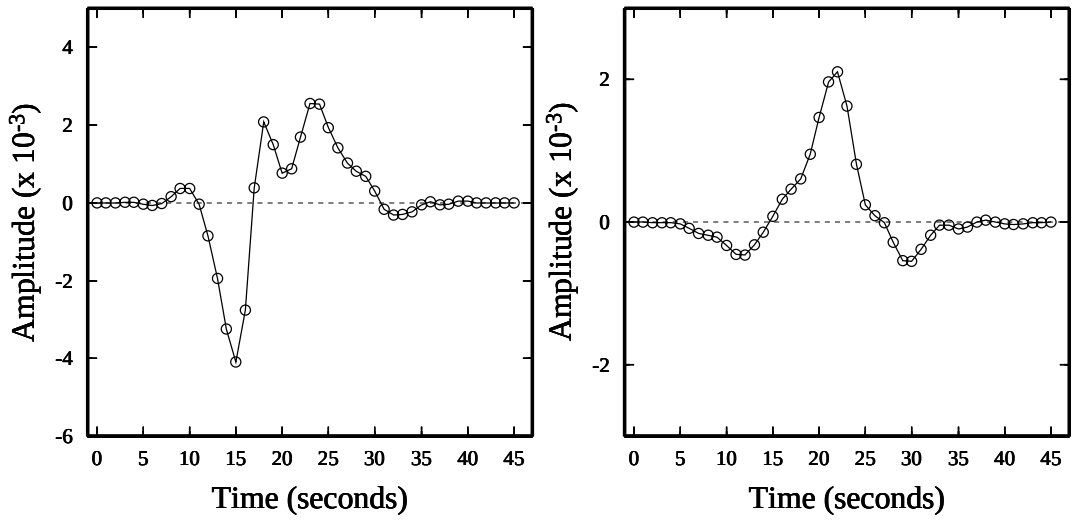


Figure 4.4: Rotated unfiltered segments of the seismogram from station AAK event 960502F. The left hand plot shows the S phase segment and the right hand plot shows the SS phase segment, both the S and SS phases are smoothed using the cosine function. The open circles show the data points and the dashed line shows the zero line. Note, both the S and SS traces end approximately on the zero line.

so that the expression becomes:

$$\chi^2 = \sum_{\omega} \frac{\left[\ln \frac{|A_{SS}(\omega)|}{|A_S(\omega)|} - (\ln \frac{G_{SS}}{G_S} - \frac{1}{2}\Delta t^* \omega)\right]^2}{\sigma^2(\omega)} \tag{4.10}$$

where Δt^* is assumed to be the $SS - S$ differential t^* i.e. for this example $\Delta t^* = t^*_{SS} - t^*_S$. The linear regression routine (Press *et al.*, 1986) calculates the gradient and intercept of the best-fit (in a least squares sense) straight line along with estimates of their uncertainties, the χ^2 value and a statistic called Q which is the "goodness-of-fit" probability that the data has this value of χ^2 or larger. Press *et al.* (1986) provide a more detailed explanation of the definition and meaning of Q.

Before examining any results obtained from the linear regression it is first necessary to explain the choice of weighting function along with the resulting errors. The form of the weighting function is discussed in Section 4.3.1. The resulting consequences for the errors in the gradient and intercept are discussed in Section 4.3.2. Some specimen results are presented in Section 4.4.

4.3.1 A matter of weighting

The data weighting is defined as follows:

$$W(\omega) = \omega \left[|A_{SS}(\omega)|^2 + |A_S(\omega)|^2\right] \tag{4.11}$$

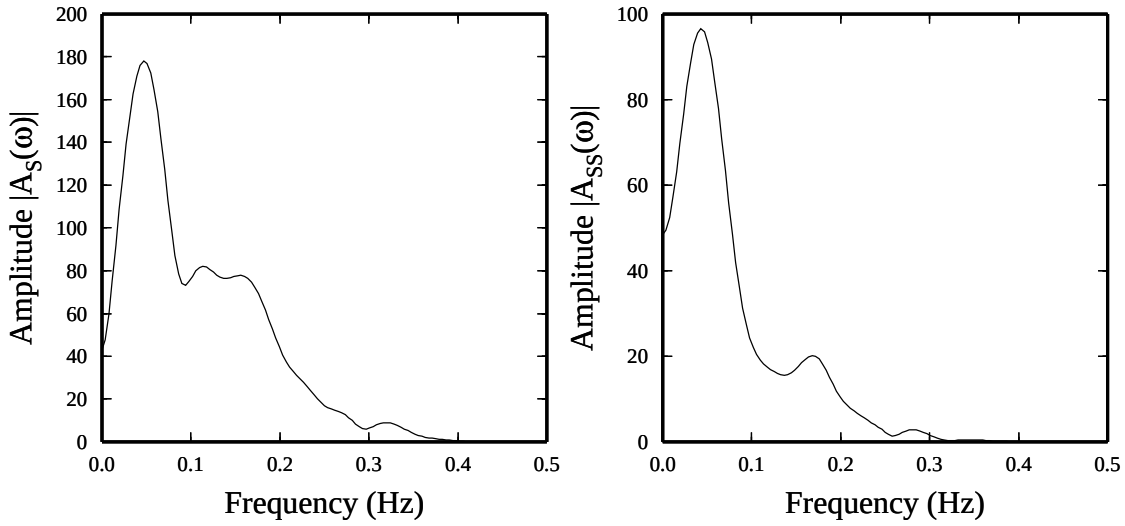


Figure 4.5: Amplitude spectra for the S (left) and SS (right) phases.

where the standard deviations are given by:

$$\sigma(\omega) = \frac{1}{\sqrt{W(\omega)}} = \frac{1}{\sqrt{\omega}} \frac{1}{\sqrt{|A_{SS}(\omega)|^2 + |A_S(\omega)|^2}} \tag{4.12}$$

$A_{SS}(\omega)$ and $A_S(\omega)$ are the SS and S amplitude spectra, ω is the angular frequency in radians per second. This weighting is chosen so as to ensure that the relevant part of the frequency spectrum is fitted for each station. An explanation for this choice of weighting now follows: Consider Figure 4.6 which shows the amplitude spectra for the S and SS phases from station AAK of event 960502F. Both $|A_S(\omega)|$ and $|A_{SS}(\omega)|$ drop off very rapidly with increasing frequency such that by 0.2 Hz the amplitudes are close to zero. As a result, fitting a straight line to the spectral ratio makes little sense for frequencies much greater than 0.2 Hz as the signal has effectively no power there. Therefore the data are weighted using the power spectra of the data. This ensures that parts of the spectra containing a large amount of power are given higher weighting than those containing little or no power, which are more liable to be contaminated with noise. This serves to eliminate the effects of spectral holes (gaps in the spectrum) and also ensures that the highest emphasis is placed on parts of the spectrum with most power, therefore ensuring that the most reliable parts of the spectrum are used to make the straight line fit. The data are also weighted with frequency as shown in Figure 4.8. Both the very low frequency (0.0-0.04 Hz) and the high frequency (> 0.3 Hz) parts of the spectrum are particularly noisy and using them may well cause distortions to the straight line fits obtained. Weighting the data with the power spectra reduces the emphasis placed on the higher frequencies. Weighting with frequency has the effect of down-weighting the very low frequencies along with broadening and smoothing the weighting function so that it does not rise and fall sharply.

The weighting function changes from one station to another depending on the amplitude (i.e.

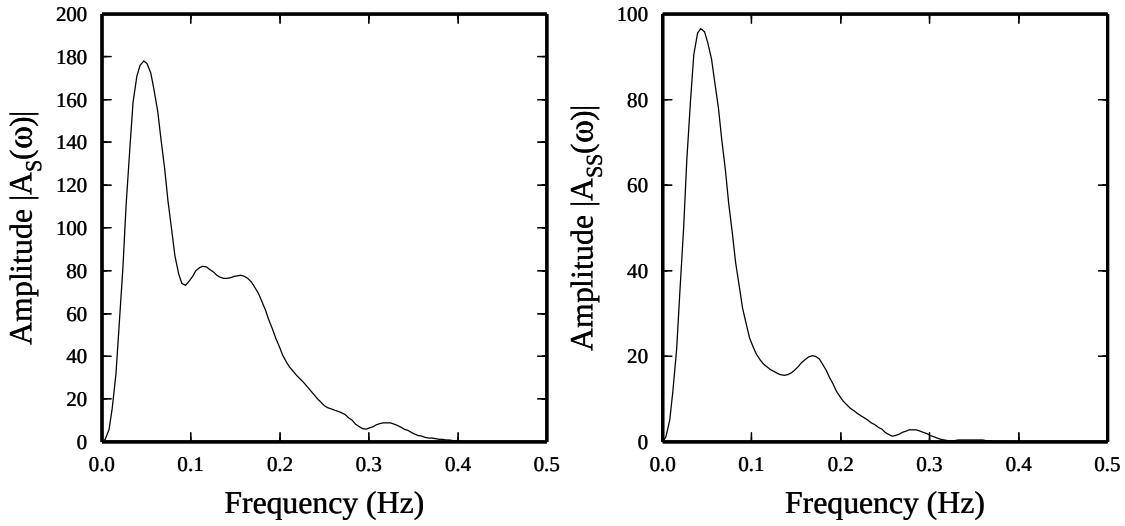


Figure 4.6: Amplitude spectra for the S (left) and SS (right) phases after application of a cosine taper between 0-0.04 Hz.

power) spectra and frequency content of the data. The weighting attempts to highlight the best interval for fitting the straight line without any sharp cut-offs or the need to specify the frequency range required thus selecting the optimal interval for each source and station pair.

4.3.2 Consequences for the errors

The use of such a weighting function requires the standard deviations obtained from the fitting program to be altered. Because the input weights and therefore standard deviations are somewhat "artificial" they must be re-scaled so that realistic values are produced by the fitting routine. Essentially we have an expression:

$$y = ax + b + \varepsilon \tag{4.13}$$

where, a is the gradient, b is the intercept and ε is used to the denote the errors. In standard statistics the variance of ε is defined as:

$$\mathrm{var}(\varepsilon) = \sigma^2 k^2 \tag{4.14}$$

where, $\mathrm{var}(\varepsilon)$ is the variance, σ is the standard deviation for a particular parameter and k is a factor which scales the errors. We now ask the question "what value of k is consistent with the data ?". For the situation where no scaling is applied the χ^2 value to be minimised is given by Equation (4.10). However we want to find what value of k is consistent with the data, i.e. we want to find which k will give a χ^2 of approximately N, where N is the total number of data points. Thus k is obtained from:

$$\chi^2 = \sum_i \frac{(y_i - ax_i - b)^2}{\sigma_i^2 k^2} \simeq N \tag{4.15}$$

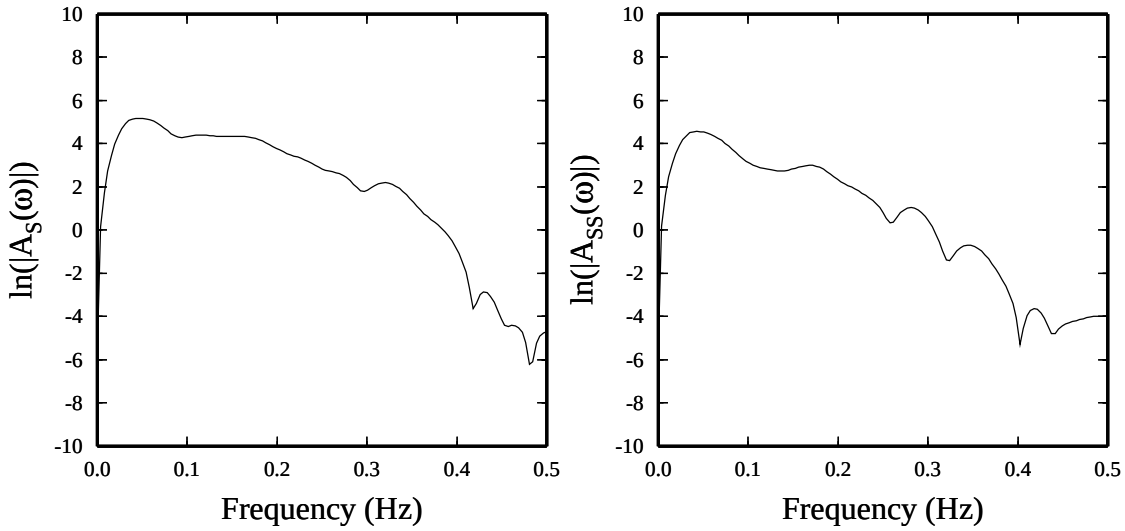


Figure 4.7: Logarithm of the amplitude spectra for the S (left) and SS (right) phases from station AAK of event 960502F. Note that the values of $A_S(0)$ and $A_{SS}(0)$ are set to be 0.0001 instead of 0 to avoid problems with the 0 Hz point.

which gives:

$$k = \sqrt{\frac{\chi^2}{N}} \tag{4.16}$$

With no scaling, the standard deviations for the parameters a and b are σ_a and σ_b respectively. With scaling these standard deviations become:

$$\sigma_a = k\hat{\sigma_a} \tag{4.17}$$

and

$$\sigma_b = k\hat{\sigma_b} \tag{4.18}$$

The $\hat{\sigma}$ values on the right hand side of these two expressions are the original values obtained from the linear regression routine. Multiplication by the k factor provides standard deviations which are related to the actual values of gradient and intercept.

In reality these error estimates probably serve little purpose at all. They provide a measure of the size of the errors in the gradient and intercept obtained from the fitting program and hence can be used as a measure of how well the straight line fits the data. However these errors take no account of any error made in windowing out the phases and so perhaps do not provide the most ideal estimate of the error in Δt^*. It is likely that the choice of phase window will be the biggest source of error. Therefore when inverting the data it is perhaps better to ignore the values of σ_a when weighting the t^* data, treating all points with equal uncertainty.

4.4 Example results from the spectral ratio method

The results from the linear regression are now used to find values of the differential t^*. Recall from Equation (4.4) that, Δt^* is given by -2 times the gradient of the straight line of the spectral ratio plotted against angular frequency, ω. Note however that the routine used to perform the Fourier transform uses frequency, f instead and therefore the resulting amplitude spectra and spectral ratios are plotted against f and not ω. This is not a problem since ω and f are linearly related via $\omega = 2\pi f$. As a result of this the value of differential t^* is actually given by $-\frac{1}{\pi}$ times the gradient of the straight line through the spectral ratio plotted against f. For example consider Figure 4.8 which shows the $SS - S$ spectral ratio against frequency f for station AAK from event 960502F. The red line shows the straight line obtained from fitting a least squares straight line to the spectral ratio between plotted between 0-0.25 Hz. Table 4.1 gives the gradient, intercept and their respective errors for each station from event 960502F including AAK. Table 4.1 also gives the PREM values of $SS - S$ differential attenuation, Δt^*_P, which are calculated from the PREM model. The value of Δt^* for station AAK is obtained by multiplying the gradient by $-\frac{1}{\pi}$ which gives the $SS - S$ differential t^* to be 2.01 s. Thus the value of differential t^* relative to the PREM value of 2.95 s is -0.94 s.

Station	Intercept b	Gradient a	σ_b	σ_a	Δt^*	$\frac{\sigma_a}{\pi}$	Δt^*_P	$\Delta t^* - \Delta t^*_P$
AAK	-0.38	-6.31	0.04	0.31	2.01	0.10	2.95	-0.95
BJT	0.56	-11.71	0.14	0.93	3.73	0.29	2.71	1.02
CMB	0.35	-11.32	0.07	0.57	3.60	0.18	2.98	0.63
DGR	1.66	-19.48	0.12	1.07	6.20	0.34	3.01	3.20
HIA	-0.22	-9.63	0.13	0.93	3.07	0.30	2.75	0.32
LSA	-0.73	-7.95	0.12	0.90	2.53	0.29	2.81	-0.28
SPA	-0.20	-8.89	0.10	0.70	2.83	0.22	2.95	-0.12
WMQ	-0.85	-6.69	0.09	0.50	2.13	0.16	2.87	-0.74

Table 4.1: Results from the spectral ratio method for event 960502F. Δt^* is the $SS - S$ differential attenuation and $\frac{\sigma_a}{\pi}$ is its standard deviation. Δt^*_P is the PREM value of $SS - S$ differential attenuation computed from the PREM tables.

4.5 Summary

In this Chapter a method for obtaining differential t^* values using a spectral ratio method is presented. Issues to note are:

- The method uses only real, raw, unfiltered seismograms which means any problems arising from

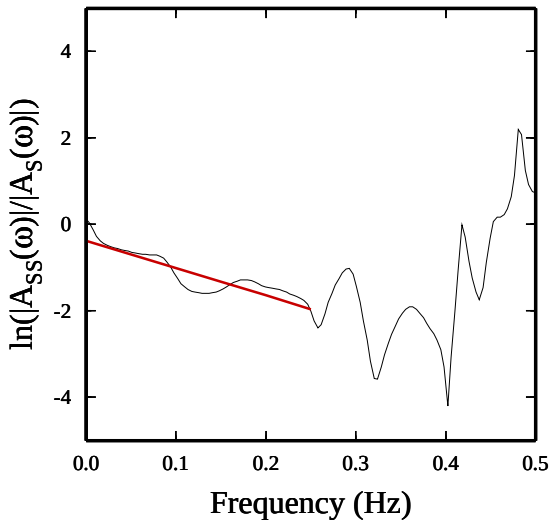


Figure 4.8: Spectral ratio for $SS - S$ plotted against frequency. The red line shows the resulting straight line fit to the data over the range 0-0.25 Hz. The gradient and intercept of this line are -6.31 and -0.31 respectively.

the use of synthetic data are eliminated.

- The method provides an alternative way for measuring Δt^* using a frequency domain measurement technique.
- It is assumed that source and receiver crustal terms cancel and also that geometrical spreading is independent of frequency.

Chapter 5

Preliminary results: examining the residuals

5.1 Introduction

The methodologies for obtaining both travel time and Δt^* residuals are described in the previous two Chapters. In this Chapter the preliminary results from both the waveform fitting and spectral ratio methods are presented. The results from these two methods are discussed separately in Section 5.2 and Section 5.3 respectively. The range and distribution of the residuals, their behaviour with epicentral distance, the geographical distribution of the residuals, the density of residuals and the distribution of errors are amongst the topics considered. In this Chapter no corrections are made to the residuals for the effects of the Earth's crust or ellipticity, only the raw residuals are considered.

5.2 Results from the waveform fitting method

In this Section the preliminary results from the waveform fitting method are presented and discussed. The waveform fitting method provides a total of 4207 residuals obtained from 597 events for the $SS-S$ study and 992 residuals obtained from 260 events for the $SSS-SS$ study. The travel time and t^* residuals are considered separately in Section 5.2.1 and Section 5.2.2 respectively.

5.2.1 Travel time residuals

The waveform fitting method provides a total of 4207 $SS-S$ and 992 $SSS-SS$ differential travel time measurements. The residuals are given relative to the PREM model. Positive residuals are obtained when the differential travel time obtained from fitting waveforms is greater than the PREM differential travel time. Negative residuals are obtained when the differential travel time obtained

from fitting waveforms is less than the differential travel time calculated from the PREM model. If a positive residual is obtained then one of the following must be true:

- The actual S wave travels faster than the PREM S wave
- The actual SS wave travels slower than the PREM SS wave

It is possible to obtain a positive residual with both statements above being true as long as the $SS-S$ travel time obtained from waveform fitting is greater than the PREM differential travel time. Similarly a negative travel time residual is obtained if one (or both) of the following is true:

- The actual S wave travels slower than the PREM S wave
- The actual SS wave travels faster than the PREM SS wave

Figure 5.1 shows the distribution of $SS-S$ travel time residuals obtained from the waveform fitting method along with a Gaussian calculated from:

$$f(x) = \frac{1}{\sigma\sqrt{2\pi}} \exp\left[-\frac{1}{2}\left(\frac{x-\mu}{\sigma}\right)^2\right] \tag{5.1}$$

where $f(x)$ is the Gaussian curve, μ is the mean of the all the data points and σ is the associated standard deviation. Figure 5.2 shows the corresponding plot for the $SSS-SS$ residuals. The $SS-S$ travel time residuals range between ± 17 s with 98% of the residuals being within ± 12 s. The mean of the $SS-S$ residuals is 0.12 s, with standard error of 0.07 s and standard deviation $\sigma = 4.54$ s. The standard error of the mean is given by $\sigma_m = \frac{\sigma}{\sqrt{N}}$, where N is the total number of measurements, which for $SS-S$ measurements is 4207. The Gaussian curve fits the data fairly well although there is a slight skewing towards the negative residuals. The $SSS-SS$ residuals range between -19.5 to $+25.3$ s, again with 98% of the residuals in the range ± 12 s. The $SSS-SS$ residuals have a mean of -0.81 s, with standard error of 0.17 s, and standard deviation $\sigma = 5.26$ s. Again the Gaussian provides a satisfactory fit to the data with a slight skew towards the negative residuals.

The relationship between travel time residual and epicentral distance is also examined. Consider Figure 5.3 which shows the $SS-S$ travel time residuals plotted in intervals of 10° in epicentral distance. The different distance ranges have different means and in general bins having more data points (e.g. $70^\circ - 80^\circ$) tend to be more symmetric in appearance than those containing fewer data points (e.g. $100^\circ - 110^\circ$). Figure 5.4 shows the corresponding plot for the $SSS-SS$ data with the residuals plotted in 15° intervals. Again the distance intervals containing most data points tend to be more symmetrical in appearance (e.g. $135^\circ - 150^\circ$) than those containing very few data points (e.g. $165^\circ - 180^\circ$). Figure 5.5 shows the average distance dependence of the $SS-S$ travel time residuals plotted as the means of 2° bins between $50^\circ - 102^\circ$. The values below each data point give the total number of points in that particular bin. At epicentral distances between $57^\circ - 67^\circ$ the residuals exhibit some scatter. Overall, the mean $SS-S$ residual tends to decrease with increasing epicentral distance until

around 85° where the mean residual starts to increase with distance. Similar behaviour is also observed by Woodward & Masters (1991a). Figure 5.6 shows the corresponding plot for the $SSS - SS$ travel time residuals. The mean $SSS - SS$ residual decreases with increasing distance, passing through zero around 150° and then increases with distance. The mean residuals between $165° - 180°$ are somewhat more scattered than at other distance ranges. The explanation for this is most likely to be that only a very small number of data points fall into these bins (as few as 1 data point in the $170° - 174°$ bin) and therefore the mean is not particularly well constrained for such distance ranges.

It is also possible examine to the geographical distribution of the $SS - S$ residuals by plotting them at the SS phase bounce point. It should be noted that this involves no formal modelling of the data, it is simply a means of plotting the residuals which gives some insight into how they are distributed geographically. Before discussing the plots it is first necessary to explain the justification for plotting the residuals at the SS phase bounce point.

For epicentral distances in excess of 50° both the direct and reflected phases sample the source and receiver regions in a similar manner. Also, both the direct and reflected phases bottom at depths of 700km or greater. The mantle is thought to be more heterogeneous at the surface than at such depths and therefore the source of any observed travel time or attenuation residual can be attributed to structure in the mantle and crust in the vicinity of the reflected (SS) phase's bounce point (Woodward & Masters, 1991a). The $SSS - SS$ residuals cannot be represented in such a way. This is because the SSS and SS phases do not follow even slightly similar paths and therefore plotting the residuals at the SS or SSS bounce points makes no sense whatsoever. As a result only maps of the $SS - S$ residuals are included in this Chapter.

Figure 5.7 shows the $SS - S$ residuals plotted at the SS bounce point. Clearly this map is difficult to interpret as the density of data points in many regions is such that many points plot on top of one another. As a means of combating this, the residuals are binned in 5° spherical caps. Figure 5.8 shows the $SS - S$ travel time residuals plotted in 5° spherical caps at the SS bounce point. Positive residuals are plotted as red crosses and negative residuals are plotted as blue triangles. Each spherical cap consists of the average of all the residuals having bounce points within a 5° radius of the centre of the cap. Plotting the data in these spherical caps results in smoothing out of the individual data. It also makes the residuals easier to interpret as it has the effect of smoothing out the small scale variability and uneven geographical distribution of measurements. The caps are chosen so that they appear at even spacing on a Hammer plot which is purely for aesthetic reasons. The latitude intervals are always in 5° increments but the longitude interval varies depending on the circumference of the Earth so that polar regions have fewer points for a given latitude than equatorial regions. Figure 5.8 shows the residuals binned in caps having at least one point in each cap. This results in 76% coverage. Figure 5.9 and Figure 5.10 show the residuals binned in spherical caps having at least 3 and 5 points respectively which reduces the coverage to 50% and 36%. These maps are included to illustrate how the coverage varies with the density of residuals. Comparison of Figure 5.8 and Figure 5.10 shows

that the coverage in the northern hemisphere is substantially denser than in the southern hemisphere. In fact if we limit ourselves to 5 points or more per cap (Figure 5.10) then there are practically no data points in South America or Africa. This is very different to the coverage obtained in Figure 5.8 where the data points are spread evenly across the globe. Figure 5.11 is used to further emphasise this. It depicts the density of bounce points in each spherical cap. The darker the shading the greater the density of coverage. White areas indicate regions where no bounce points occur. The density is highest across the Pacific with in excess of 350 bounce points occurring in some caps.

The majority of the positive residuals are found in Antarctica, eastern Asia, Indonesia, along the spreading ridges in the southern Pacific and Indian Oceans, and along the western coast of North America. The majority of the negative residuals are found to the east of South America, along the mid-Atlantic ridge, in the north east of North America and in the western Pacific Ocean close to Japan.

5.2.2 t^* residuals

The waveform fitting method also provides 4207 $SS-S$ and 992 $SSS-SS$ differential t^* (i.e. Δt^*) residuals. The residuals are calculated relative to the PREM differential t^* values. A positive residual is obtained when the differential attenuation (i.e. Δt^*) obtained from fitting waveforms is greater than the PREM value (i.e. Δt^*_{PREM}). A negative residual is obtained when the differential attenuation obtained from waveform fitting is less than the PREM value. Since the residuals are obtained from differential measurements several factors may give rise to a positive or negative residual. For example a positive residual is obtained if one or both of the following is true:

- The actual S wave has a higher value of t^* than the PREM S wave. i.e. the actual S wave is attenuated more than the PREM S wave.
- The actual SS wave has a lower value of t^* than the PREM value. i.e. the actual SS wave is attenuated less than the PREM SS wave.

Again, as with the travel time residuals, it is possible to obtain a positive t^* residual with the both of the above statements above true. So long as the difference between the actual $t^*_{SS}-t^*_S$ is greater than the corresponding PREM value, then a positive residual will be obtained. Similarly a negative t^* residual is obtained if one or both of the following is true:

- The actual S wave has a lower value of t^* than the PREM S wave. i.e. the actual S wave is attenuated less than the PREM S wave.
- The actual SS wave has a higher value of t^* than the PREM SS wave. i.e. the actual SS wave is attenuated more than the PREM SS wave.

Now that we have defined what is meant by a positive or negative residual we may proceed to discuss the residuals themselves. Figure 5.12 shows the distribution of $SS-S$ differential t^* residuals obtained from the waveform fitting method along with the relevant Gaussian. Figure 5.13 shows the corresponding

plot for the $SSS - SS$ residuals. The $SS - S$ t^* residuals range between -6.7 to $+12.5$ s, with 95% of the residuals between ± 5.0 s and 73% between ± 3.0 s. The mean of the $SS - S$ residuals is -0.18 s with a standard error of 0.04 s and a standard deviation of, $\sigma = 2.69$ s. The Gaussian provides a reasonably good fit to the $SS - S$ residuals with a slight skewing towards the negative residuals. The fit is not as good as for the travel time measurement probably due to the intrinsic problems in making attenuation measurements, although the fit is by no means poor either. The $SSS - SS$ t^* residuals range between -6.6 to $+11.8$ s with 91% between ± 5.0 s and 68% between ± 3.0 s. The mean of the $SSS - SS$ residuals is 0.36 s with standard error of 0.1 s and a standard deviation of, $\sigma = 3.01$ s. Again the Gaussian provides a satisfactory fit to the data which is not quite as good as that obtained for the $SS - S$ case.

The relationship between the epicentral distance and t^* residual is also examined. Figures 5.14 and 5.15 show the differential t^* residuals plotted for different epicentral distance ranges. The $SS - S$ residuals are plotted in 10° intervals from 50° to 110°. The $SSS - SS$ residuals are plotted in 15° intervals from 90° to 180°. The histograms in Figure 5.14 show that the residuals are symmetrically distributed within each distance range. The only exception is for epicentral distances between $100° - 110°$ but this is likely to be due to the much smaller number of points falling into that distance range compared with the other ranges. Figure 5.15 shows similar behaviour with the distance ranges $150° - 165°$ and $165° - 180°$ having less symmetrical distributions which is again probably due to having fewer data points than the other distance ranges.

Figure 5.16 shows the average distance dependence of the $SS - S$ differential t^* residuals plotted as the means of 2° bins between 50° to 102°. As with the travel time residuals the values below each data point give the total number of data points in that distance bin. For epicentral distances between $50° - 57°$ the mean residual is constant at around -0.5 s. Between $57° - 63°$ the mean residual decreases to around -1.5 s. Beyond that point the mean residual tends to decrease with increasing distance passing through zero at around 80° and then increase with distance until around 93°. From $93° - 102°$ the mean residual decreases with increasing distance. Figure 5.17 shows the average distance dependence of the $SSS - SS$ differential t^* residuals plotted as the means of 4° bins between $90° - 180°$. For distances between $95° - 110°$ the average t^* remains roughly constant at around -0.7 s. From $110° - 125°$ the average residual increases to around 1.0 s. Between $125° - 155°$ the mean residual gradually increases with distance. At epicentral distances beyond 155° the average t^* residual behaves erratically, however these distance ranges contain as few as 1 data point so are not such reliable representations of the mean.

As with the travel time residuals, the geographical distribution of the $SS - S$ residuals is also examined. Figure 5.18 shows the $SS - S$ t^* residuals plotted at the SS bounce point. Again interpreting this map is difficult and so the residuals are plotted in 5° spherical caps. Figure 5.19 shows the $SS - S$ t^* residuals plotted in 5° spherical caps at the SS bounce point. Positive residuals are plotted as red crosses and negative residuals are plotted as blue triangles. The spherical caps are as described

in Section 5.2.1. Each cap contains at least 1 point which results in 76% coverage. Figure 5.20 and Figure 5.21 show the t^* residuals binned in spherical caps having at least 3 and 5 points per cap giving coverage of 50% and 36% respectively. Again these extra maps are included to illustrate how the coverage varies across the globe. The dataset used is the same as for the travel time residuals and therefore the same patterns found in Section 5.2.1 are observed. i.e. restricting the number of points to at least 3 per cap significantly reduces the coverage in the southern hemisphere. This is further emphasised by Figure 5.11 which shows the density of bounce points in each spherical cap.

Overall the maps show more negative (blue triangles) residuals than positive (red crosses) residuals. The means of the cap averaged data are -0.43, -0.36 and -0.30 for minimums of 1, 3 and 5 points per cap respectively. As the minimum number of points per cap is increased from 1 to 5 the average decreases towards zero and towards the average of all the $SS-S$ t^* measurements (=-0.18 s). Unlike the travel time data it is far harder to describe the behaviour of the t^* residuals as they form less coherent patterns and overall exhibit more random behaviour. The largest areas of negative residuals are found across Australia, northern Canada, around the western Pacific and across central South America. Positive residuals are found in small pockets across the globe with the Pacific Ocean having a slightly higher concentration.

5.2.3 What are the errors ?

The waveform fitting routine provides an estimate of the error in the values of differential travel time and attenuation. This error estimate is given as a standard deviation in seconds. For the $SS-S$ travel time residuals, the standard deviations vary between 0.07-1.27 s with 92% falling below 0.5 s. For the $SS-S$ differential t^* measurements the errors vary between 0.07-2.74 s with 59% below 0.5 s and 94% below 1.0 s. Histograms showing the distribution of the errors in travel time and t^* residuals are given in Figures 5.22 and 5.23 respectively. For both the travel time and t^* residuals, the distribution of errors exhibits a sharp rise to a maximum and then a more gradual fall off. The spread of errors is greater for the attenuation measurements as might be expected due to the difficulties in making measurements of Δt^*. The errors in the t^* residuals can be as large as 2.7 s which may be greater than the size of the residual itself.

For the $SSS-SS$ residuals the errors in travel time range between 0.11-1.03 s with 81% being below 0.5 s. The errors in $SSS-SS$ t^* residuals range between 0.06-1.83 s with 34% below 0.5 s and 90% below 1.0 s. The distribution of the errors in the $SSS-SS$ travel time and attenuation residuals are shown in Figures 5.24 and 5.25 respectively. The distribution of errors for the $SSS-SS$ measurements is very similar to that of the $SS-S$ measurements except that the spread is marginally wider.

The waveform fitting method also yields the fit parameter which is used to measure how well two waveforms fit one another The definition of the fit parameter is provided in Section 3.4.1. For the $SS-S$ measurements the fit parameter ranges between 0.01-0.90. For the $SSS-SS$ measurements,

the fit parameter ranges between 0.014-0.66. The use of the fit parameter will be discussed in more detail in Chapter 6.

5.3 Results from the spectral ratio method

In this section the preliminary results from the spectral ratio method are presented. The spectral ratio method provides 3246 Δt^* residuals from 548 events for the $SS-S$ study and 885 Δt^* residuals from 218 events for the $SSS-SS$ study.

The residuals are all calculated relative to the PREM differential t^* residuals. This means that a positive residual is obtained when the differential attenuation (i.e. Δt^*) obtained from the spectral ratio method is greater than the PREM value (i.e. Δt^*_{PREM}). Likewise a negative residual is obtained when the differential attenuation obtained from the spectral ratio method is less than the PREM value. Figure 5.26 shows the distribution of $SS-S$ differential t^* residuals obtained from the spectral ratio method along with the relevant Gaussian. Figure 5.27 shows the corresponding plot for the $SSS-SS$ residuals. The $SS-S$ residuals range between -11.6 to $+10.0$ s with 95% between ± 6.0 s, 87% between ± 5.0 s and 51% between ± 3.0 s. The residuals have a mean of -2.87 s with standard error of 0.03 s. The standard deviation is, $\sigma = 1.95$ s. The Gaussian provides a good fit to the $SS-S$ residuals.

The $SSS-SS$ residuals range between -10.6 to $+10.3$ s with 95% between ± 6.0 s, 85% between ± 5.0 s and 32% between ± 3.0 s. The mean of the $SSS-SS$ residuals is -3.52 s with standard error of 0.06 s. The standard deviation is, $\sigma = 1.80$ s. The Gaussian provides reasonable fit to the $SSS-SS$, however the fit is significantly worse than for the $SS-S$ dataset.

Also considered is the distribution of residuals with varying epicentral distance ranges. Figure 5.28 and Figure 5.29 show the differential t^* residuals plotted for different epicentral distance ranges. The $SS-S$ residuals are plotted in 10° intervals from 50° to 110°. The $SSS-SS$ residuals are plotted in 15° distance intervals from 90° to 180°. The histograms in Figure 5.28 shows that the residuals are symmetrically distributed within each distance range except for the $100°-110°$ bin. Once more this is probably because the $100°-110°$ bin contains far fewer data points than the others. The histograms in Figure 5.29 show a symmetric distribution of $SSS-SS$ residuals for each distance range.

Figure 5.30 shows the average distance dependence of the $SS-S$ differential t^* residuals plotted as the means of 2° bins between 50° and 102°. The values below each point give the total number of residuals for that 2° bin. Over the distance range the mean remains between approximately -2.5 to -3.5 s. As the epicentral distance increases from 50° to 65° the mean residual decreases from around -2.5 s to around -3.5 s. Between 65° to 90° the mean differential t^* residual increases to around -2.5 s. Just beyond 90° the mean residual jumps to around -3.1 s and then continues to decrease with increasing epicentral distance. Figure 5.31 shows the average distance dependence of the $SSS-SS$ residuals plotted as the means of 4° bins between 90° to 180°. Between the distance range 105° to 155° the mean t^* residual remains fairly constant at approximately -3.0 s. Outside this distance range

($90^\circ - 105^\circ$ and $155 - 180^\circ$) the mean residual behaves more erratically. For the larger distances this is probably due to the small number of points in each distance bin.

The t^* values obtained from the spectral ratio method have a significant non zero mean for both the $SS-S$ and $SSS-SS$ datasets. The $SS-S$ residuals have a mean of -2.87 s and the $SSS-SS$ residuals have a mean of -3.52 s. Because of this large and negative non zero mean, plotting the geographical distribution of $SS-S$ residuals is irrelevant. Essentially this is because the maps obtained would show only negative results and a map showing purely blue triangles and nothing else is of limited use in describing the distribution of residuals. However we do include a plot depicting the density of residuals for the $SS-S$ dataset. Figure 5.32 shows the density of $SS-S$ residuals plotted at the SS bounce point in 5° spherical caps. The plot is very similar to that shown in Figure 5.11 as may perhaps be expected since the source and station distributions are very similar for both the waveform fitting and spectral ratio methods.

5.3.1 What are the errors ?

Residuals obtained from the spectral ratio method have an error associated with them. The method for calculating this error is described in Section 4.3.2. The error in the $SS-S$ differential t^* residuals ranges between 0.02-1.0 s with 96% of errors below 0.5 s. For the $SSS-SS$ residuals obtained from the spectral ratio method the error in t^* residuals ranges between 0.06-1.09 s with 95% of errors below 0.5 s. The reliability of these errors however is somewhat doubtful. Histograms showing how the distribution of the errors in the $SS-S$ and $SSS-SS$ are provided by Figure 5.33 and Figure 5.34 respectively. The histograms show a sharp increase in the error in Δt^* with maxima around 0.25 s and 0.2 s for the $SS-S$ and $SSS-SS$ measurements respectively. Beyond the maxima the distributions tail off gradually. The distributions are skewed in this way because the errors in measuring t^* values cannot be negative or zero.

5.4 Comparison with other studies

In this section we compare the maps of $SS-S$ travel time and attenuation residuals with the results from other studies. The travel time residuals are compared with the results of Woodward & Masters (1991a). Figure 5.35 shows cap-averaged $SS-S$ travel time residuals from Woodward & Masters (1991a). The maps shown by Figures 5.9 and 5.35 show many similarities. Both maps show positive residuals along the mid oceanic ridges (East Pacific rise, South East Indian rise) and the back-arc regions of the west Pacific. Also both maps show negative residuals across the western Pacific, South America, Australia and north eastern America and Canada.

We compare the $SS-S$ t^* residuals with the results of Bhattacharyya *et al.* (1996). Figure 5.36 shows the cap-averaged $SS-S$ Δt^* values for caps with 5 or more measurements obtained by Bhattacharyya *et al.* (1996). The maps shown by Figures 5.21 and 5.36 show some similarity. Negative

residuals are observed across Australia in both maps and positive residuals are observed along the north west coast of Alaska and to the south east of Hawaii on both maps. There are also many areas where the two maps are in disagreement.

5.5 Preliminary discussion of results

In this Chapter the results obtained from both the waveform fitting and spectral ratio method are presented. The residuals obtained using the waveform fitting method take similar values to those found by other researchers. In particular the $SS-S$ travel time residuals fall within approximately the same range as that obtained by Woodward & Masters (1991a). The $SS-S$ differential t^* measurements are more problematic. They are almost a factor of 2 larger than those obtained by Bhattacharyya *et al.* (1996). The t^* residuals also have a considerable negative mean which was not observed by Bhattacharyya *et al.* (1996).

The residuals obtained using the spectral ratio method are more questionable. For both the $SS-S$ and $SSS-SS$ measurements the mean is large and negative. The size of this mean suggests that we are not only measuring t^* but perhaps that something else is contaminating the signal. The spectral ratio method uses raw seismograms which makes windowing of the phases more difficult than for filtered data. It is therefore possible that the signal is contaminated with noise or with other phases. The windowing of the phases is performed visually and therefore perhaps there is a tendency to select those waveforms which have higher than average amplitude (corresponding to low attenuation) than those with lower amplitudes. As a result a negative mean is not unexpected but the size of the mean obtained for measurements made using the spectral ratio method is too large to be explained by this. Something must be contaminating the signal or biasing it in some way.

Other researchers (e.g. Flanagan & Wiens (1990, 1994)) have successfully measured attenuation using frequency domain based spectral ratio measurements. Although the method used in this study is similar to that employed by other researchers, we have been unable to obtain successful measurements of Δt^*. The testing performed in Section C.2 proves that the spectral ratio method of this study is at least in principle capable of retrieving a known value of Δt^*. This testing verifies that if the only contribution to the spectral ratio is from attenuation then the value of Δt^* obtained will correctly give the amount of attenuation applied. The testing does not provide any estimate of the amount of contamination due to interfering phases or to any bias introduced from the picking procedure. It is quite possible that these two factors could explain the apparent problems with the spectral ratio method. It is also possible that analysing and accounting for the noise in the signal could improve the results. Finally there is a possibility that the padding of the waveforms in the time domain prior to applying the Fourier transform could affect the the amplitudes of the spectra. It is likely that the problems experienced with measuring attenuation using the spectral ratio method are due to a combination of these, and possibly other factors. Investigation of the problems associated with the

spectral ratio method of this study should be the subject of future research.

A comparison of Figures 5.8 and 5.19 shows some correlation between regions having faster than average travel times with regions of lower than average attenuation. For example blue triangles are observed on both maps across the western Pacific, across north eastern Canada, and off the southern tip of Africa. Some correlation between regions having slower than average travel times and higher than average attenuation is also observed. For example red crosses are observed on both maps across the southern Pacific, Central America and off the west coast of North America and Canada. It is encouraging that such correlations are observed. If a wave takes longer than average to travel through the Earth then it has most likely encountered a region of higher than average temperature. Intrinsic attenuation is temperature dependent and therefore we should expect that a slow travel time should correlate with higher than average attenuation and vice versa.

The maps of travel time or Δt^* residuals plotted at the SS bounce point may provide some insight into the geographical distribution of the residuals but they do not give any information about the structure of the mantle. For example, a positive $SS - S$ travel time residual is obtained when the actual $SS-S$ time is greater than the PREM time. However there is no way of telling *how* the positive residual is obtained. It could be due to the actual SS ray taking longer than the PREM SS ray (i.e. the actual SS ray travels slower than the PREM ray) or because the actual S ray takes less time than the PREM S ray (i.e. the actual S ray travels faster than the PREM ray). The positive residual could even be obtained due to both of these factors as discussed earlier. The only way of being able to resolve this problem is to model the data. Modelling will also enable us to *see* the geographical patterns associated with the $SSS - SS$ data. This modelling will be the subject of the next chapter.

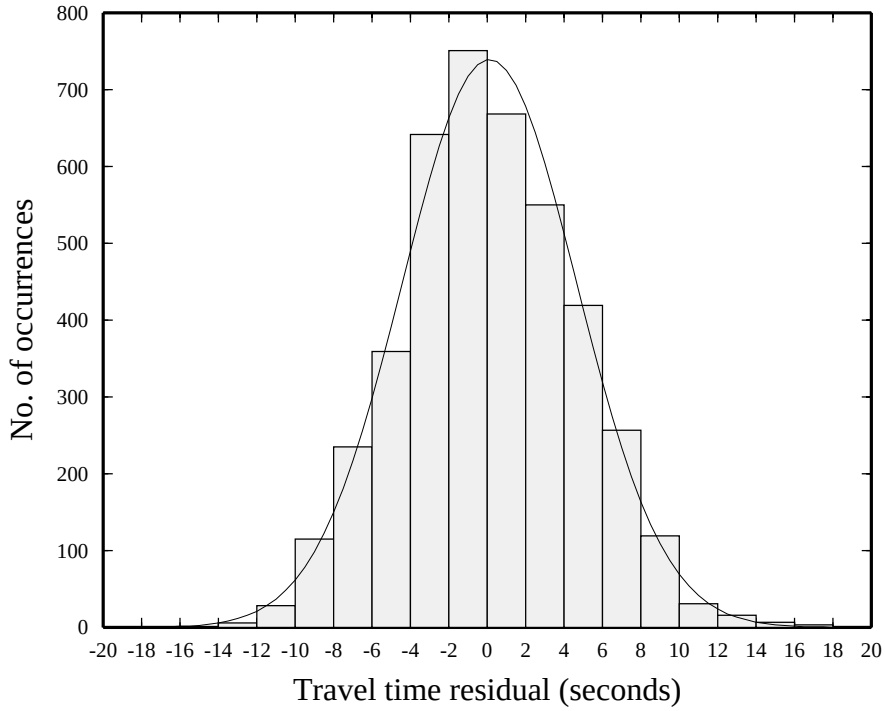


Figure 5.1: Distribution of travel time residuals for the $SS-S$ data obtained from the waveform fitting method.

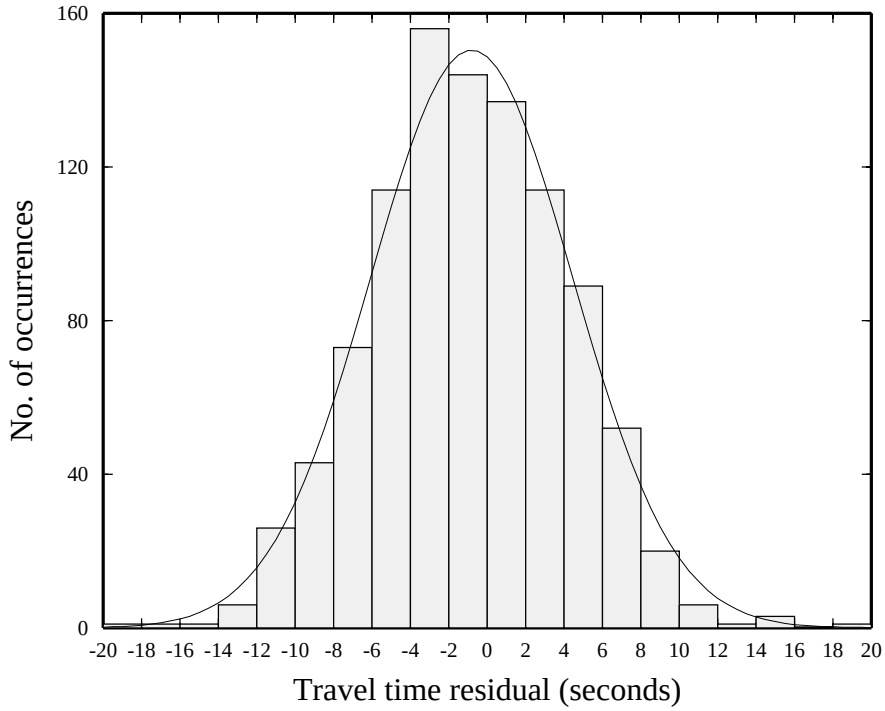


Figure 5.2: Distribution of travel time residuals for the $SSS-SS$ data obtained from the waveform fitting method.

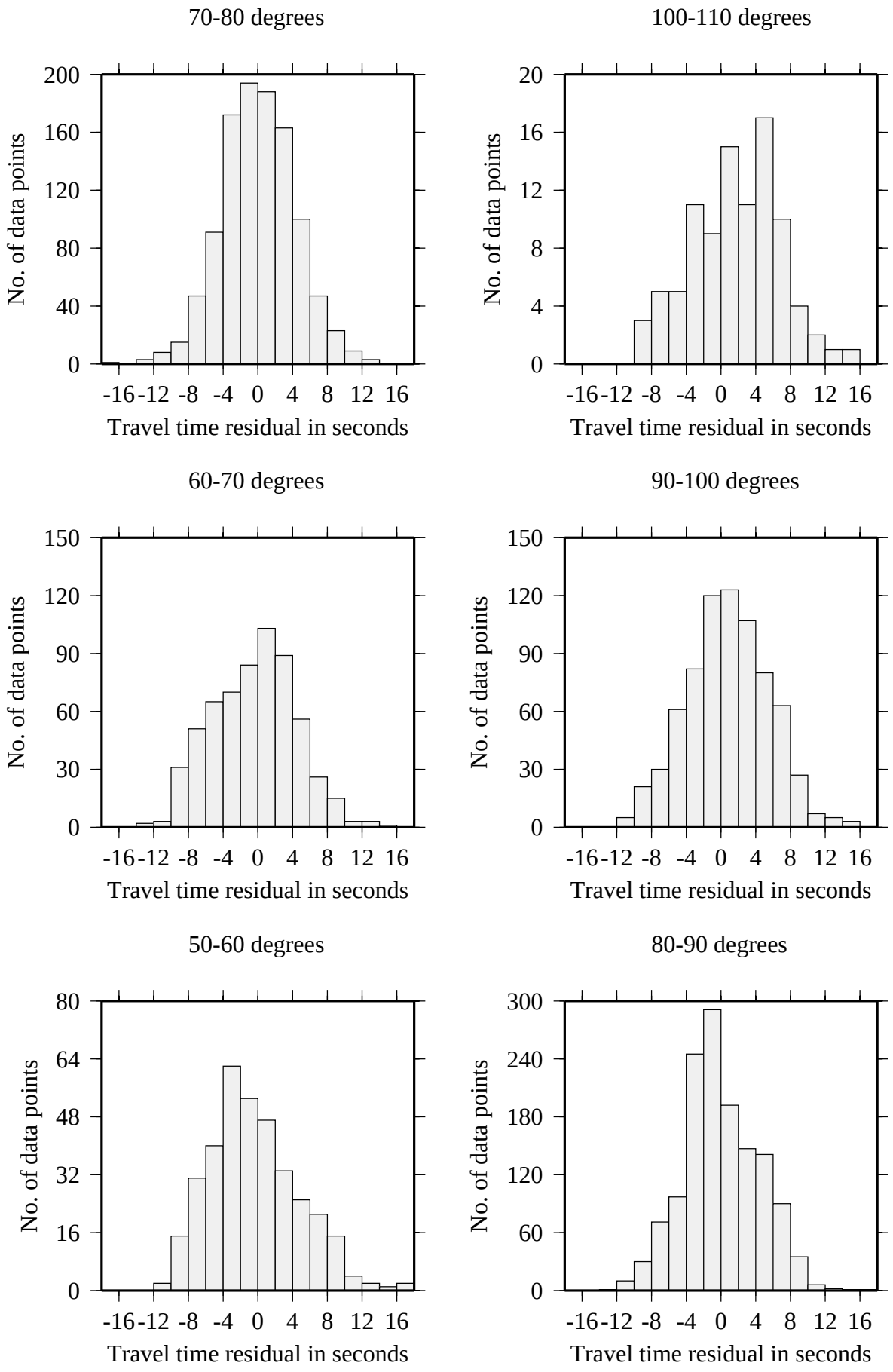


Figure 5.3: Distribution of $SS - S$ travel time residuals for different epicentral distance ranges using data obtained from the waveform fitting method.

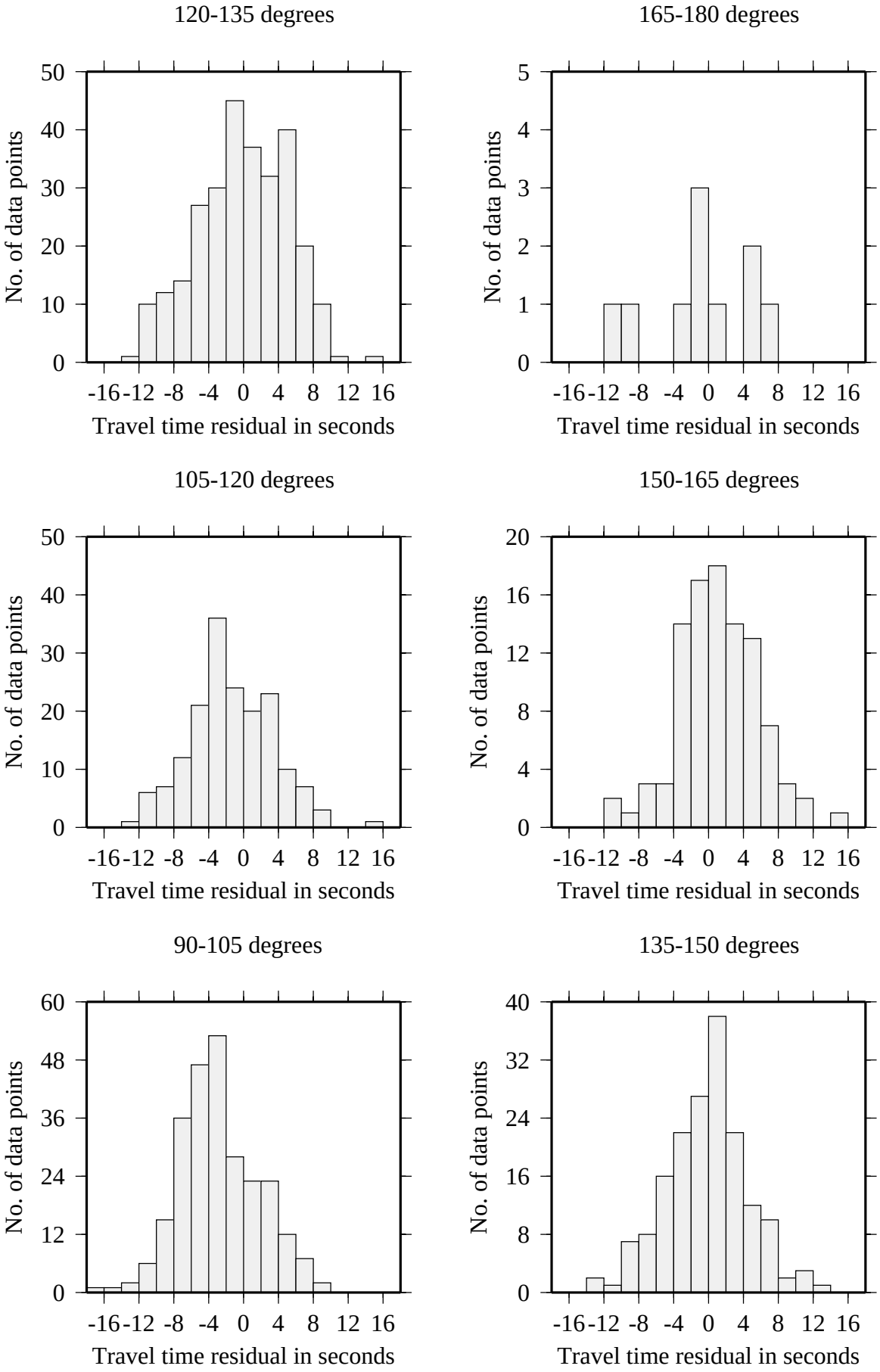


Figure 5.4: Distribution of $SSS-SS$ travel time residuals for different epicentral distance ranges using data obtained from the waveform fitting method.

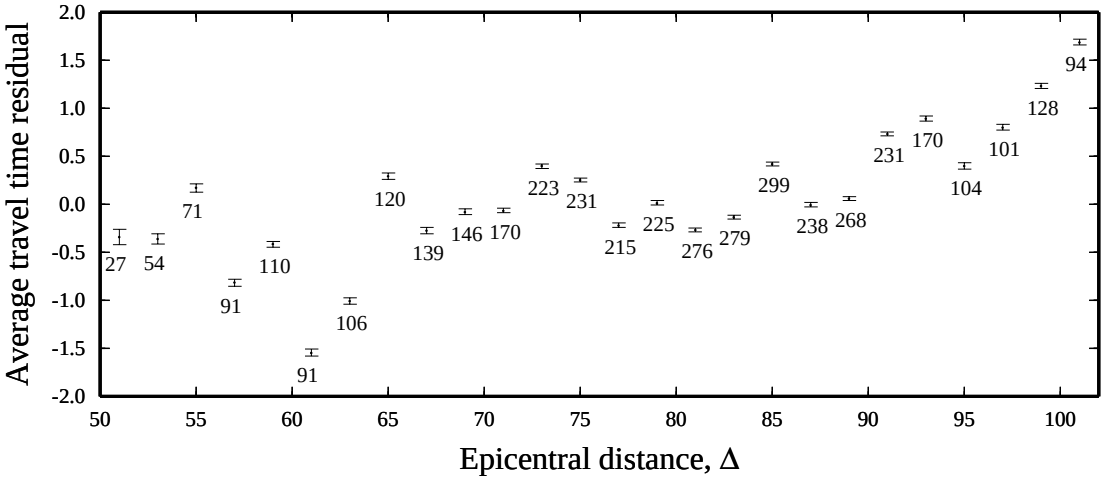


Figure 5.5: Distance dependence of $SS - S$ travel time residuals plotted as the means of 2° bins for epicentral distances between $50° - 102°$. The numbers directly below each point give the total number of residuals for that 2° bin.

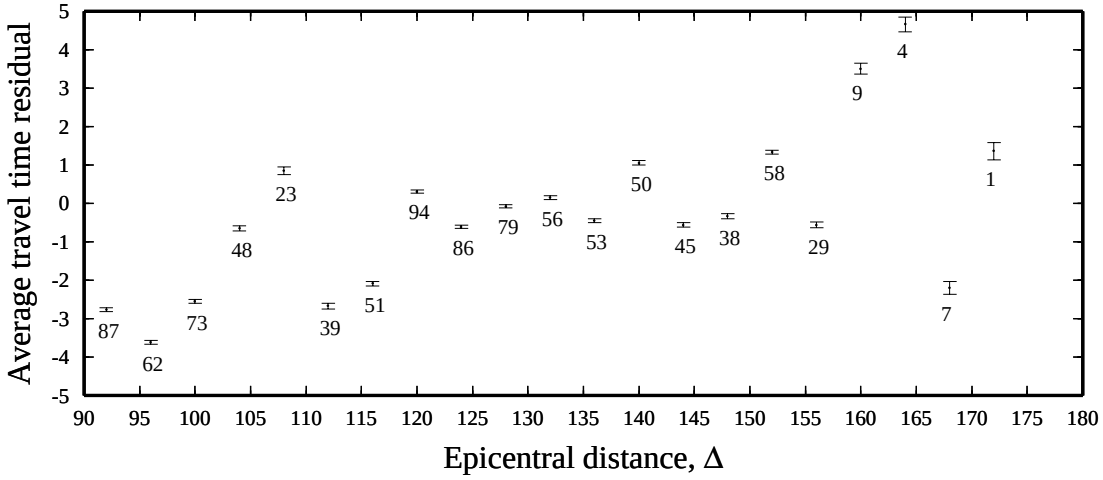


Figure 5.6: Distance dependence of $SSS - SS$ travel time residuals plotted as the means of 4° bins for epicentral distances between $90° - 180°$. The numbers directly below each point give the total number of residuals for that 4° bin.

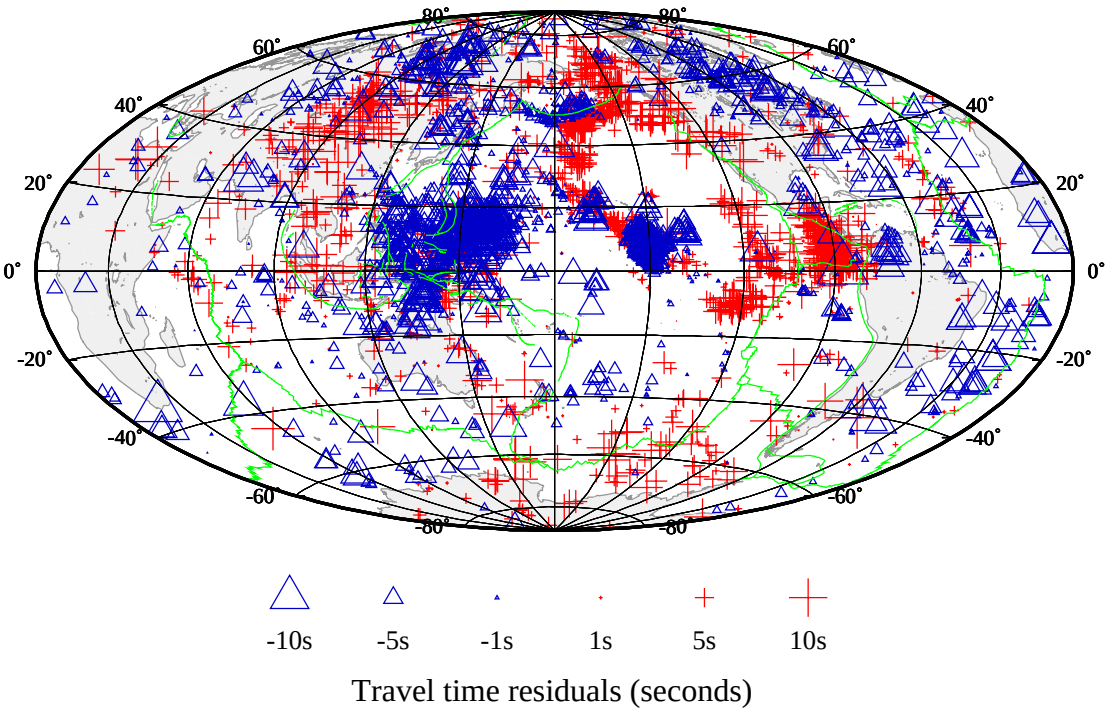


Figure 5.7: Travel time residuals for the $SS - S$ data plotted at the SS bounce point. Note that many residuals plot on top of each other making the map difficult to interpret.

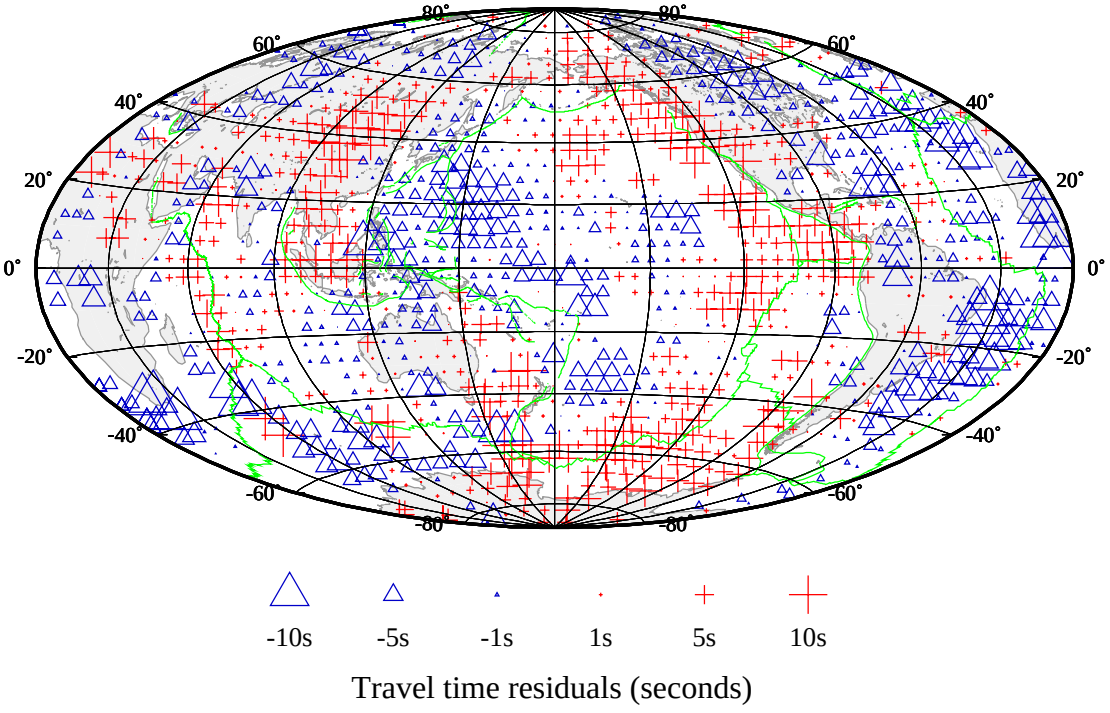


Figure 5.8: Travel time residuals for the $SS - S$ data in 5° spherical caps - 1 point or more per cap.

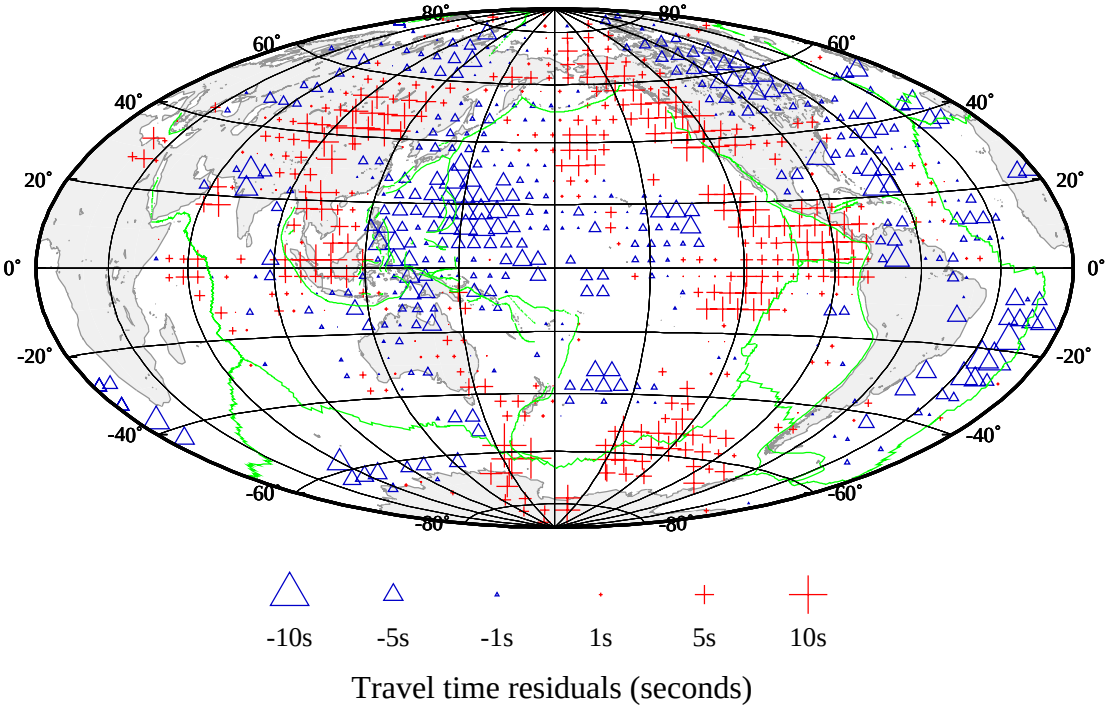


Figure 5.9: Travel time residuals for the $SS - S$ data in 5° spherical caps - 3 points or more per cap.

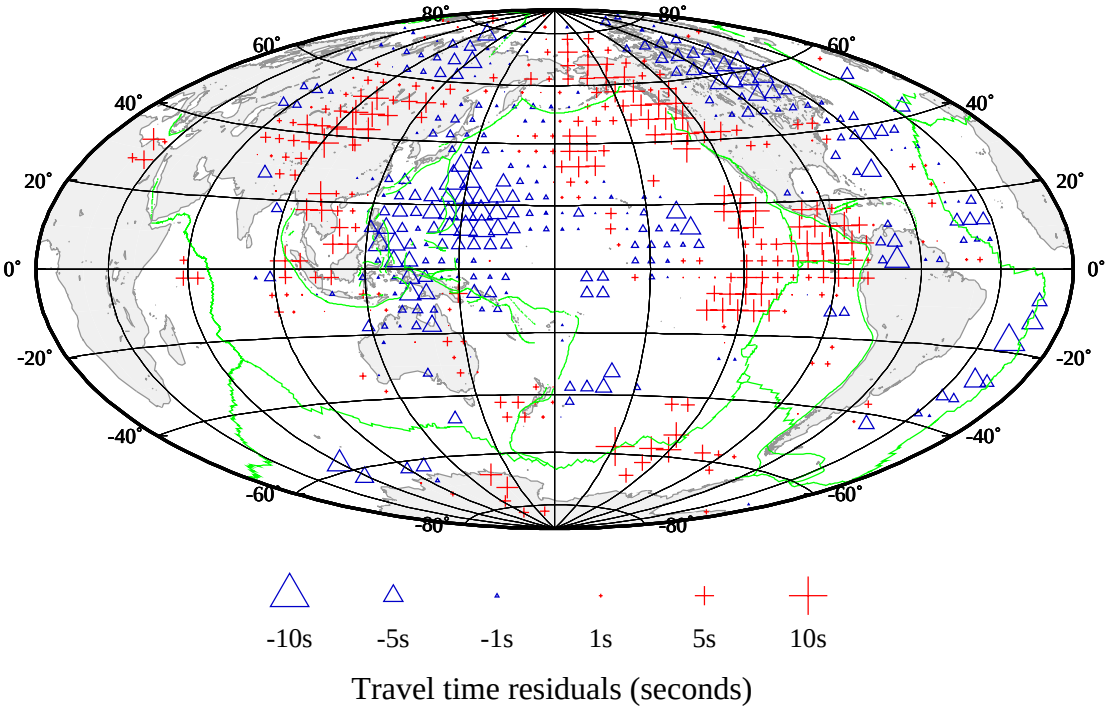


Figure 5.10: Travel time residuals for the $SS - S$ data in 5° spherical caps - 5 points or more per cap.

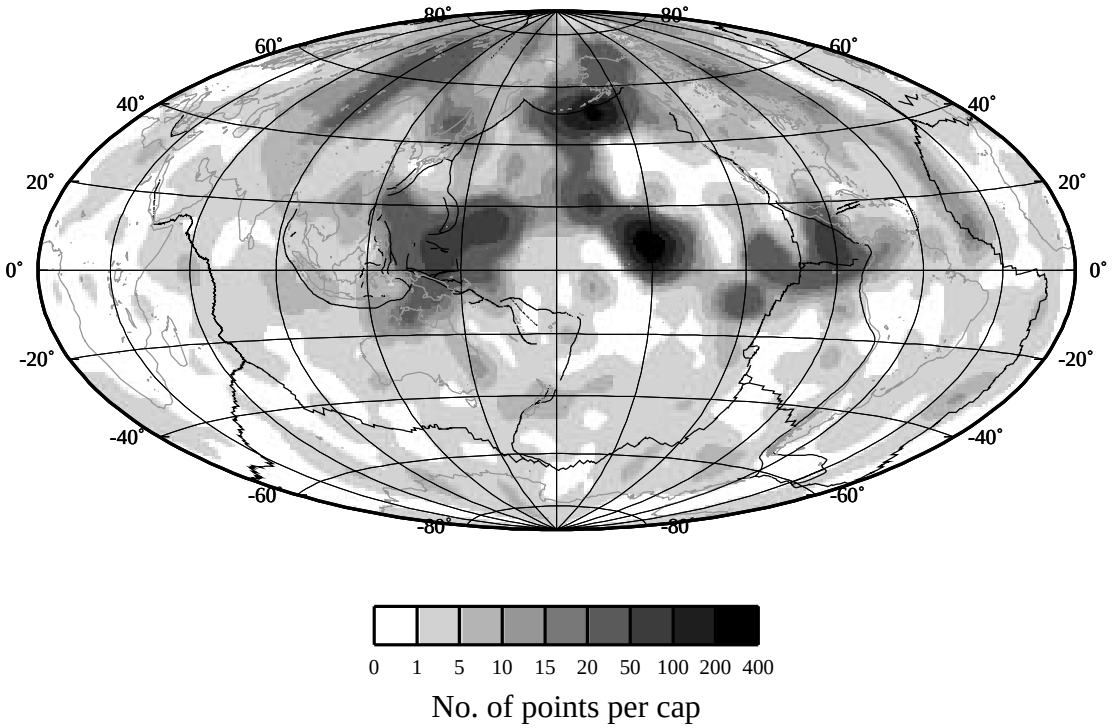


Figure 5.11: Density of measurements for the waveform fitting method plotted in 5° spherical caps.

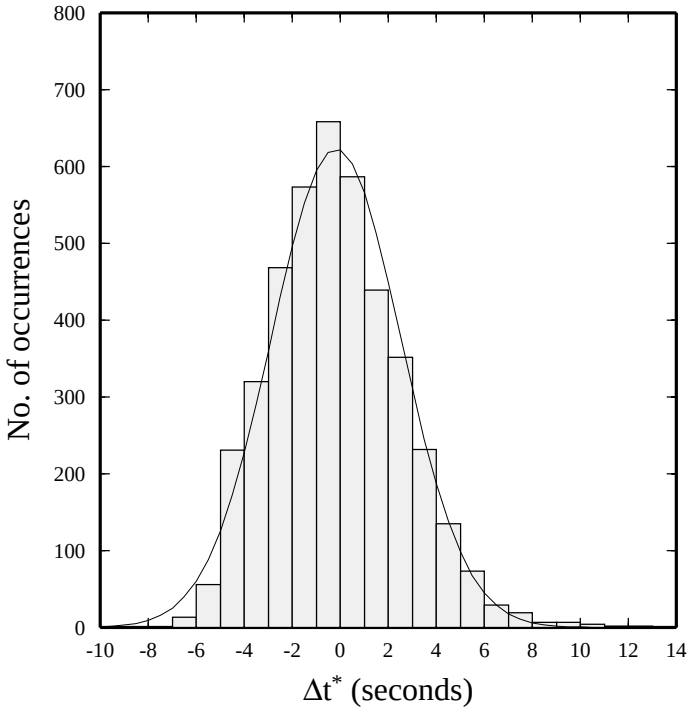


Figure 5.12: Distribution of Δt^* residuals for the $SS - S$ data obtained from the waveform fitting method. The Δt^* values are plotted relative to PREM.

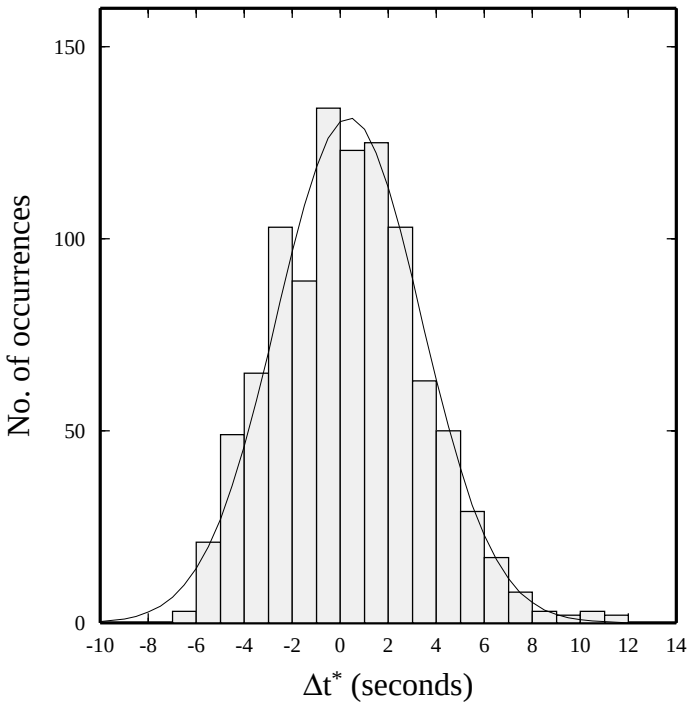


Figure 5.13: Distribution of Δt^* residuals for the $SSS - SS$ data obtained from the waveform fitting method. The Δt^* residuals are plotted relative to PREM.

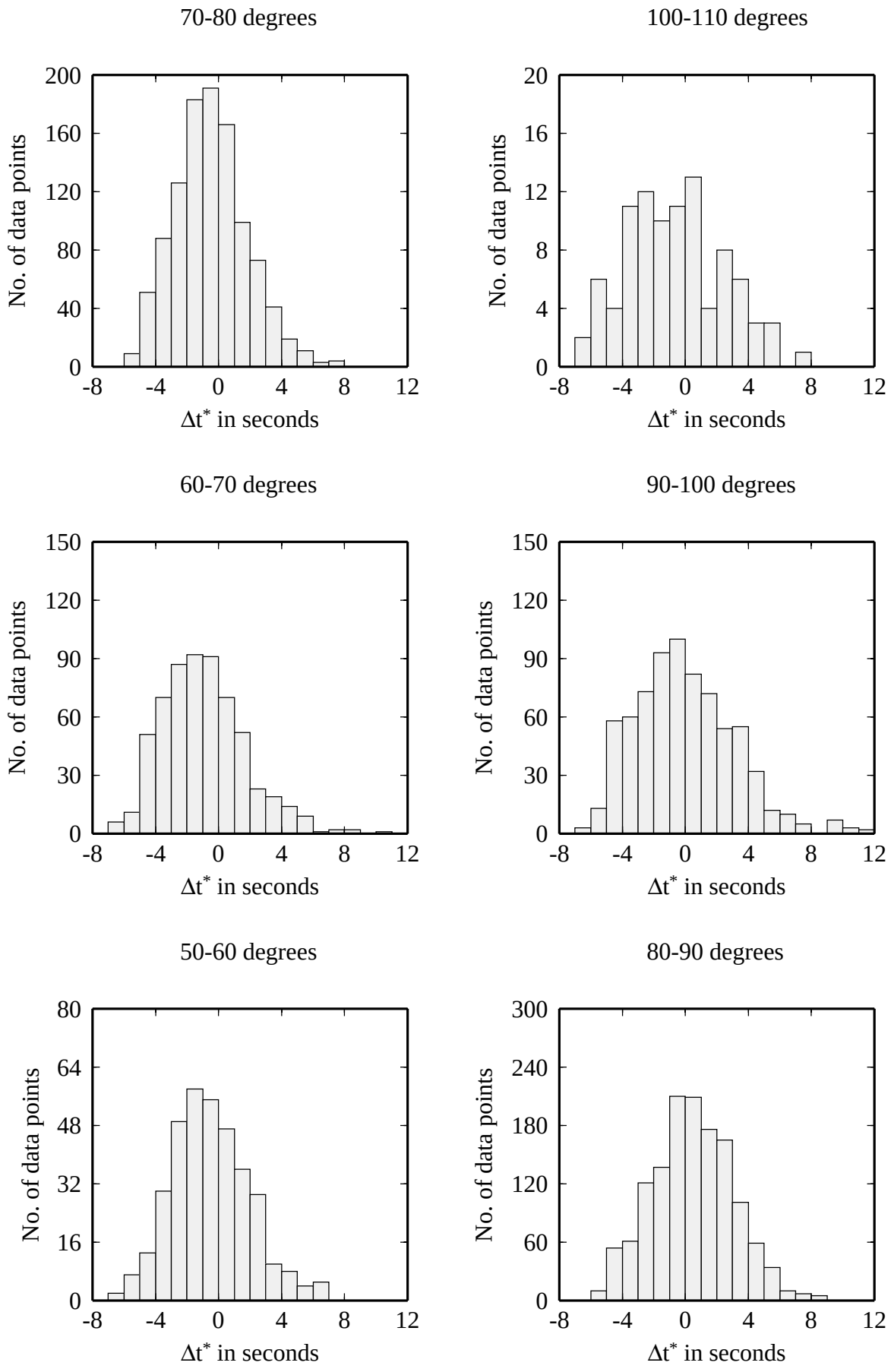


Figure 5.14: Distribution of $SS - S$ Δt^* residuals for different epicentral distance ranges using data obtained from the waveform fitting method.

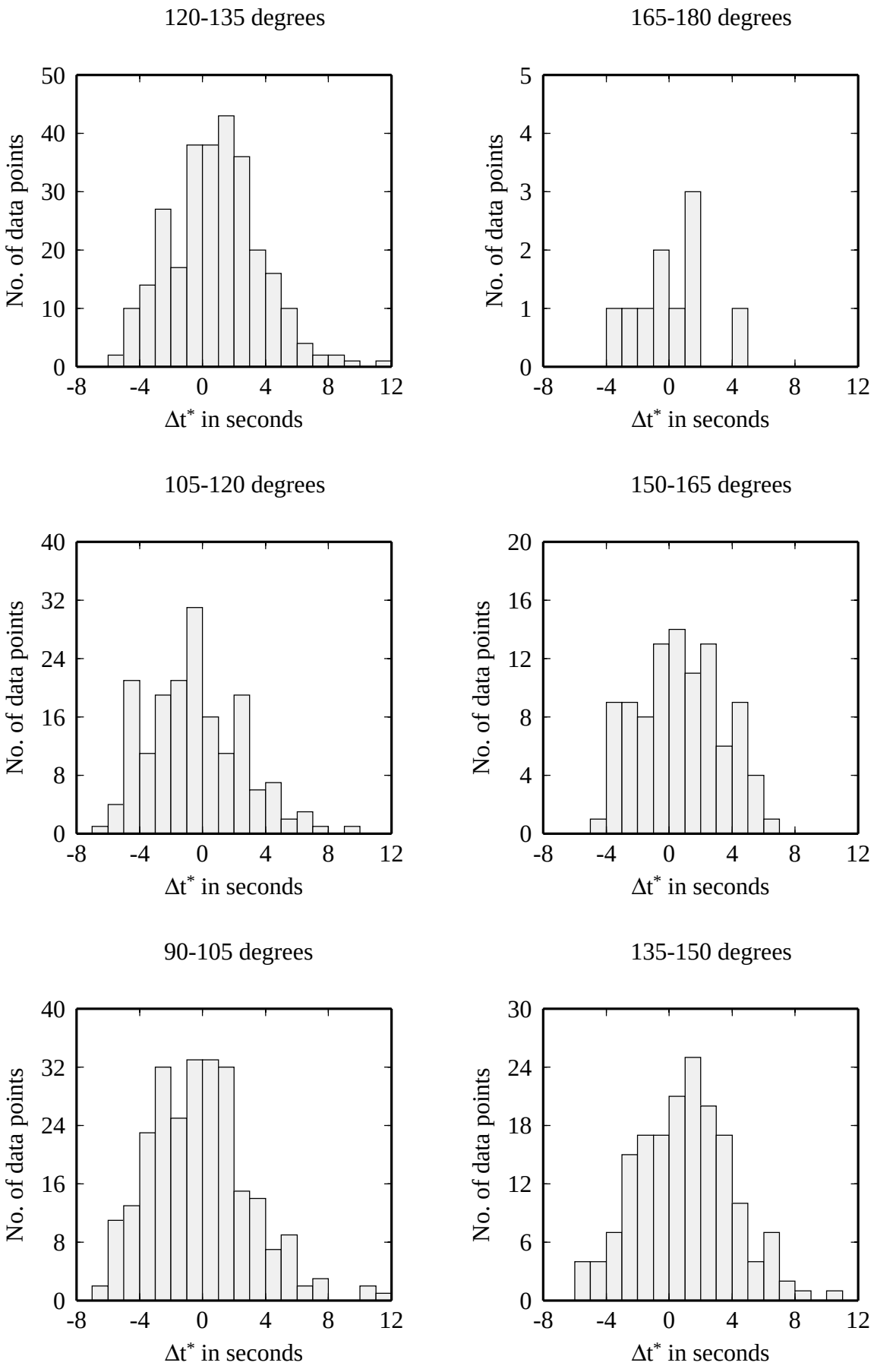


Figure 5.15: Distribution of $SSS-SS$ Δt^* residuals for different epicentral distance ranges using data obtained from the waveform fitting method.

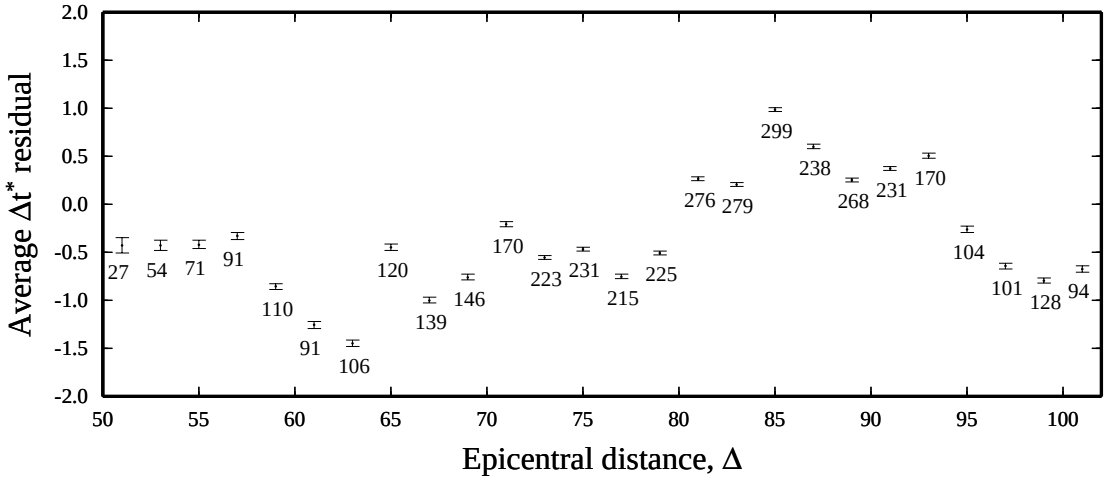


Figure 5.16: Distance dependence of $SS - S$ t^* residuals plotted as the means of 2° bins for epicentral distances between $50° - 102°$. The numbers directly below each point give the total number of residuals for that 2° bin.

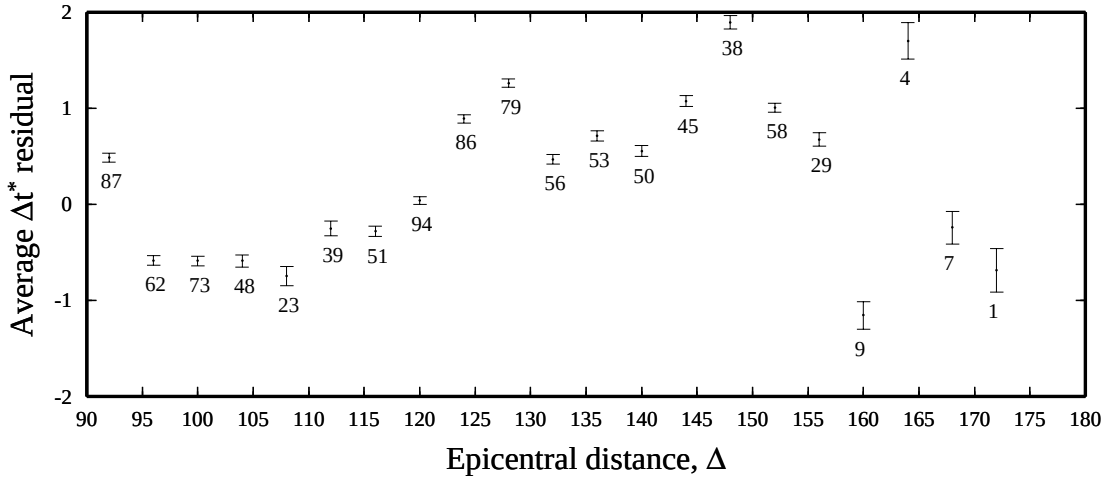


Figure 5.17: Distance dependence of $SSS - SS$ t^* residuals plotted as the means of 4° bins for epicentral distances between $90° - 180°$. The numbers directly below each point give the total number of residuals for that 4° bin.

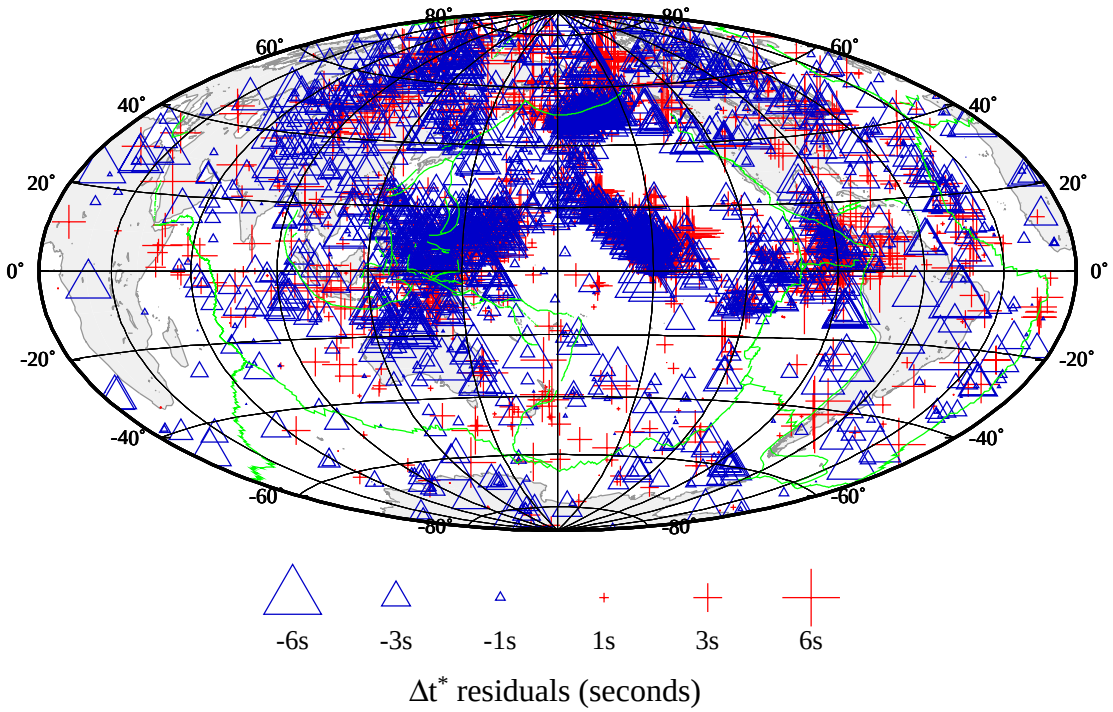


Figure 5.18: Δt^* residuals, plotted relative to PREM at the SS bounce point for the $SS - S$ data

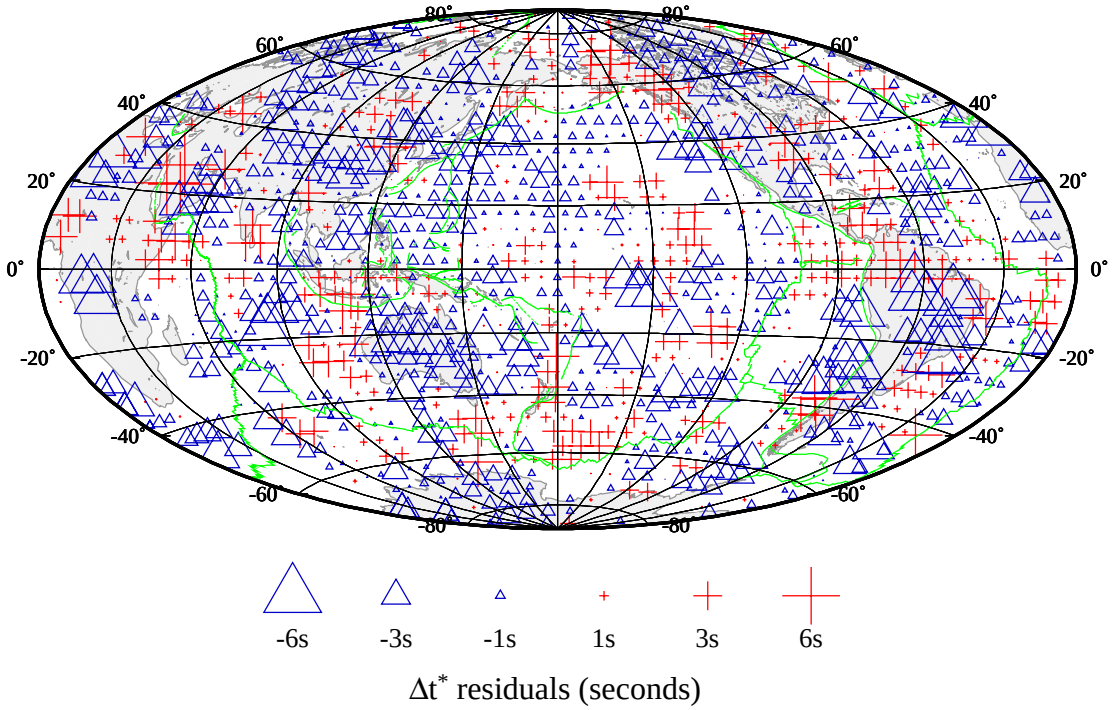


Figure 5.19: Δt^* residuals, plotted relative to PREM, for the $SS - S$ data in 5° spherical caps - 1 point or more per cap.

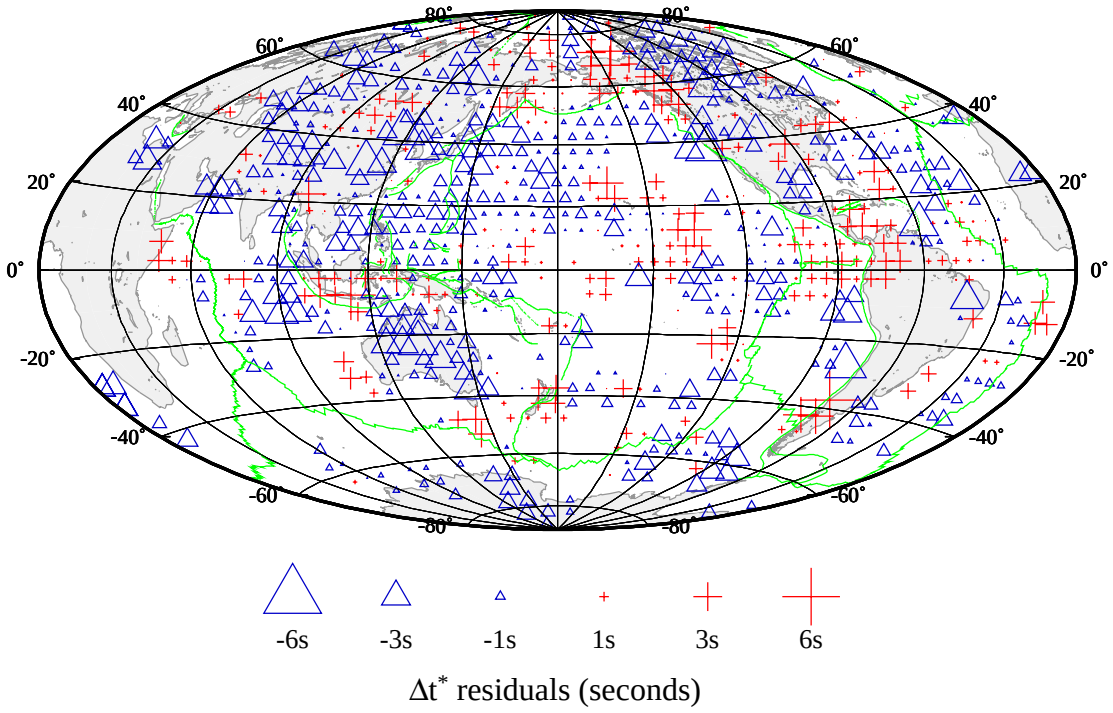


Figure 5.20: Δt^* residuals, plotted relative to PREM, for the $SS - S$ data in 5° spherical caps - 3 points or more per cap.

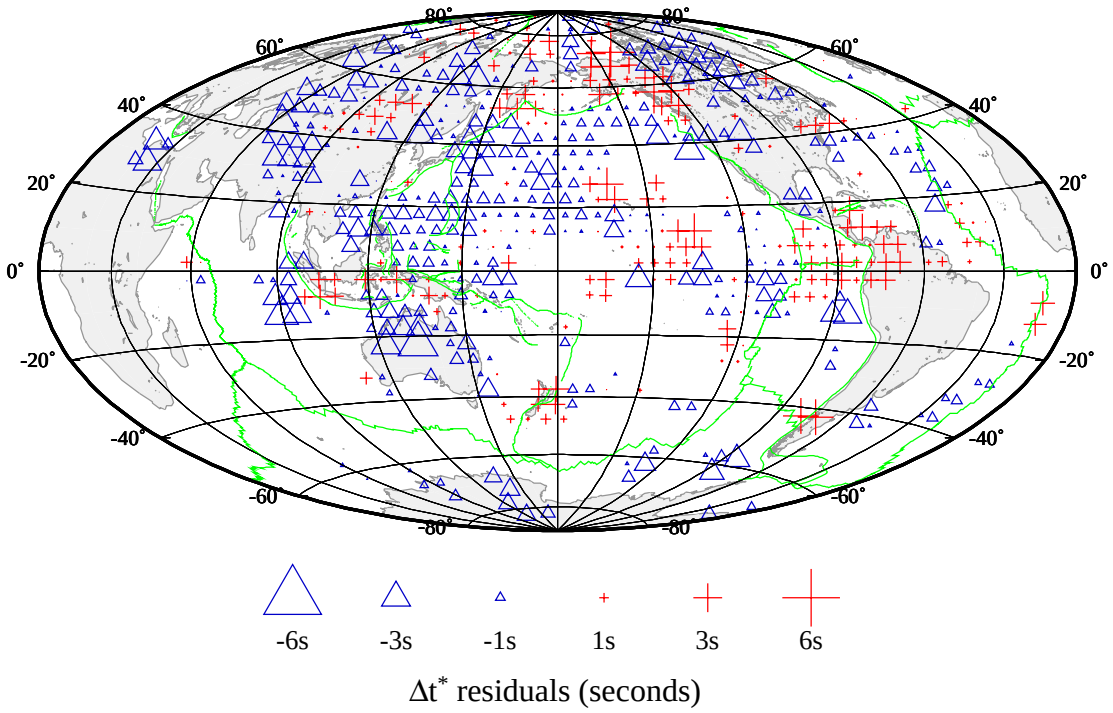


Figure 5.21: Δt^* residuals, plotted relative to PREM, for the $SS - S$ data in 5° spherical caps - 5 points or more per cap.

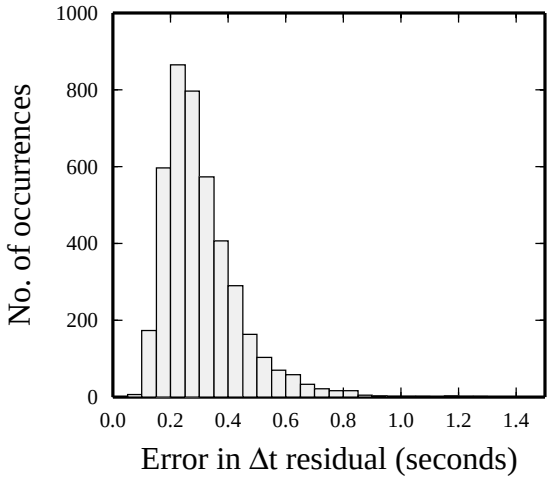


Figure 5.22: Distribution of the errors in the $SS - S$ differential travel time measurements obtained from the waveform fitting method.

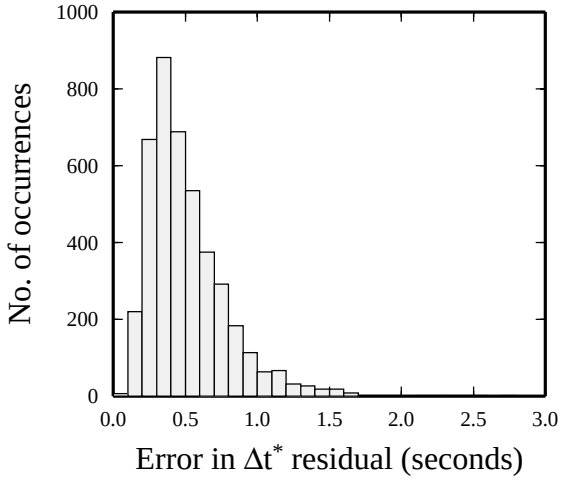


Figure 5.23: Distribution of the errors in the $SS - S$ differential t^* measurements obtained from the waveform fitting method.

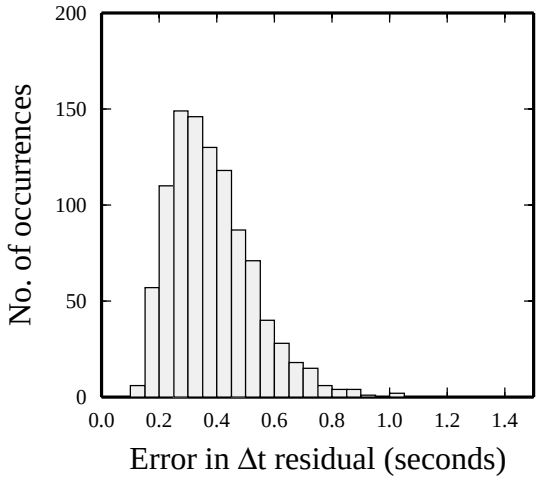


Figure 5.24: Distribution of the errors in the $SSS - SS$ differential travel time measurements obtained from the waveform fitting method.

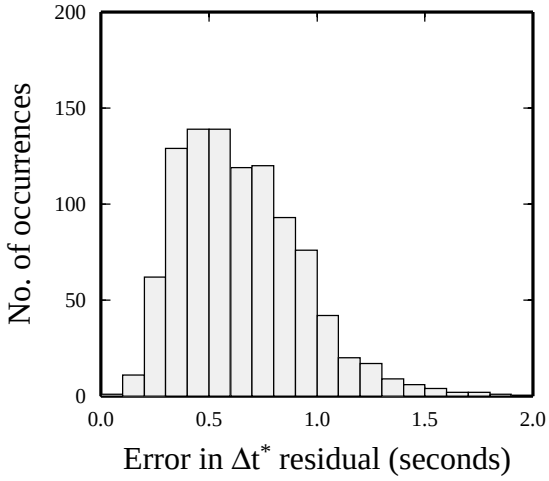


Figure 5.25: Distribution of the errors in the $SSS - SS$ differential t^* measurements obtained from the waveform fitting method.

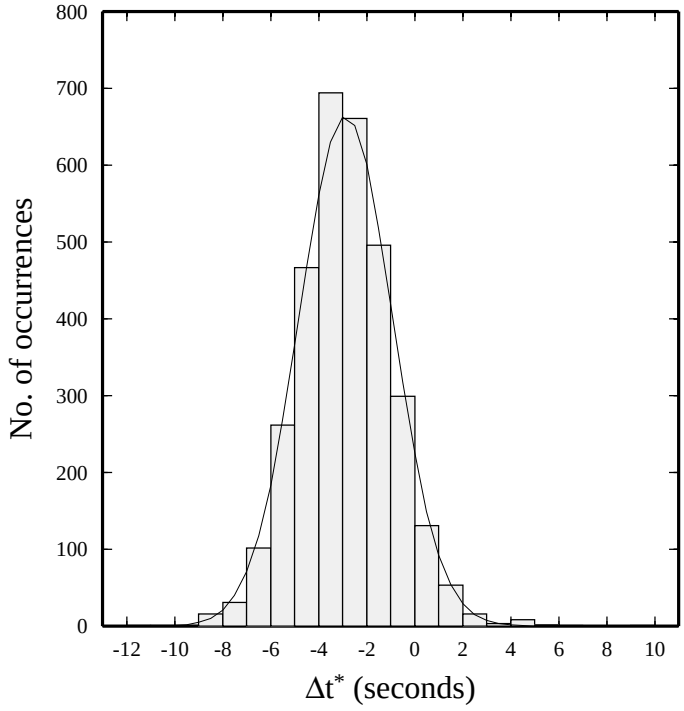


Figure 5.26: Distribution of Δt^* residuals for the $SS - S$ data obtained from the spectral method. The Δt^* residuals are plotted relative to the PREM values.

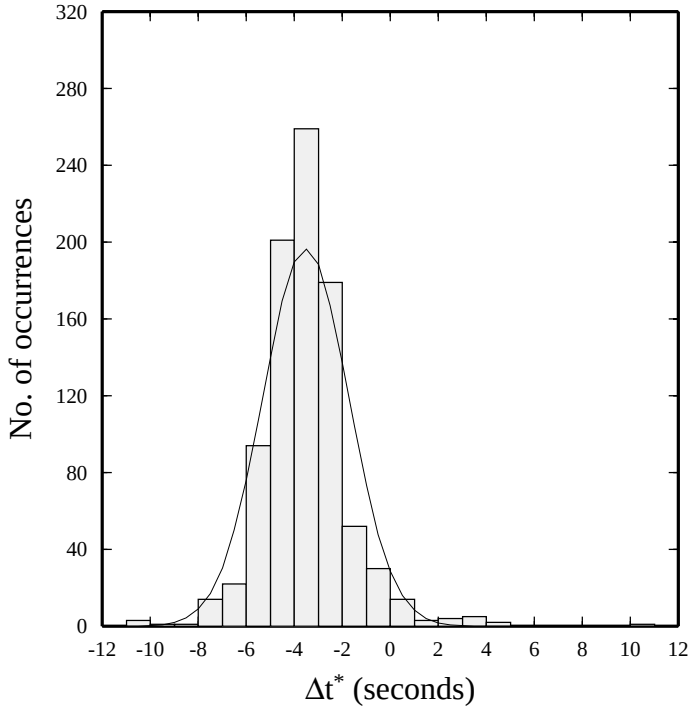


Figure 5.27: Distribution of Δt^* residuals for the $SSS - SS$ data obtained from the spectral method. The Δt^* residuals are plotted relative to the PREM values.

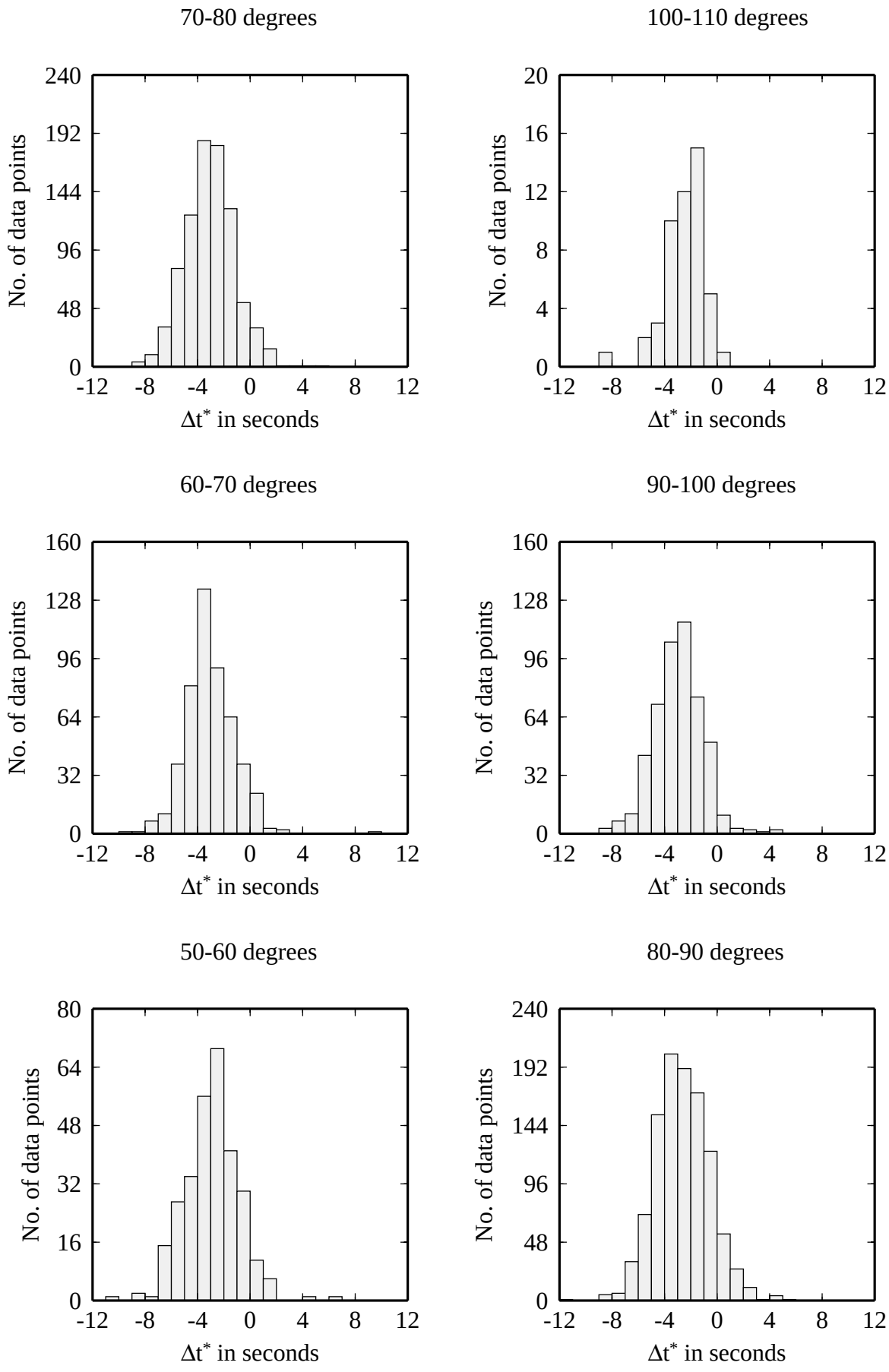


Figure 5.28: Distribution of $SS - S$ Δt^* residuals for different epicentral distance ranges using data obtained from the spectral ratio method.

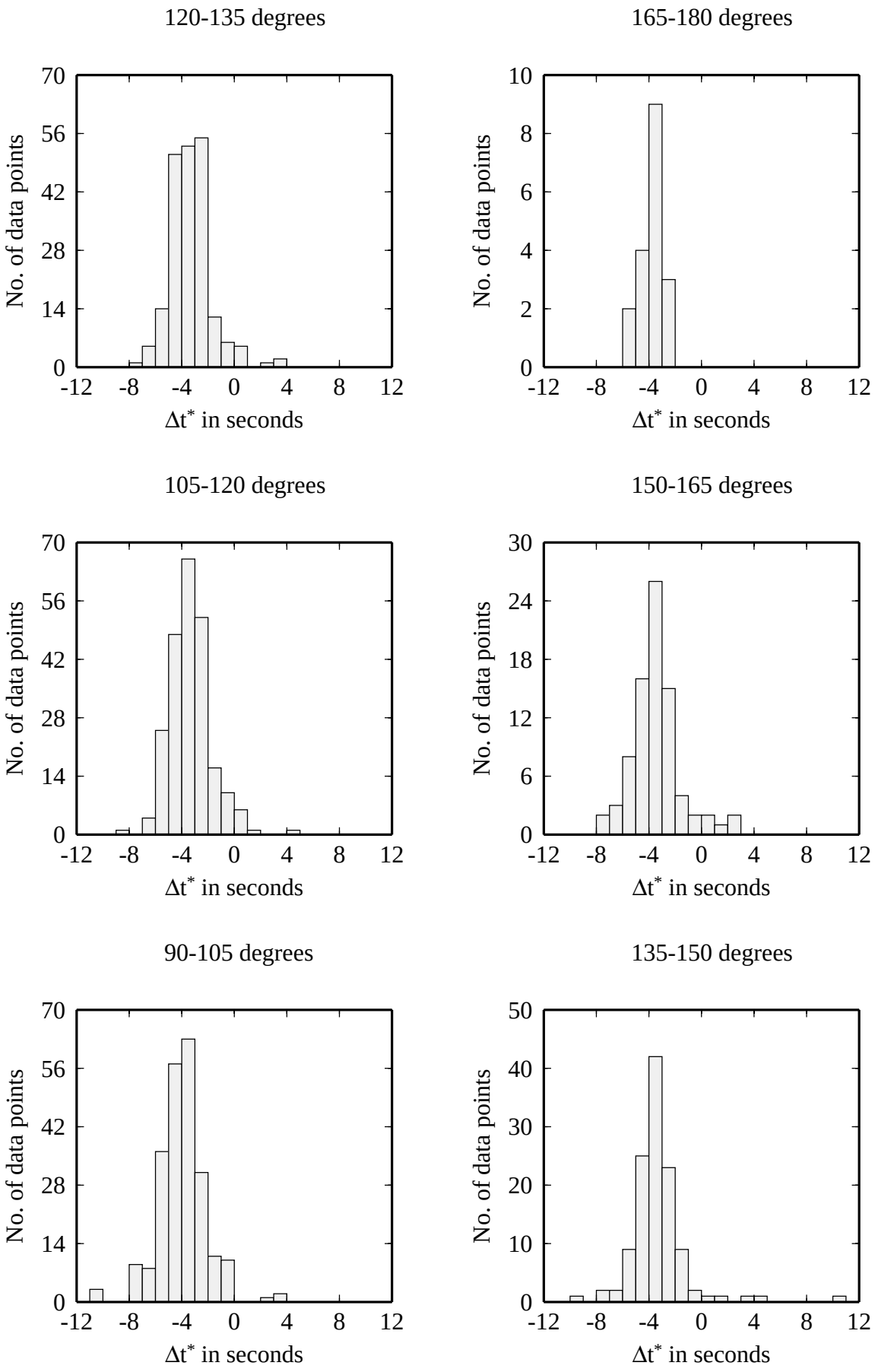


Figure 5.29: Distribution of $SSS - SS$ Δt^* residuals for different epicentral distance ranges using data obtained from the spectral ratio method.

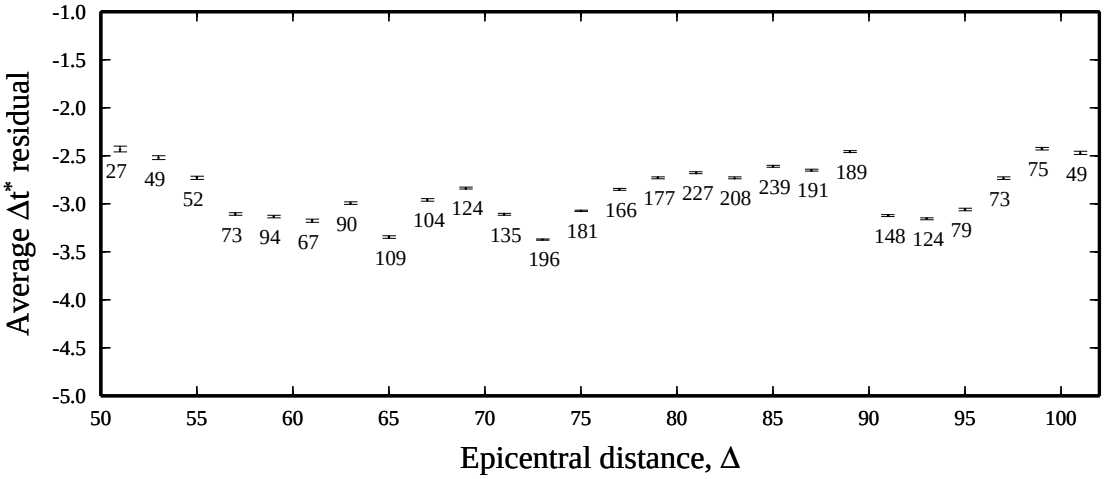


Figure 5.30: Distance dependence of $SS - S$ t^* residuals obtained from the spectral ratio method, plotted as the means of 2° bins for epicentral distances between $50° - 102°$. The numbers directly below each point give the total number of residuals for that 2° bin.

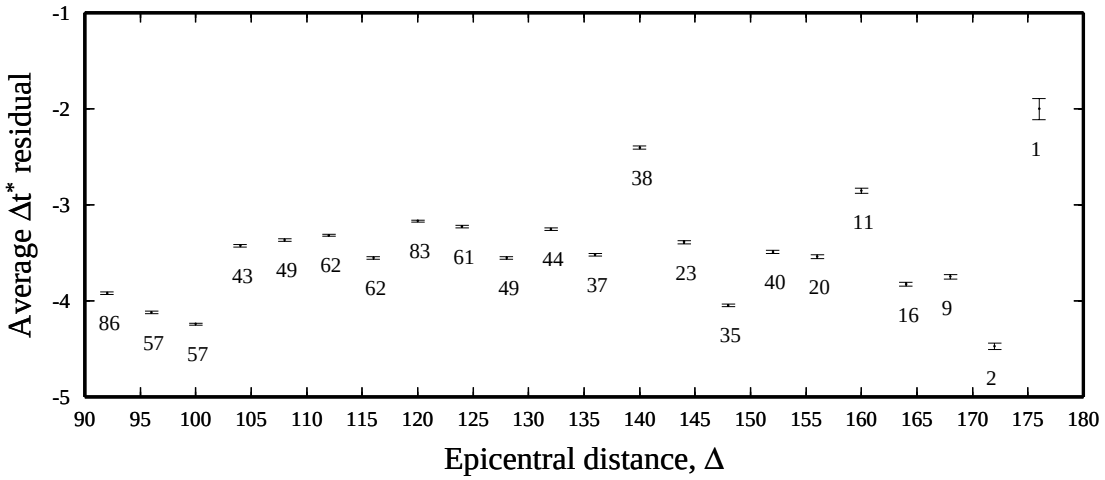


Figure 5.31: Distance dependence of $SSS - SS$ t^* residuals obtained from the spectral ratio method, plotted as the means of 4° bins for epicentral distances between $90° - 180°$. The numbers directly below each point give the total number of residuals for that 4° bin.

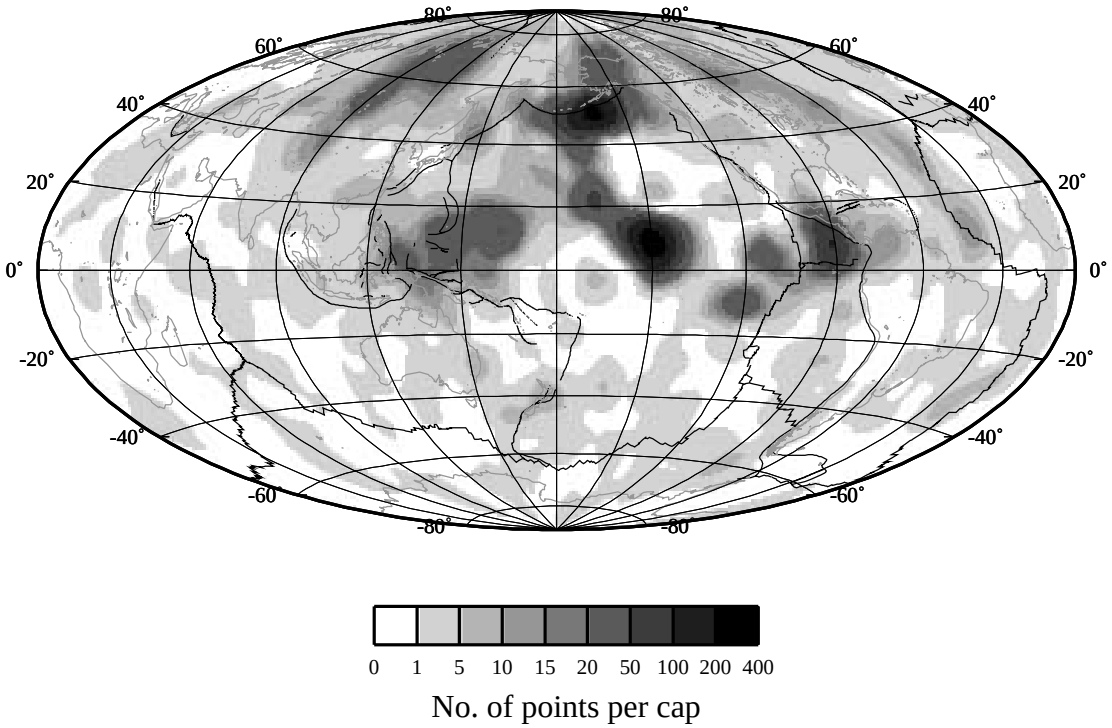


Figure 5.32: Density of measurements for the spectral ratio method plotted in 5° spherical caps.

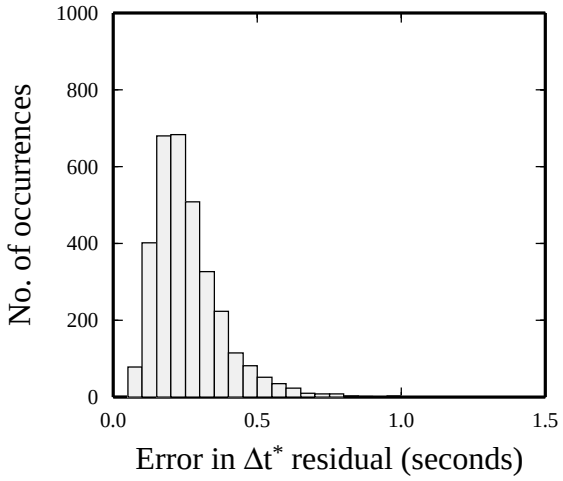


Figure 5.33: Distribution of the errors in $SS - S$ differential t^* measurements obtained from the spectral ratio method.

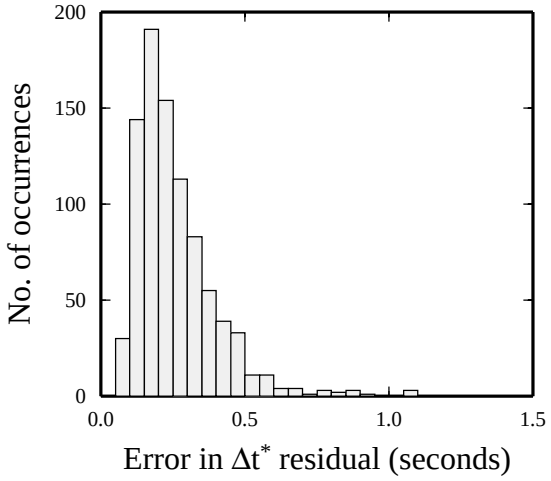


Figure 5.34: Distribution of the errors in $SSS - SS$ differential t^* measurements obtained from the spectral ratio method.

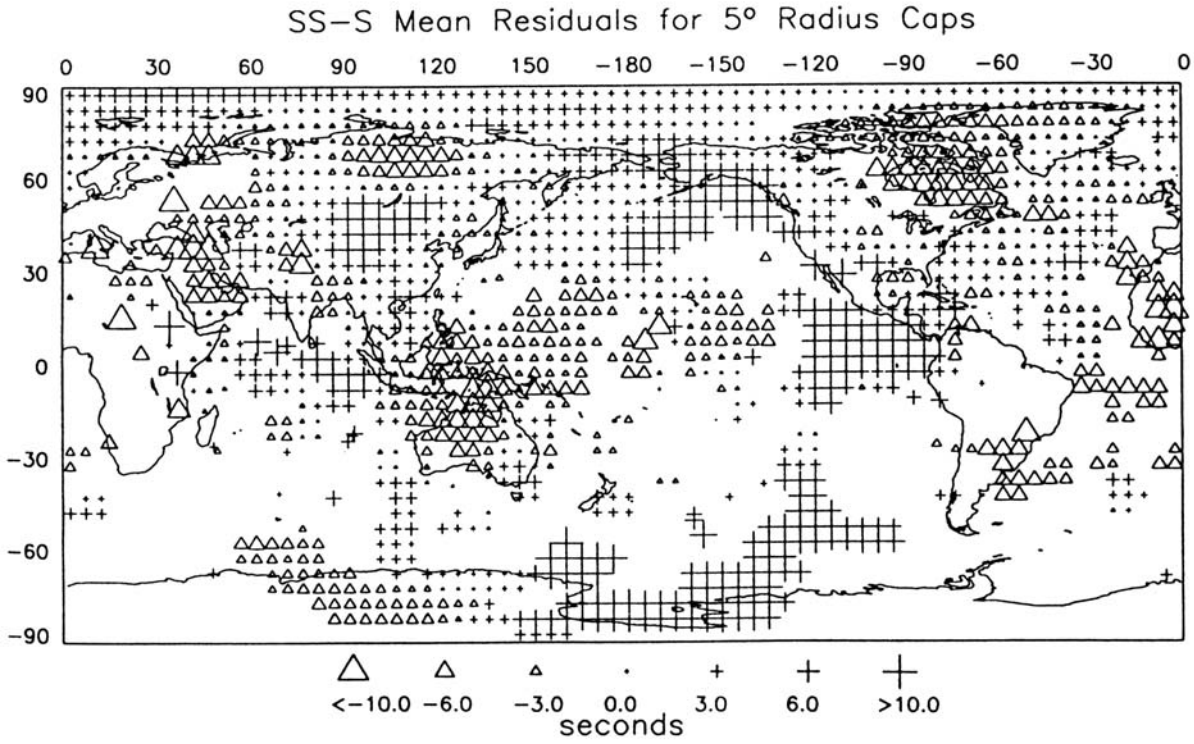


Figure 5.35: Map showing the smoothed $SS - S$ travel time residuals. Reproduced from Woodward & Masters (1991a)

The figure originally located here has been removed from this version of the thesis for copyright reasons.

Figure 5.36: Map of cap-averaged t^* values (with respect to the reference radial Q_β model of PREM) computed from stacked amplitude spectra averaged out in spherical caps of 5° radius. The mean of the cap-averaged t^* values (0.24s) is subtracted from the values before plotting. Each of the caps have at least 5 measurements. Reproduced from Bhattacharyya *et al.* (1996)

Chapter 6

Three dimensional modelling of the data

6.1 Introduction

The raw residuals for travel time and attenuation are presented in Chapter 5. In Chapter 5 no formal modelling of the data is performed, the data are simply displayed in a variety of different ways. Whilst presenting the results in this manner is a necessary step in the analysis it provides only limited insight into the three dimensional structure of the Earth. In this chapter we seek to use the data to produce three dimensional models of Earth structure.

Detailed three dimensional maps of global Earth structure are of great importance for the understanding of mantle dynamics. Seismologists have been producing three dimensional models of Earth structure since the late 1970's. The construction of these models has involved utilising a variety of different data types and modelling techniques. The majority of the models produced so far have sought to describe velocity variations within the Earth. However, to date, there are very few models describing the variation of attenuation within the Earth. The attenuation models that have been produced tend to be incompatible with each other, suggesting significant shortcomings in the existing models.

We construct three dimensional models of the variation of velocity and attenuation throughout the mantle i.e. we obtain models $m(r, \theta, \phi)$ where $m(r, \theta, \phi)$ describes the lateral and radial variation of either seismic velocity or intrinsic attenuation. We can represent $m(r, \theta, \phi)$ as $m(\boldsymbol{x})$ which simplifies the algebra slightly.

6.2 Formulation of the problem

We use the travel time, Δt, or attenuation, Δt^*, residuals to obtain a model of the variations of shear velocity or shear attenuation within the Earth. Consider first the construction of a model for shear

attenuation: i.e. we want to find q_μ as a function of r, θ and ϕ. Recall that $q_\mu(r,\theta,\phi) = \frac{1}{Q_\mu}$. Also recall from the definition of t^* 1.3, that the t^*'s for the S and SS paths are respectively:

$$t^*_S = \int_S q_\mu(r,\theta,\phi)d\tau \tag{6.1}$$

$$t^*_{SS} = \int_{SS} q_\mu(r,\theta,\phi)d\tau \tag{6.2}$$

where the integrals are calculated along the S or SS rays. The data obtained from the waveform fitting or spectral ratio methods provide values for $\Delta t^* = (t^*_{SS} - t^*_S)$ for a particular ray path. We refer to the values of Δt^* as the data, denoted d where:

$$d = (t^*_{SS} - t^*_S) = \int_{SS} q_\mu(r,\theta,\phi)d\tau - \int_S q_\mu(r,\theta,\phi)d\tau \tag{6.3}$$

For $SSS - SS$ residuals the value of d is clearly:

$$d = (t^*_{SSS} - t^*_{SS}) = \int_{SSS} q_\mu(r,\theta,\phi)d\tau - \int_{SS} q_\mu(r,\theta,\phi)d\tau \tag{6.4}$$

Now consider the construction of a model for shear velocity denoted $\frac{\delta v}{v_s}(r,\theta,\phi)$. The algebra is nearly identical to that detailed above except d is given by: $d = \Delta t = t_{SS} - t_S$ and therefore d can be written:

$$d = (t_{SS} - t_S) = -\int_{SS} \frac{\delta v}{v_s}(r,\theta,\phi)d\tau + \int_S \frac{\delta v}{v_s}(r,\theta,\phi)d\tau \tag{6.5}$$

Similarly for $SSS - SS$ measurements, d is defined as:

$$d = (t_{SSS} - t_{SS}) = -\int_{SSS} \frac{\delta v}{v_s}(r,\theta,\phi)d\tau + \int_{SS} \frac{\delta v}{v_s}(r,\theta,\phi)d\tau \tag{6.6}$$

Clearly the above expressions for d are valid for a single data point only. If a model for the variations in a particular seismic parameter is to be obtained then many data points are required. The model is found using a least squares procedure and d becomes a column vector, $\boldsymbol{d}$, containing all the data values.

6.3 Model parameterisation

The three dimensional models of the Earth are parameterised using spherical harmonic basis functions to describe the lateral variations and spline functions for the depth dependence. See Appendix A.1 for the definitions of the spherical harmonic functions. A model of seismic anomalies (either velocity or attenuation) is given by:

$$m(r,\theta,\phi) = m(\boldsymbol{x}) = \sum_{klm} C_{klm} Y^m_l(\theta,\phi) f_k(r) \tag{6.7}$$

where C_{klm} are the model parameters to be solved for, $Y_l^m(\theta, \phi)$ are the spherical harmonics and $f_k(r)$ are the radial basis functions (depth splines) shown in Figure 6.1. The splines are defined from the Moho to the core mantle boundary with the spline knot spacing increasing with depth. $f_k(r)$ is defined to be the cubic spline having value 1 at the k^{th} knot and 0 at all other knots. There are 21 knots ($k = 0$ corresponds to the Moho, $k = 20$ corresponds to the CMB), such that the spacing of the first two knots is 50 km, with the spacing between successive knots increasing by a constant ratio r (≈ 1.10). The unequal spacing is to allow variations at shallow depths to be more easily resolved. This is because the source of any seismic anomaly is anticipated to be in the upper mantle and not in the lower mantle which is thought to be quite homogeneous. Figure 6.1 shows all 21 depth splines for completeness, however for the majority of this thesis only the top 6 splines are utilised. Figure 6.2 shows a close up of these splines along with depth at the maximum sensitivity. Using only the top 6 splines limits the models to depths less than 400 km, however since we expect the anomalous signal to be attributed to sources above this depth this is not considered to be a problem.

Unless otherwise stated all the attenuation models in this thesis are constructed using spherical harmonics up to degree and order 8. This results in $(8 + 1)^2 = 81$ unknowns associated with each depth parameter. Hence if 6 depth splines are used then the total number of unknowns to be solved for is given by $81 \times 6 = 486$. The velocity models are constructed using harmonics of degree and order 12 using only the top 6 depth splines. This results in a total of $(12 + 1)^2 \times 6 = 1014$ unknowns for the velocity models. Similarly if harmonics up to degree and order 20 are used and the model extends throughout the whole mantle the number of unknowns is $(20 + 1)^2 \times 21 = 441 \times 21 = 9261$. The total number of unknowns is denoted, n.

6.4 Modelling of seismic parameters using weighted damped least squares

Three dimensional models of the variations in attenuation and shear velocity are obtained by inverting the travel time and attenuation residuals. The method of inversion is that of damped weighted least squares where we seek to find the model $\boldsymbol{m}$ by solving the equation:

$$\boldsymbol{A}\boldsymbol{m} = \boldsymbol{d} \tag{6.8}$$

where $\boldsymbol{d}$ is the data vector, $\boldsymbol{m}$ is the model vector and $\boldsymbol{A}$ is the matrix of derivatives relating $\boldsymbol{d}$ and $\boldsymbol{m}$. Details of this method are explained in Appendix A.2. Explicitly the data vector is a column vector

with the differential travel time or attenuation residuals as its elements i.e.

$$\boldsymbol{d} = \begin{pmatrix} d_1 \\ d_2 \\ \vdots \\ d_{N-1} \\ d_N \end{pmatrix} \tag{6.9}$$

where each d_i is a single differential travel time or attenuation residual. The solution to 6.8 is given by:

$$\boldsymbol{m} = \boldsymbol{M}^{-1}\boldsymbol{U}\hat{\boldsymbol{\Lambda}}^{-1}\boldsymbol{U}^T\boldsymbol{A}'^T\boldsymbol{D}\boldsymbol{d} \tag{6.10}$$

See Appendix A.2 for the definitions of the terms in this equation. The resulting model, $\boldsymbol{m}$, will consist of a total of $(l_m+1)^2 N_s$ of parameters where l_m is the maximum degree of spherical harmonic and N_s is the number of depth splines used in the parameterisation of the model. The model parameters are ordered spline by spline in order of increasing depth e.g.

$$\boldsymbol{m} = \begin{pmatrix} \boldsymbol{m}_1 \\ \boldsymbol{m}_2 \\ \vdots \\ \boldsymbol{m}_{N_s-1} \\ \boldsymbol{m}_{N_s} \end{pmatrix} \tag{6.11}$$

where each $\boldsymbol{m}_i$ is a column vector containing the $(l_m+1)^2$ spherical harmonic coefficients associated with depth spline i.

The inversions are performed using a series of computer programs. The first calculates the $\boldsymbol{A}'^T\boldsymbol{A}'$ and associated matrices. The second program inverts this matrix resulting in a model for either q_μ or $\frac{\delta v}{v_s}$. A third program is then used to calculate parameters such as the variance ratio to test how well the model fits the input data.

6.5 Data selection

Given a noisy dataset, the process of data selection is particularly important. In Chapter 2, the data retrieval process allowed only 597 out of around 2900 events to be selected for processing, however further selection must be performed before inverting the data. The least squares inversion procedure requires a normal distribution of measurements so we must check that the data possess such a distribution. Also, least squares is particularly sensitive to outliers and therefore these should be removed. Although it is important to remove the outliers, it is also important not to restrict the dataset so severely so as to significantly alter the shape of the normal distribution.

For data obtained using the waveform fitting method, only data points with fit parameters of 0.2 or less are selected for use in the inversion process as these are considered to be most reliable. This reduces the $SS - S$ dataset from 4207 to 2537 points and the $SSS - SS$ dataset from 992 to 387 points. The distributions of these reduced datasets are provided by Figure 6.3 for the travel time data and Figure 6.4 for the t^* data. It is clear from these two figures that no removal of outliers is necessary. For data obtained using the spectral ratio method we do not trust the errors estimates and so choose to invert the entire dataset consisting of 3246 residuals for the $SS - S$ and 885 residuals for the $SSS - SS$ data. The distributions of the t^* residuals obtained using the spectral ratio method are given by Figures 5.26 and 5.27 for the $SS - S$ and $SSS - SS$ datasets respectively. Again, the removal of outlying data points is unnecessary.

6.6 Damping

The inversion is performed by eigenvalue decomposition. The damping is achieved by selecting a value of η which defines the eigenvalue cut-off (see Appendix A.2 for the definition of η). This eigenvalue cut-off can be chosen either from the value of η directly ($\lambda_i = \eta\lambda_{max}$) or by examining the relationship between λ_i and the the resulting variance ratio. The effects of damping are best illustrated by considering the trade off between the variance ratio and model size. Figure 6.5 shows the relationship between the model size and the number of effective eigenvalues. The model size, $|\boldsymbol{m}|$, is defined as:

$$|\boldsymbol{m}| = \sqrt{\left(\sum_{i=1}^{n} m_i^2\right)} \tag{6.12}$$

where m_i is the i^{th} element of the model vector and n is the total number of model parameters as described earlier. The number of effective eigenvalues, λ_e, is calculated from:

$$\lambda_e = \sum_{k=1}^{n} \frac{\lambda_k}{\lambda_k + \eta\lambda_{max}} \tag{6.13}$$

where λ_k is the k^{th} eigenvalue, η is the cut-off parameter used to define where to begin tapering the eigenvalues, and λ_{max} is the maximum eigenvalue and is equal to λ_1.

Figure 6.6 shows the relationship between the variance ratio and the number of effective eigenvalues. The variance ratio is defined in Appendix A.4. These two figures clearly illustrate the trade off between the variance ratio and model size. As the number of effective eigenvalues is increased (see Figure 6.5) the model size increases gradually until around η_{12} where it increases rapidly. Conversely, the variance ratio decreases as the number of effective eigenvalues increases. Ideally the best model would have as small a variance ratio as possible. However from inspection of Figure 6.5 and Figure 6.6 it is clear that a compromise must be reached. In order to minimise the variance ratio whilst keeping the model size constrained we use a value of $\eta = 0.005$ in the inversion procedure.

For reference, a degree 8, 6 spline inversion for q_μ is used to produce the results in Figures 6.5 and 6.6.

6.7 Data weighting

In a least squares inversion the *data error* for all measurements should be equal to ensure that the resulting model is not distorted by poor measurements. The data errors may be set as the σ's from the waveform fitting or spectral ratio methods. Following the inversion the data error can be estimated *a posteriori*.

The waveform fitting and spectral ratio methods both provide error estimates for the differential travel time and attenuation residuals. If we use these error estimates to define the data weighting for the inversion procedure then the value of χ^2 obtained for each data point is $\neq 1$. The value of χ^2 is generally much greater than 1. We conclude that the errors provided by the waveform fitting and spectral ratio methods are greatly underestimated. We therefore choose to weight all data points equally (i.e. we set all values of $\sigma = 1.0$) which reduces the inversion problem to that of damped least squares.

6.8 Corrections to the travel time residuals

The travel time residuals must be corrected for the effects of the Earth's ellipticity and varying crustal structure. Section 6.8.1 describes the crustal corrections and Section 6.8.2 describes the ellipticity corrections.

6.8.1 Crustal corrections using CRUST 5.1

The structure of the crust at the SS and SSS bounce points can greatly influence the differential travel time measurements. It is widely acknowledged that correcting for crustal structure is important in the construction of three dimensional Earth models (Woodhouse & Dziewonski, 1984). We correct the differential travel time measurements for the effects of the Earth's crust using the model CRUST 5.1 from Mooney *et al.* (1998). CRUST 5.1 is a global model of crustal structure defined in $5^\circ \times 5^\circ$ tiles. Each of the 2592 $5^\circ \times 5^\circ$ tiles is assigned one of 139 different crustal profiles. Each profile describes the crust and uppermost mantle by a series of eight layers: (1) ice, (2) water, (3) soft sediments, (4) hard sediments, (5) crystalline upper crust, (6) middle crust, (7) lower crust, and (8) uppermost mantle. The uppermost mantle, layer (8), is simply equal to the PREM model at the appropriate depth. Each layer has a thickness, crustal P velocity, S velocity and density assigned to it. CRUST 5.1 is constructed using seismic refraction data where available. In regions where no refraction data are available the crustal structure is estimated using statistical averages based on a significantly larger database of crustal structure than that used in other studies. Essentially, in regions where no refraction

data are available the crustal structure is predicted by assigning one of the 139 crustal profiles to the region. This assignment is made based on the crustal age and tectonic setting of the region. Figure 6.7 gives the global distribution of the primary crustal types used in the construction of CRUST 5.1. Figure 6.8 shows the total thickness of CRUST 5.1. The crustal corrections to the differential travel times are calculated as follows:

1. Calculate the travel time, tt_M, from top of the crust down to a base depth using the CRUST 5.1 model. (N.B. The model CRUST 5.1 is identical to PREM from the base of the lowest crustal layer)

2. Calculate the travel time, tt_P, from the top of the crust down to the base depth using the PREM model.

For $SS - S$ data this calculation is performed for the crust at the SS bounce point. For $SSS - SS$ data, it is necessary to calculate the correction due to the SS bounce point and both SSS bounce points. The base depth is chosen to be 80 km as this depth is deeper than the thickest part of CRUST 5.1. The crustal correction to the differential travel time for a particular bounce point is then given by $d_c = 2(tt_M - tt_P)$. The factor of two arises as the ray passes through the crust twice at the bounce point. Clearly the crustal corrections will be greatest in regions where CRUST 5.1 differs most from PREM, e.g. regions of thickened crust and the oceans. This is illustrated by Figure 6.9 which shows crustal corrections calculated for $SS - S$, where the corrections are calculated at the SS bounce point. As expected, Figure 6.9 shows continental regions to have positive corrections and oceanic regions to have negative corrections to the travel time. This is essentially because PREM under-estimates the thickness of the crust for the continental areas and over-estimates the crustal thickness for oceanic regions. The effect of crustal corrections on the differential travel times for $SS - S$ are as follows:

- If CRUST 5.1 is thicker than PREM (i.e. continental regions) then the true SS ray travelled through extra crust and so the differential $SS - S$ time is larger than it should be.

- If CRUST 5.1 is thinner than PREM (i.e. oceanic regions) then the true SS ray travelled through less crust and so the differential $SS - S$ time is less than it should be.

The effects of the crust are removed from the differential travel time before inversion. This is achieved by subtracting the travel time due to passage through the crust from each of the differential travel time measurements, so the data vector becomes:

$$\boldsymbol{d}' = \boldsymbol{d} - \boldsymbol{d_c} \tag{6.14}$$

where $\boldsymbol{d_c}$ is a column vector of length N containing the crustal corrections in seconds for each element of $\boldsymbol{d}$.

6.8.2 Ellipticity corrections

It is also important to take into account the influence of the Earth's ellipticity on the seismic travel times. The PREM model is based on a spherical Earth. The real Earth is however an oblate spheroid where the radius at the equator is greater than the radius at the poles. As a result we should expect the PREM travel time for a bounce point at the equator to be under-estimated and the PREM travel time for a bounce point at the pole to be over-estimated.

The ellipticity corrections to the travel times are made using the methods described by Kennett & Gudmundsson (1996). They use the ray based approach of Dziewonski & Gilbert (1976) to provide tabulated ellipticity coefficients for a wide range of seismic phases including S and SS. They also provide a theory for combining different phases which allows the ellipticity correction for SSS to be computed.

For the S and SS paths we use the ellipticity coefficients as provided by Kennett & Gudmundsson (1996). For SSS rays, the ray path is split into two legs as shown by Figure 6.10. The total distance between the source, **S**, and receiver, **R** is given by Δ. The first leg is from the source, **S**, to point **X** at a distance Δ_1 and may be treated as an S ray. For the second leg, point **X**, is treated as an apparent source (at the surface reflection point) and the calculation is performed over the distance Δ_2. The second leg may be treated as an SS ray. Splitting the ray into two legs allows the ellipticity coefficient to be computed for each leg independently.

Given the ellipticity coefficients for the S, SS and SSS rays the corrections to the $SS-S$ and $SSS-SS$ differential travel times are easily computed. Following the notation of Kennett & Gudmundsson (1996), the travel time correction to be added to PREM for a given seismic phase is:

$$\delta t(z_s, \vartheta_0, \Delta, \zeta) = \frac{1}{4}(1 + 3\cos 2\vartheta_0)\sigma_0(z_s, \Delta) + \frac{\sqrt{3}}{2}\sin 2\vartheta_0 \cos\zeta\sigma_1(z_s, \Delta) + \frac{\sqrt{3}}{2}\sin^2\vartheta_0 \cos 2\zeta\sigma_2(z_s, \Delta) \tag{6.15}$$

where ϑ_0 is the epicentral colatitude-latitude, ζ is the azimuth from the epicentre to the receiver, Δ is the epicentral distance, z_s is the source depth and σ_0, σ_1 and σ_2 are the ellipticity coefficients.

For $SS-S$ measurements the correction to the differential travel time due to the Earth's ellipticity is given by, E_{SS-S}:

$$E_{SS-S} = \delta t_{SS}(z_s, \vartheta_0, \Delta, \zeta) - \delta t_S(z_s, \vartheta_0, \Delta, \zeta) \tag{6.16}$$

Similarly for $SSS - SS$ measurements the ellipticity correction is given by, E_{SSS-SS}:

$$E_{SSS-SS} = \delta t_{SSS}(z_s, \vartheta_0, \Delta, \zeta) - \delta t_{SS}(z_s, \vartheta_0, \Delta, \zeta) \tag{6.17}$$

The subscripts S, SS and SSS indicate that the calculation is made using the ellipticity coefficients calculated for that phase.

As with the crustal corrections, the ellipticity corrections are removed from the the differential

travel time before inversion. Thus the data vector becomes:

$$\boldsymbol{d'} = \boldsymbol{d} - \boldsymbol{d_c} - \boldsymbol{d_e} \tag{6.18}$$

where $\boldsymbol{d_e}$ is a column vector of length N containing the ellipticity corrections in seconds obtained for each element of $\boldsymbol{d}$. $\boldsymbol{d_c}$ is as stated in Section 6.8.1. The vector, $\boldsymbol{d'}$, is the data vector which is used in the subsequent inversions to obtain three dimensional models of seismic velocity.

6.9 Velocity models

In this section the velocity models obtained from inversion of the travel time residuals obtained using the waveform fitting method are presented. We consider separately the models obtained from inverting the $SS - S$ dataset (Section 6.9.1), the $SSS - SS$ dataset (Section 6.9.2) and the combined $SS - S$ and $SSS - SS$ dataset (Section 6.9.3). All the velocity models are expanded up to degree 12 over the top 6 depth splines and therefore each model has a total of 1014 parameters associated with it.

6.9.1 $SS - S$ models

In this section we present the velocity models obtained using only the $SS - S$ dataset. Figures 6.11(a) and 6.11(b) show the velocity model MVSSa obtained with no crustal or ellipticity corrections applied. Figures 6.12(a) and 6.12(b) show the model obtained with crustal corrections from CRUST 5.1 applied, denoted MVSSb. Figures 6.13(a) and 6.13(b) show the model obtained with both the crustal and ellipticity corrections applied before inversion, denoted MVSSc. Each figure shows the lateral variation of $\frac{\delta v}{v_s}$ over a range of depths from 50 km to 329 km. The orange red colouring is used to show low velocities and the blue colours are used to show higher than average (PREM) velocities. The variations of $\frac{\delta v}{v_s}$ are given as a percentage variation from the PREM model. Each map is accompanied by a histogram which shows the amplitude spectra of the spherical harmonics for that depth. The maps show the models plotted for spherical harmonics 1 through 12 excluding the degree 0 term. The amplitude of the degree zero term is included on the histograms of the amplitude spectra. Table 6.1 summarises the different $SS - S$ velocity models.

Velocity model	N	Variance ratio	λ_e	χ^2	$\frac{\chi^2}{N}$	Mean of the N residuals
MVSSa	2535	0.37	118.89	18162.06	7.16	5.84E-03
MVSSb	2535	0.36	118.69	20030.88	7.90	-0.66
MVSSc	2535	0.35	118.69	20235.01	7.98	-0.81

Table 6.1: Summary of the different $SS - S$ velocity models. N is the total number of data points used and λ_e is the number of effective eigenvalues.

Model MVSSa shows some correlation with known tectonic features: low velocities at mid ocean ridges (e.g. around the Pacific) and higher than average velocities on the continents. The same pattern is observed for all depths with the size of the anomalies increasing slightly with depth. For model MVSSa the amplitude of the degree 0 term is practically zero - essentially because the mean of the N residuals used to compute the model is also ≈ 0. Because the same pattern is observed at all depths it is impossible to attribute the features of model MVSSa to a specific depth (see Section 6.11 for a discussion of the depth resolution problem).

Model MVSSb includes the crustal corrections calculated using CRUST 5.1. The effect of the crustal corrections is to make oceanic regions more negative (slower) and continental regions more positive (faster). Compare the dark red areas on Figures 6.11(a) and 6.11(b) with the dark red areas on Figures 6.12(a) and 6.12(b).

Model MVSSc includes both crustal and ellipticity corrections. The effect of the ellipticity corrections is more subtle and visually there is very little difference between the models MVSSb and MVSSc. Comparison of Figures 6.12(a) with 6.13(a) and Figures 6.12(b) with 6.13(b) show that the effect of ellipticity corrections is to decrease the velocities across polar regions and to increase the velocities across equatorial regions. This effect is however quite subtle and the crustal corrections dominate. Again, model MVSSc shows low velocities at mid ocean ridges and higher than average velocities across continental areas.

6.9.2 $SSS - SS$ models

In this section the models obtained from inverting the $SSS-SS$ dataset are presented. Figures 6.14(a) and 6.14(b) show the velocity model MVSSSa, resulting from inversion of the $SSS - SS$ dataset with no crustal or ellipticity corrections applied to the residuals. Figures 6.15(a) and 6.15(b) show the model obtained with crustal corrections from CRUST 5.1 applied, denoted MVSSSb. Figures 6.16(a) and 6.16(b) show the velocity model MVSSSc with both crustal and ellipticity corrections applied. Table 6.2 summarises the different $SSS - SS$ velocity models.

Velocity model	N	Variance ratio	λ_e	χ^2	$\frac{\chi^2}{N}$	Mean of the N residuals
MVSSSa	386	0.20	125.08	1889.66	4.88	-0.63
MVSSSb	386	0.20	124.91	2195.50	5.69	-1.44
MVSSSc	386	0.21	124.91	2210.11	5.73	-1.42

Table 6.2: Summary of the different $SSS - SS$ velocity models. N is the total number of data points used and λ_e is the number of effective eigenvalues.

Models MVSSSa, MVSSSb and MVSSSc are very similar. Application of the crustal and ellipticity corrections does not alter the velocity model obtained greatly. This is because the crustal and ellipticity

corrections are obtained from contributions from both the SS and SSS bounce points and thus their effects are more complex. Due to the similarity of the three models we only describe model MVSSSc, models MVSSSa and MVSSSb are included for completeness and to illustrate this similarity.

Model MVSSSc is constructed using the $SSS - SS$ travel time residuals with both crustal and ellipticity corrections applied before inversion. Although only 386 residuals are used in the inversion the resulting velocity model is still encouraging. Model MVSSSc shows variations in $\frac{\delta v}{v_s}$ up to $\pm 8\%$, slightly larger than the variations observed for the $SS - S$ dataset ($\pm 6\%$). The model shows some correlation with the tectonic features: low velocities underlying mid ocean ridges and high velocities underlying continental regions. In particular the mid Atlantic ridge shows up as seismically slow which is not observed in the $SS - S$ models. Australia and South America are observed as high velocity anomalies. There are many similarities between model MVSSSc and MVSSc, particularly around the Pacific where both models show the mid ocean ridges to be low velocity features. Both models also show a seismically fast region to the south east of Japan - perhaps this could be related to subduction ? That the two models show such similarity despite the sparse nature of the $SSS - SS$ dataset is very promising.

6.9.3 Combining the $SS - S$ and $SSS - SS$ models

We construct a joint $SS - S$ and $SSS - SS$ model by combining the derivative matrices for the $SS - S$ dataset with those for the $SSS - SS$ dataset. This is possible because the dimensions of the two sets of derivative matrices are the same. This combined derivative matrix is inverted, resulting in a velocity model which contains information from both the $SS - S$ and $SSS - SS$ datasets. The number of $SS - S$ residuals is far greater than the number of $SSS - SS$ residuals and therefore we should expect that the joint model will be dominated by the $SS - S$ data. A consequence of this is that the joint model will fit the $SS - S$ dataset far better than it fits the $SSS - SS$ dataset. If the number of $SS - S$ and $SSS - SS$ residuals were equal, we should expect the resulting joint model to fit the two datasets equally well. However since this is not the case we seek a compromise. Essentially we want to weight the $SS - S$ and $SSS - SS$ datasets in such a way as to produce a joint model which fits both datasets equally well. Figure 6.17 shows the variance ratios obtained for the $SS - S$ and $SSS - SS$ datasets (computed against the joint model) for different weightings. The weightings used are defined as follows:

$$w_1 = \frac{1}{f_1} \tag{6.19}$$

and

$$w_2 = \frac{1}{f_2} \tag{6.20}$$

where w_1 is the weight used for the $SS - S$ dataset and w_2 is the weight used for the $SSS - SS$ dataset. f_1 and f_2 are factors used to up-weight or down-weight the $SS - S$ or $SSS - SS$ datasets. For Figure 6.17, f_1 and f_2 take values ranging between 1000.0 and 1.0. Point C (Figure 6.17) corresponds

to down-weighting the $SSS-SS$ dataset (where $f_1 = 1.0$, $f_2 = 1000.0$) so that the resulting models is essentially the same as a model constructed from $SS-S$ residuals only. Point D corresponds to down-weighting the $SS-S$ dataset (where $f_1 = 1000.0$, $f_2 = 1.0$) so that the resulting model is essentially the same as a model obtained using only $SSS-SS$ residuals. Point A corresponds to equal weighting (i.e. $f_1 = f_2 = 1.0$) of the two datasets. Whilst point A provides satisfactory variance ratios for both datasets it is possible to improve the $SSS-SS$ variance ratio by moving down the curve (i.e. up-weighting the $SSS-SS$ data) to point B. Point B corresponds to values of $f_1 = 2.5$ and $f_2 = 1.0$ and corresponds to an equal improvement to the variance ratios of the $SS-S$ and $SSS-SS$ datasets. Point B is chosen by calculating the ratios $\frac{v_1}{v_{1min}}$ and $\frac{v_2}{v_{2min}}$ where v_1 and v_2 are the variance ratios for the $SS-S$ and $SSS-SS$ datasets for a given choice of weighting and v_{1min} and v_{2min} are the minimum variance ratios for the $SS-S$ and $SSS-SS$ datasets (e.g. for Figure 6.17 $v_{1min} = 0.35$ and $v_{2min} = 0.21$). The point along the curve where the two ratios are equal corresponds to an equal amount of improvement in the two variance ratios (point B). Thus we can use the weighting given by point B in the inversion procedure to obtain a joint model in which both the $SS-S$ and $SSS-SS$ datasets fit the model as well as possible.

Figures 6.18(a) and 6.18(b) show the velocity model obtained from inverting both the $SS-S$ and $SSS-SS$ datasets with equal weighting. Figures 6.19(a) and 6.19(b) show the velocity model obtained by inverting the datasets with the "best" weighting defined by point B. The two combined models look very similar as is to be expected however the variance ratio obtained for the re-weighted model is lower meaning that model MVCOMB2 provides an improved fit to the data (see Table 6.3). The amplitude of MVCOMB2 is slightly greater than that of MVCOMB1. This is because model MVCOMB2 is weighted towards the $SSS-SS$ model which is itself slightly larger than the $SS-S$ model.

Velocity model	N	Variance ratio	λ_e	χ^2	$\frac{\chi^2}{N}$	Mean of the N residuals
MVCOMB1	2921	0.38	135.67	25441.76	8.71	-0.89
MVCOMB2	2921	0.33	144.55	6569.06	2.25	-0.89

Table 6.3: Summary of the different velocity models obtained from the combined $SS-S$ and $SSS-SS$ datasets. N is the total number of data points used and λ_e is the number of effective eigenvalues.

6.10 Attenuation models

In this section we present the attenuation models obtained from inverting the t^* residuals obtained from both the waveform fitting method (Section 6.10.1) and the spectral ratio method (Section 6.10.2). The attenuation models are expanded up to degree 8 over the top 6 depth splines and therefore each model has a total of 486 parameters associated with it.

6.10.1 Attenuation models obtained from the results of the waveform fitting method

Figures 6.20(a) and 6.20(b) show the attenuation model, denoted MQSS, obtained from inverting the $SS - S$ t^* dataset. Figures 6.21(a) and 6.21(b) show the model, denoted MQSSS, obtained from inverting the $SSS - SS$ dataset. Figures 6.22(a) and 6.22(b) show the model obtained from inverting the joint $SS - S$ and $SSS - SS$ dataset with equal weighting, denoted MQCOMB1. The re-weighted joint model MQCOMB2 is shown by Figures 6.24(a) and 6.24(b). Each figure shows the lateral variation of Δq_μ over a range of depths from 50 km to 329 km. The maps are plotted for spherical harmonics of degree 1 through 8 excluding the degree 0 term. Each map is accompanied by a histogram showing the amplitude spectra of the spherical harmonics for that depth.

The combined models MQCOMB1 and MQCOMB2 are obtained using the methods described in Section 6.9.3. Figure 6.23 shows the variance ratios obtained for the $SS - S$ and $SSS - SS$ (computed against model MQCOMB1) for different weightings. Note that the colour scale for the attenuation maps is reversed. The blue colours correspond to areas in which the attenuation is less than in PREM and the red colours correspond to areas in which the attenuation is greater than in PREM. Table 6.4 summarises the different attenuation models.

Model MQSS is the attenuation model calculated from only the $SS - S$ residuals. The variations in Δq_μ lie between ± 0.016. The model shows low attenuation across Australia, Africa, South America and Western Europe with regions of high attenuation to the east of Africa and around the mid ocean ridges. The Pacific Ocean is slightly more complex: the western Pacific is less attenuating than the eastern Pacific but the overall pattern is somewhat oscillatory. As with the velocity models we observe similar patterns at all depths with a tendency for the size of the anomalies to increase slightly with depth. The amplitude spectrum of MQSS is dominated by the degree 0 term. This is because the $SS - S$ differential t^* residuals used to construct the model have a large and negative non zero average. If the degree 0 term is plotted then the maps become bluer, i.e. less attenuating and the high attenuation features become much smaller.

Model MQSSS is the model obtained from inversion of the $SSS - SS$ t^* residuals. The amplitude of the variations in Δq_μ is between ± 0.024, slightly larger than for model MQSS. This is possibly because the $SSS - SS$ dataset contains far fewer data points. Model MQSSS shows areas of high attenuation along some mid ocean ridges, around the eastern Pacific and over both North and South

America. Areas of low attenuation are observed over Africa, Australia, Europe, parts of Asia and along a band across the northern Pacific. There is a very intense area of low attenuation in the middle of the Atlantic, however the data coverage in this region is particularly sparse and therefore this anomaly may be unreliable. As with the other models there is little variation with depth, except that the size of the anomalies tends to increase slightly with increasing depth. Unlike model MQSS, the amplitude of the degree 0 term is comparable with that of the other harmonics.

As with the velocity models, the combined $SS-S$ and $SSS-SS$ attenuation models look similar to the original MQSS model. Model MQCOMB1 is the combined Δq_μ model calculated using equal weighting for the $SS-S$ and $SSS-SS$ datasets. The $SS-S$ and $SSS-SS$ datasets are re-weighted using the method described by Section 6.9.3. Figure 6.23 shows the variance ratios for the $SS-S$ and $SSS-SS$ datasets for different weightings. Point A shows the point of equal weighting and point B shows the point at which equal improvement of the variance ratios of both datasets occurs. The weighting at point B corresponds to values of $f_1 = 2.5$ and $f_2 = 1.0$ where f_1 and f_2 are as described in Section 6.9.3. These values of f_1 and f_2 up-weight the $SSS-SS$ dataset relative to the $SS-S$ dataset. Model MQCOMB2 is calculated using this weighting.

Models MQCOMB1 and MQCOMB2 look quite similar to each other. Model MQCOMB2 emphasises slightly more features from the $SSS-SS$ model since that dataset is weighted higher. E.g. the large red region to the south west of Africa and the deep blue area in the middle of the Atlantic are much more pronounced on model MQCOMB2 as these features are associated with the $SSS-SS$ model, MQSSS. The size of the degree 0 term relative to the other harmonics is greatly reduced in model MVCOMB2 compared to model MQCOMB1. The amplitude of the variations in Δq_μ is greater for model MQCOMB2 (± 0.02) as the $SSS-SS$ data is up-weighted compared to model MQCOMB1 which varies between ± 0.016. Model MQCOMB2 has little depth resolution - the same pattern is observed at all depths with a slight increase in the size and intensity of the anomalies with depth. The pattern observed is similar to that of model MQSS, with high attenuation around the Pacific rim, across large areas of the Pacific and off the west coast of Africa. Low attenuation is observed across most of Europe, Russia, Asia, Africa, Australia and part of North America.

Attenuation model	N	Variance ratio	λ_e	χ^2	$\frac{\chi^2}{N}$	Mean of the N residuals
MQSS	2537	0.81	66.77	12014.36	4.74	-0.65
MQSSS	387	0.59	69.29	1534.50	3.97	-0.61
MQCOMB1	2924	0.83	71.36	14521.10	4.97	-0.65
MQCOMB2	2924	0.77	74.56	3843.08	1.31	-0.65

Table 6.4: Summary of the different attenuation models obtained using residuals from the waveform fitting method. N is the total number of data points used, λ_e is the number of effective eigenvalues.

6.10.2 Attenuation models obtained from the results of the spectral ratio method

The models discussed in this section are calculated from the differential t^* residuals obtained using the spectral ratio method. Figures 6.25(a) and 6.25(b) show the attenuation model, MSRMSS, obtained from inverting $SS - S$ differential t^* residuals. Figures 6.26(a) and 6.26(b) show the model, MSRMSSS, obtained from inverting the $SSS - SS$ residuals. Figures 6.27(a) and 6.27(b) show the model, MQSRMCOMB1, obtained from inverting the combined $SS - S$ and $SSS - SS$ dataset with equal weighting of the two datasets. Model MQSRMCOMB2 is the re-weighted combined model shown by Figures 6.29(a) and 6.29(b). Figure 6.28 shows the variance ratios for the $SS - S$ and $SSS - SS$ datasets for different weightings. As with the previous sections, point A corresponds to equal weighting (used for model MQSRMCOMB1) and point B corresponds to the point at which there is equal improvement in both the $SS - S$ and $SSS - SS$ variance ratios (used for model MQSRMCOMB2). The data weightings at point B correspond to values of $f_1 = 2.0$ and $f_1 = 1.0$ i.e. the $SSS - SS$ dataset is up-weighted.

All the models obtained using residuals from the spectral ratio method possess a very large degree 0 component. The reason for this large degree zero component is that the mean of the residuals is large and negative (see Table 6.5). This large degree 0 term is also the reason for the low variance ratios obtained.

MQSRMCOMB2 shows areas of low attenuation around the eastern Pacific rim, across North America and Australia. High attenuation is observed around the western Pacific rim, along a band running North-South in the Pacific Ocean and along the mid oceanic ridge running from the west of India to South of Australia.

Attenuation model	N	Variance ratio	λ_e	χ^2	$\frac{\chi^2}{N}$	Mean of the N residuals
MQSRMSS	3246	0.29	65.01	11252.5	3.47	-2.87
MQSRMSSS	885	0.18	72.75	2482.66	2.81	-3.52
MQSRMCOMB1	4131	0.27	72.33	14409.60	3.49	-3.01
MQSRMCOMB2	4131	0.24	75.32	5621.36	1.36	-3.01

Table 6.5: Summary of the different attenuation models obtained using residuals from the spectral ratio method. N is the total number of data points used, λ_e is the number of effective eigenvalues.

6.11 Resolution tests

A discussion of resolution is given by Appendix A.3. In this section we discuss the resolving powers of our models using resolution tests. Testing the resolution of model requires a "test" model for

which all the model parameters are known. Typically, the test models used in seismic tomography are checkerboard type patterns. The procedure is as follows:

1. Generate the predicted data from the test model using the derivative matrices calculated for the real dataset.

2. Invert the predicted data using the same damping and weighting as for the real dataset to obtain the output model.

We perform the resolution test for checkerboards at depths of 74 km and 256 km. The checkerboard patterns are generated for $l = 12$ and $m = 6$. Figures 6.30(a) and 6.30(b) show the input test model for a checkerboard at a depth of 74km. The amplitude of the input model is much greater at 74 km than at other depths (64% at 74km and less than 1% at other depths). Also note that the amplitude spectra contain only a degree 12 component. Figures 6.31(a) and 6.31(b) show the resulting output model obtained using the $SS-S$ dataset. Figures 6.32(a) and 6.32(b) show the output model obtained using the $SSS-SS$ dataset. Figures 6.33(a) and 6.33(b) show the output model obtained using the combined $SS-S$ and $SSS-SS$ dataset. The three output models exhibit the same features:

- The checkerboard pattern is well preserved meaning lateral resolution is good.

- The pattern is observed across all depths meaning depth resolution is poor.

- The amplitude of the model is approximately the same at all depths although there is a slight increase in amplitude with depth.

- The amplitude spectra now contain small contributions from degrees 0 through 11, although the degree 12 component is dominant.

The models obtained using an input checkerboard at 256 km are very similar. For reference Figure 6.34 shows the input model for a checkerboard at 256 km. Figure 6.35 shows the output model obtained using the combined $SS-S$ and $SSS-SS$ datasets. The results of the resolution testing lead to the following conclusions:

- The lateral resolution of the models is good.

- The depth resolution is poor.

This means that we cannot attribute the lateral variations of $\frac{\delta v}{v_s}$ or Δq_μ observed in the models to a particular depth. The model becomes smeared out over the whole depth range selected for inversion.

In Chapter 7 the data of this study will be combined with other data to provide better resolved models.

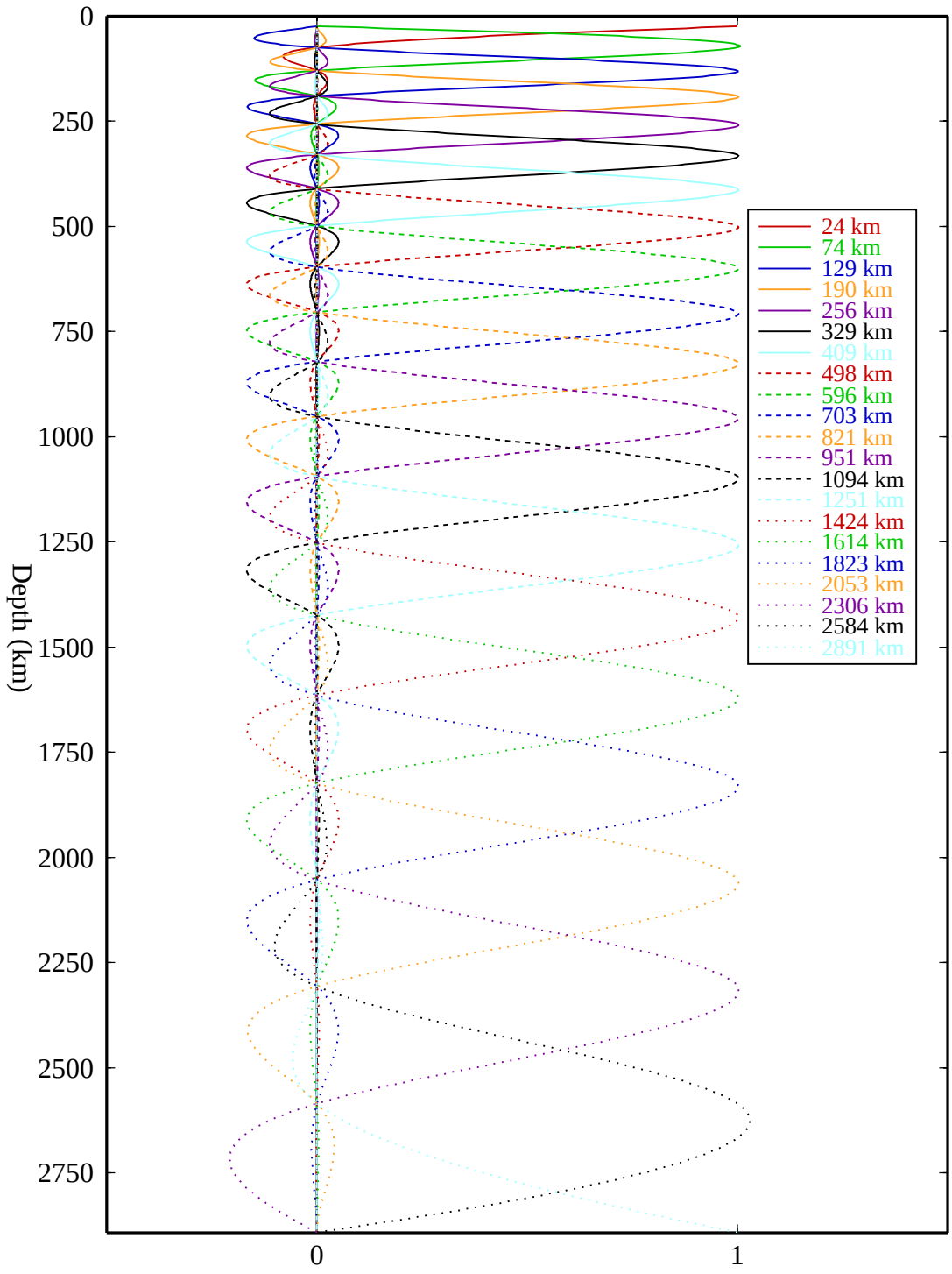


Figure 6.1: Depth splines, $f_k(r)$, for $k = 1, 2 \ldots 20$. The legend gives the depth at the maximum.

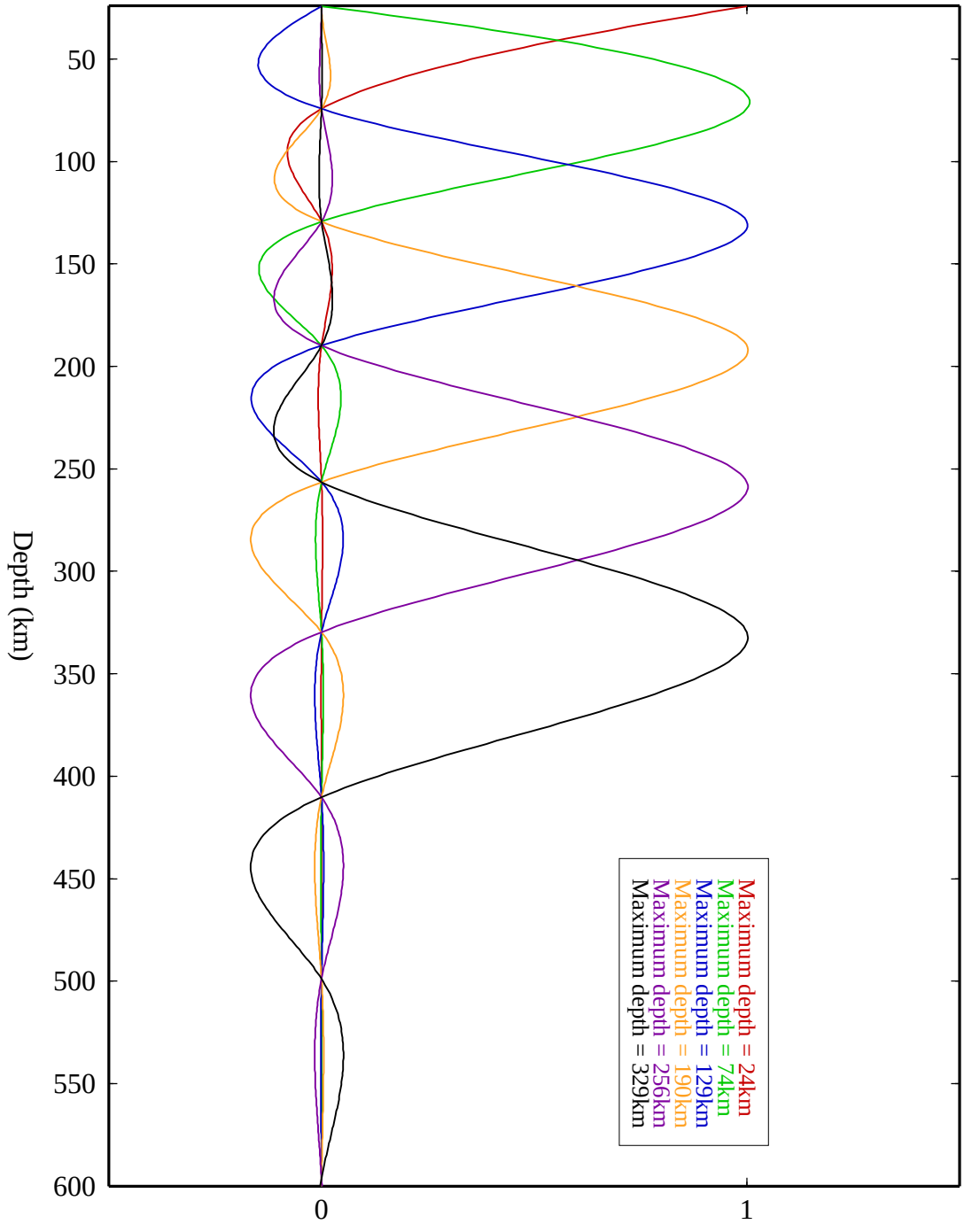


Figure 6.2: Depth splines for $k = 1, 2 \ldots 6$ along with the depth at which the maximum of each spline occurs.

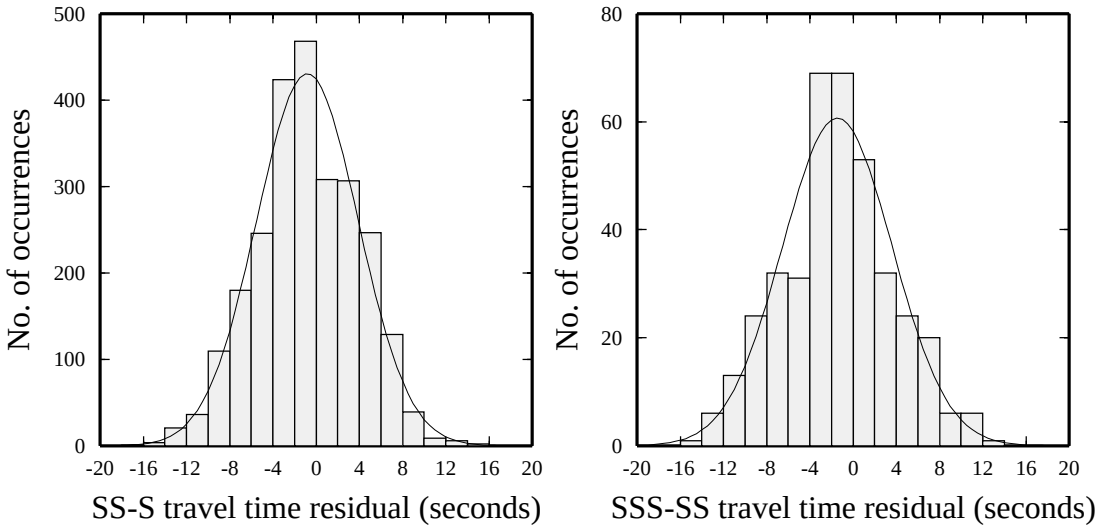


Figure 6.3: Distribution of travel time residuals with fit parameters of 0.2 or less obtained from the waveform fitting method. The left hand plot shows the distribution for the $SS - S$ dataset, the right hand plot shows the distribution for the $SSS - SS$ dataset.

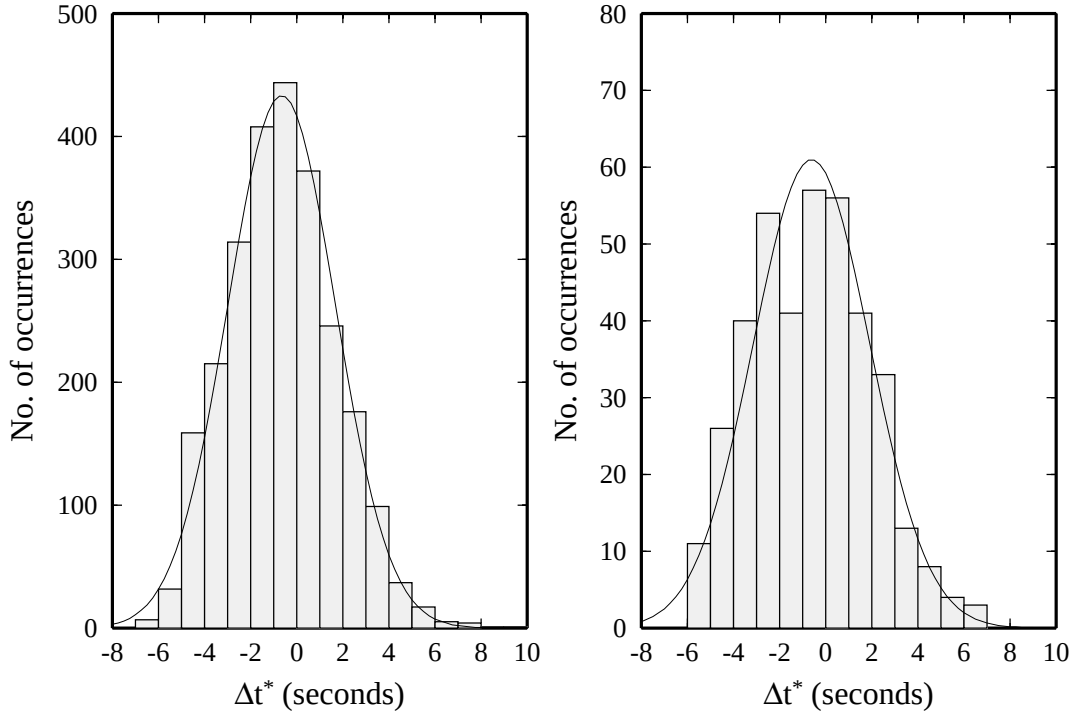


Figure 6.4: Distribution of t^* residuals with fit parameters of 0.2 or less obtained from the waveform fitting method. The left hand plot shows the distribution for the $SS - S$ dataset, the right hand plot shows the distribution for the $SSS - SS$ dataset.

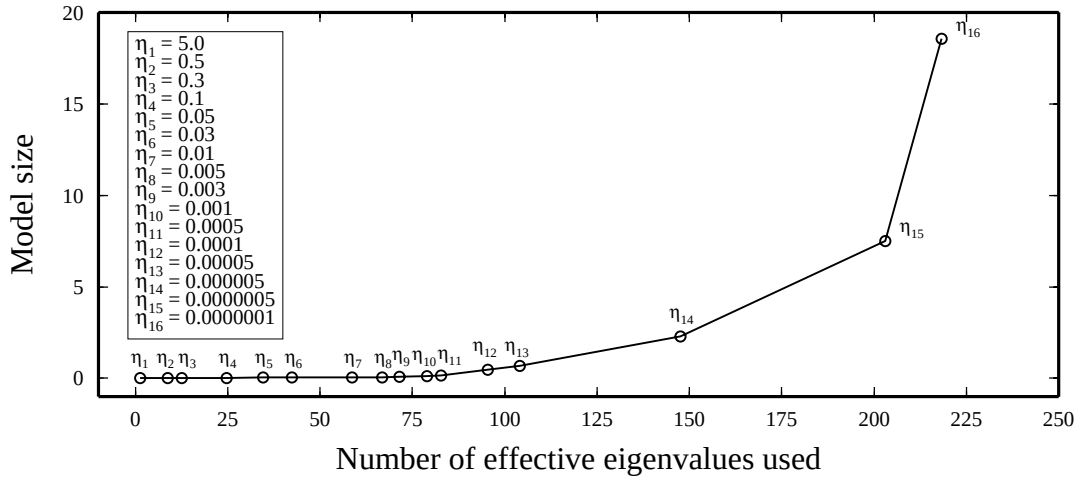


Figure 6.5: Relationship between model size and the number of effective eigenvalues used. The number beside each data point gives the value of η used for the inversion. For reference, a degree 8, 6 spline inversion for q_μ was used to obtain the results shown here.

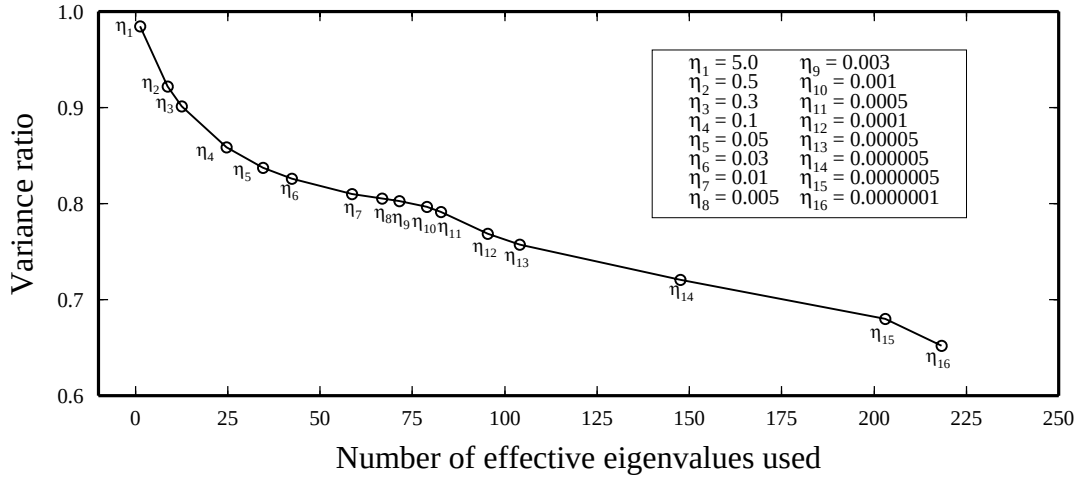


Figure 6.6: Relationship between the variance ratio and the number of effective eigenvalues used. The number beside each data point gives the value of η used for the inversion. For reference, a degree 8, 6 spline inversion for q_μ was used to obtain the results shown here.

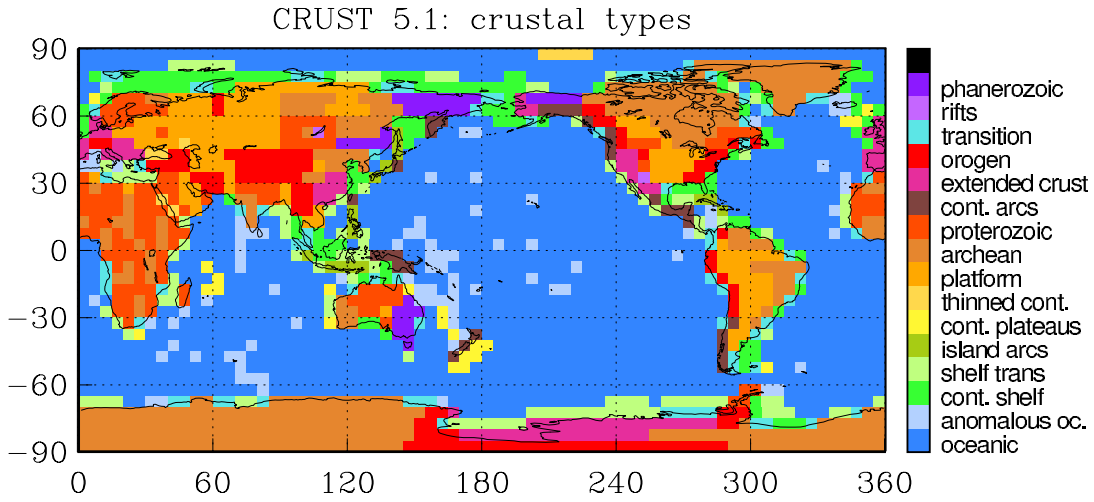


Figure 6.7: Crustal types from CRUST 5.1, reproduced from Mooney *et al.* (1998). The crustal structure in unmeasured regions has been extrapolated using statistical averages of regions of similar tectonic setting.

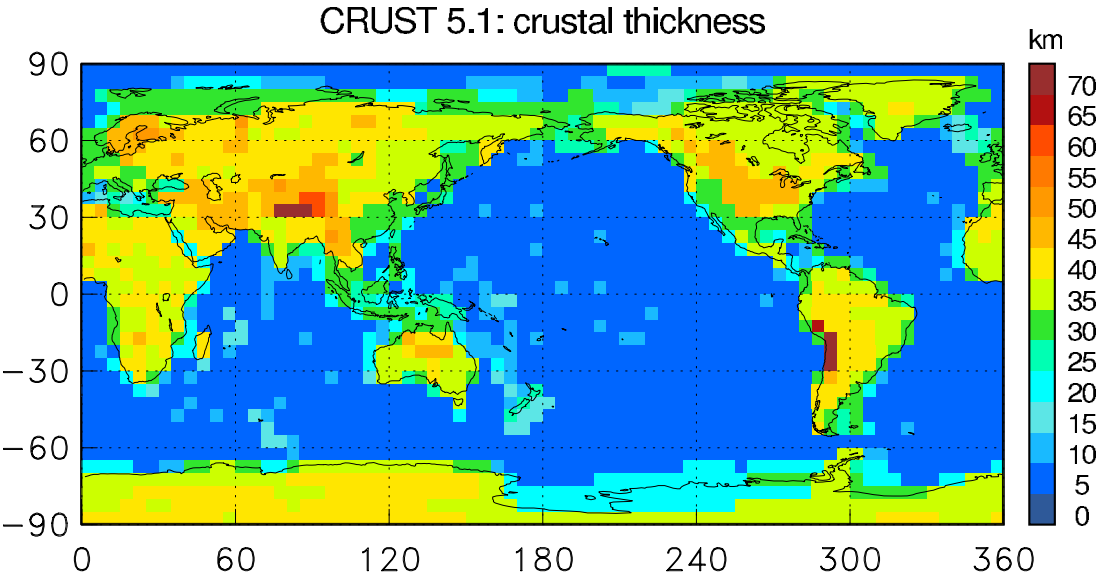


Figure 6.8: Global crustal thickness, including topography above sea level but not bathymetry of CRUST 5.1 (reproduced from Mooney *et al.* (1998)).

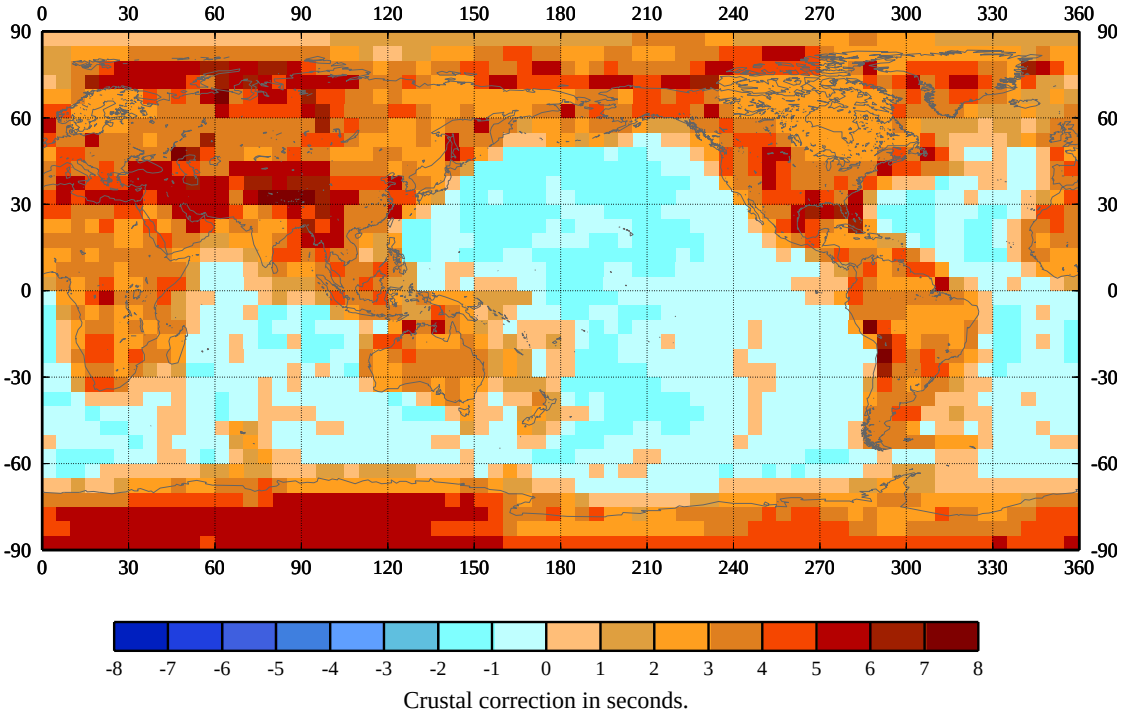


Figure 6.9: Crustal corrections for $SS - S$ calculated for a grid of hypothetical bounce points in 5° intervals. The oceans exhibit negative corrections, whereas the continents show positive corrections.

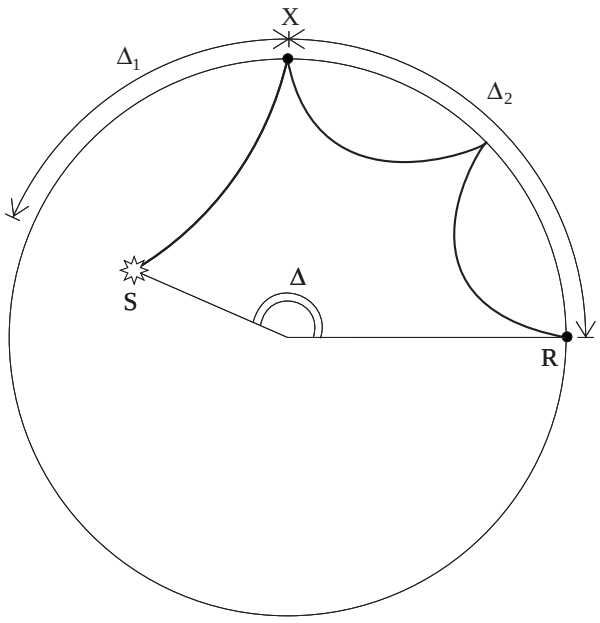


Figure 6.10: Schematic showing how a SSS ray may be split into two legs denoted by 1 and 2. The first leg is an S ray over the distance Δ_1, the second leg is an SS ray over the distance Δ_2.

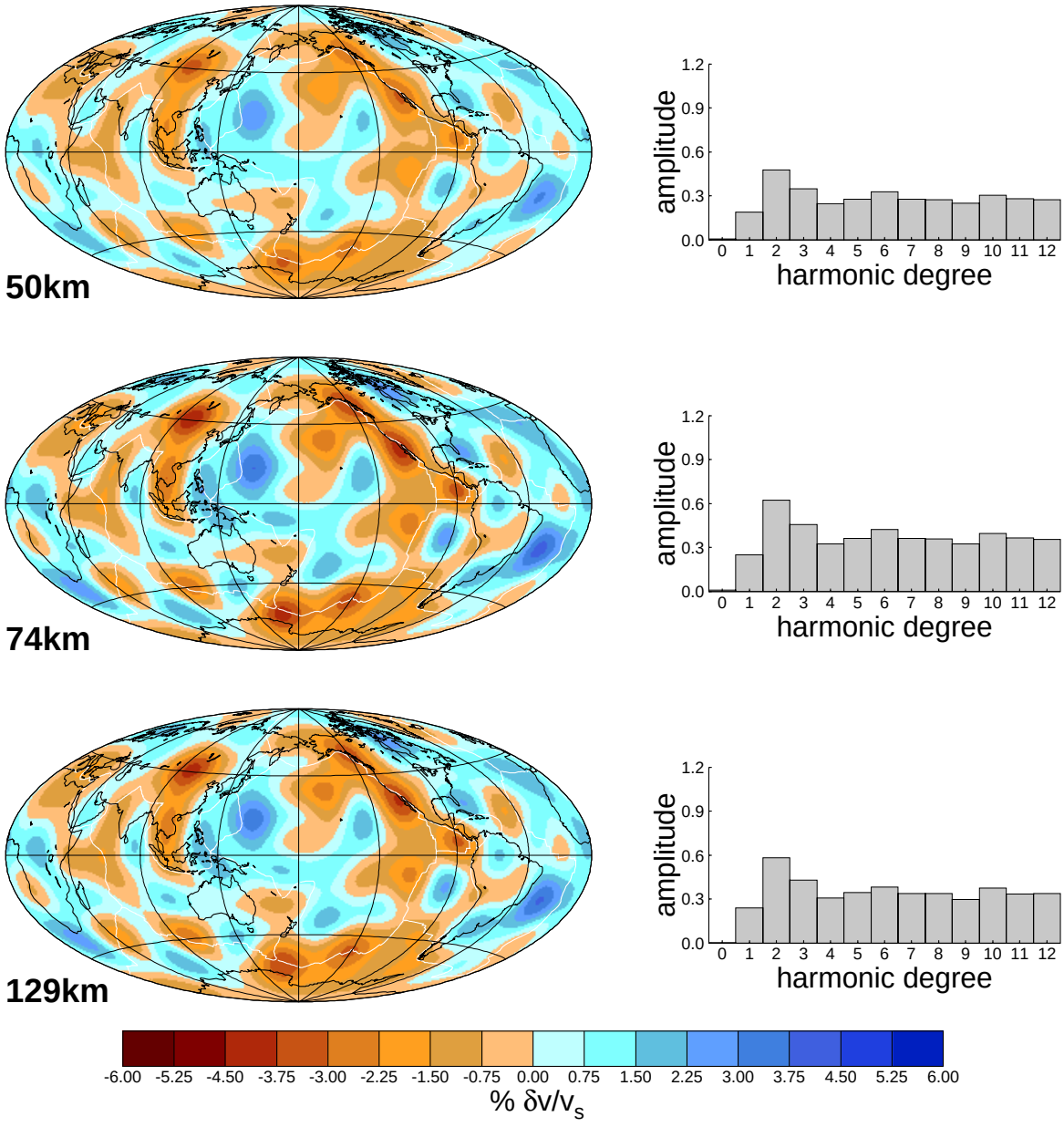


Figure 6.11(a): Model MVSSa: $SS - S$ velocity model with no corrections applied for depths 50-129 km

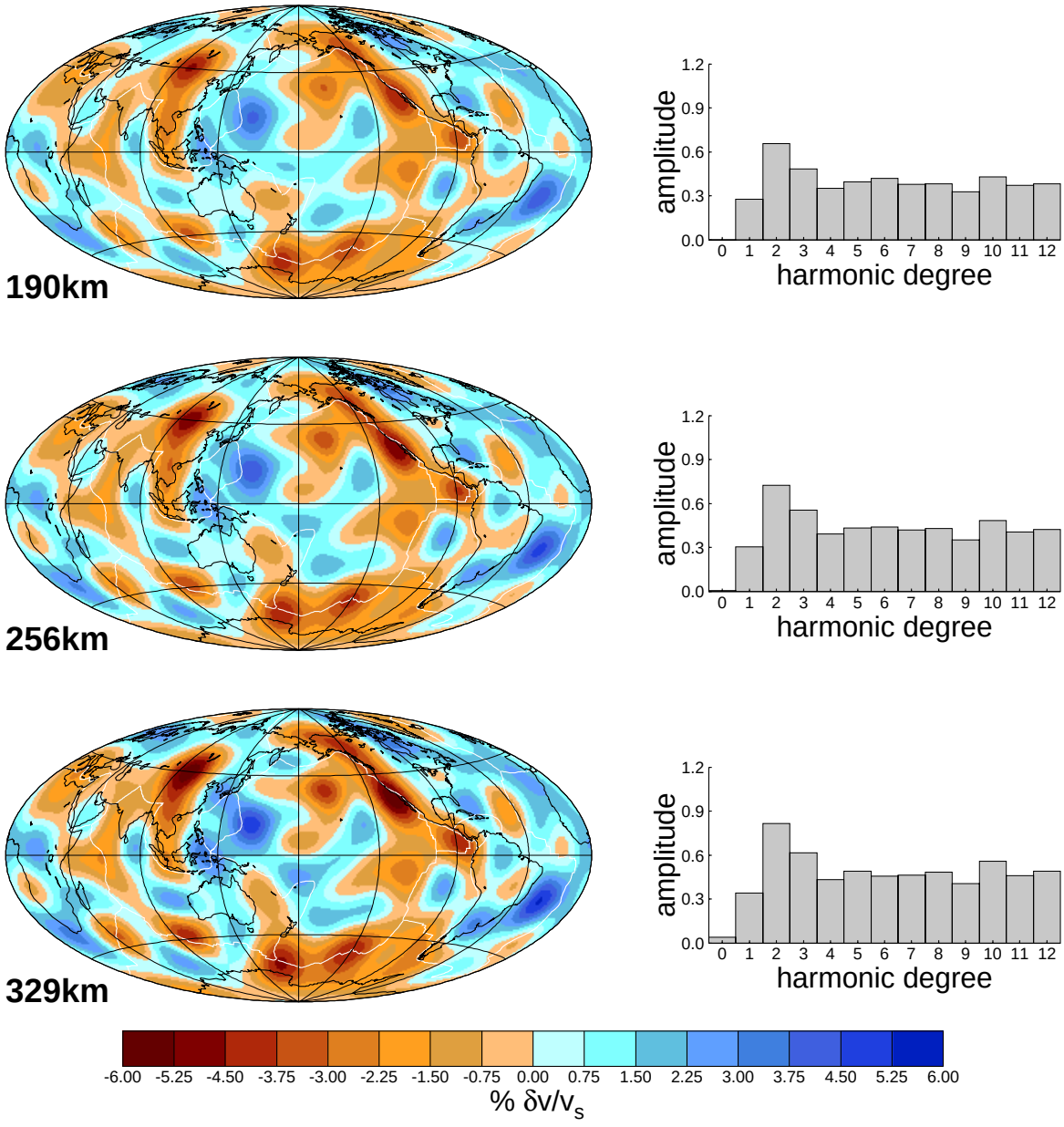


Figure 6.11(b): Model MVSSa: $SS - S$ velocity model with no corrections applied for depths 190-329 km

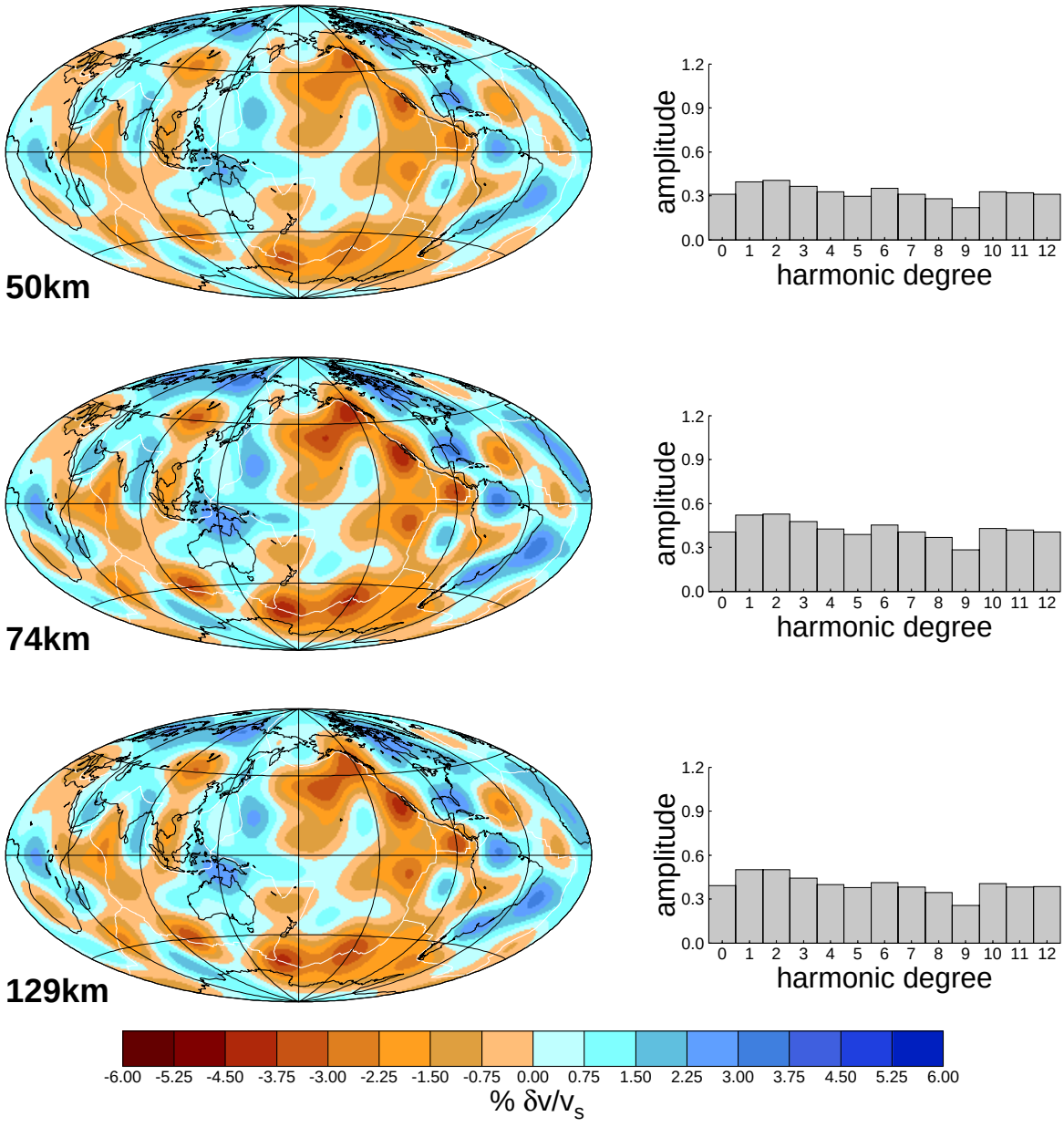


Figure 6.12(a): Model MVSSb: $SS-S$ velocity model with only crustal corrections applied for depths 50-129 km

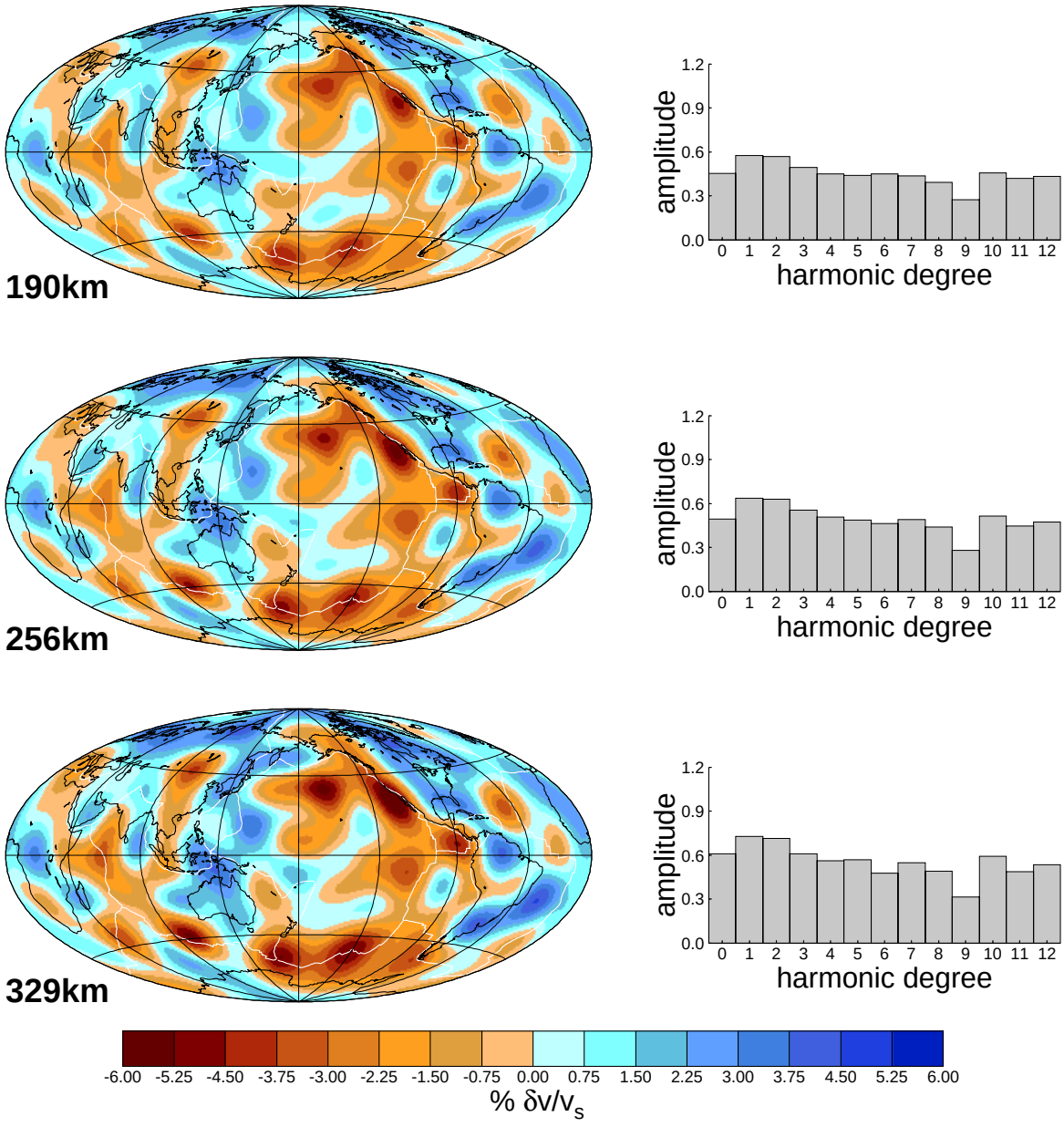


Figure 6.12(b): Model MVSSb: $SS-S$ velocity model with only crustal corrections applied for depths 190-329 km

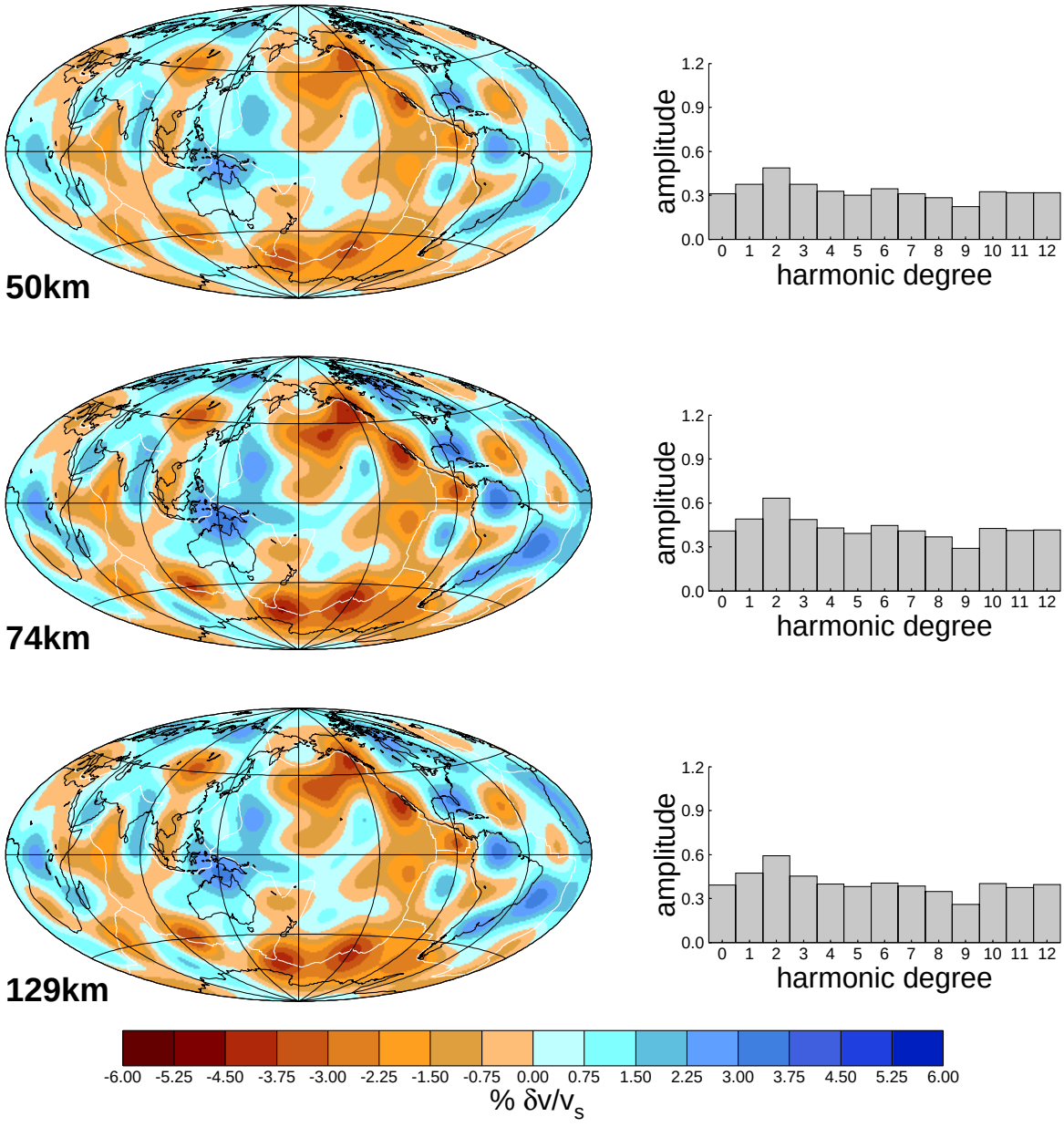


Figure 6.13(a): Model MVSSc: $SS - S$ velocity model with crustal and ellipticity corrections applied for depths 50-129 km

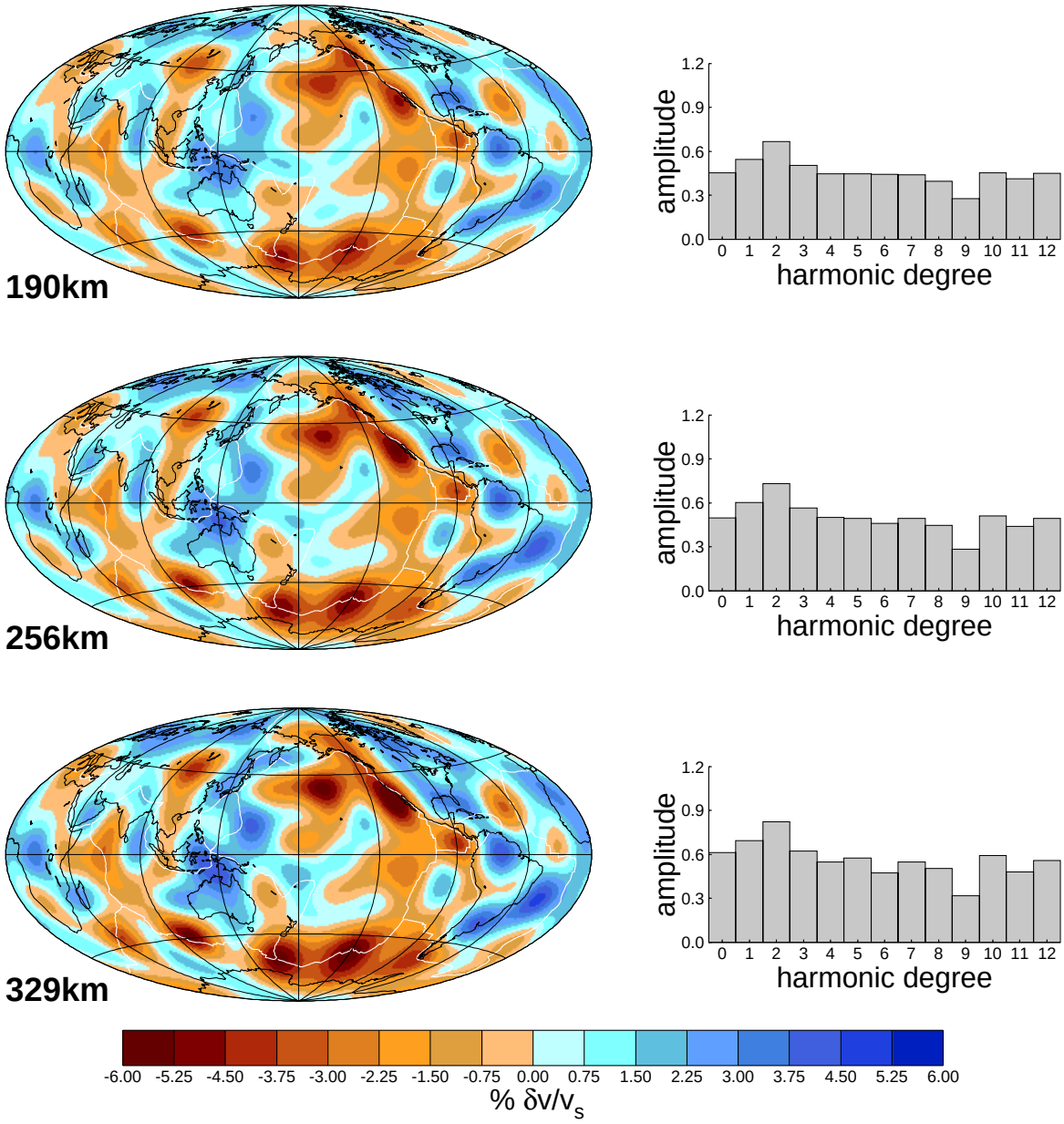


Figure 6.13(b): Model MVSSc: $SS - S$ velocity model with crustal and ellipticity corrections applied for depths 190-329 km

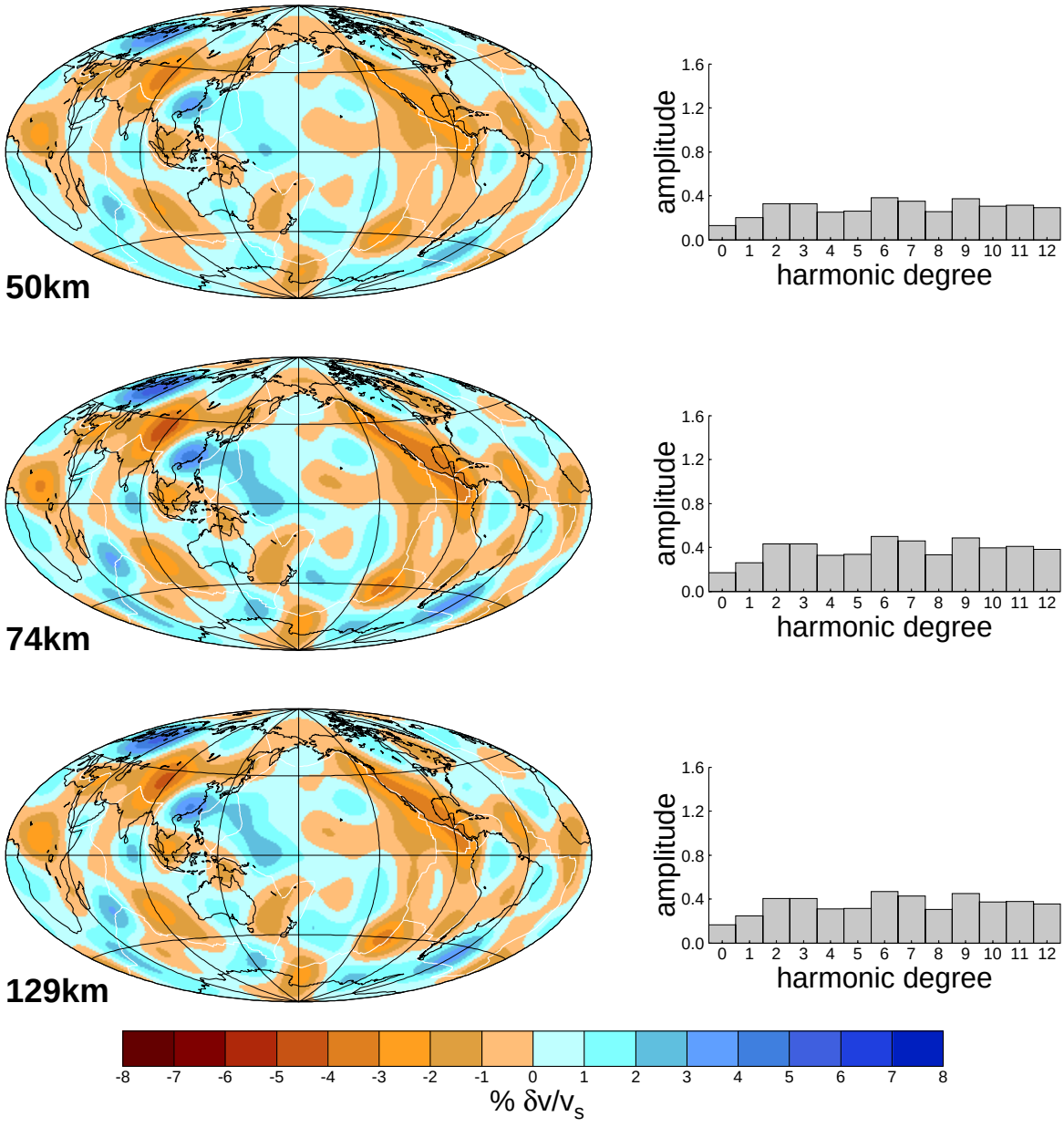


Figure 6.14(a): Model MVSSSa: $SSS - SS$ velocity model with no corrections applied for depths 50-129 km

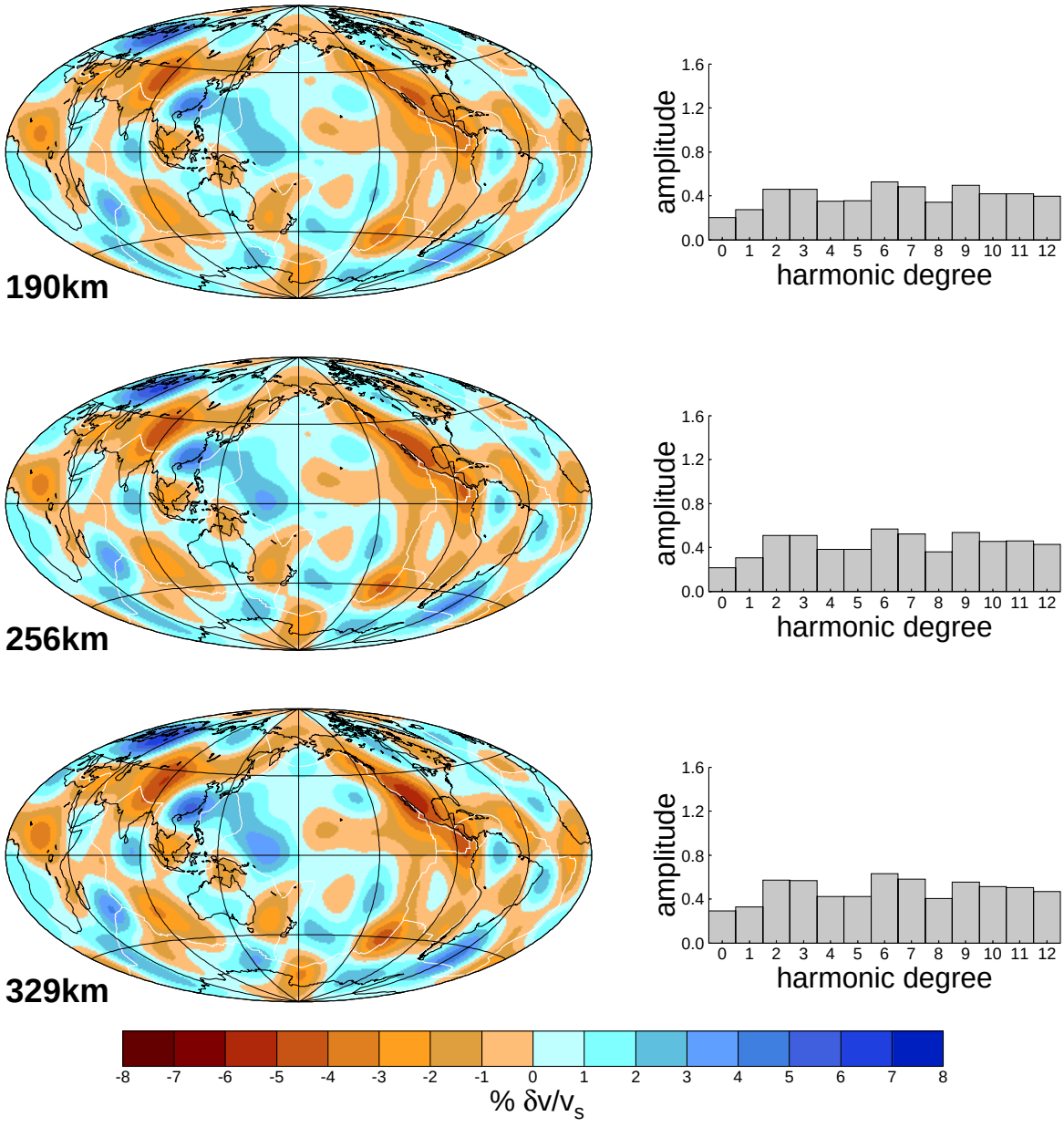


Figure 6.14(b): Model MVSSSa: $SSS - SS$ velocity model with no corrections applied for depths 190-329 km

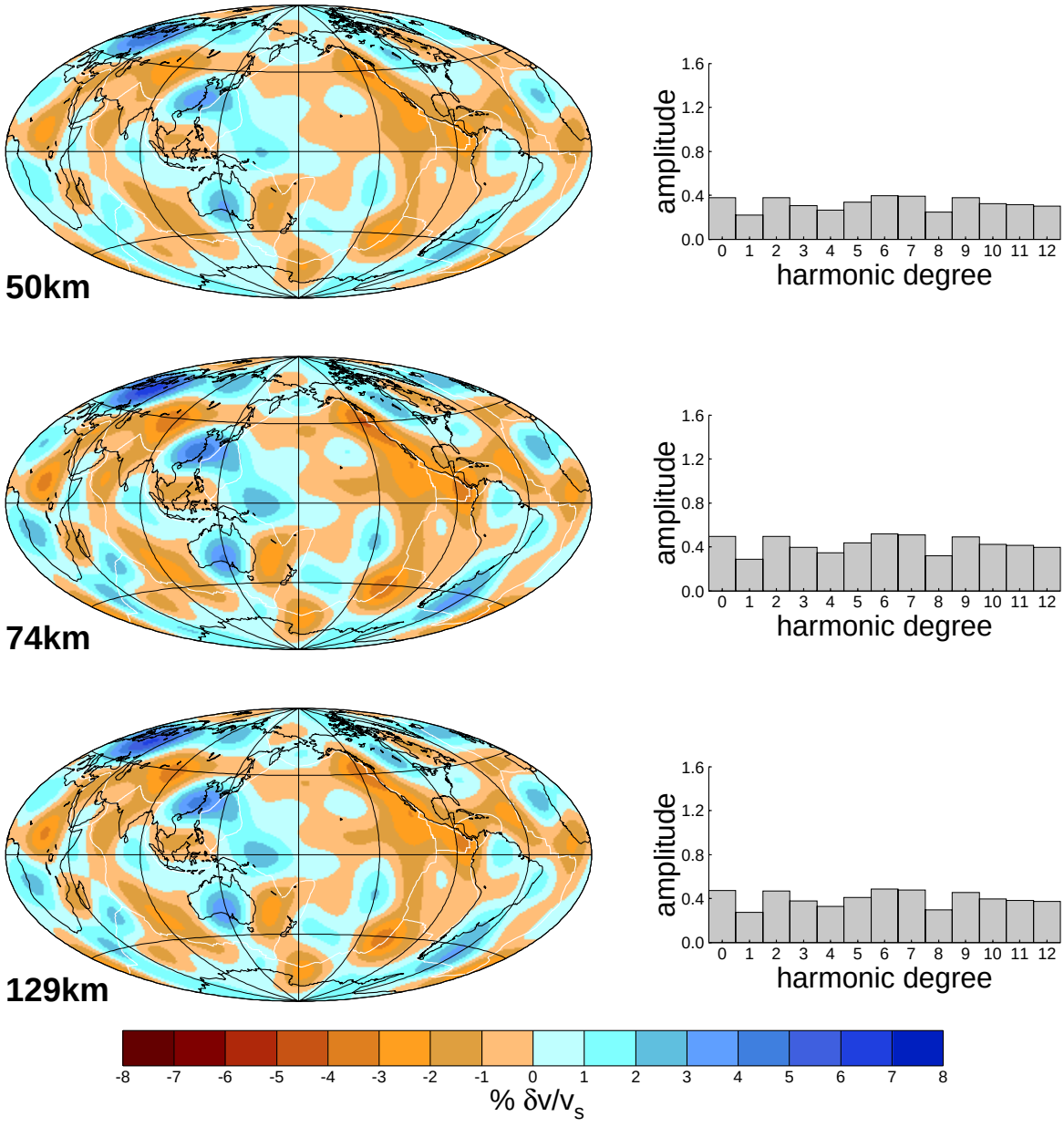


Figure 6.15(a): Model MVSSSb: $SSS - SS$ velocity model with only crustal corrections applied for depths 50-129 km

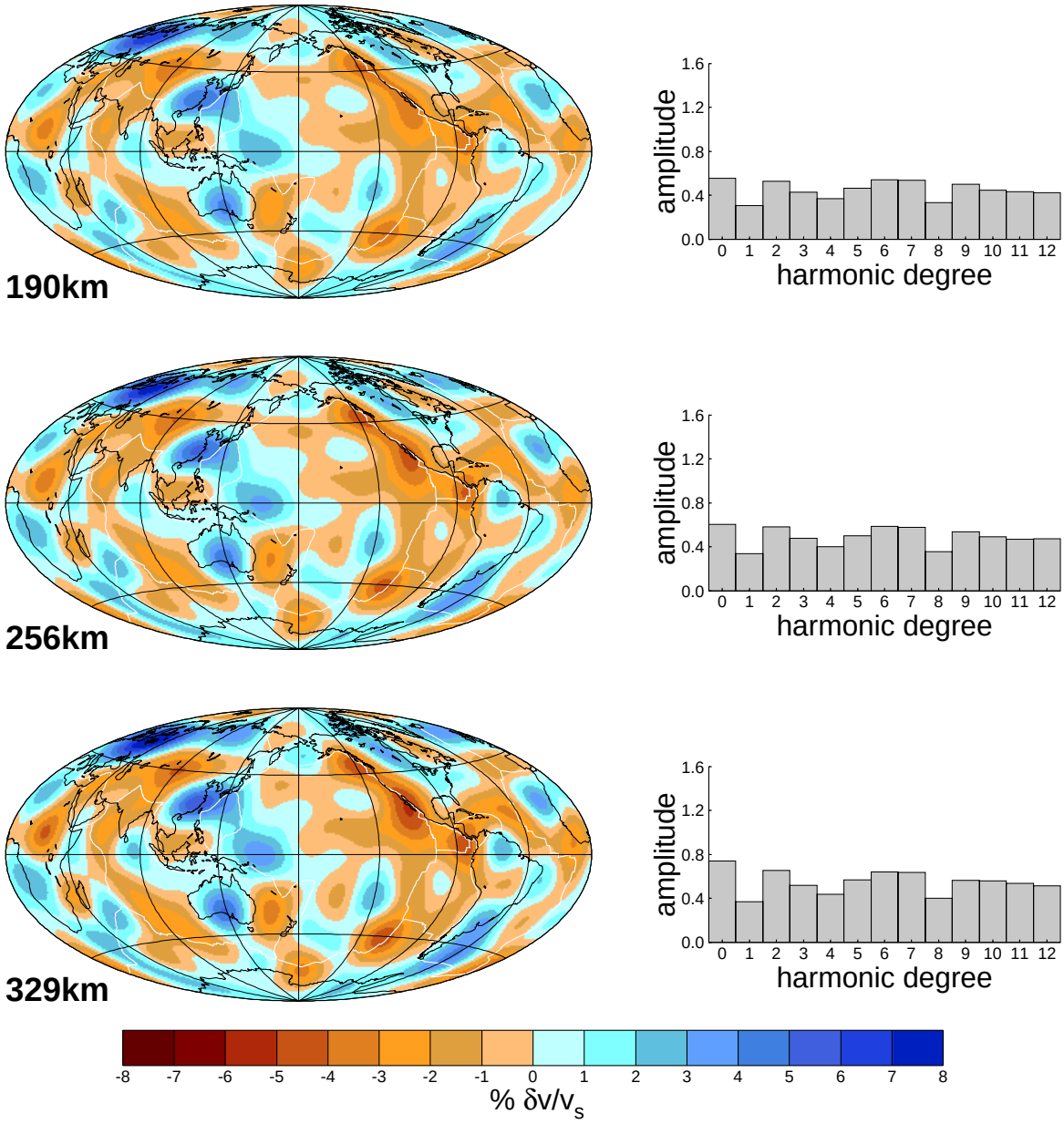


Figure 6.15(b): Model MVSSSb: $SSS - SS$ velocity model with only crustal corrections applied for depths 190-329 km

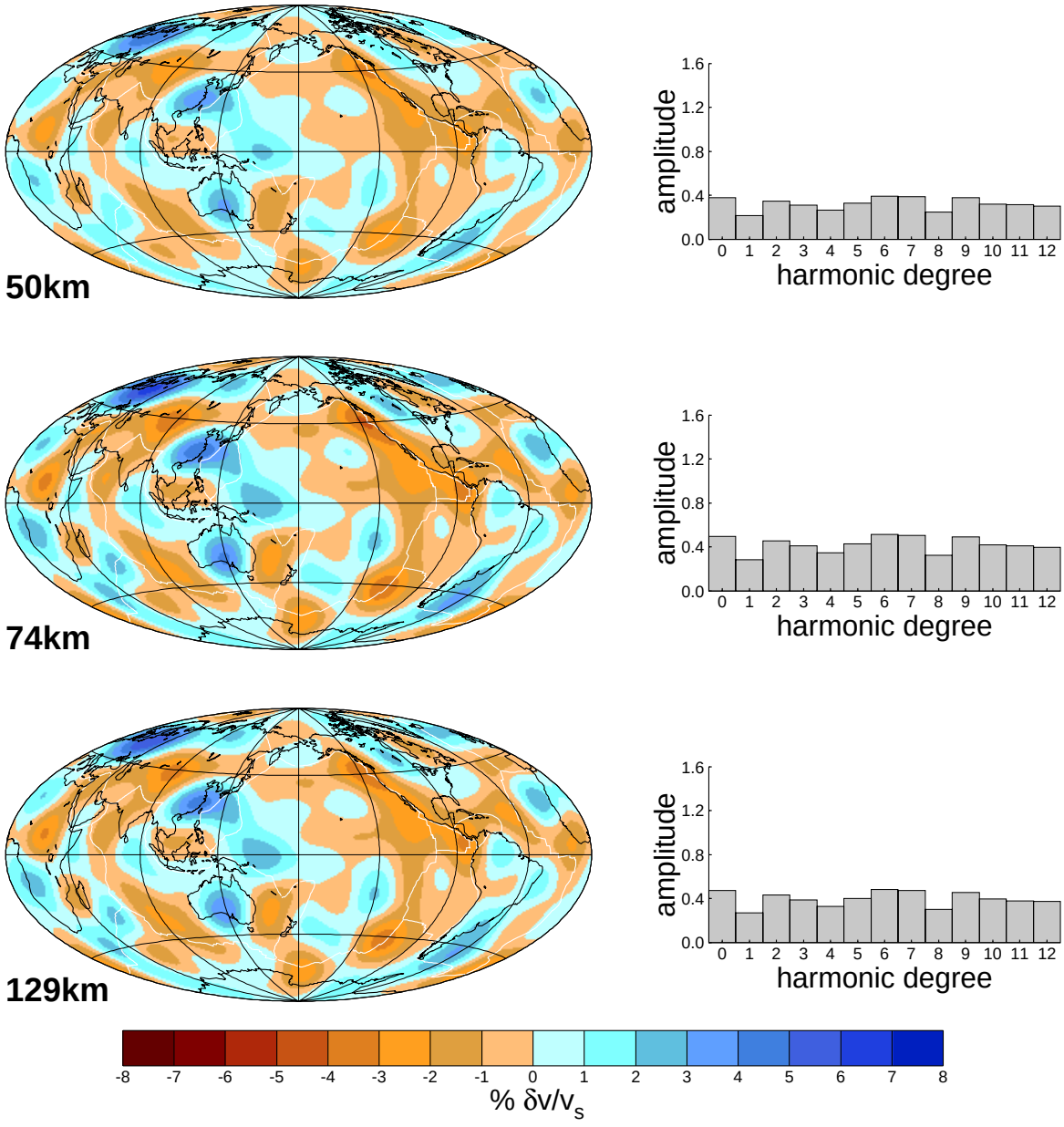


Figure 6.16(a): Model MVSSSc: $SSS - SS$ velocity model with crustal and ellipticity corrections applied for depths 50-129 km

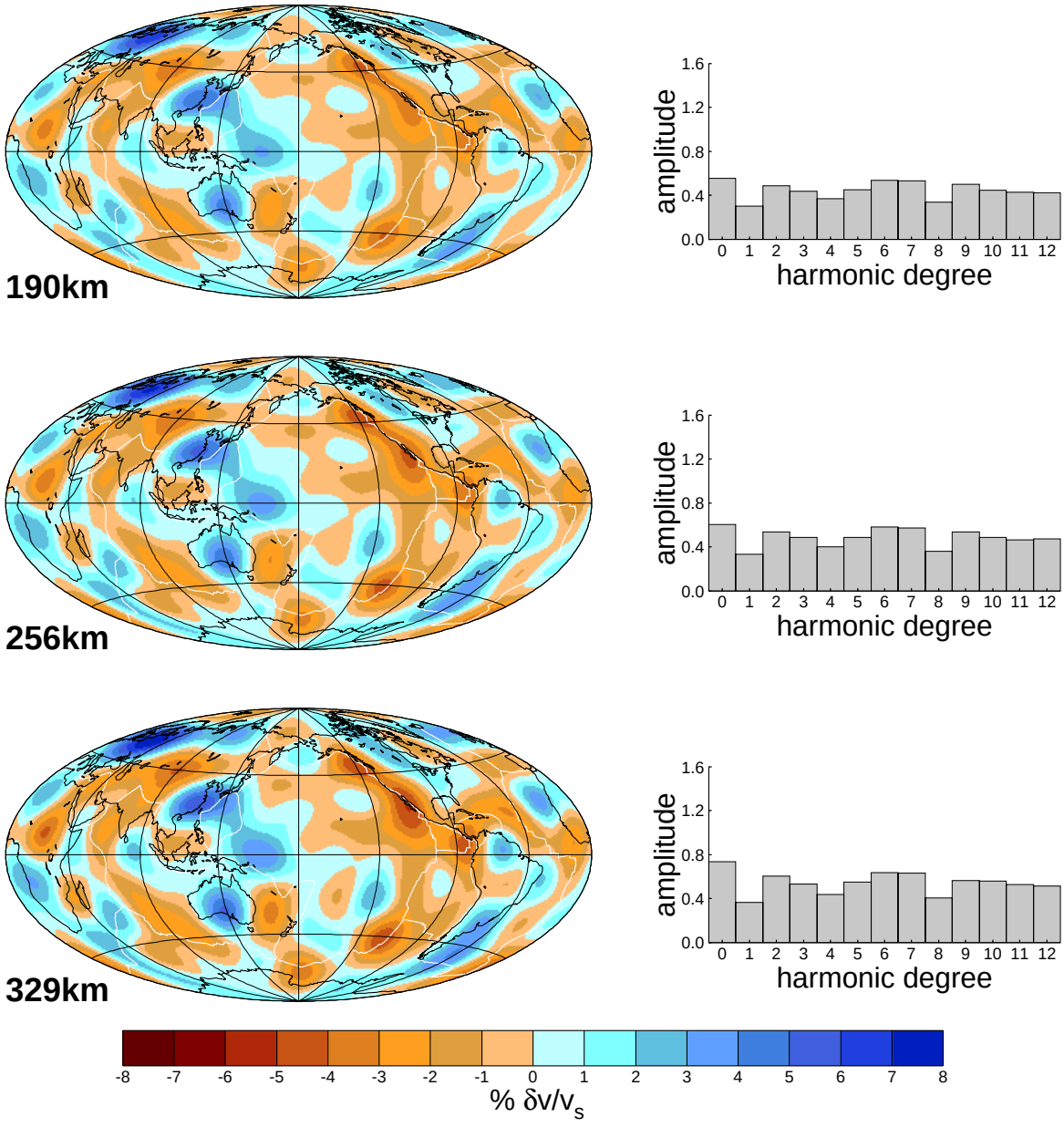


Figure 6.16(b): Model MVSSSc: $SSS - SS$ velocity model with crustal and ellipticity corrections applied for depths 190-329 km

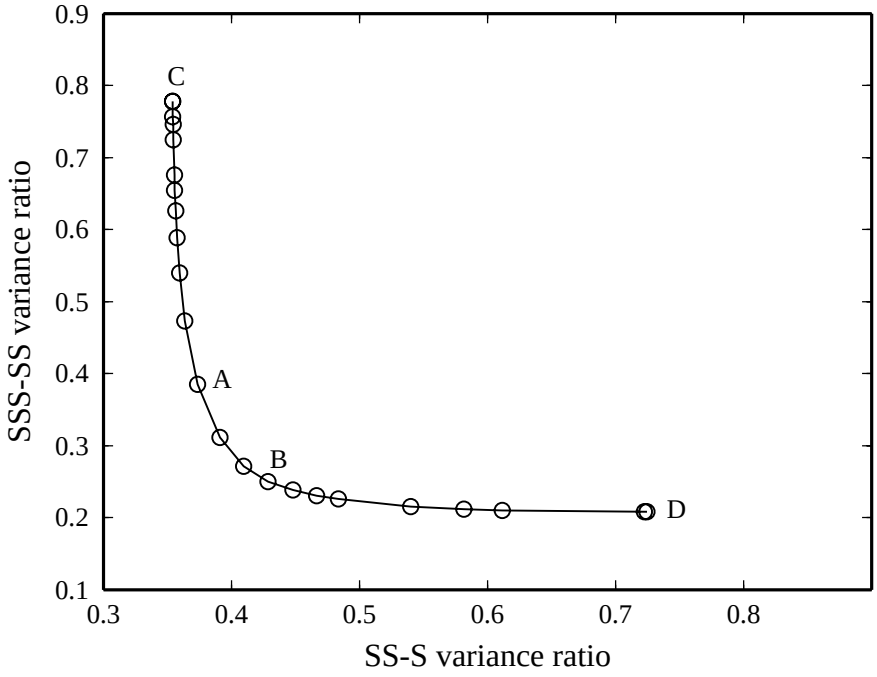


Figure 6.17: Variance ratio of $SSS - SS$ data against variance ratio of $SS - S$ data for the combined model. Point A shows the point of equal weighting and point B shows the point of equal improvement of the $SSS - SS$ and $SS - S$ variance ratios.

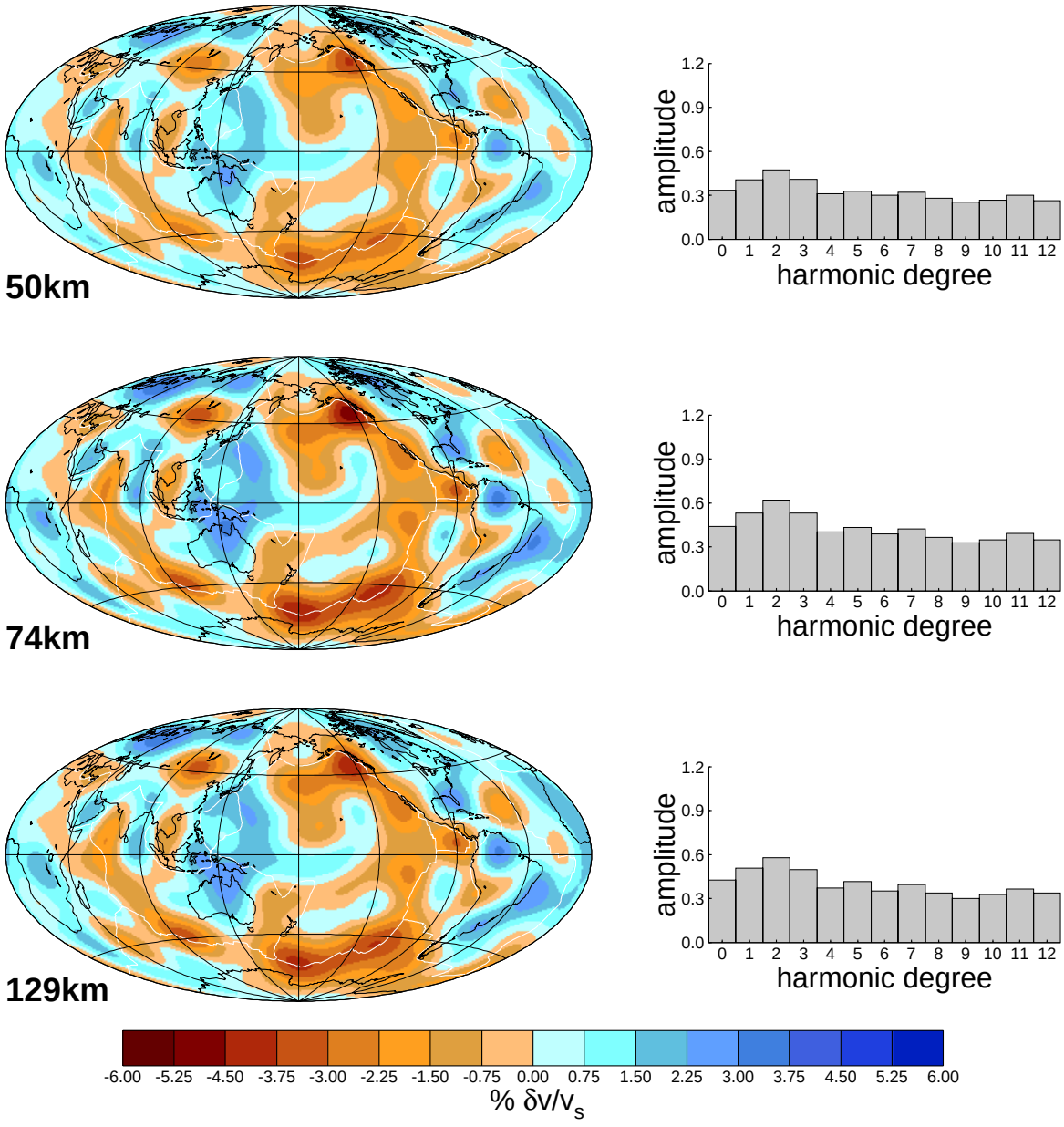


Figure 6.18(a): Model MVCOMB1: Combined velocity model with crustal and ellipticity corrections applied for depths 50-129 km

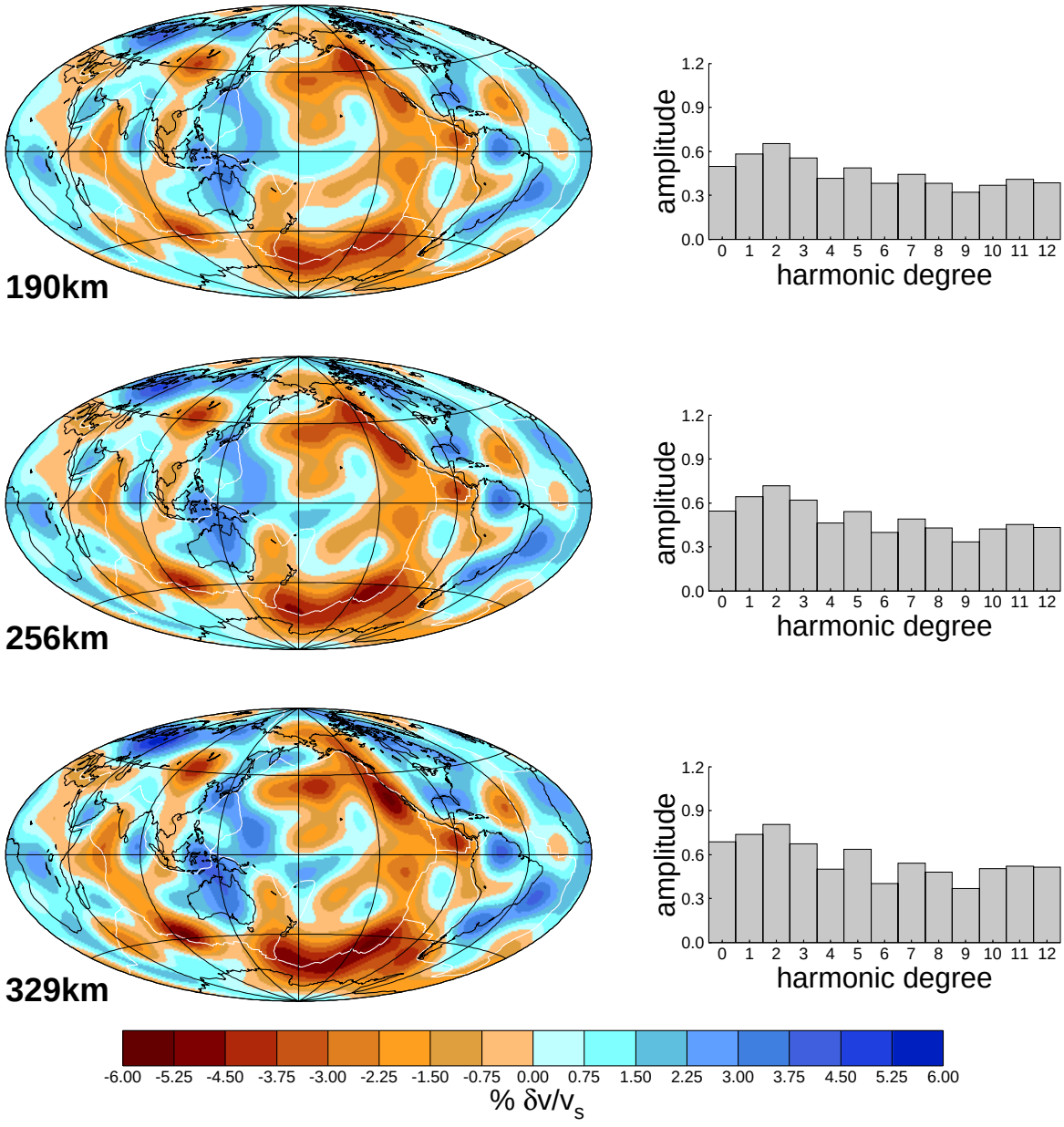


Figure 6.18(b): Model MVCOMB1: Combined velocity model with crustal and ellipticity corrections applied for depths 190-329 km

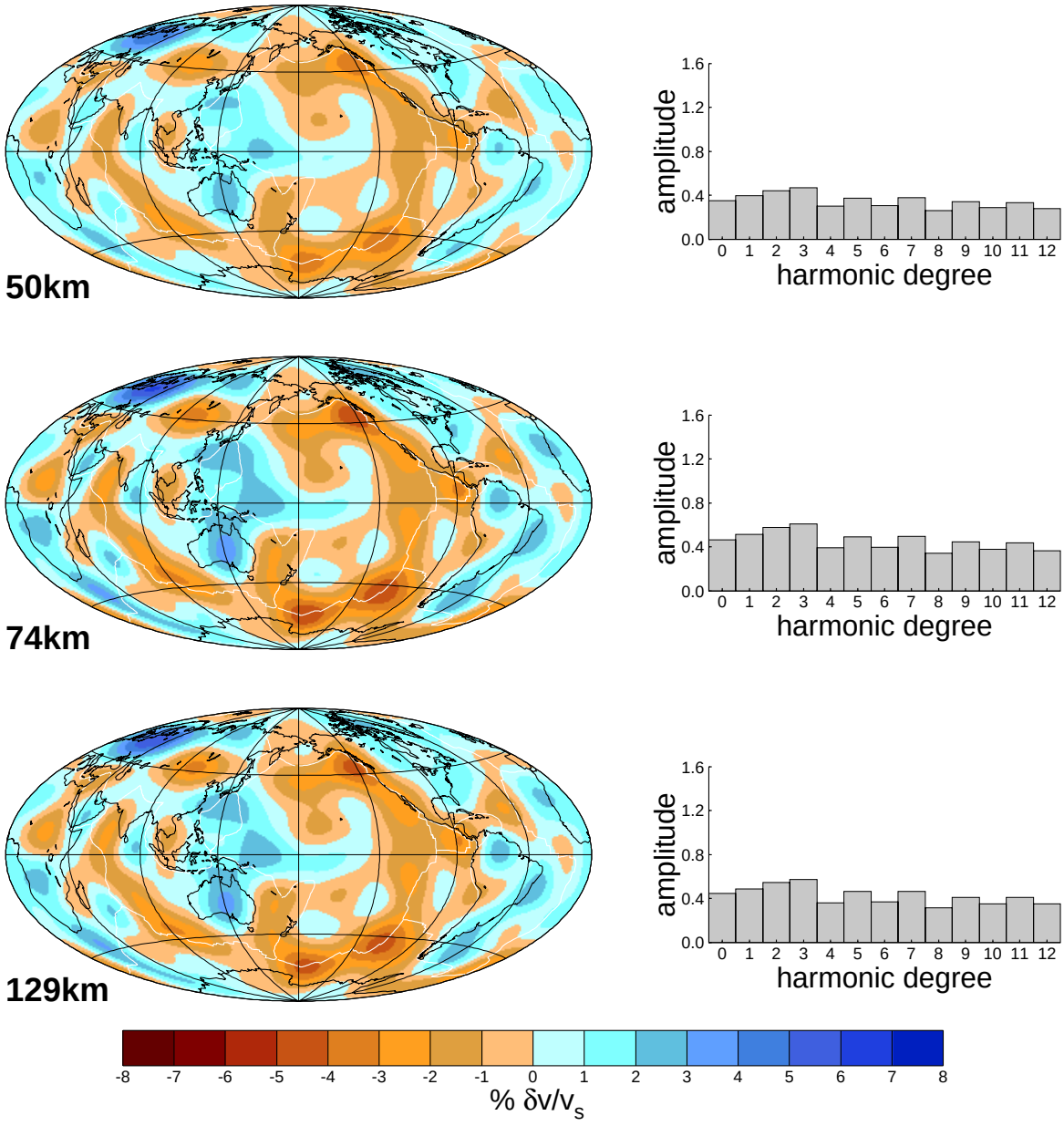


Figure 6.19(a): Model MVCOMB2: Combined velocity model with crustal and ellipticity corrections applied for depths 50-129 km. The weightings used are $w_1 = \frac{1}{2.5}$ and $w_2 = 1.0$

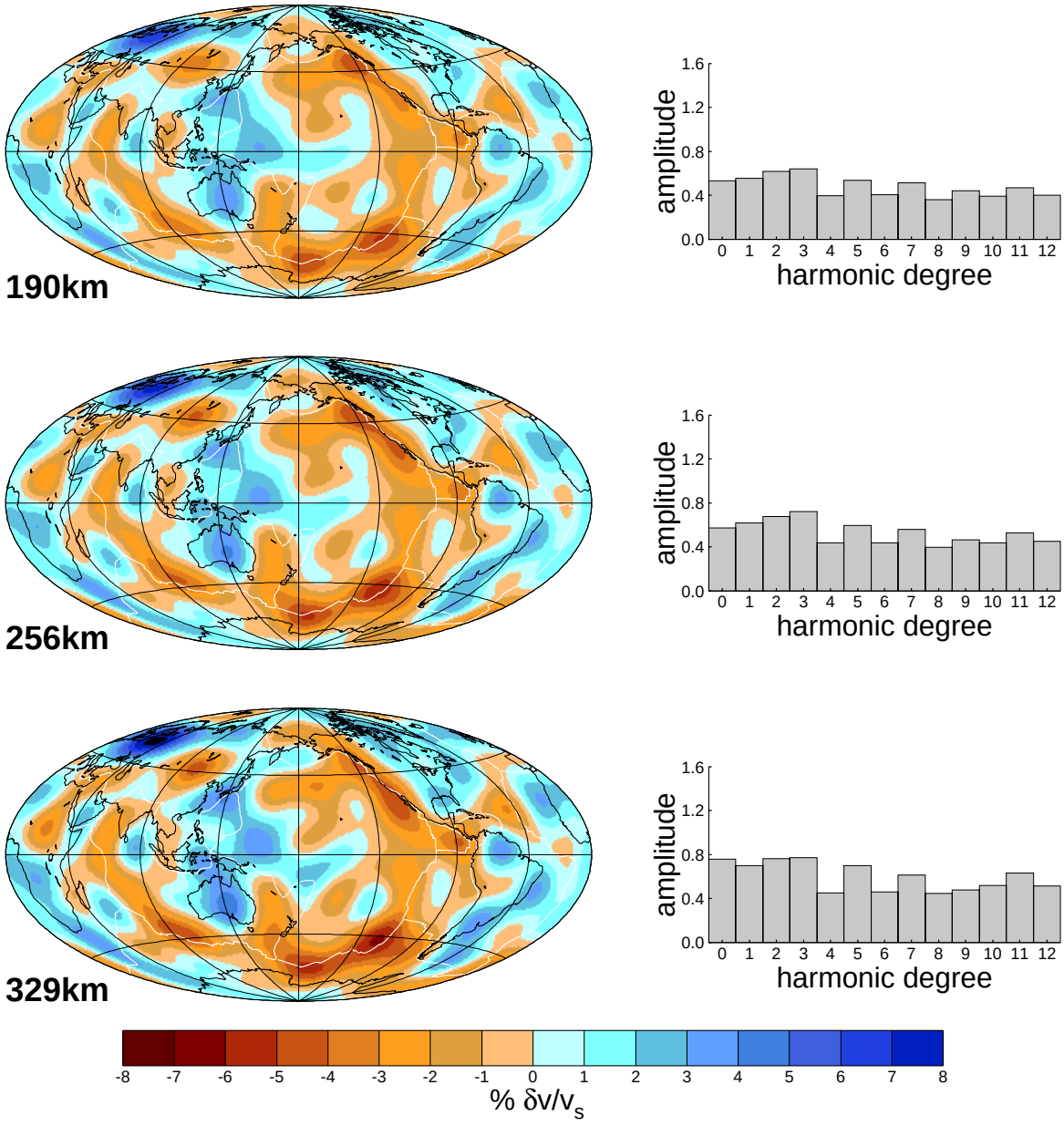


Figure 6.19(b): Model MVCOMB2: Combined velocity model with crustal and ellipticity corrections applied for depths 190-329 km. The weightings used are $w_1 = \frac{1}{2.5}$ and $w_2 = 1.0$

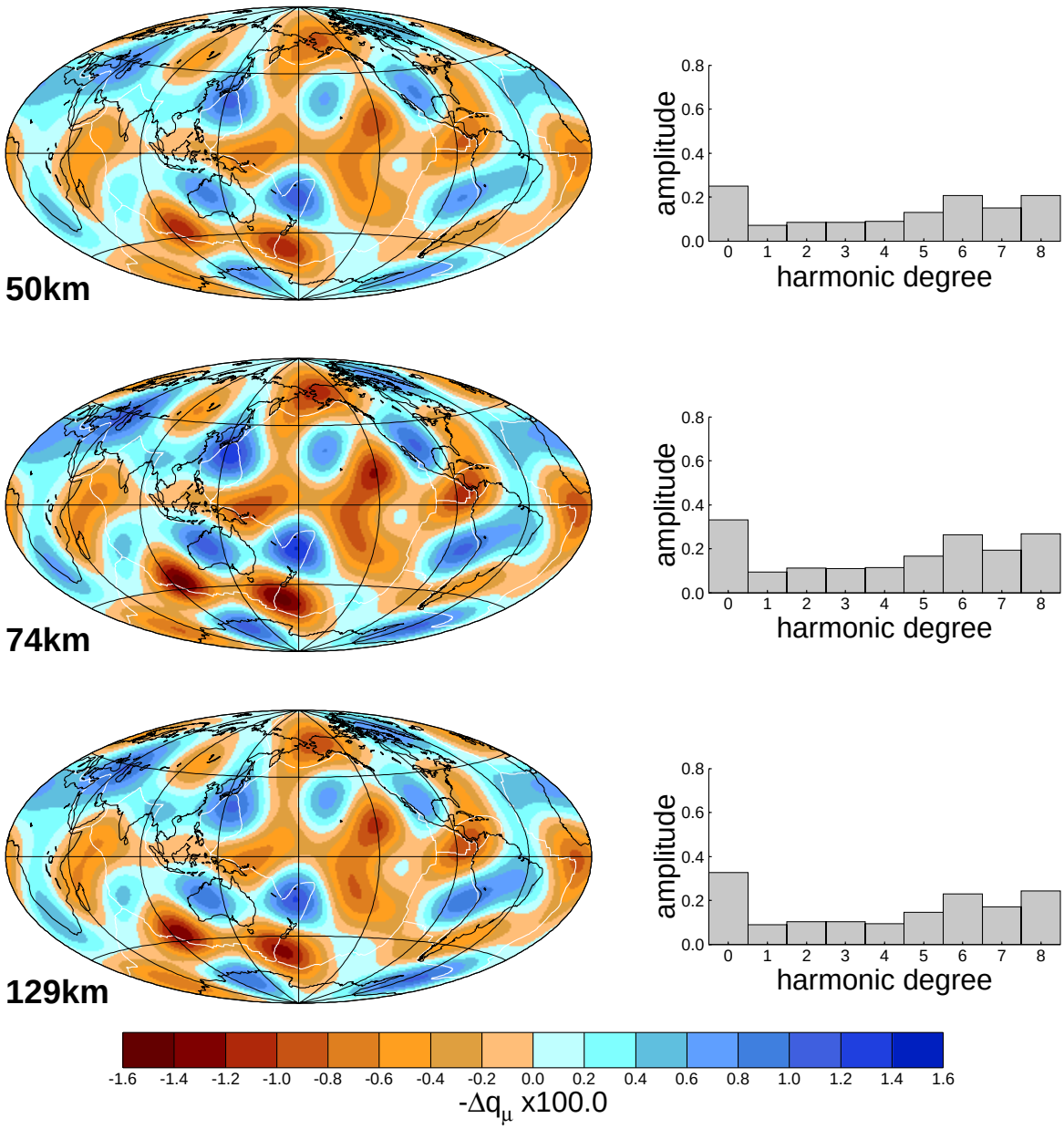


Figure 6.20(a): Model MQSS: $SS - S$ attenuation model for depths 50-129 km

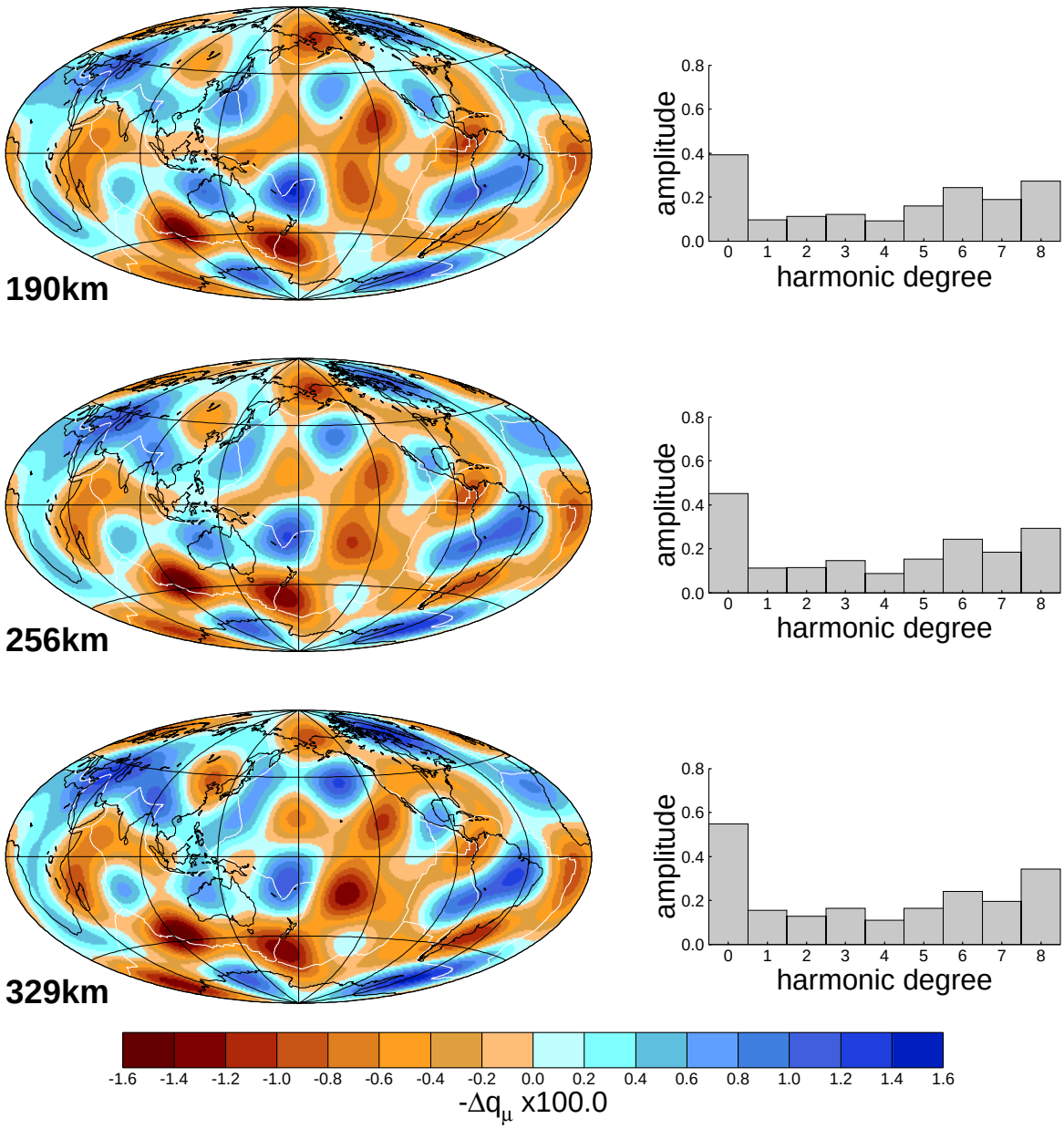


Figure 6.20(b): Model MQSS: $SS - S$ attenuation model for depths 190-329 km

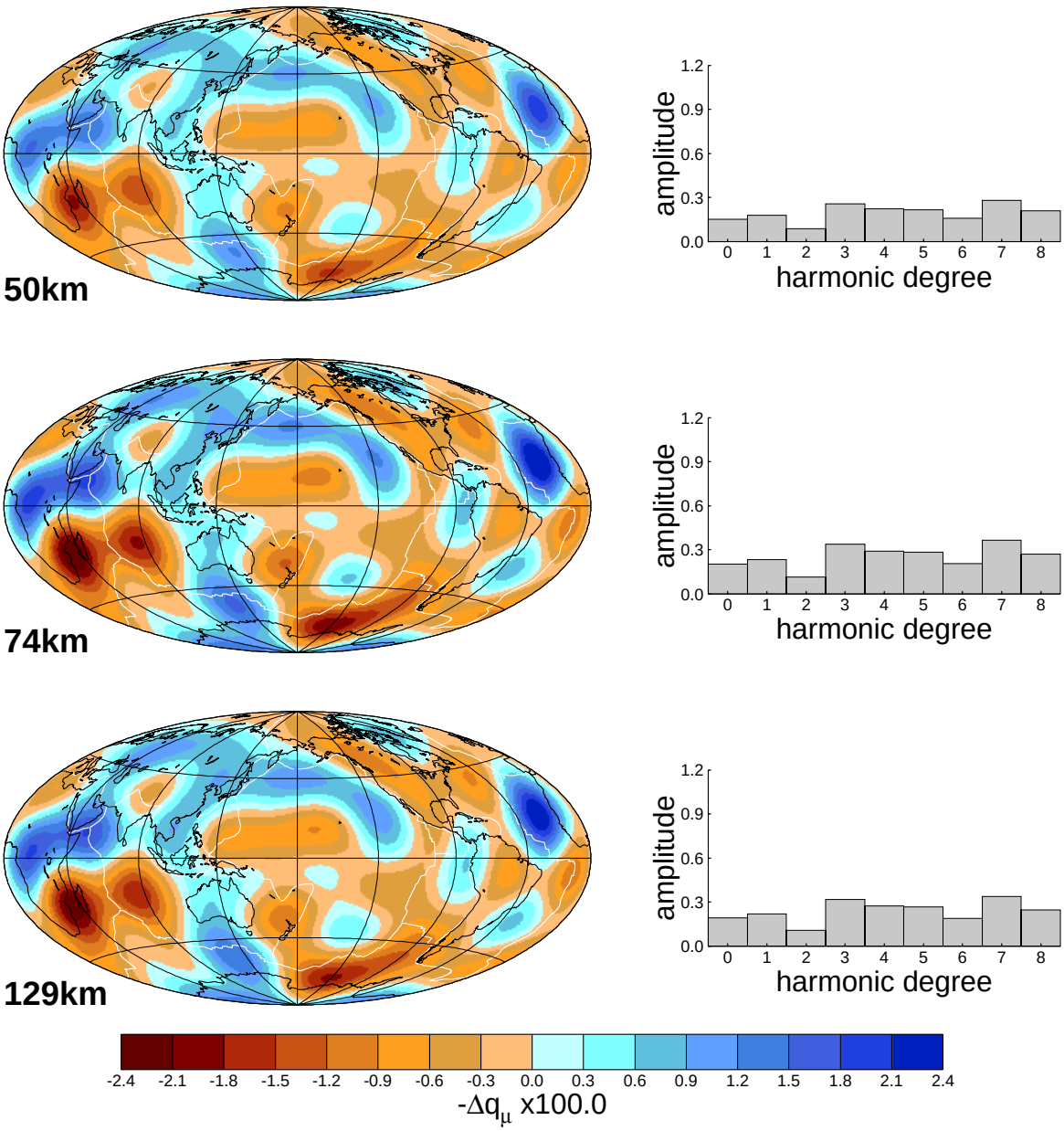


Figure 6.21(a): Model MQSSS: $SSS - SS$ attenuation model for depths 50-129 km

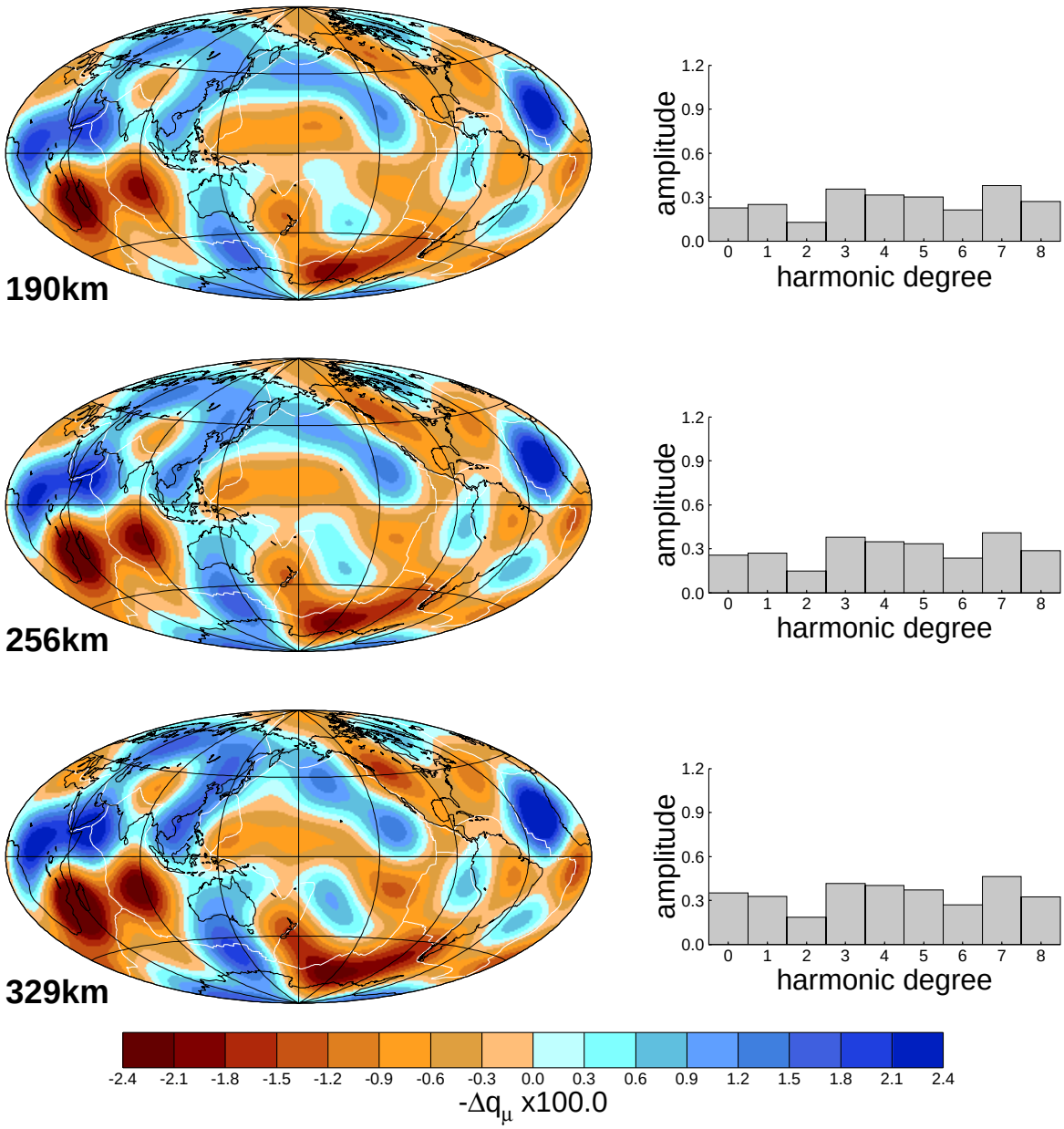


Figure 6.21(b): Model MQSSS: $SSS - SS$ attenuation model for depths 190-329 km

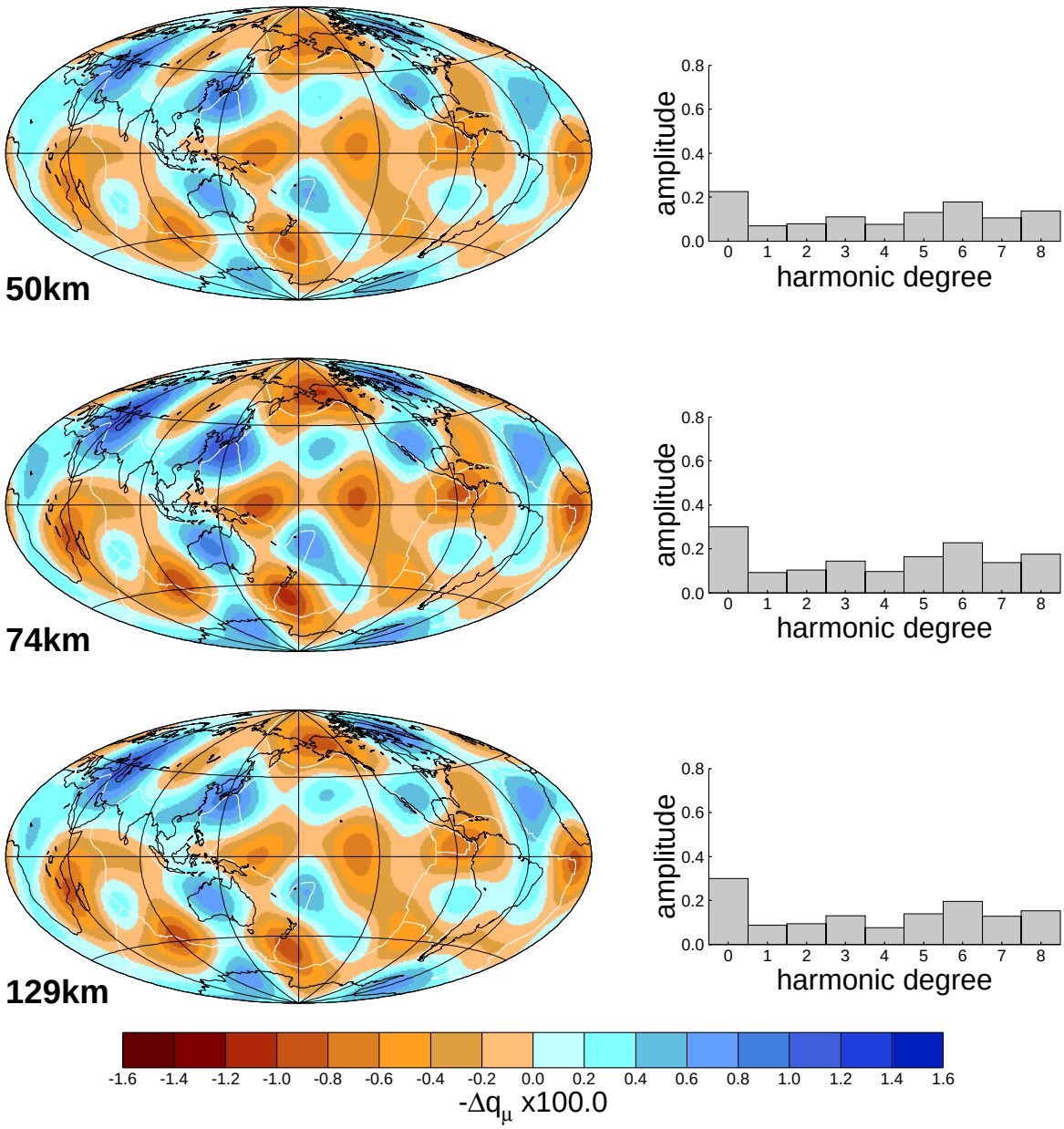


Figure 6.22(a): MQCOMB1: Combined attenuation model for depths 50-129 km

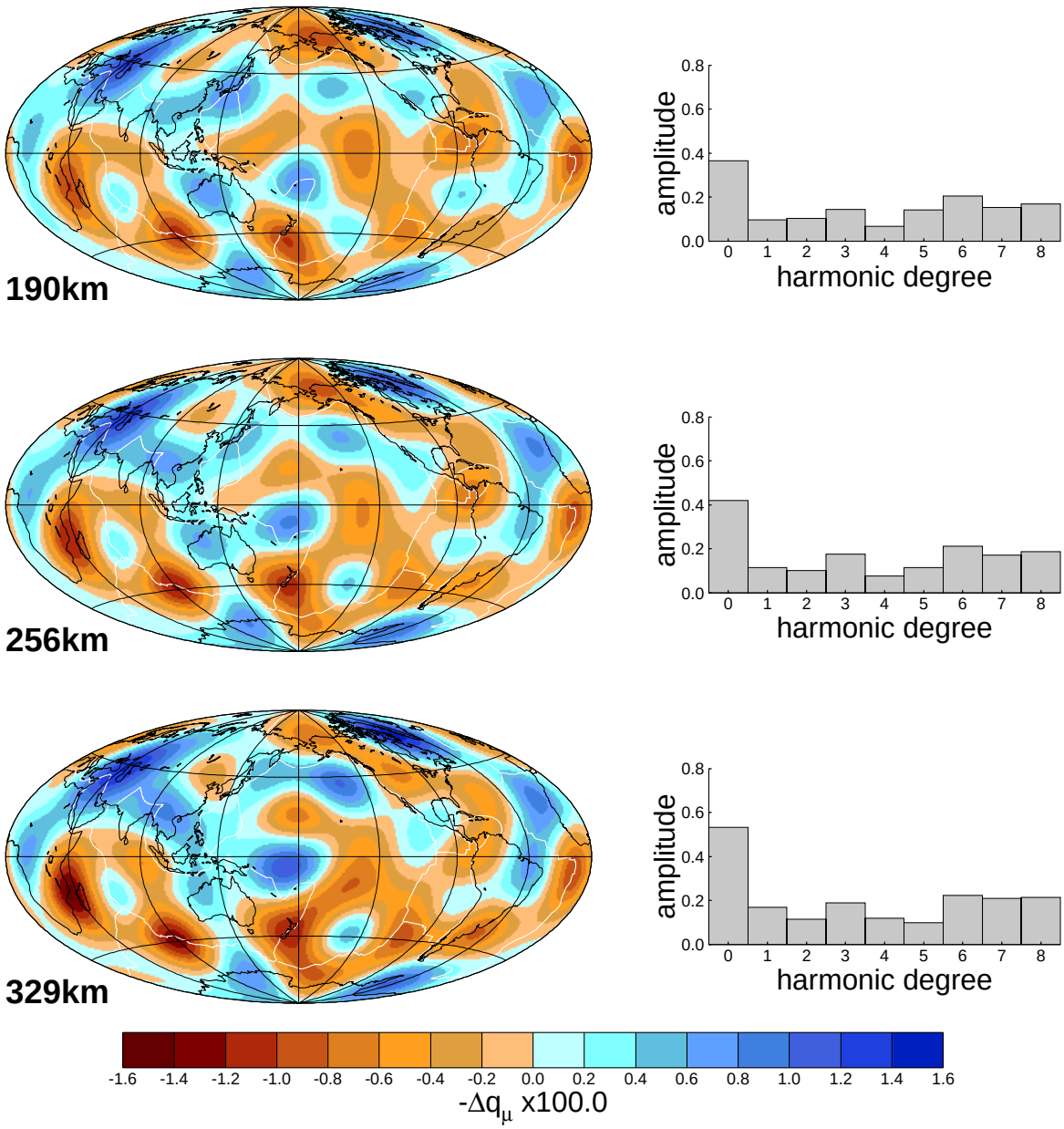


Figure 6.22(b): MQCOMB1: Combined attenuation model for depths 190-329 km

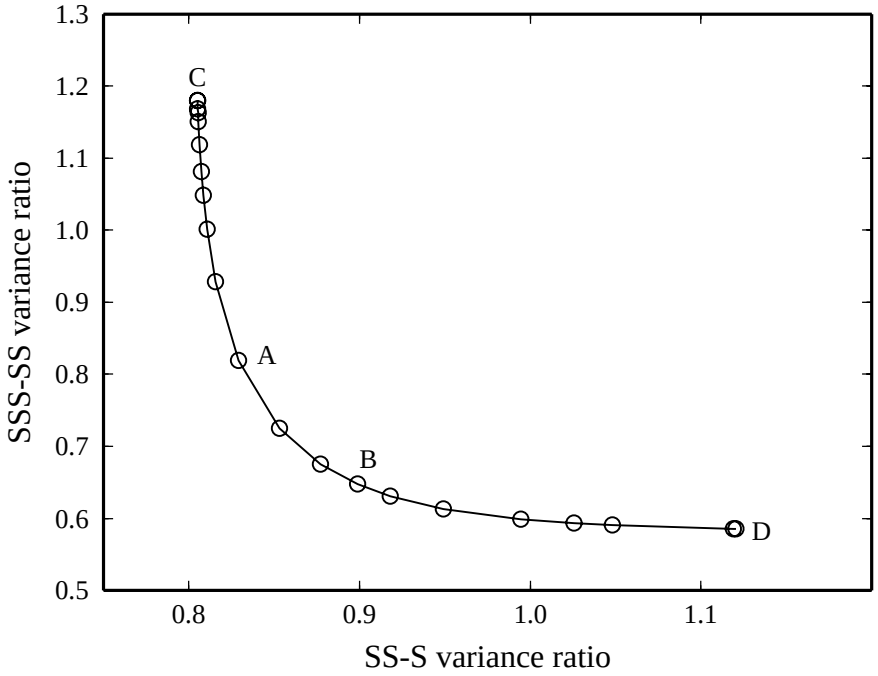


Figure 6.23: Variance ratio of $SS - S$ data against variance ratio of $SSS - SS$ data for the combined model for different weightings. Point A is the point of equal weighting. Point B is the point of equal improvement of the $SS - S$ and $SSS - SS$ variance ratios.

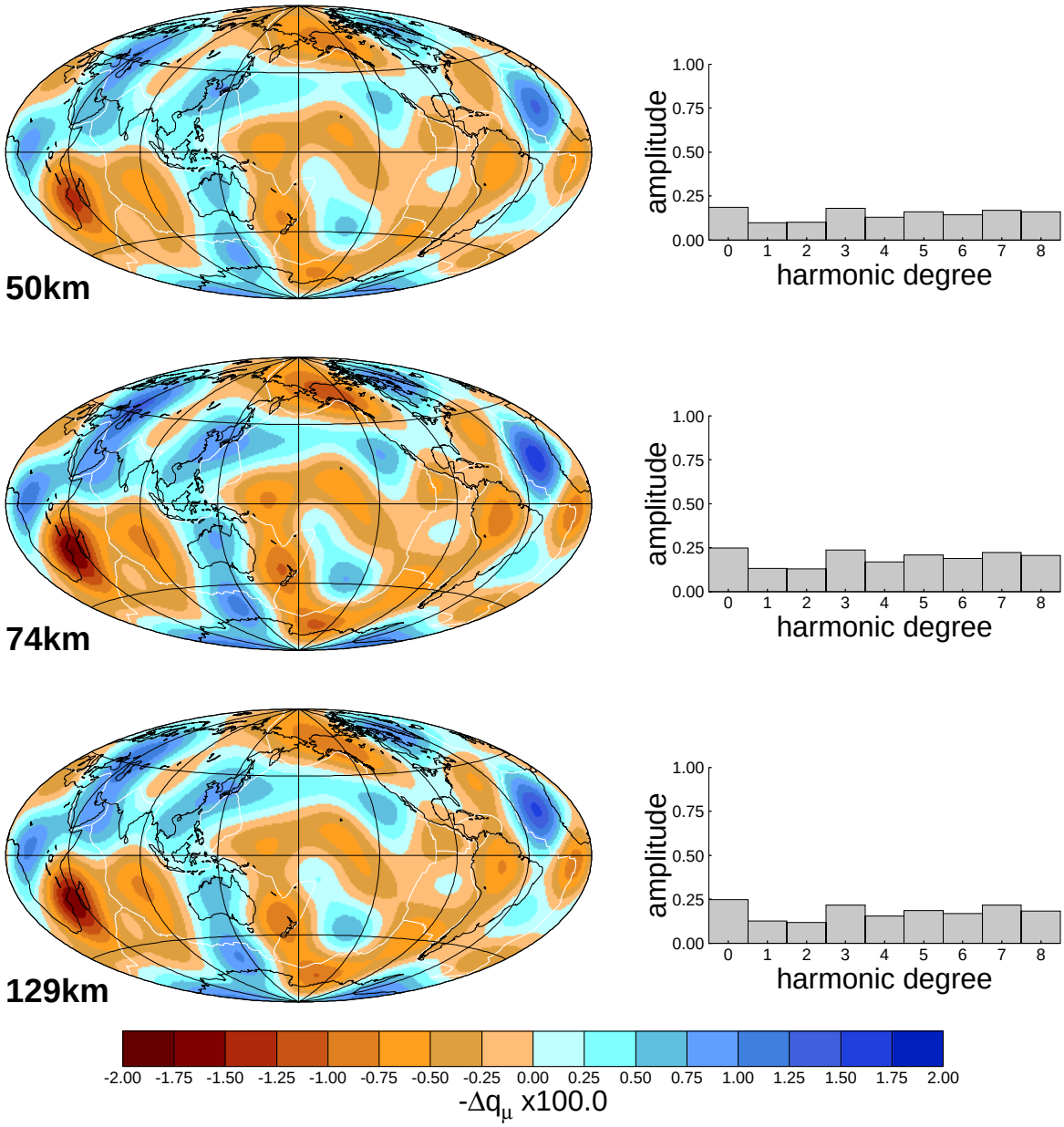


Figure 6.24(a): MQCOMB2: Combined attenuation model for depths 50-129 km. The weightings used are $w_1 = \frac{1}{2.5}$ and $w_2 = 1.0$

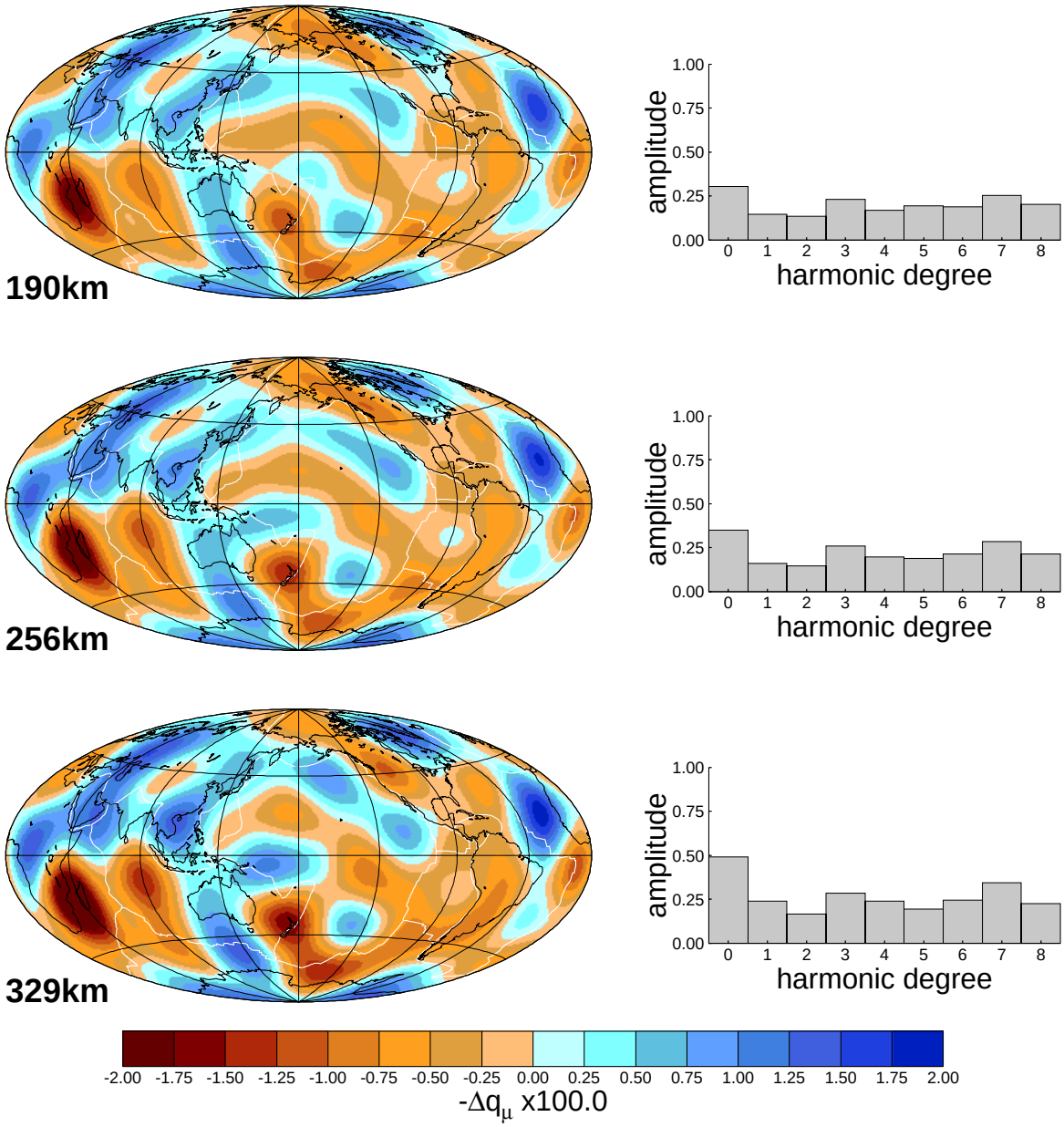


Figure 6.24(b): MQCOMB2: Combined attenuation model for depths 190-329 km. The weightings used are $w_1 = \frac{1}{2.5}$ and $w_2 = 1.0$

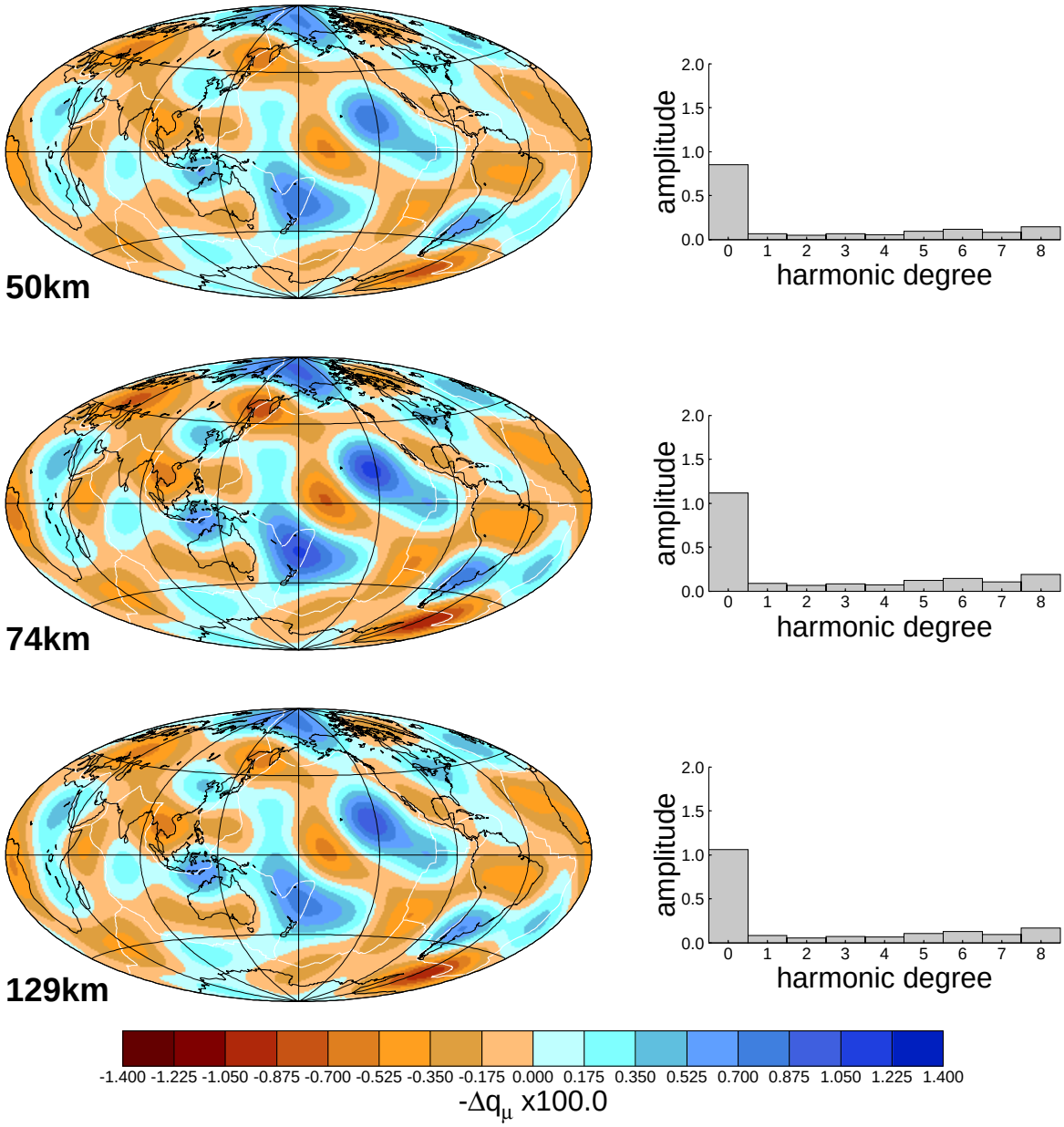


Figure 6.25(a): MQSRMSS: $SS - S$ attenuation model from spectral ratio measurements for depths 50-129 km

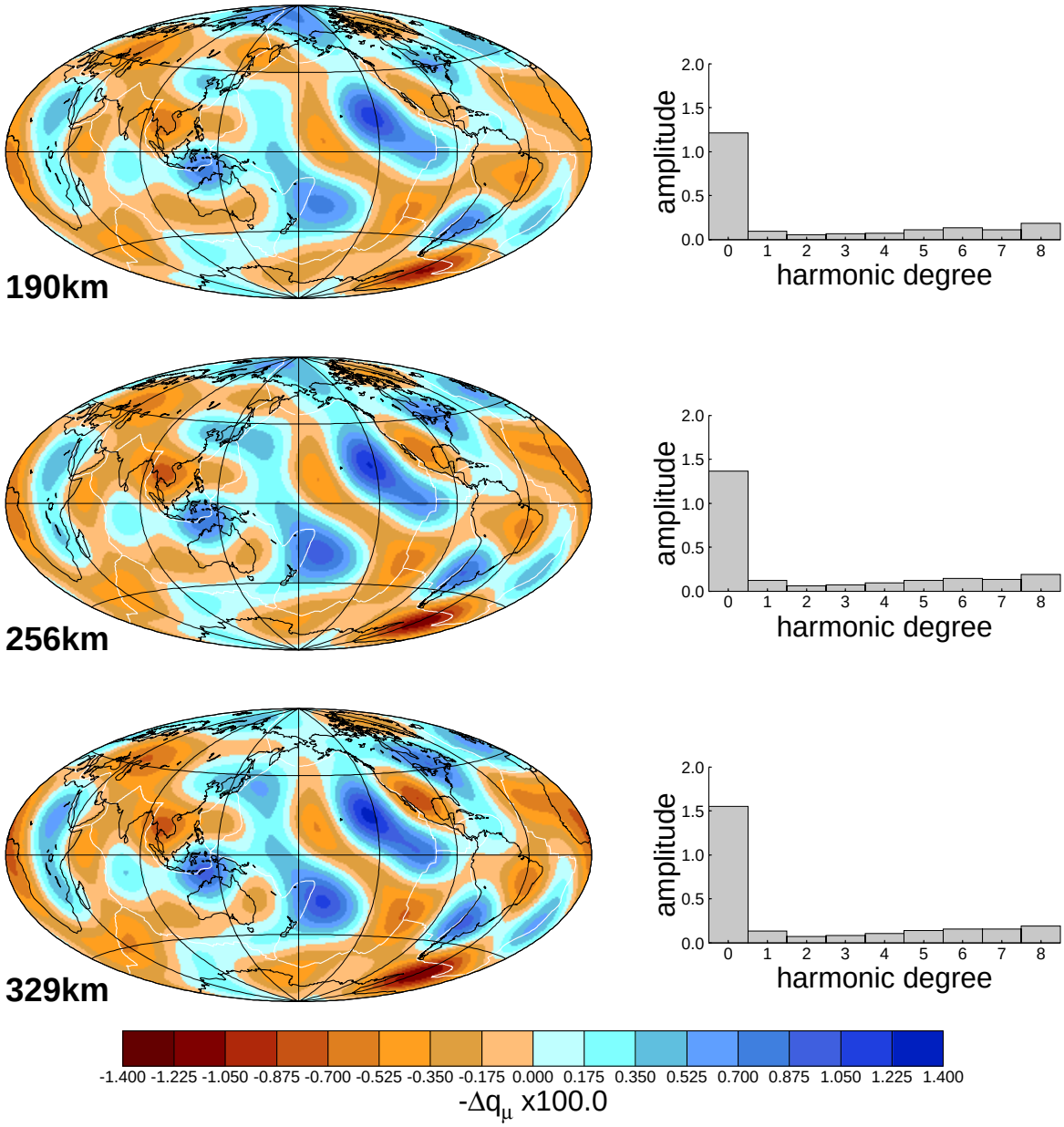


Figure 6.25(b): MQSRMSS: $SS - S$ attenuation model from spectral ratio measurements for depths 190-329 km

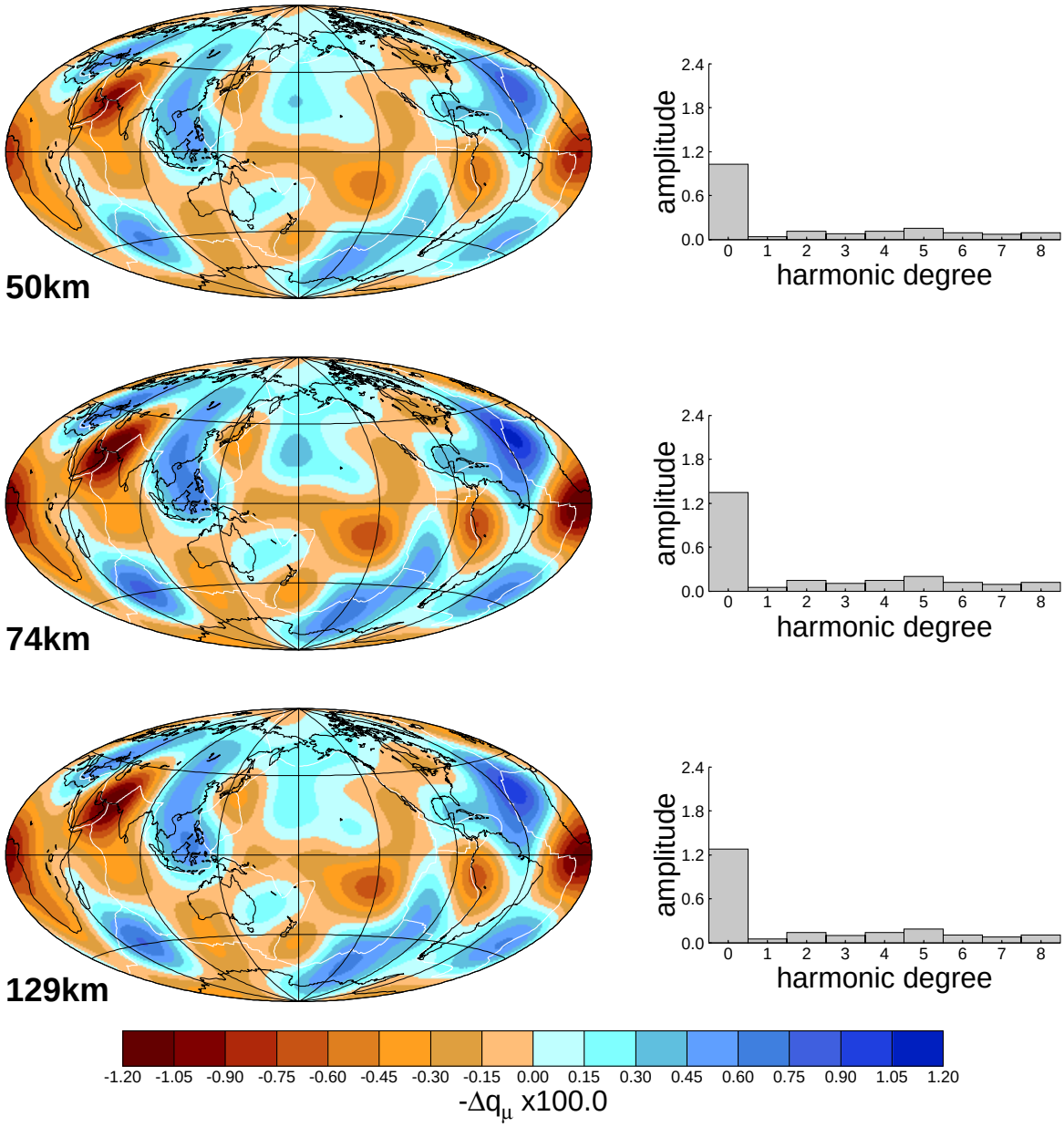


Figure 6.26(a): MQSRMSSS: $SSS-SS$ attenuation model from spectral ratio measurements for depths 50-129 km

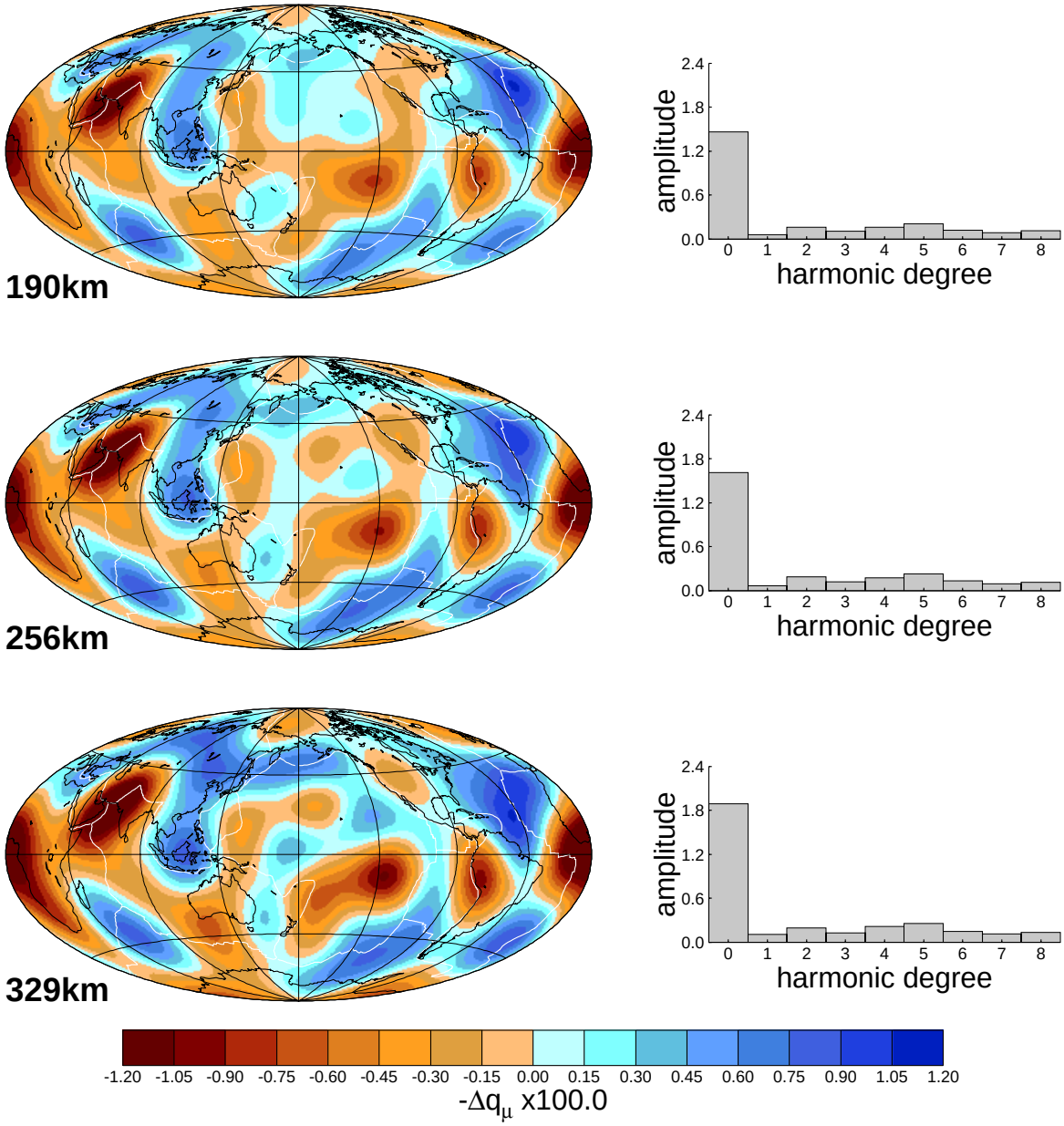


Figure 6.26(b): MQSRMSSS: $SSS - SS$ attenuation model from spectral ratio measurements for depths 190-329 km

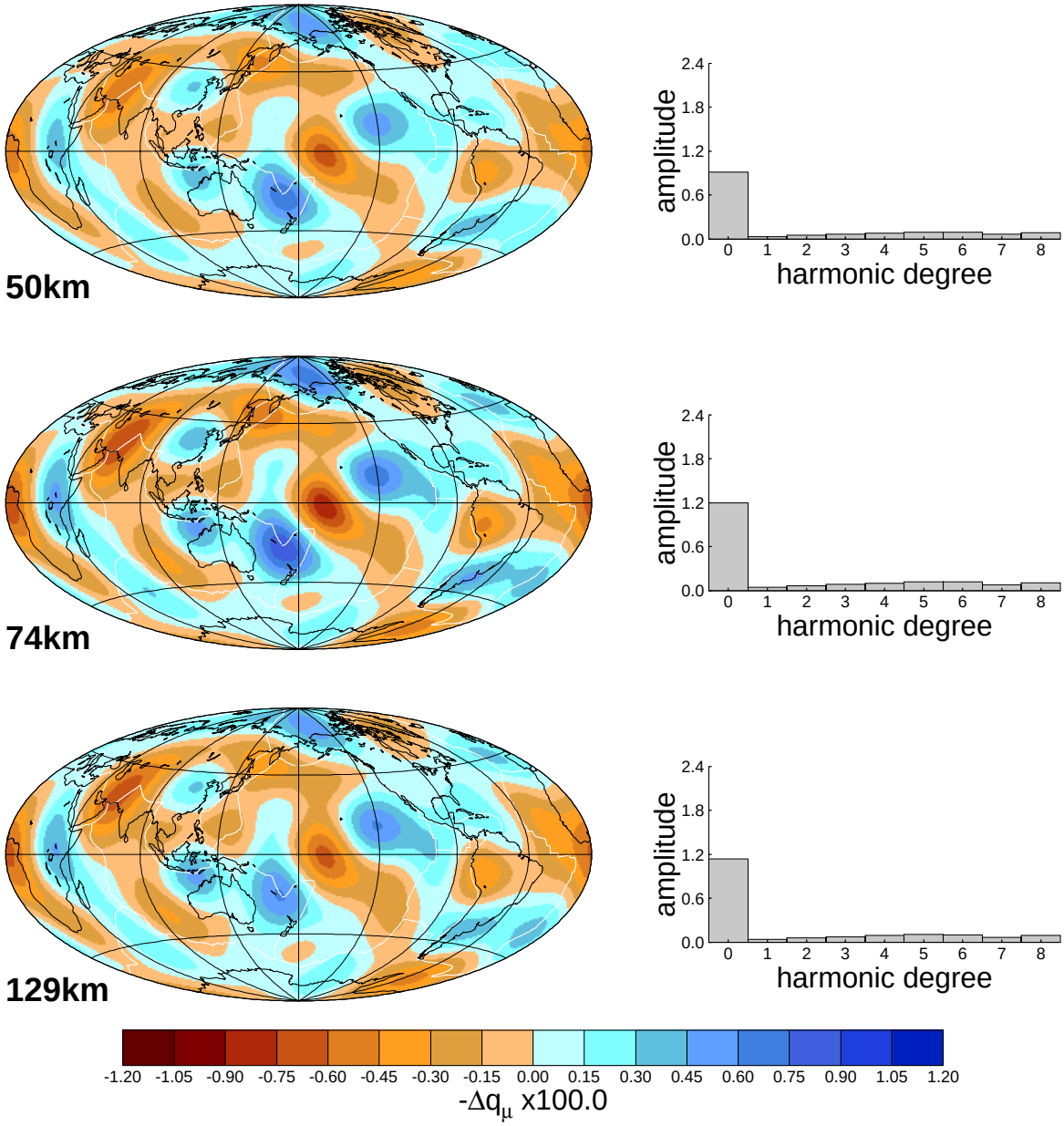


Figure 6.27(a): MQSRMCOMB1: Combined attenuation model from spectral ratio measurements for depths 50-129 km

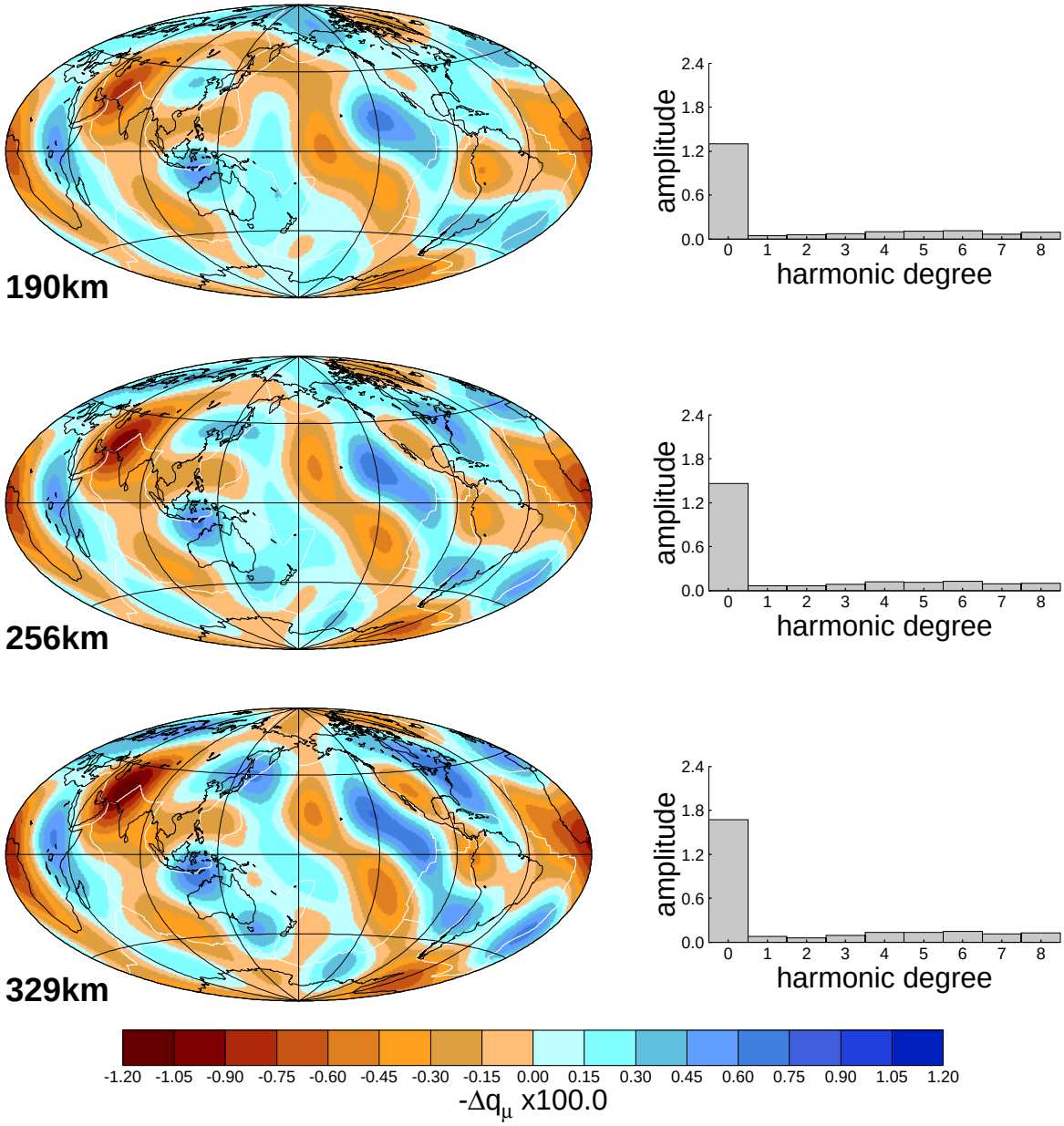


Figure 6.27(b): MQSRMCOMB1: Combined attenuation model from spectral ratio measurements for depths 190-329 km

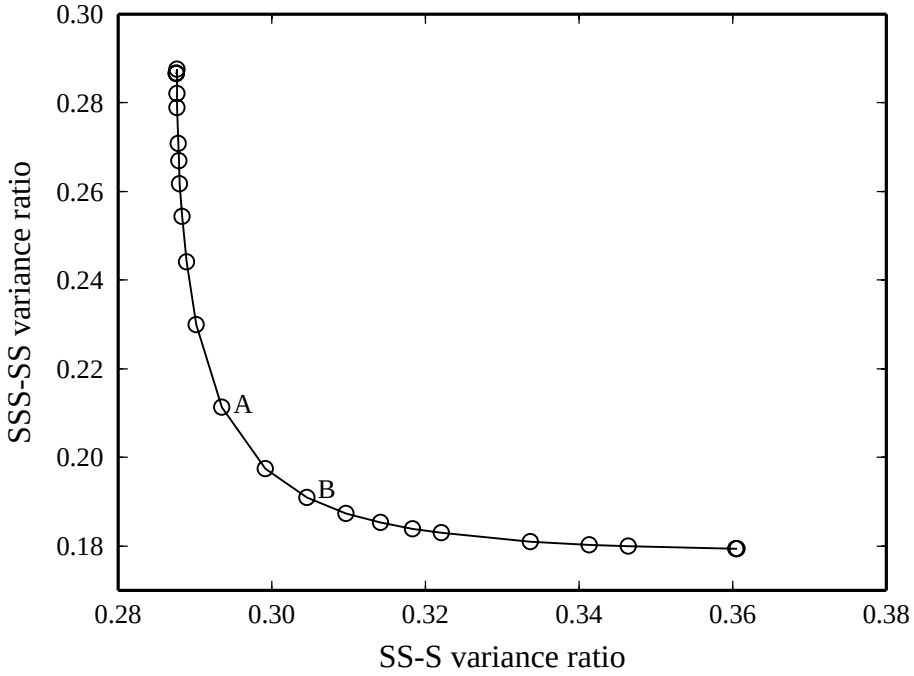


Figure 6.28: Variance ratio of $SSS - SS$ data against variance ratio of $SS - S$ data for the combined model. Point A indicates equal weighting of the two datasets. Point B indicates the point of equal improvement for the variance ratios of the $SS - S$ and $SSS - SS$ datasets.

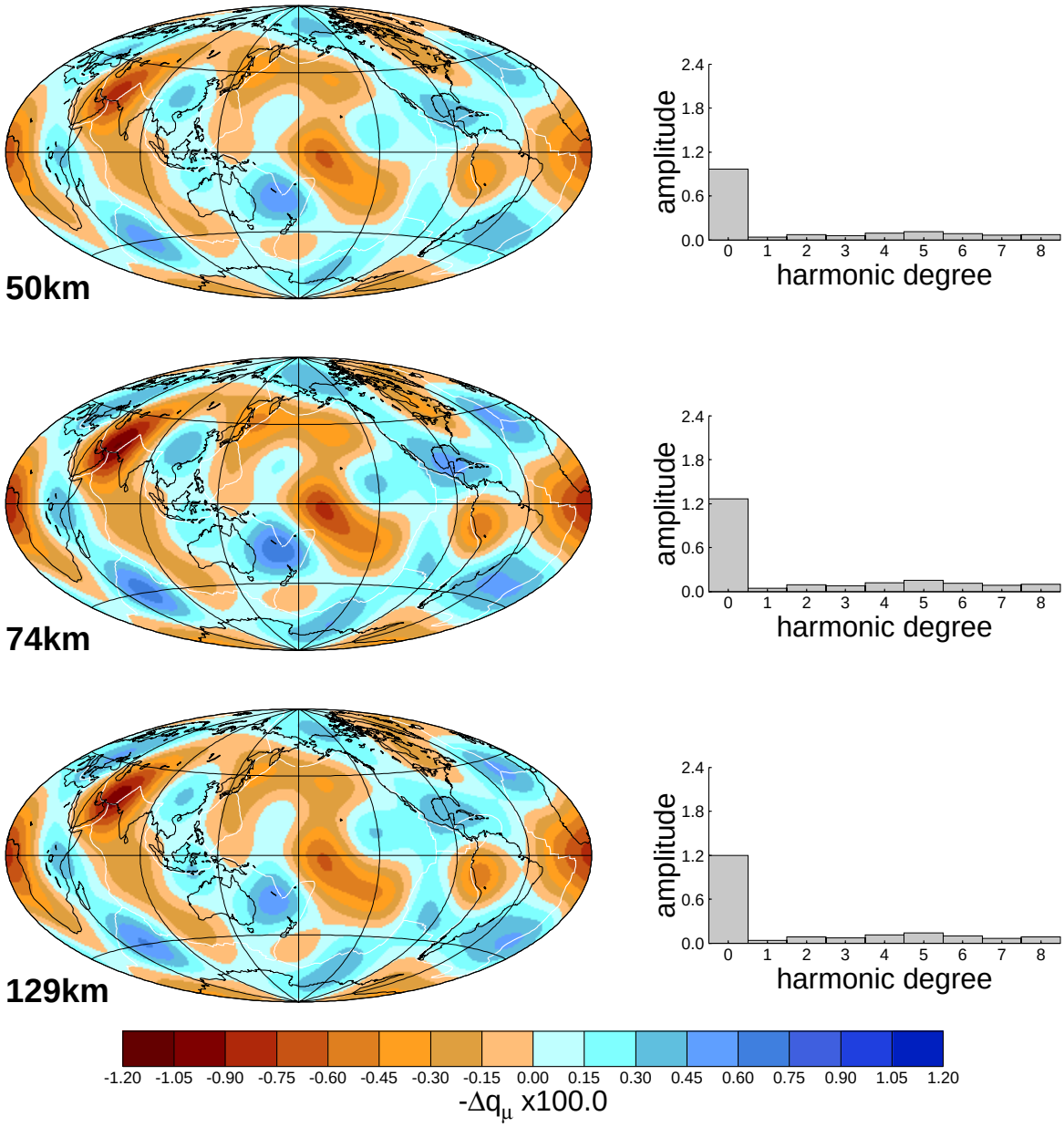


Figure 6.29(a): MQSRMCOMB2: Combined attenuation model from spectral ratio measurements for 50-129 km. The weightings used are $w_1 = \frac{1}{2.0}$ and $w_2 = 1.0$

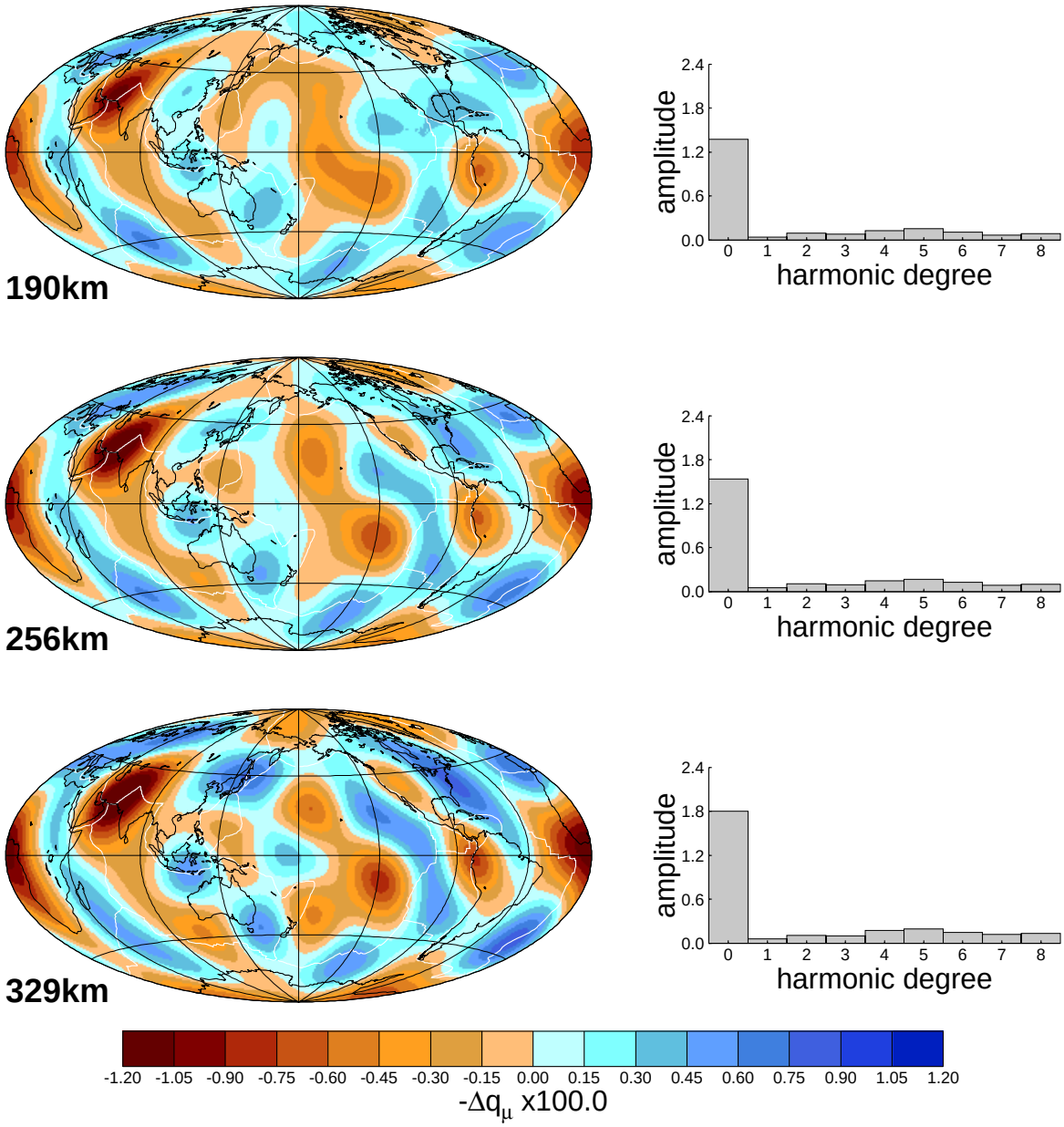


Figure 6.29(b): MQSRMCOMB2: Combined attenuation model from spectral ratio measurements for 50-129 km. The weightings used are $w_1 = \frac{1}{2.0}$ and $w_2 = 1.0$

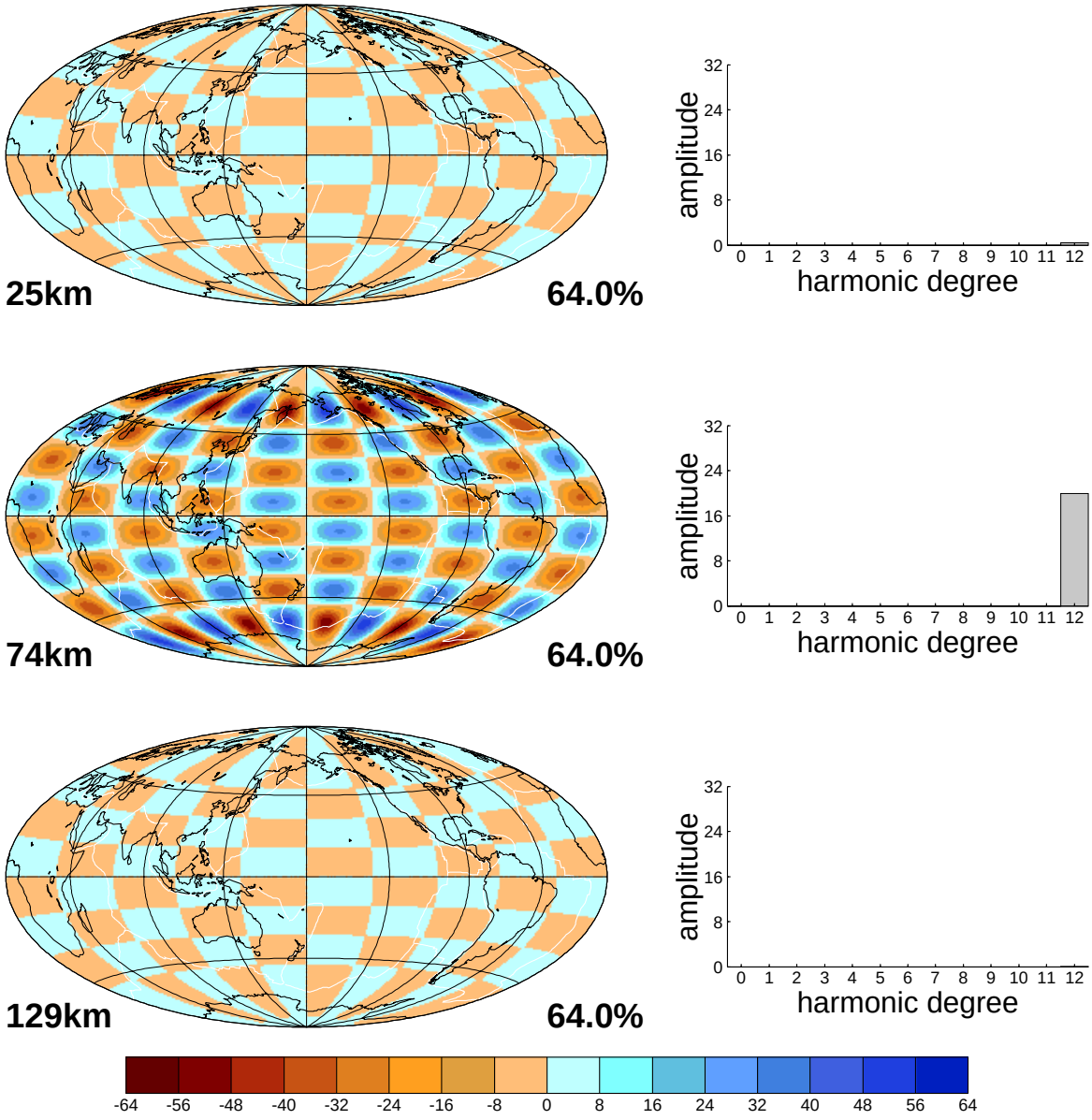


Figure 6.30(a): Input checkerboard pattern at 74 km for depths 25-129 km

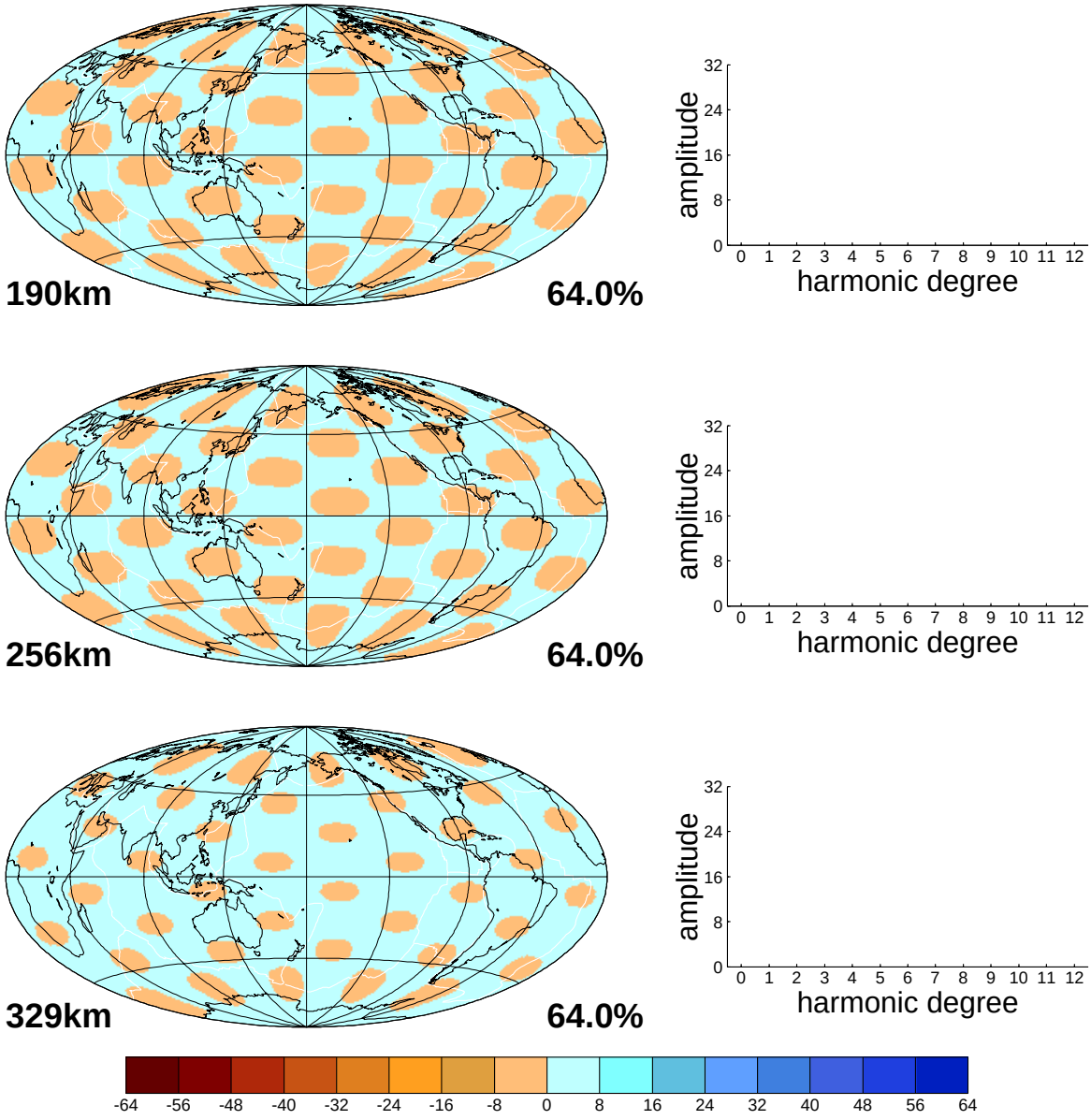


Figure 6.30(b): Input checkerboard pattern at 74 km for depths 190-329 km

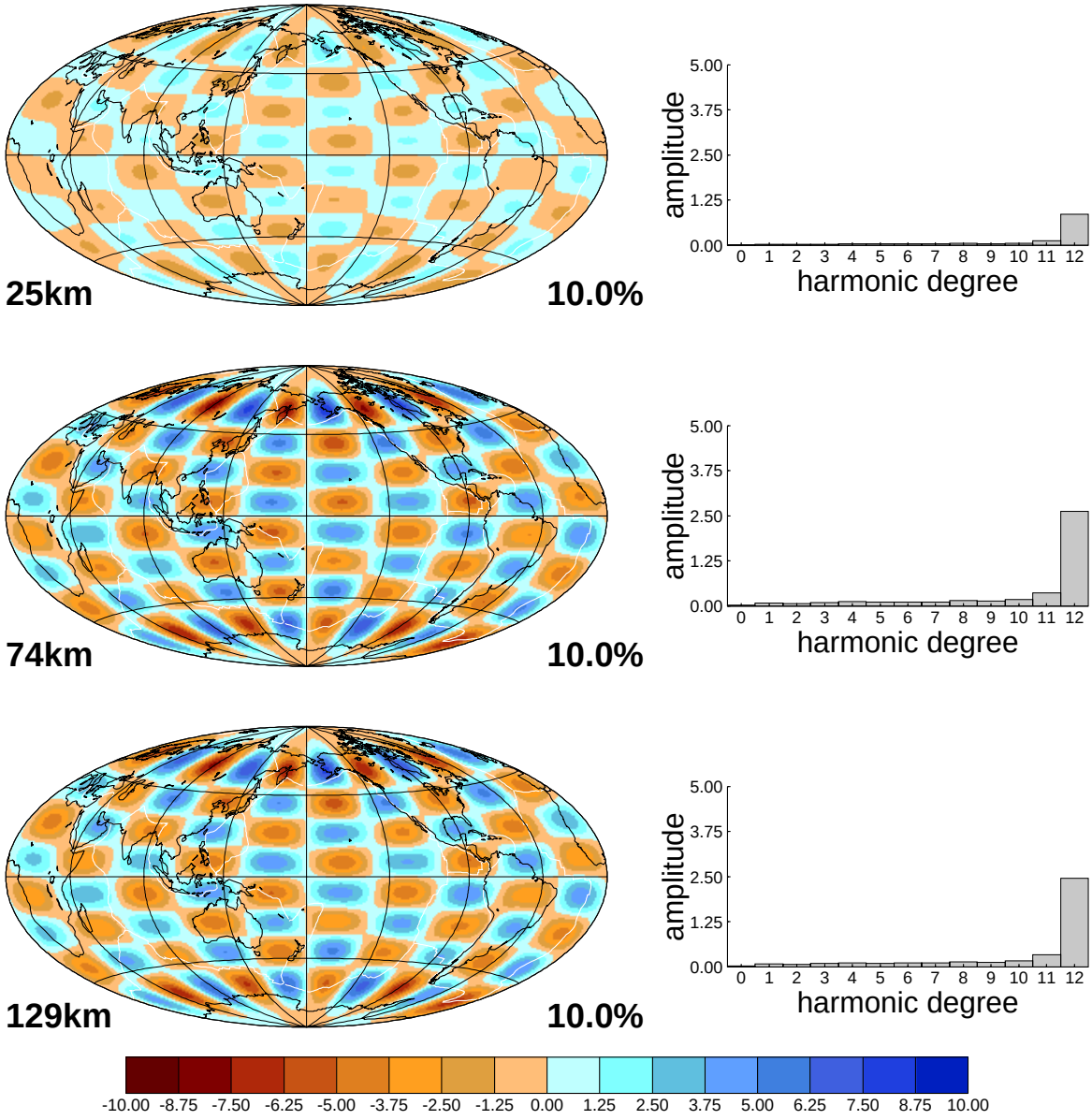


Figure 6.31(a): Output for $SS - S$ dataset for depths 25-129 km

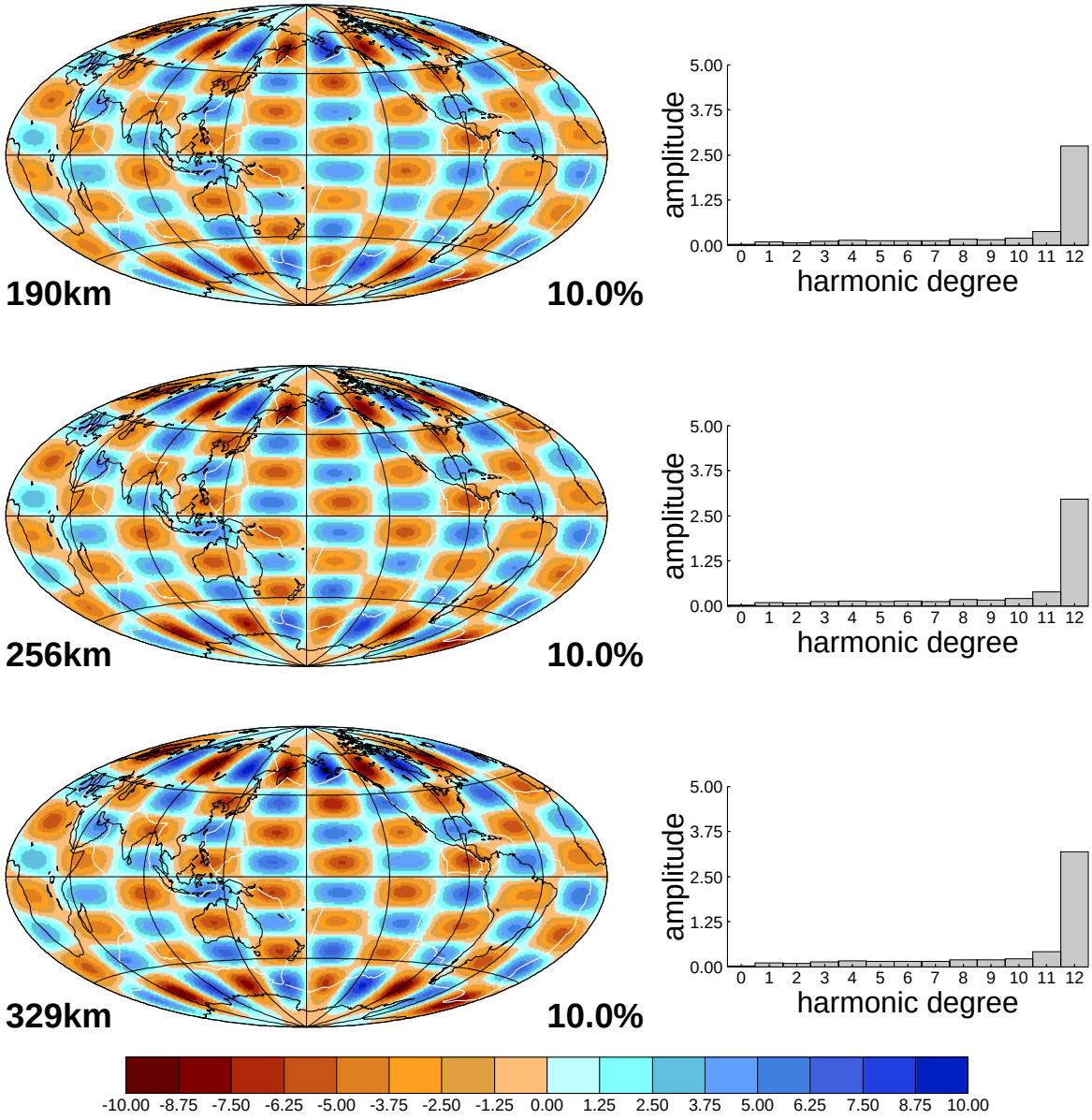


Figure 6.31(b): Output for $SS - S$ dataset for depths 190-329 km

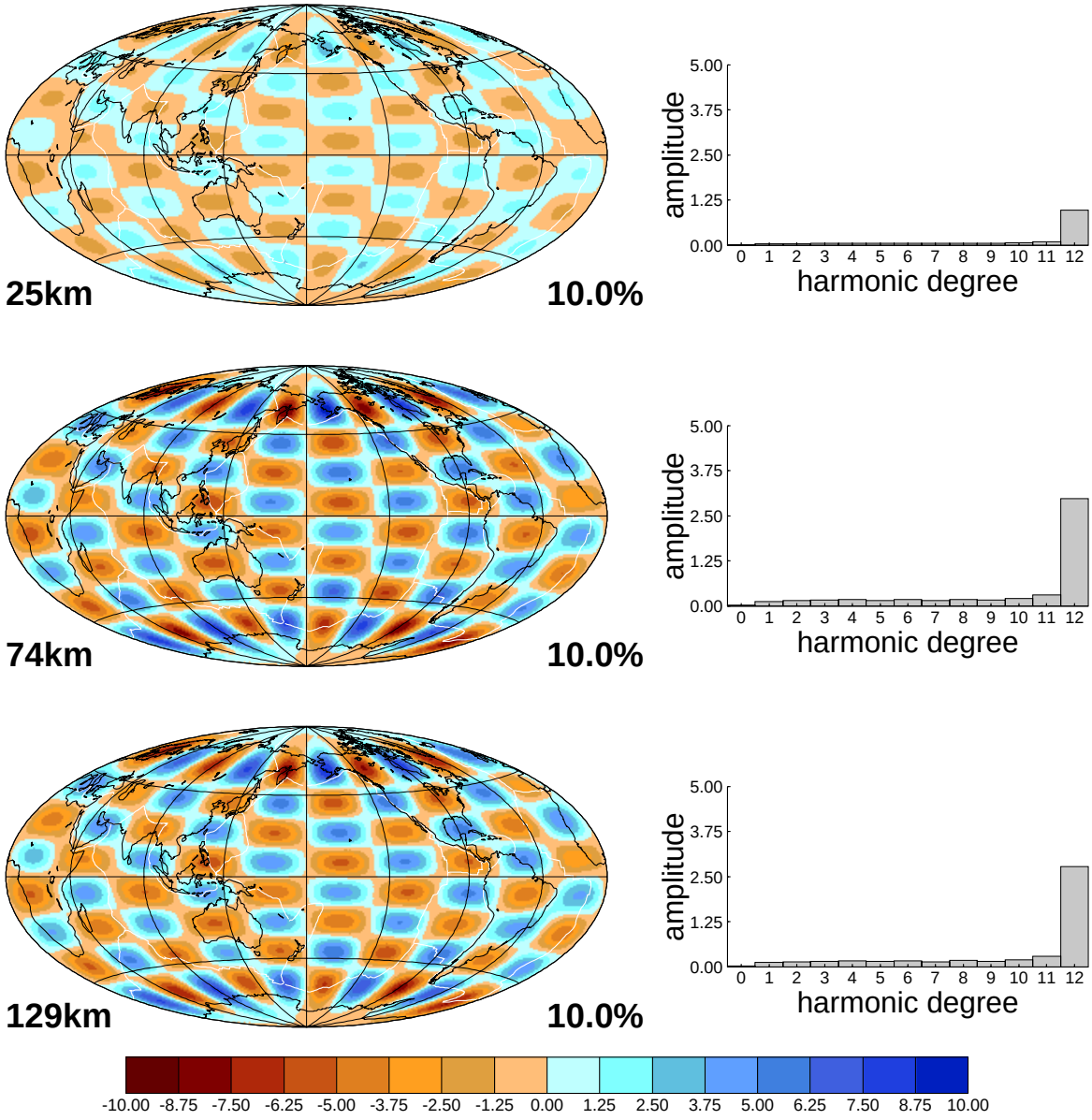


Figure 6.32(a): Output for $SSS - SS$ dataset for depths 25-129 km

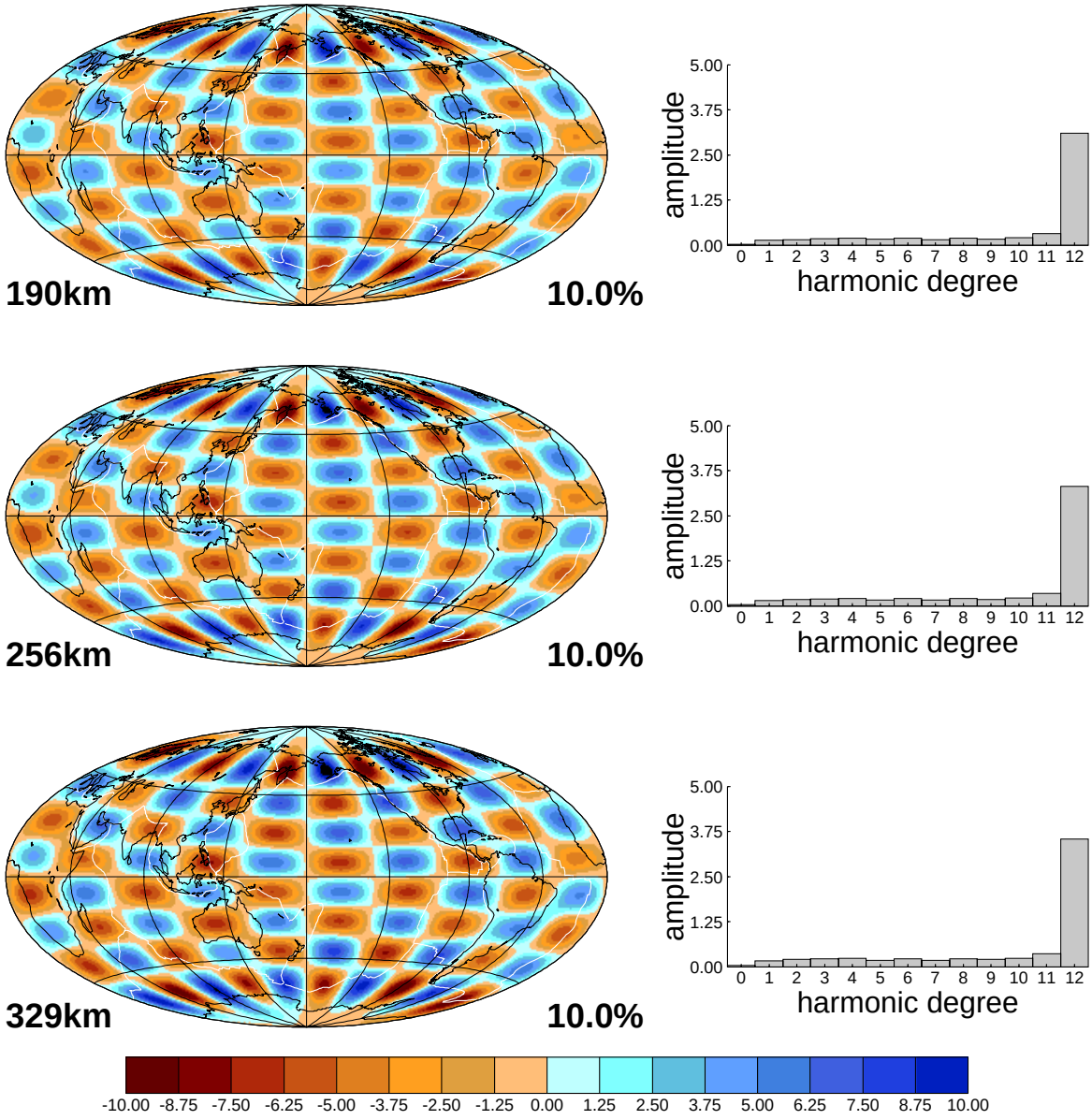


Figure 6.32(b): Output for $SSS - SS$ dataset for depths 190-329 km

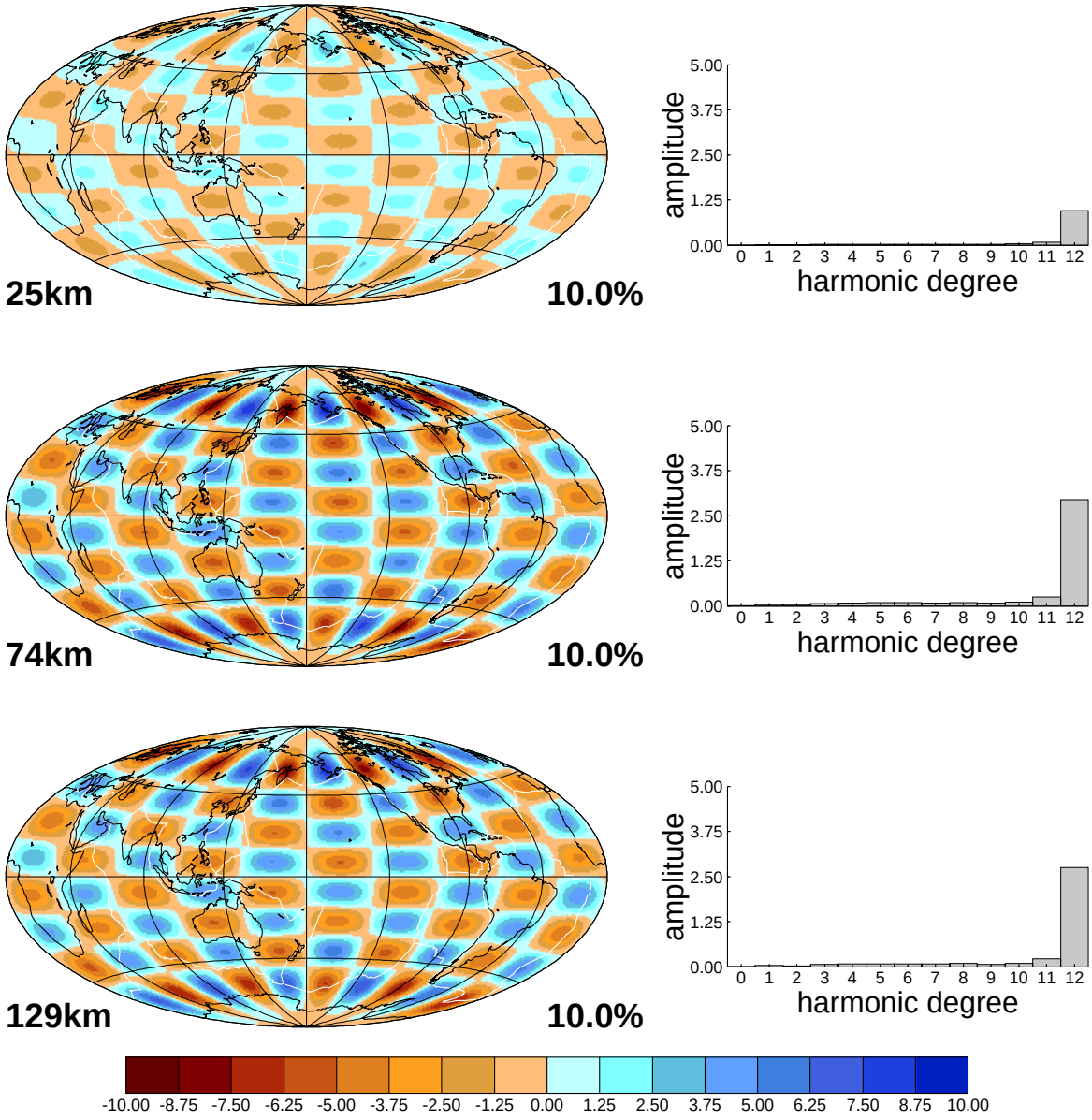


Figure 6.33(a): Output for combined dataset for depths 25-129 km

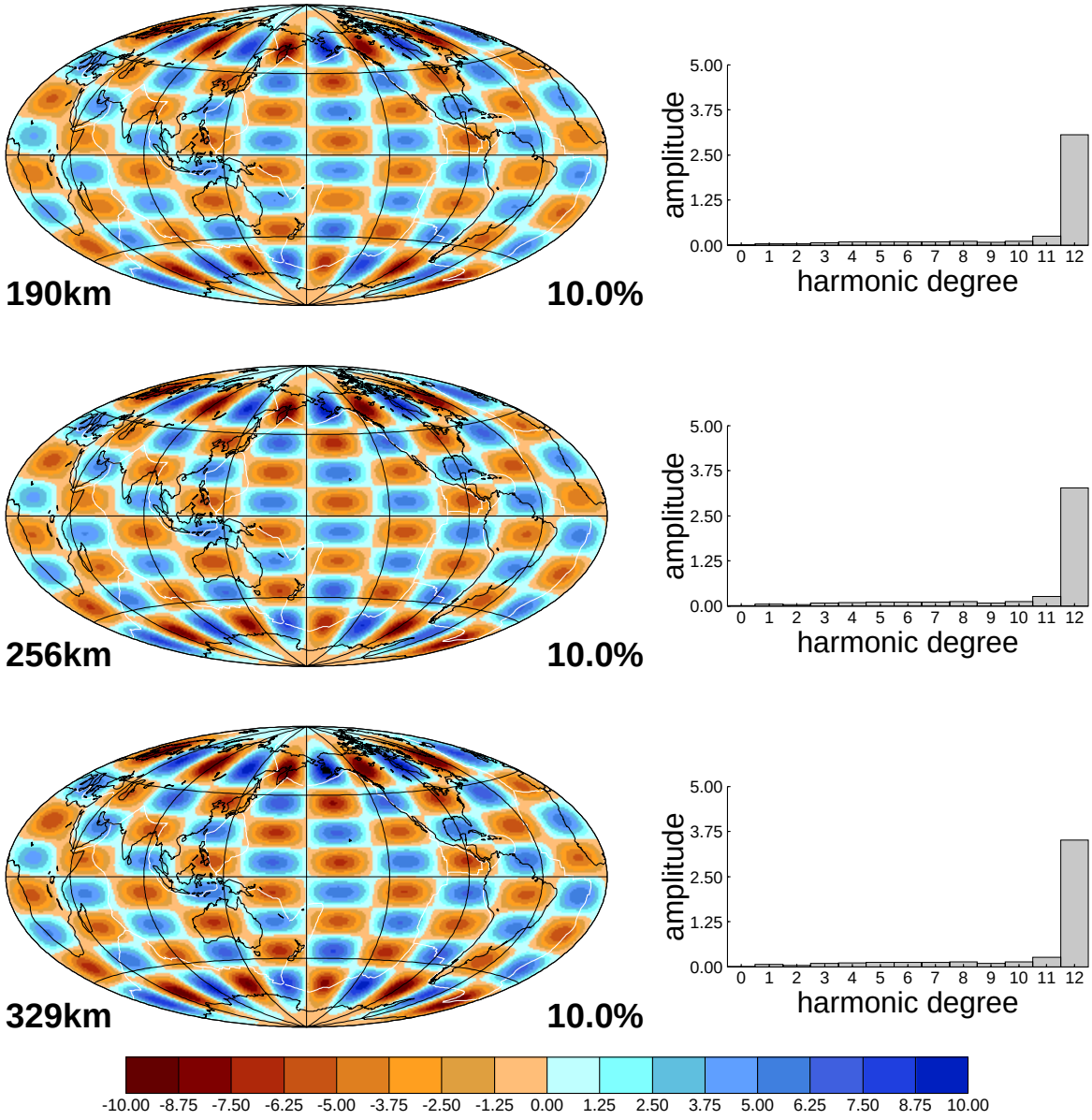


Figure 6.33(b): Output for combined dataset for depths 190-329 km

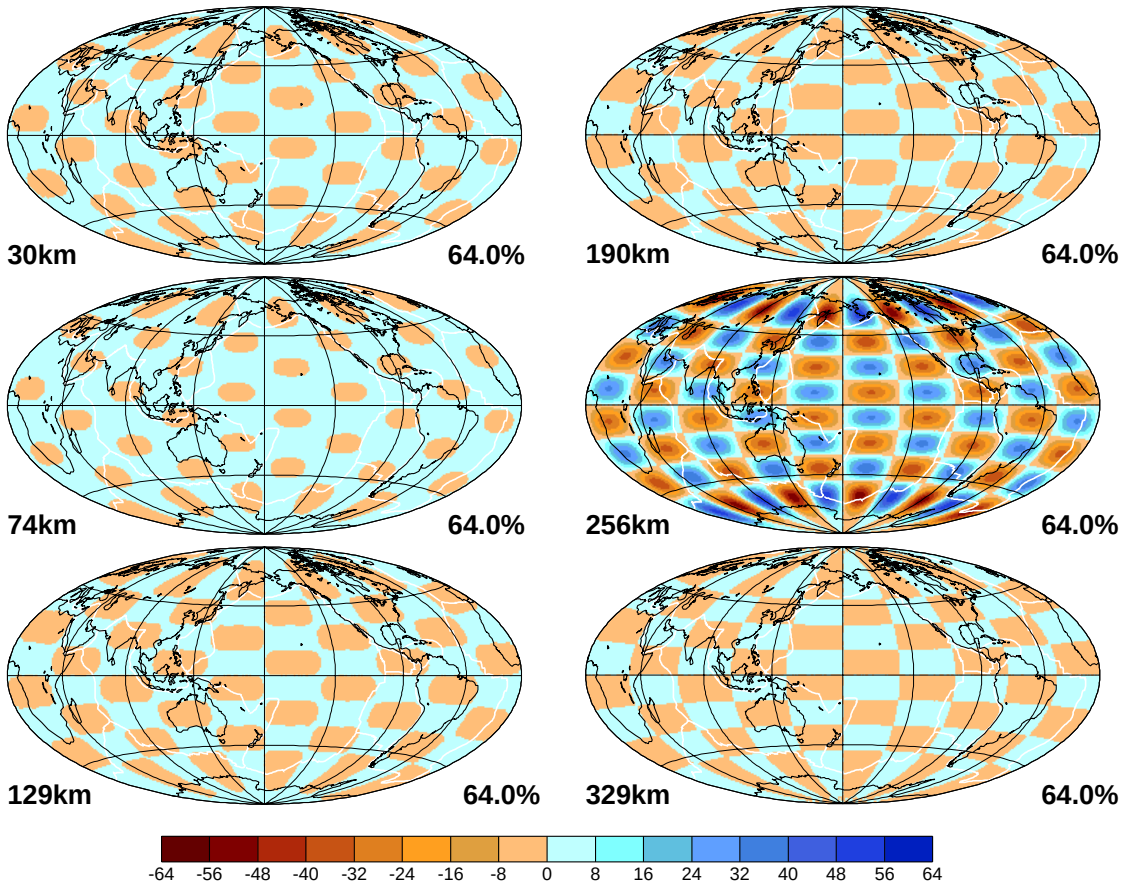


Figure 6.34: Input checkerboard at 256km for depths 30-329 km

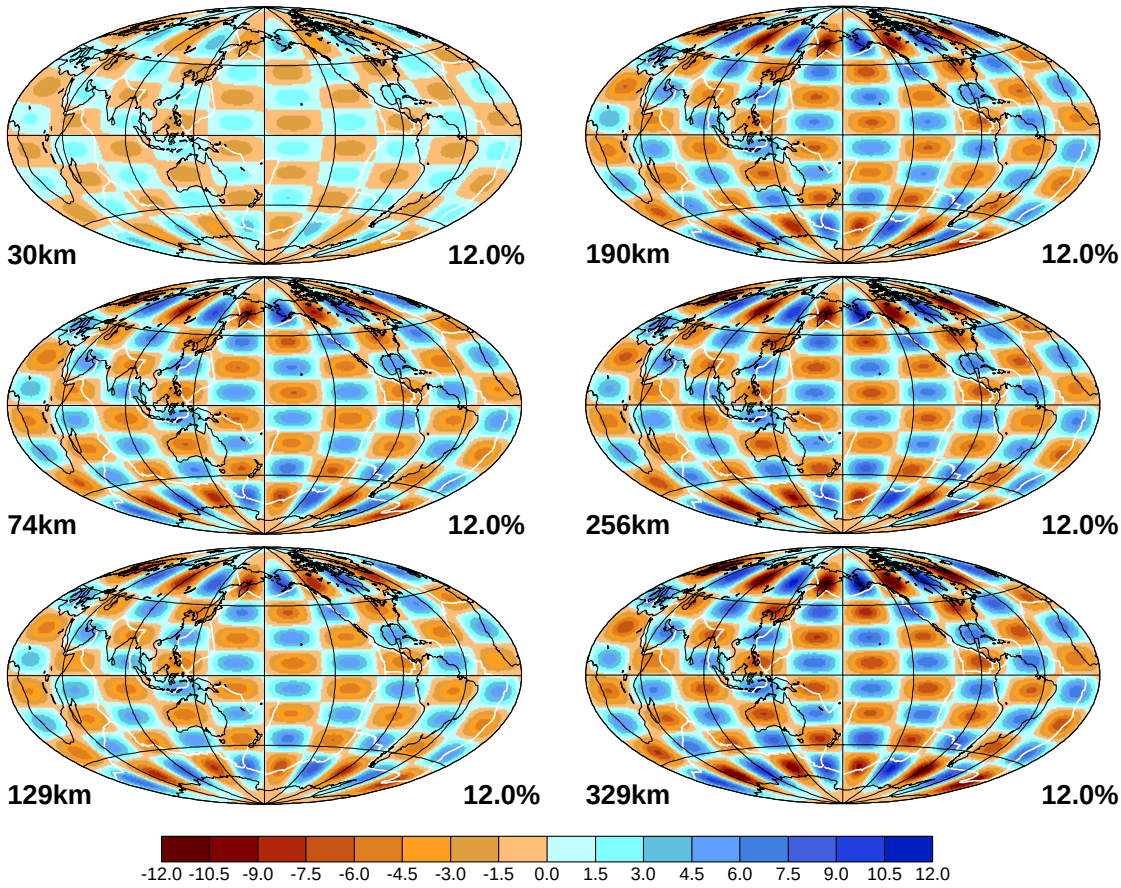


Figure 6.35: Output for combined dataset for depths 30-329 km

Chapter 7

Combining body wave and surface wave measurements

The models presented in Chapter 6 are constructed using only a small number of measurements. For example the $SSS - SS$ velocity model is constucted from only 386 travel time residuals. Clearly this number of points is insufficient to obtain a detailed model and this is why we combine the $SSS - SS$ and $SS - S$ datasets. Combination of the two datasets allows greater confidence to be assigned to the resulting model as it has been constructed from data of more than one type. This principle can be extended to include other data types. In this chapter models combining body wave and surface wave data are presented. Section 7.1 presents the model resulting from combining the t^* residuals obtained from the waveform fitting method with the surface wave dataset of Selby (1998). Section 7.2 presents the velocity model obtained by combining the travel time residuals with surface wave measurements of Van Heijst (1997).

7.1 Attenuation model from body wave and surface wave data

In this section the initial attempts at combining body wave and surface wave data to obtain a joint attenuation model are presented. An earlier attempt at combining body wave and surface wave data has been made by Bhattacharyya *et al.* (1996) and Bhattacharyya (1996). Figure 8.12 shows the model resulting from these studies. Subsequently Selby (1998) combined the $SS - S$ data of this thesis with minor and major arc fundamental mode Rayleigh waves in the period range 70-170 s to obtain a combined q_μ model.

The method is similar to that described in Chapter 9 of Selby (1998). However we attempt to improve the resulting model by inclusion of the $SSS - SS$ body wave data. We also examine the effects of inequality of the degree zero terms which are not accounted for by Selby (1998). The combined model is calculated for spherical harmonics up to degree 8 over the top 6 depth splines. The

means of the body wave datasets are removed before inversion. We invert for the combined model as follows:

1. Calculate separately $\boldsymbol{A_b}^T\boldsymbol{A_b}$, $\boldsymbol{A_b}^T\boldsymbol{d_b}$ and $\boldsymbol{A_s}^T\boldsymbol{A_s}$, $\boldsymbol{A_s}^T\boldsymbol{d_s}$ where $\boldsymbol{A_b}$ and $\boldsymbol{A_s}$ are the derivative matrices for the body wave and surface wave datasets respectively. $\boldsymbol{d_b}$ and $\boldsymbol{d_s}$ are the body wave and surface wave data respectively.

2. Calculate the $\boldsymbol{A}^T\boldsymbol{A}$ matrix from: $\boldsymbol{A}^T\boldsymbol{A} = w_b(\boldsymbol{A_b}^T\boldsymbol{A_b}) + w_s(\boldsymbol{A_s}^T\boldsymbol{A_s})$. This is possible because $\boldsymbol{A_b}^T\boldsymbol{A_b}$ and $\boldsymbol{A_s}^T\boldsymbol{A_s}$ have the same dimensions.

3. Calculate the $\boldsymbol{A}^T\boldsymbol{d}$ matrix from: $\boldsymbol{A}^T\boldsymbol{d} = w_b(\boldsymbol{A_b}^T\boldsymbol{d_b}) + w_s(\boldsymbol{A_s}^T\boldsymbol{d_s})$.

4. Invert $\boldsymbol{A}^T\boldsymbol{A}$ using various weights (see below) to determine which model best fits both surface wave and body wave data. The method of inversion is identical to that used in Chapter 6 apart from this additional weighting.

The weighting used is:

$$w_s = \eta \qquad w_b = (1 - \eta) \tag{7.1}$$

where w_b is the weighting applied to the body wave dataset and w_s is the weighting applied to the surface wave dataset. The value of η varies between 0 and 1 where $\eta = 0$ corresponds to using body wave data only and $\eta = 1$ corresponds to using surface wave data only. Figure 7.1 shows the variance ratios obtained for the body wave and surface wave datasets for a range of weightings. The L-shape of the curve indicates that there is some compatibility between the two datasets. On Figure 7.1, point b corresponds to a model calculated from body wave data alone i.e. for $\eta = 0$. Point a corresponds to a model calculated from surface wave data only, i.e. $\eta = 1$. Point c is the point at which the best compromise between the two datasets is reached (Section 6.9.3 provides a more detailed explanation of this type of plot). From examination of Figure 7.1 it is clear that the behaviour of the models is not symmetric: the surface wave dataset does not succeed in fitting the body wave data. The reason for this asymmetry is that the degree 0 or spherical components of the two models are not identical. To investigate this we calculate the variance ratios for the body wave and surface wave datasets with the degree zero term removed. This results in another L-shaped curve shown by Figure 7.2, which is more symmetric in appearance than Figure 7.1. Again point c marks the "best" model. Figure 7.3 shows the model obtained using the weightings given by point c of Figure 7.1. Figure 7.4 shows the model obtained using the weightings given by point c of Figure 7.2. The models shown by Figures 7.3 and Figure 7.4 are extremely similar except that the amplitude of anomalies in Figure 7.4 is slightly larger. The model shown by Figure 7.4 is subsequently referred to as model MQBS.

Model MQBS shows a pattern of attenuation which is correlated with the ocean-continent pattern. Low attenuation is observed across the continents and high attenuation is observed across many oceanic regions. We also observe some correlation of high attenuation with the distribution of hot-spots. It is encouraging to see that combining the two datasets has produced a model which is not that dissimilar

from the original body wave and surface wave models. The compatibility of the two datasets allows us to assign greater confidence to the resulting model. Since the body wave and surface wave data sample the Earth in different ways we can conclude that the signal observed is most likely to be due to attenuation and not to other factors, e.g. focusing or defocusing.

7.2 Velocity model from body wave and surface wave data

In this section we combine our body wave measurements with surface wave measurements from Van Heijst (1997). An earlier version of this model including only the $SS-S$ body wave data is presented in Van Heijst *et al.* (1998).

The body wave dataset is identical to that used for constructing model MVCOMB1 and consists of a total of 2921 measurements of differential travel time, 2535 from $SS-S$ measurements and 386 $SSS-SS$ measurements. Note that no weighting of the individual $SS-S$ and $SSS-SS$ datasets is performed. Both ellipticity and crustal corrections from CRUST 5.1 are applied to the travel time residuals.

The surface wave dataset consists of close to a million Rayleigh wave fundamental mode and overtone dispersion measurements that are made for minor arcs (Van Heijst, 1997) and major arcs. A full description of the measurement technique is given by Van Heijst (1997). The surface wave dataset is corrected for the effects of the crust using CRUST 5.1. Corrections for the Earth's ellipticity are also applied to the surface wave data before inversion.

The method for combining the two datasets is similar to that described by Section 7.1. Essentially the procedure is as follows:

1. Calculate $\boldsymbol{A_b}^T\boldsymbol{A_b}$ and $\boldsymbol{A_b}^T\boldsymbol{d_b}$ for the body wave dataset.
2. Calculate $\boldsymbol{A_s}^T\boldsymbol{A_s}$ and $\boldsymbol{A_s}^T\boldsymbol{d_s}$ for the surface wave dataset.
3. Add together the two $\boldsymbol{A}^T\boldsymbol{A}$ and $\boldsymbol{A}^T\boldsymbol{d}$ type matrices.
4. Invert $\boldsymbol{A}^T\boldsymbol{A}$ as normal to obtain the joint model.

The surface wave data are weighted with respect to their estimated standard error (see Van Heijst (1997) for details). The travel time data are included as anomalies in seconds. This gives a reasonable relative weighting of the two datasets. This procedure is necessary as otherwise the effects of the body wave data would be swamped by the immense number of surface wave measurements. Effectively the result is that the relative weighting of the two datasets is $1:1$. Figures 7.5(a), 7.5(b) and 7.5(c) show the resulting velocity model over a range of different depths. The model resulting from combination of the body wave and surface wave datasets is denoted MVBS.

The surface wave data have high sensitivity to around 1200 km, between 1200 km to around 1500 km the surface wave data have limited sensitivity (see Appendix E of Van Heijst (1997) for details).

From 1500 km to 2100 km the sensitivity from both datasets is low. From around 2100 km to the CMB the body wave data have some sensitivity from the turning of the deepest S rays. This deep structure is entirely due to the body wave dataset. We should be careful when interpreting the model at great depth as the coverage of the body wave data is very sparse. Between 1200 - 2100 km neither dataset has much sensitivity and therefore we should not place much trust in the model at such depths.

At depths less than 1000 km, model MVBS is similar to model S20RMC18 of Van Heijst (1997). For reference model S20RMC18 is included in Appendix B using the colour scale adopted by Van Heijst (1997). In particular we observe slow mid ocean ridges and convergent margins at depths 50 km, 74 km and partially at 129 km. The continents are observed as fast features to around 256 km. The rift valley in Africa is slow down to 256 km. Between 409-703 km the model is dominated by high velocity anomalies associated with subduction and the central Pacific remains slow. For the depth range 951 km - 1251 km the largest anomalies are high velocities in northern Africa, eastern Asia and North America. Between 1424 km - 1823 km there is little sensitivity and the model size decreases accordingly. At depths greater than 2053 km some features start to re-appear: low velocities across the Pacific Ocean and high velocities in eastern Asia. These features gradually get more intense and reach a maximum at a depth of 2584 km. This pattern is also observed at 2981 km but with much smaller amplitude.

The variance ratio obtained for the body wave data calculated against model MVBS is 0.13. This corresponds to a variance reduction of 87% which means that model MVBS is capable of explaining 87% of the body wave dataset variance. From this it can be concluded that the body wave and surface wave datasets are compatible. This compatibility of the two datasets allows increased confidence to be given to the resulting model.

The model is calculated in collaboration with Van Heijst.

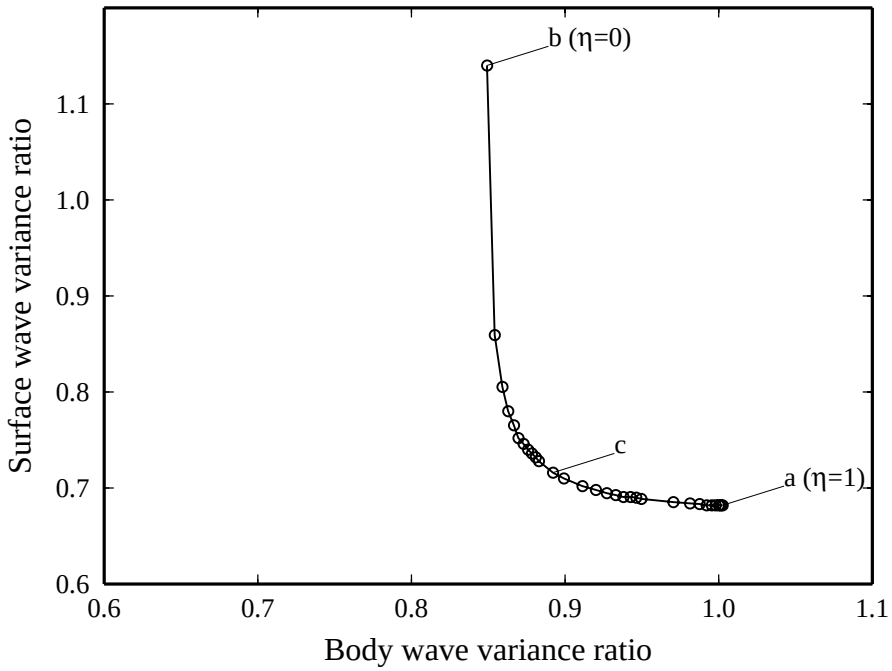


Figure 7.1: Surface wave against body wave variance ratios for the combined model, degree zero term included.

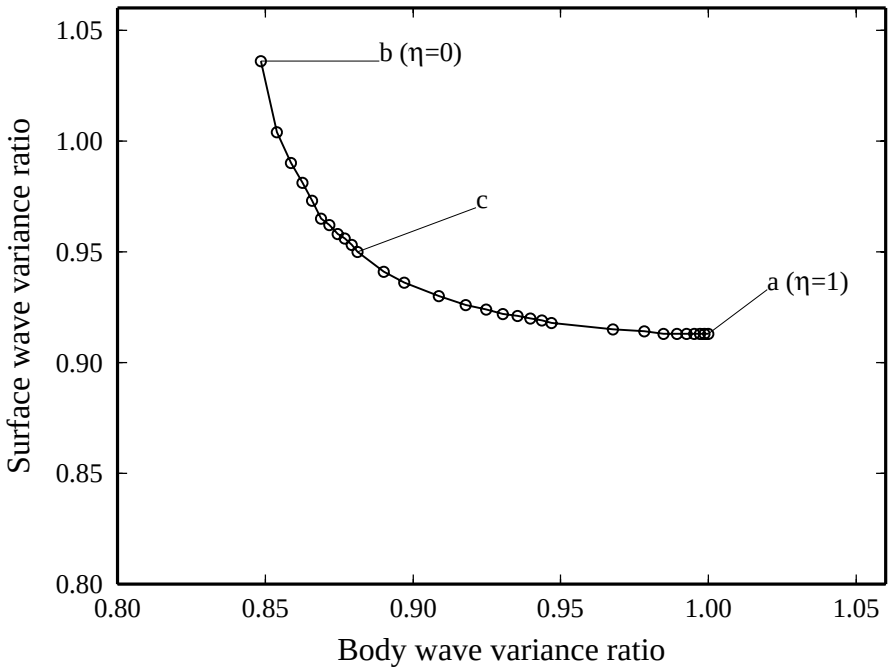


Figure 7.2: Surface wave against body wave variance ratios for the combined model with the degree zero term removed.

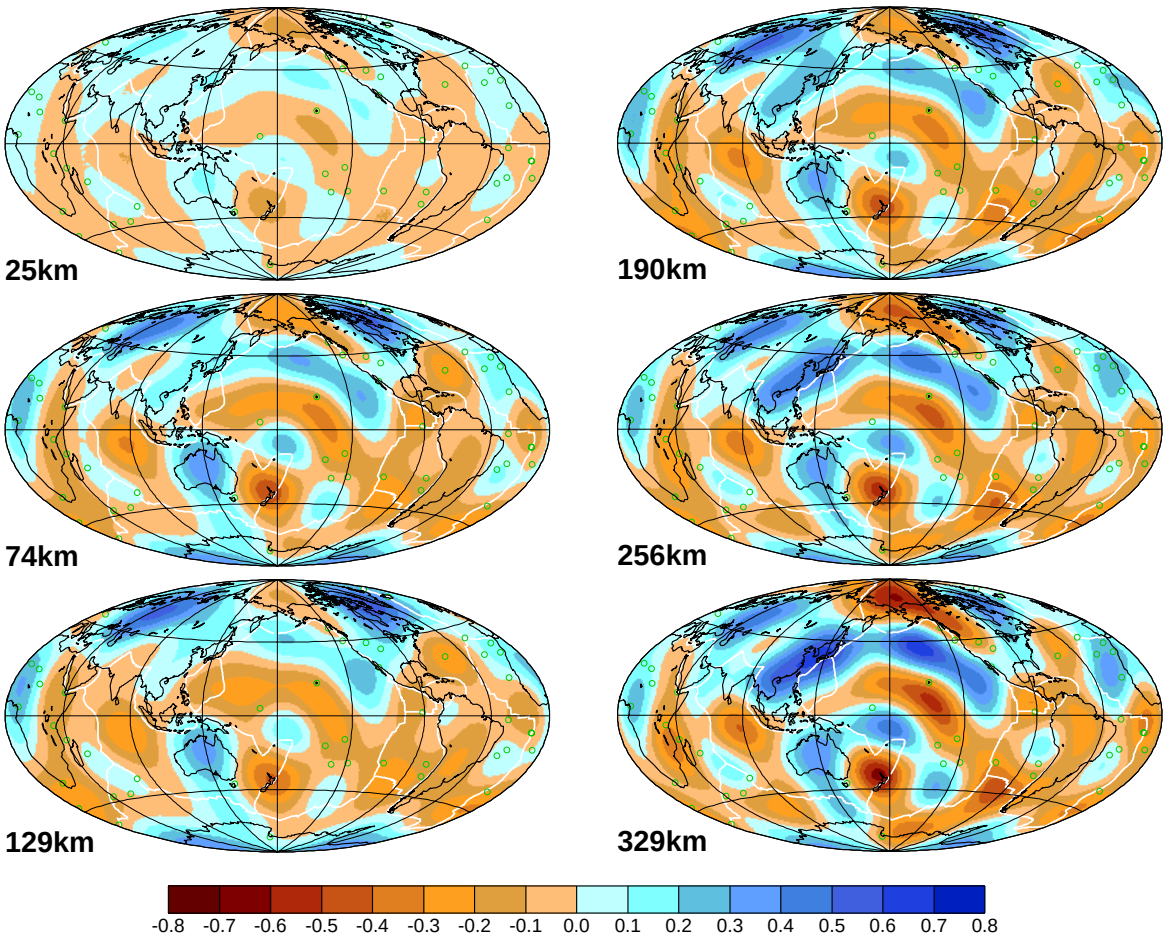


Figure 7.3: q_μ model constructed from combination of the $SS - S$ and $SSS - SS$ datasets with the surface wave data of Selby (1998) using the "best" model from Figure 7.1.

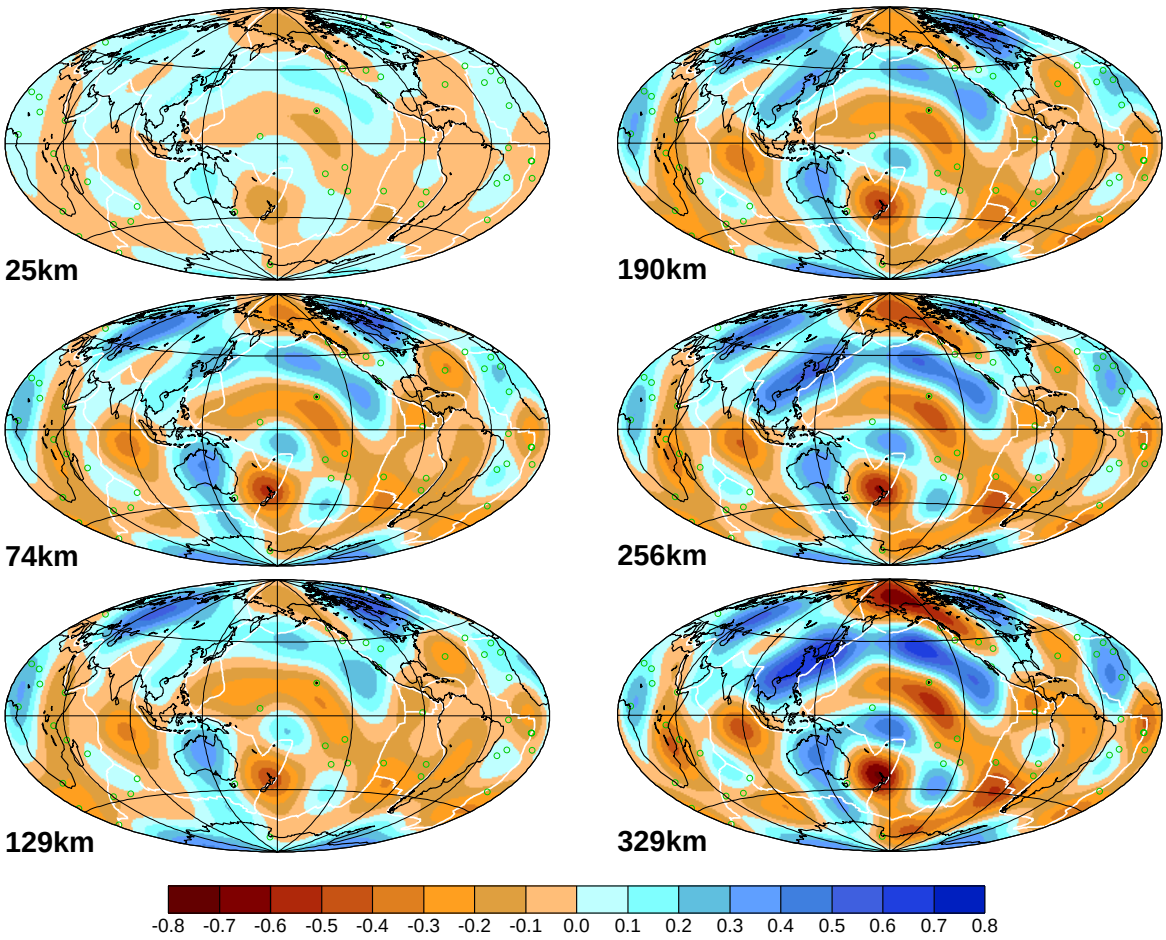


Figure 7.4: Model MQBS: q_μ model constructed from combining the $SS - S$ and $SSS - SS$ datasets with the surface wave data of Selby (1998) using the "best" model from Figure 7.2.

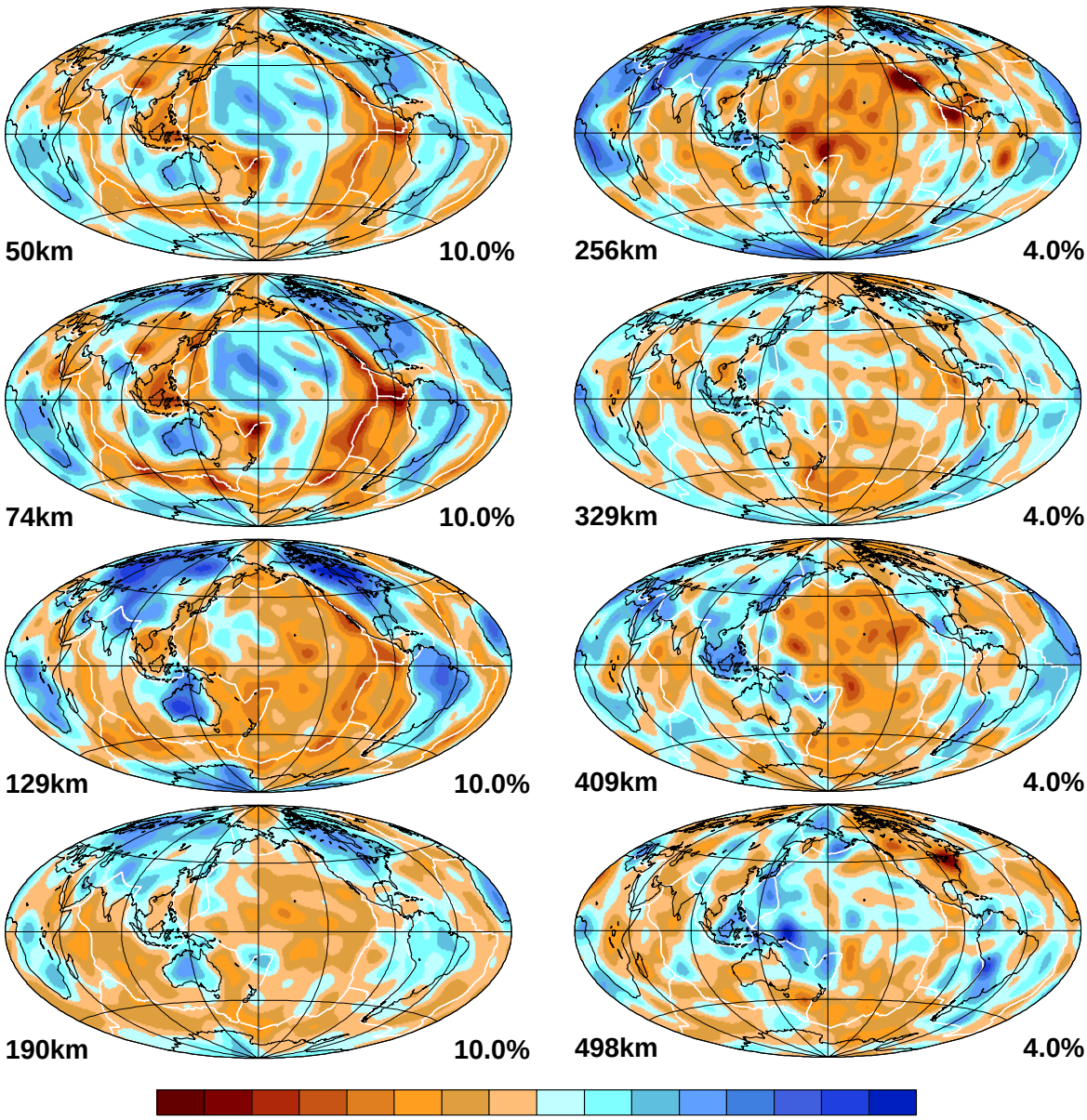


Figure 7.5(a): Velocity model MVBS for depths 50 - 498 km.

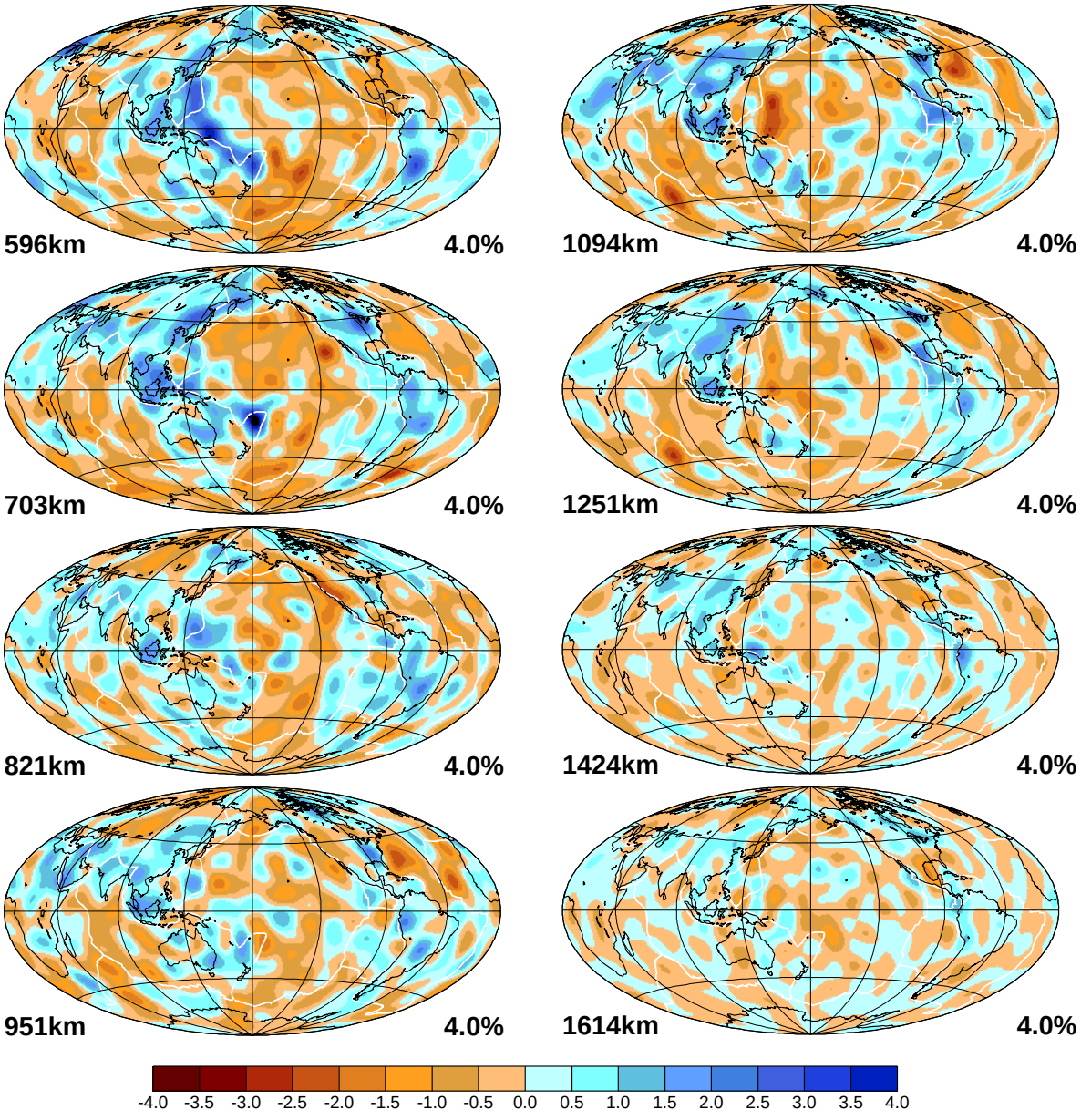


Figure 7.5(b): Velocity model MVBS for depths 596 - 1614 km.

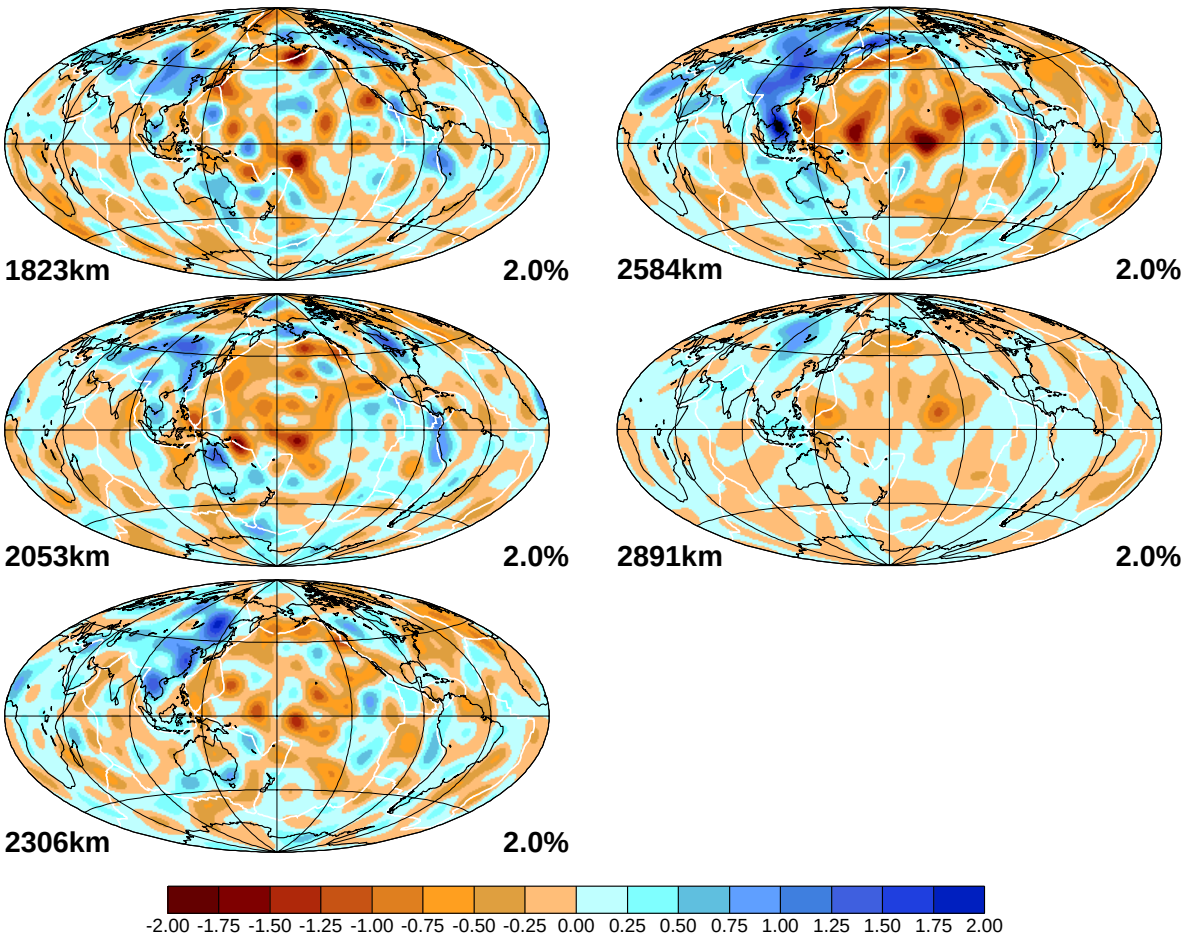


Figure 7.5(c): Velocity model MVBS for depths 1823 - 2891 km.

Chapter 8

Discussion

In this chapter the velocity and attenuation models presented in Chapters 6 and 7 are discussed. The velocity models are discussed in Section 8.1 and the attenuation models are discussed in Section 8.2. The velocity and attenuation models are compared with each other in Section 8.3. The models obtained from the combination of body wave and surface wave data are discussed in Section 8.4. The models are compared with existing work in Section 8.5. The geophysical implications of the models are discussed in Section 8.6.

8.1 Discussion of the velocity models

In this section models MVSSc, MVSSSc and MVCOMB2 (Figures 6.13(a,b), 6.16(a,b) and 6.19(a,b) respectively) are discussed and compared with each other. Note that each of these models include both crustal and ellipticity corrections.

A comparison of models MVSSc, MVSSSc and MVCOMB2 shows only subtle differences between the three models. The main difference between model MVSSc and MVSSSc is that the mid Atlantic ridge is observed as a low velocity feature on model MVSSSc and is neither high or low on model MVSSc. Also model MVSSSc shows the East African rift valley to be a low velocity feature whereas the model MVSSc shows this to be a higher than average velocity feature. The reason for these two differences is probably due to differences in coverage; the $SS-S$ dataset has very few bounce points across Africa and in the Atlantic whereas the $SSS-SS$ dataset has denser coverage across both these regions. Compare Figures 8.1 and 8.2 which show the density of the bounce point distribution for both the $SS-S$ and $SSS-SS$ datasets respectively. Note that Figure 8.1 is identical to Figure 5.11. Figure 8.2 shows the density of both the SS and SSS bounce points together. That the $SS-S$ and $SSS-SS$ datasets produce such similar models is noteworthy. It means that the two datasets are compatible with each other. Also, that the $SSS-SS$ dataset produces such a convincing model of shear velocity perturbation from a sparse number of data points is very encouraging.

Model MVCOMB2 is obtained by inversion of the combined $SS-S$ and $SSS-SS$ datasets.

The weighting of the two datasets is determined using the "L-shaped" curve given by Figure 6.17. This weighting results in model MVCOMB2 being the "best" model for the combined $SS-S$ and $SSS-SS$ datasets. Areas of low velocity correlate with ridges and convergent margins. The velocities along the faster spreading ridges such as the East Pacific Rise are lower than the velocities along slower spreading ridges such as the mid Atlantic ridge. Areas of low velocity are also observed to the North of the African rift valley and in a region across Asia to the north east of India. Areas of high velocity correlate with the continents: e.g. Australia, South America, much of Eurasia, Africa and the north east of America and Canada are all observed to have higher than average velocities. Much of the Atlantic Ocean is also observed to have higher than average velocity. As with both models MVSSc and MVSSSc the velocities across the Pacific ocean are observed to increase westwards, with distance from a spreading centre.

The lack of depth resolution means that it is impossible to attribute the regions of high or low velocity to particular depths. Many other studies of lateral variations in upper mantle shear velocity have observed such correlation with surface tectonics. Comparisons with previous work are made in Section 8.5.1

8.2 Discussion of the q_μ models

In this section the attenuation models MQSS, MQSSS and MQCOMB2 (Figures 6.20(a,b), 6.21(a,b) and 6.24(a,b) respectively) are discussed and compared.

Model MQSSS has many features in common with model MQSS but there are several differences: The region of extremely low attenuation to the west of Africa is considerably more intense in model MQSSS, South America appears as a strong low attenuation feature in model MQSS whereas it appears as a weak high attenuation feature in model MQSSS. Model MQSSS has an area of very high attenuation to the east of southern Africa. This feature also appears on model MQSS but it is not as intense. Both models show a region of high attenuation to the north east of India however this region lies further south on model MQSSS. Each of these discrepancies can be attributed to data coverage. Examination of Figures 8.1 and 8.2 show that the coverage across South America is particularly poor (assuming that variation in q_μ can be represented at the bounce points), and therefore care should be taken when interpreting the maps across this region. The other differences between models MQSS and MQSSS could also be related to coverage problems as they coincide with regions where the density of bounce points is low.

Model MQCOMB2 is the "best" q_μ model obtained from inverting both the $SS-S$ and $SSS-SS$ datasets simultaneously. As a result it exhibits features from both models MQSS and MQSSS. Areas of high attenuation, with the exception of South America, correlate with spreading centres and convergent margins. E.g. high attenuation is observed along the East Pacific Rise, Pacific-Antarctic Rise, the Macquarie Ridge and Kermadec-Tonga Trench. Continental areas generally correlate with regions of

lower than average attenuation (Australia, Antarctica and much of Eurasia, Africa and North America) with the exception of South America which appears as a region of higher than average attenuation. The amplitude of the variations in δq_μ lie between ± 0.020.

There still remains the problem of the degree 0 term. As mentioned in Chapters 5 and 6, the t^* residuals have a non zero mean. This means that the models of q_μ have a significant degree 0 term. This is not entirely unexpected, as the t^* residuals are calculated relative to values predicted by the PREM model. The variations in Q of the PREM model were not calculated using body wave data, in fact normal mode measurements of Q were used. It is therefore hardly surprising that the q_μ models calculated using body wave data (this thesis) exhibit a degree zero term which does not correspond with PREM. We believe that the degree 0 term gives evidence of frequency dependence of q_μ in the frequency range 15-150 s, which should be studied further in the future. The size of the q_μ variations means that the probable source of the q_μ anomalies is in the low velocity zone (depths 80-220 km). This is consistent with the observations of Durek *et al.* (1993). They suggest that the source region of anelastic heterogeneity lies in the shallow mantle between depths of 100-300 km.

8.3 Comparison of the velocity and attenuation models

There are many similarities between the velocity and attenuation models. From a physical point of view regions of high attenuation should correlate with regions of low velocity and vice versa. This is because intrinsic attenuation is temperature dependent: high attenuation is associated with high temperature and vice versa. High temperatures can also be attributed to low velocities since in general an increase in temperature results in a decrease in velocity (since the density of mantle material decreases with increasing temperature, assuming no change in pressure). Comparison of the models obtained from inversion of the combined $SS-S$ and $SSS-SS$ datasets i.e. comparison of models MVCOMB2 and MQCOMB2 leads to the following conclusions:

- Areas of low attenuation tend to correlate with areas of high velocity: e.g. across Australia and Eurasia.
- Areas of high attenuation tend to correlate with areas of low velocity: e.g. along the ridges surrounding the Pacific Ocean and along the Atlantic-Indian ridge.

To further investigate the correlation between attenuation and velocity the correlation coefficient between models MVCOMB2 and MQCOMB2 is calculated for a range of depths. Table 8.1 gives the correlation coefficients obtained by comparing model MVCOMB2 with MQCOMB2 for depths 50, 74, 129, 190, 256 and 329 km. Also included is the probability that the correlation is not obtained by chance. The routine used to calculate the correlation coefficients and probability value is described by Press *et al.* (1986) pp 484-488. Perfect correlation results in a correlation coefficient of 1. Table Table 8.1 shows that there is a degree of correlation between models MVCOMB2 and MQCOMB2,

however the correlation coefficient never exceeds 0.25.The probabilities that the correlation arose by random chance are all less than 0.05 which meaning that there is greater than 95% chance that the correlation coefficient obtained is real.

Depth	Correlation coefficient	Probability
50	0.25	0.02
74	0.25	0.03
129	0.24	0.03
190	0.25	0.03
256	0.23	0.04
329	0.24	0.03

Table 8.1: Correlation coefficient between models MVCOMB2 and MQCOMB2 for various depths. The probability value gives the probability that the correlation could have arisen by chance.

8.4 Discussion of the combined body wave and surface wave models

In this section the models obtained by combination of body wave and surface wave data are discussed. Model MVBS is the velocity model obtained by combining the body wave dataset with the surface wave dataset of Van Heijst (1997). Model MQBS is the attenuation model obtained by combining the body wave dataset with the surface wave dataset of Selby (1998). Model MVBS is discussed first in Section 8.4.1, followed by model MQBS (Section 8.4.2).

8.4.1 Model MVBS

Model MVBS, (Figures 7.5(a), 7.5(b) and 7.5(c)), is obtained by inversion of a combination of body wave and surface wave data. The body wave dataset is identical to that used in the construction of model MVCOMB1 and consists of 2921 measurements of differential travel time, 2535 from $SS-S$ measurements and 387 $SSS-SS$ measurements. The body wave data are mainly sensitive to structure in the upper mantle but they also have sensitivity in the lower mantle due to the turning of the S rays in this region. However care should be taken when interpreting the model at such depths due to the limited number of rays involved. The surface wave and overtone data have sensitivity to the upper 1200 km with reduced sensitivity to deeper structure.

Unlike the models obtained from inversion of the body wave datasets, model MVBS has good depth resolution to depths of at least 1200 km. This is due to the inclusion of the surface wave and overtone dataset. For the depth range 50-74 km model MVBS is characterised by low velocities along mid ocean ridges and convergent margins. These low velocities are also observed at 129 km but the intensity is

lower. The continents are observed as high velocity features to depths of around 256 km and possibly deeper. The African rift valley is observed as a low velocity feature to depths of around 256-329 km. Over the depth range 409-703 km the model is dominated by the high velocity anomalies associated with subduction and the central Pacific remains an area of low velocity. Between depths of 951-1251 km the largest anomalies are high velocities in northern Africa, eastern Asia and North America. From 1424-1823 km there is little sensitivity and the model size decreases accordingly. At depths greater than 2053 km some features start to re-appear: low velocities across the Pacific Ocean with high velocities in eastern Asia. These features become more intense with increasing depth, reaching a maximum at a depth of 2584 km. This pattern is also observed at 2981 km but with reduced amplitude. For depths greater than 2053 km the large scale pattern shows a ring of high velocities surrounding the Pacific, with an area of low velocity across the centre of the Pacific.

8.4.2 Model MQBS

Model MQBS, (Figure 7.4), is obtained by inversion of the combined body wave and surface wave datasets. Model MQBS shows a pattern of attenuation correlated with the ocean-continent pattern and with some surface tectonic features. Low attenuation is observed across many continental regions: e.g. across Australia, eastern Africa, Eurasia, Antarctica and North America. High attenuation is observed across much of the Pacific, Indian and Atlantic Ocean. There is also correlation between areas of high attenuation and tectonically active regions. For example, high attenuation is observed along the Pacific-Antarctic ridge, the mid Atlantic ridge and the region surrounding the Caribbean. The vertical resolution is not sufficient to allow discussion of changes in attenuation with depth. There is a slight increase in amplitude with depth.

The fact that the the two datasets can be combined so successfully is very encouraging. Bhattacharyya (1996) did not succeed in obtaining a model for variations in q_μ which could fit adequately both body wave and surface wave datasets. Also, because the two datasets sample the Earth in different ways it leads to the conclusion that the signal observed is indeed reflecting attenuation.

8.5 Comparisons with existing work

In this section the final models of velocity and attenuation presented by this study are compared with previous work. Chapter 1 provides a general discussion of previous velocity and attenuation studies. Section 8.5.1 compares velocity models MVCOMB2 and MVBS with existing velocity models. Section 8.5.2 compares models MQCOMB2 and MQBS with existing models of attenuation.

8.5.1 Velocity models

In this section the velocity models, MVCOMB2 and MVBS, are compared with existing models.

Figures 8.3(a) and 8.3(b) show the three dimensional shear velocity model, S12_WM13, obtained by Su *et al.* (1994). Figures 8.4(a) and 8.4(b) show the shear velocity model, SAW12D, obtained by Li & Romanowicz (1996). Figure 8.5 shows the shear velocity model, S16B30, of Masters *et al.* (1996). Each of these models are constructed using a combination of body wave and surface wave data. In addition, model S1630B also uses normal mode structure coefficients to provide additional constraints on the shear velocity structure. The features common to these models are summarised in Section 1.9.

Model MVCOMB2

The most realistic comparisons are obtained by comparing model MVCOMB2 with previous models. Although only $SS-S$ and $SSS-SS$ data are used in the construction of model MVCOMB2 some striking similarities are observed between it and existing models. Comparison of model MVCOMB2, (Figures 6.19(a) and 6.19(b)), with depths 50 and 200 km of model S12_WM13, (Figure 8.3(a)), results in many similarities. The correlation of high and low velocity anomalies with tectonic features is similar in each model. The relative intensity of the high velocity anomaly across Africa is less on model MVCOMB2 than model S12_WM13 at 200 km. However the amplitude of this high velocity feature is approximately the same in each model (note the changes in scale on Figure 8.3(a)). Comparison with of model MVCOMB2 with depths 150, 250 km of model SAW12D (Figure 8.4(a)), again shows many similar features. The most significant difference between the two models lies in the region around the western Pacific rim. This feature is observed as a high velocity anomaly on model SAW12D, but as a low velocity anomaly on model MVCOMB2. Comparison with depths 70 and 170 km of model S16B30, (Figure 8.5), again shows many similarities. Despite being expanded to spherical harmonics of degree 16, Figure 8.5, is dominated by large scale features. This makes visual comparison of the two models quite tricky, however the large scale features appear to be in good agreement.

Model MVBS

If model MVBS (Figures 7.5(a), 7.5(b) and 7.5(c)), is compared with existing models of shear velocity perturbation then many similarities are observed. In the upper mantle model MVBS shows correlation with tectonic features: high velocities underlying continental regions and low velocities underlying spreading ridges. Similar features have been observed by many studies in particular Su *et al.* (1994), Li & Romanowicz (1996) and Masters *et al.* (1996).

Model MVBS has some sensitivity in the lowermost mantle from the the turning of the deepest S rays. The number of rays passing through this region is insufficient to justify expansion up to degree 20. Consider Figure 8.6 which shows model MVBS over depths 1823-2891 km for spherical harmonics of degree 1 through 12. This allows the large scale pattern of heterogeneity to be more easily observed. Figure 8.7 shows model S12_WM13 plotted over the same depth range using the colour scale adopted in this thesis. Figure 8.8 shows model MVBS plotted over the same depth range but only including terms up to degree 8. Figure 8.9 shows the shear velocity model, U84L85/SH of Woodhouse & Dziewonski (1989) for spherical harmonics up to degree 8, again over the depth range 1823-2891 km. Comparison

of these maps gives rise to a remarkable number of similarities. The maps are characterised by a ring of high velocities circumscribing the Pacific with low velocities observed across the central Pacific. Of the two degree 12 maps, model S12_WM13 shows larger amplitude anomalies. Ignoring the difference in amplitude the main difference is observed across southern Africa. Model S12_WM13 shows a region of very low velocity across this region whereas model MVBS does not.

Comparison of the degree 8 maps (Figures 8.8 and 8.9) also shows a great deal of similarity, particularly in the large scale features.

8.5.2 q_μ models

In this section we make brief comparisons of the attenuation models MQCOMB2 and MQBS with existing models. Model MQCOMB2 is compared with model QR19 of Romanowicz (1995) and model QMU3b of Selby (1998). Figure 8.10 shows model QR19 of Romanowicz (1995) for depths 100-555 km. The main features of this model are discussed in Section 1.7.3. Figure 8.10 shows lateral variations of Q expressed as a percentage with respect to the average value in each layer. The use of a percentage scale distorts the results and makes their interpretation somewhat difficult. At depths where Q is large, the variations observed will seem significant when in fact they will have very little effect (recall that $Q = \frac{1}{q_\mu}$). Therefore at depths greater than 250 km the large anomalies in model QR19 are exaggerated. Limited similarity between models QR19 and MQCOMB2 is observed. Depth 310 km of QR19 shows the highest amount of correlation with MQCOMB2, however there are still many features which do not agree.

Model QMU3b of Selby (1998) is shown by Figure 8.11 for depths 24-703 km. The compatibility of models QMU3b and MQCOMB2 has already been discussed in Section 7.1. In the top 200 km, model QMU3b shows areas of low attenuation across Asia, Europe, North America, Australia, Antarctica and to a lesser extent across Africa and South America. Areas of high attenuation are observed along the plate boundaries. At depths greater than 200 km many of these features persist except across South America which changes to a region of high attenuation. However, Selby (1998) states that the variation in structure with depth should be treated with caution. Model MQCOMB2 has many features in common with model QMU3b.

Model MQBS is the third attempt at combining body wave and surface wave datasets to obtain a model of lateral variations in q_μ. Earlier attempts have been made by Bhattacharyya (1996) and Selby (1998). Since the combined model of Selby (1998) utilises much of the body wave data of this study model MQBS is only compared with the q_μ model obtained by Bhattacharyya (1996). Figure 8.12 shows the q_μ obtained by Bhattacharyya (1996) from the combination of body wave and surface wave datasets. The scale is such that dark areas correspond to regions of higher than average attenuation, light areas correspond to regions of lower than average attenuation. This model exhibits some erratic variations with depth, in fact it seems to shows significant instability with depth, the light and dark areas oscillate over the top three layers. Figure 8.13 shows the model obtained from

the body wave dataset used in the construction of the combined surface wave and body wave model shown in Figure 8.12. If the body wave data and surface wave data are compatible then these two plots should show some similarity; they do not. Model MQBS, on the other hand, shows good compatibility of the body wave and surface wave datasets and therefore it is suggested that little trust should be placed in the combined model obtained by Bhattacharyya (1996). Comparison of the model shown in Figure 8.12 with model MQBS shows, as expected very little similarity.

8.6 Geophysical implications

Figures 8.14 and 8.16 show models MVBS and MQBS respectively. Each figure has the global distribution of hotspots superimposed as green circles. Consider first, model MVBS: at a depth of 129 km the hotspots appear to coincide with regions of low velocity. Figure 8.15 gives the values of Δt obtained at each of the hotspot locations for model MVBS at a depth of 129 km. 74% of the hotspots (35 hotspots) plot to the right of the zero line, i.e. where the model has lower than average velocity. 26% (12 hotspots) plot to the left of the zero line corresponding to high velocity in the model. This suggests that there is some correlation between the hotspots and regions of lower than average velocity. The situation is similar for model MQBS. Figure 8.17 shows the values of Δt^* obtained at each of the hotspot locations for model MQBS at a depth of 129 km. 57% of the hotspots plot to the right of the zero line (27 hotspots) where model MQBS has higher than average attenuation. 43% of the hotspots (20 hotspots) plot to the left of the zero line corresponding with low attenuation. We use this as evidence that the hotspots tend to coincide with regions of higher than average attenuation.

To support this, we also include the results of a statistical test to investigate the likelihood of the distributions of the hotspots with Δt and Δt^* arising by chance. A *Kolmogorov-Smirnov* (K-S) test is used to estimate the probability that the hotspot distribution and the distribution of model values arise from different distributions and whether or not this could have happened by chance. Further details of the K-S test and the Fortran algorithm are given by Press *et al.* (1986) pp 472-475. Essentially the K-S test is used to show that two distributions differ and gives the probability of two distributions being different due to chance. A probability of 0.05 corresponds to a 5% chance that two distributions are different by random chance. The K-S test is applied the hotspot distribution for against Δt and to the distribution of Δt as obtained from model MVBS. The resulting probability is 0.02, i.e. there is only a 2% chance that the two distributions are different by chance and that the correlation between hotspots and regions of low velocity is most likely to be real. Applying the K-S test to the distribution of hotspots with Δt^* and the distribution of Δt^* as obtained from model MQBS results in a probability of 0.02. This means that there is only an 2% chance that the two distributions differ by chance and therefore the correlation between regions of high attenuation and hotspots is most likely to be a real effect. Lower significance levels (typically between 0.15-0.25) are observed for the other depths.

Since hotspots are generally associated with higher than average temperature, the correlations of

the hotspot pattern with models MVBS and MQBS is perhaps not unexpected. Note that in calculating the model values at the hotspot locations the degree 0 terms are removed so as to prevent bias from the spherical average of the model.

The correlation between tectonic features and the observed velocity and attenuation anomalies has been discussed in the previous sections. In summary, it is found that regions of low velocity tend to correlate with the spreading ridges and convergent margins. Regions of high velocity tend to correlate with continental regions. The velocities observed across the Pacific increase westwards which is related to the aging and therefore cooling of the oceanic lithosphere with distance from a spreading ridge. The ridges and convergent margins are characterised by high attenuation features with low attenuation generally observed underlying continental areas. These observations are consistent with the expectations of plate tectonics and with many previous studies of upper mantle velocity structure.

We also examine the correlation between models MVBS and MQBS. The highest correlation between the two models is observed in the low velocity zone. This is consistent with the conclusions of Durek *et al.* (1993), that temperature variations in the LVZ contribute strongly to wave attenuation. Table 8.2 gives the correlation coefficients over a range of depths along with the probability of the correlation arising by chance. The routine used to calculate the correlation coefficients is as described in Section 8.3.

Depth	Correlation coefficient	Probability
25	0.21	0.05
74	0.22	0.06
129	0.48	0.00
190	0.50	0.00
256	0.26	0.02
329	0.28	0.01

Table 8.2: Correlation coefficient between models MVBS and MQBS for various depths. The probability value gives the probability that the correlation could have arisen by chance.

Whether the mantle convects as a whole (whole mantle convection) or whether it convects separately between the upper and lower mantle (layered convection) has long been a subject of debate in Earth Sciences. The strongest evidence for layered convection arises from isotopic analysis. The observed isotope ratios require the existence of a reservoir of pristine mantle material at depth which has not gone through the cycle of exhumation at a mid ocean ridge and subsequent subduction (O'Nions & Tolstikhin, 1996). Seismologists have attempted to determine the type of convection that occurs by imaging the downwellings (slabs) associated with subduction. Generally, the observation of high velocity structures which extend across the 670 km discontinuity into the lower mantle have been assumed to support whole mantle/single layer convection (for examples see Woodhouse & Dziewonski (1989); van der Hilst *et al.* (1997)).

Recently, several studies have suggested that two layer convection is possible but that the level of stratification occurs at approximately 1600 km depth and not 670 km (Kellogg *et al.*, 1999; van der Hilst & Kárason, 1999).

In most areas of subduction, model MVBS (figures 7.5(a),7.5(b),7.5(c)) shows high velocity anomalies to be continuous across the 670 km discontinuity with some high velocity anomalies extending to depths of 1251 km. Therefore model MVBS is in support of whole mantle convection or at least convection occurring across the 670 km discontinuity. Model MVBS has limited sensitivity in the depth range 1424-1823 km and therefore we cannot make any inference as to the possible boundary for two layer convection occurring at a depth of 1600 km.

Although many studies have succeeded in imaging the high velocity downwellings associated with subduction, the nature of mantle upwelling is far less obvious. The imaging of upwellings is generally more difficult than imaging the long slabs forming the downwellings. Upwellings (e.g. hotspot plumes, mid ocean ridges etc) are likely to occur in relatively aseismic regions and as a result are not as well sampled by seismic data, particularly in the shallow mantle (Grand *et al.*, 1997). Also using the first arrivals of seismic waves results in a bias toward high velocity anomalies as they will arrive before low velocity anomalies and therefore their waveforms will be less distorted by noise or interfering phases. Finally it is possible that upwellings may be overlooked if they are cylindrical in shape as suggested by Bercovici *et al.* (1989), and they may also become more focused as they ascend.

The three dimensional models of mantle convection obtained by Bercovici *et al.* (1989) reveal the upwelling cylindrical plumes and downwelling planar sheets to be the primary features of mantle convection. They suggest that the cylindrical mantle plumes that cause hotspots such as Hawaii are likely to be the only form of active mantle upwelling. Their model simulations did not result in the development of sheet-like upwellings that can be associated with mid-ocean ridges. It has therefore been suggested that mid ocean ridges are a passive phenomena resulting from the tearing of the surface plates due to the pull of the descending slabs. The ray coverage of model MVBS in the deepest 1000 km of the mantle is insufficient to allow the imaging of narrow plume type structures. Therefore we cannot make any statement regarding the geodynamical implications of model MVBS with regard to deep seated mantle plumes.

In Section 1.9 the features common to most models of shear velocity were summarised. In the upper mantle the large scale structure conforms to that expected from plate tectonics: high velocities underlying continental shields and platforms, low velocities underlying spreading ridges. These features are seen to extend to depths of 350 km Woodhouse & Dziewonski (1984), 300 km (Su *et al.*, 1994), 300-400 km (Masters *et al.*, 1996), 320-400 km (Grand, 1994) and possibly as deep as 450 km Li & Romanowicz (1996), although generally the high velocity anomalies are observed to extend to greater depths than the low velocity anomalies. The ridge structures in model MVBS are observed as low velocity features to depths of around 129 km, whereas the continents are observed as high velocity features to around 256 km.

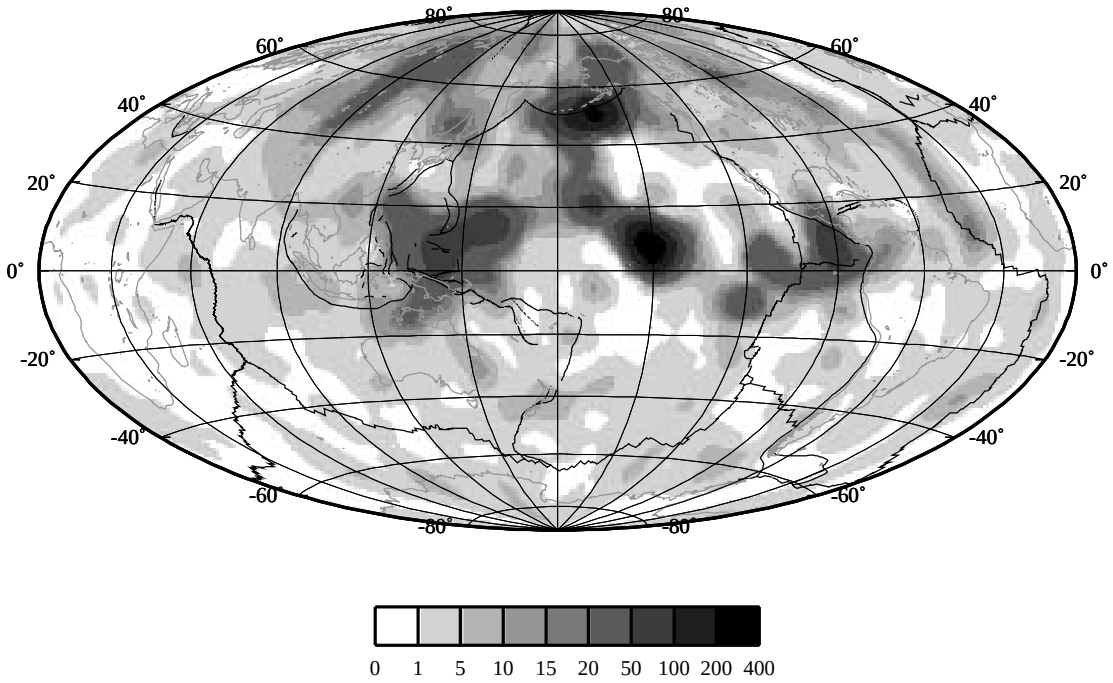


Figure 8.1: Density of measurements for the $SS - S$ dataset, plotted in 5° spherical caps. Note this figure is identical to Figure 5.11.

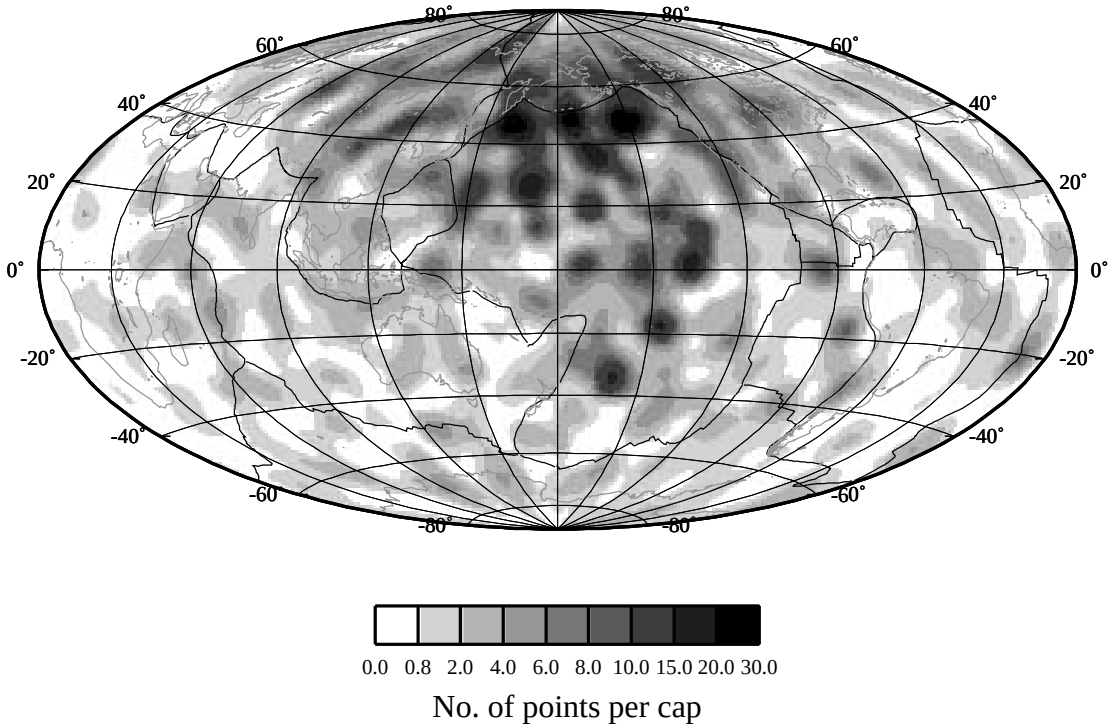


Figure 8.2: Density of measurements for the $SSS - SS$ dataset, plotted in 5° spherical caps.

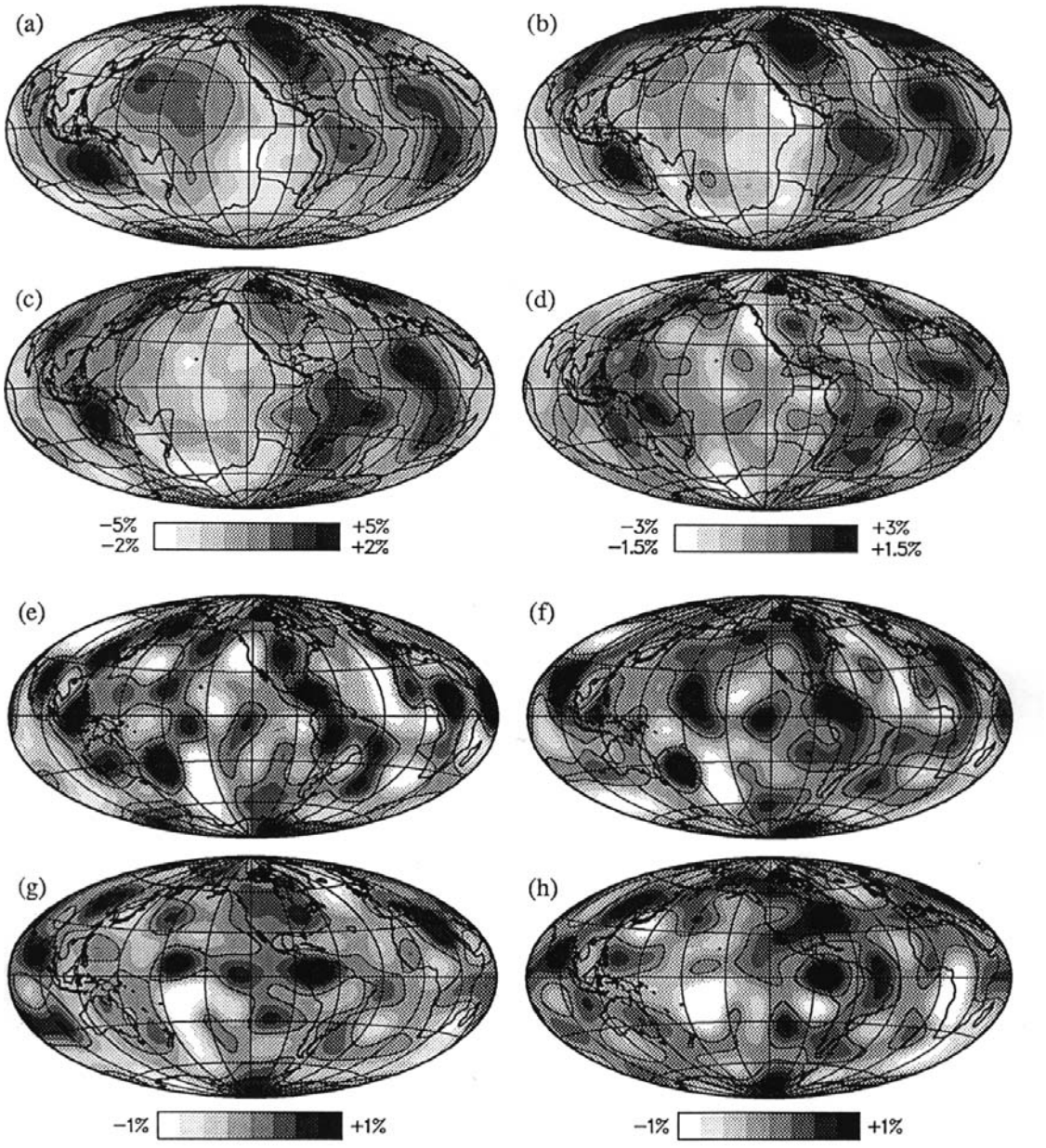


Figure 8.3(a): Velocity model from Su *et al.* (1994) for 12 different depths: (a) 50, (b) 200, (c) 400, (d) 650, (e) 900, (f) 1150, (g) 1450, (h) 1750, (i) 2050, (j) 2350, (k) 2600, (l) 2850 km. The double notations on the scale bars correspond to the top and bottom map respectively.

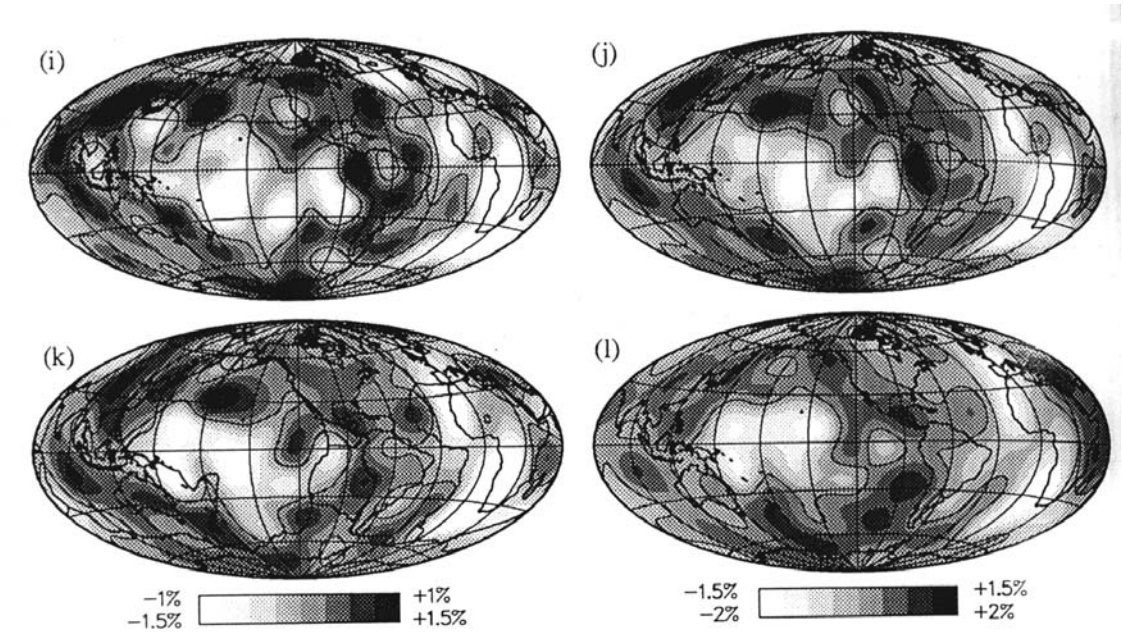


Figure 8.3(b): Velocity model from Su *et al.* (1994) for 12 different depths: (a) 50, (b) 200, (c) 400, (d) 650, (e) 900, (f) 1150, (g) 1450, (h) 1750, (i) 2050, (j) 2350, (k) 2600, (l) 2850 km. The double notations on the scale bars correspond to the top and bottom map respectively.

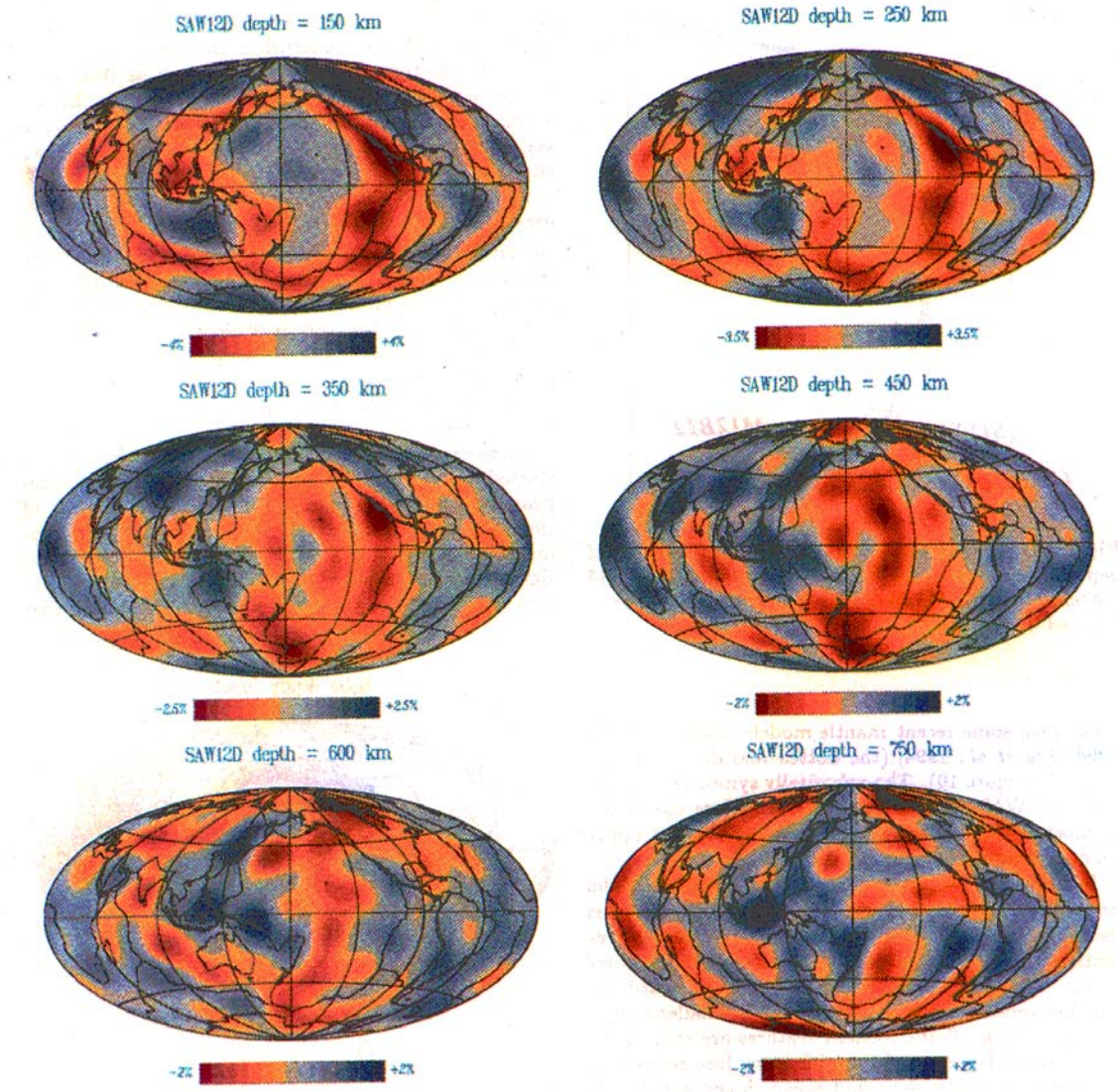


Figure 8.4(a): Reprint of Plate 1 from Li & Romanowicz (1996), depths 150 - 750 km.

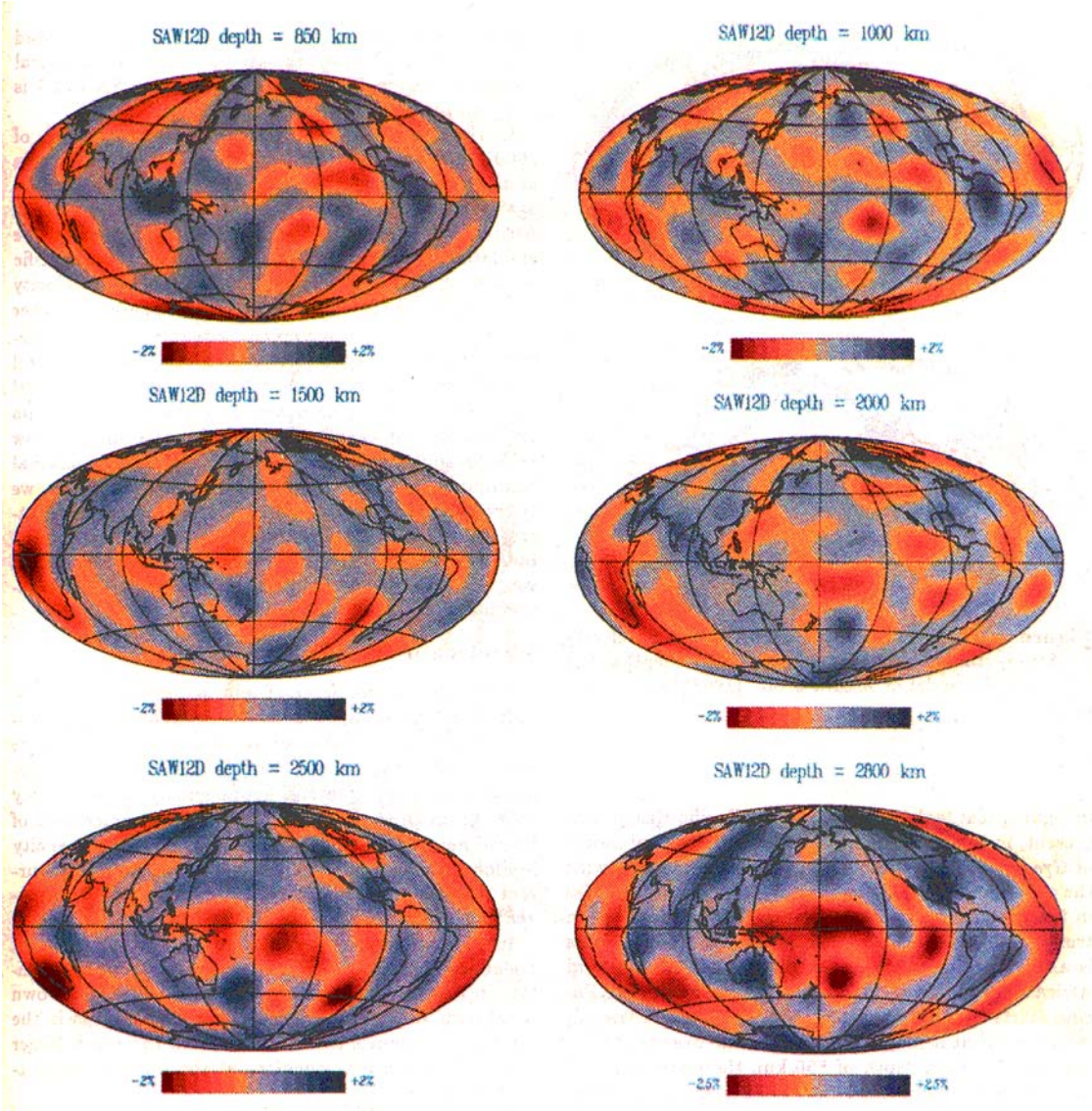


Figure 8.4(b): Reprint of Plate 1 from Li & Romanowicz (1996), depths 850 - 2800 km.

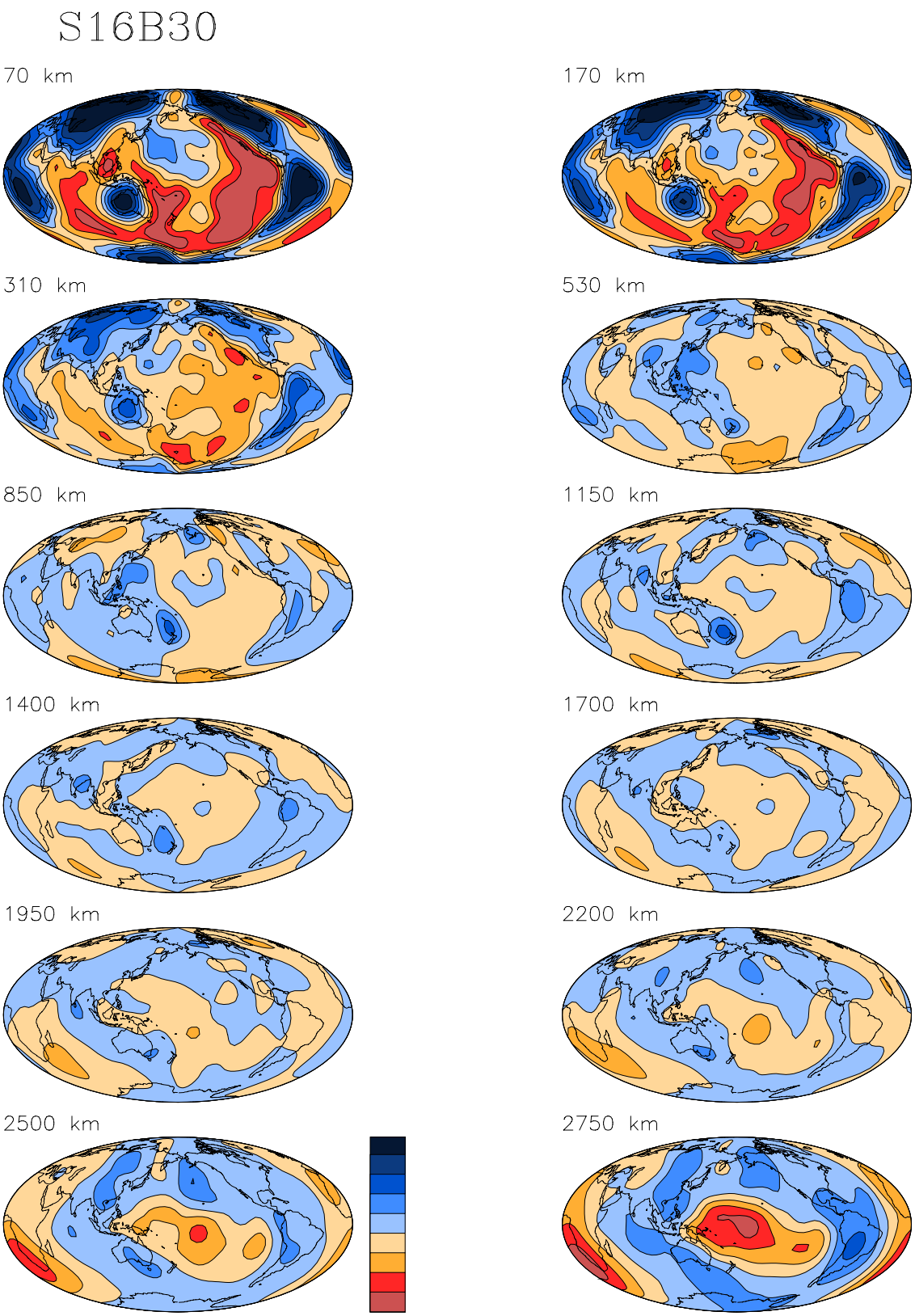


Figure 8.5: Model S16B30 reproduced from Masters *et al.* (1996). Note that the scale bar is in variation of $\frac{\delta v}{v}$ and not percent.

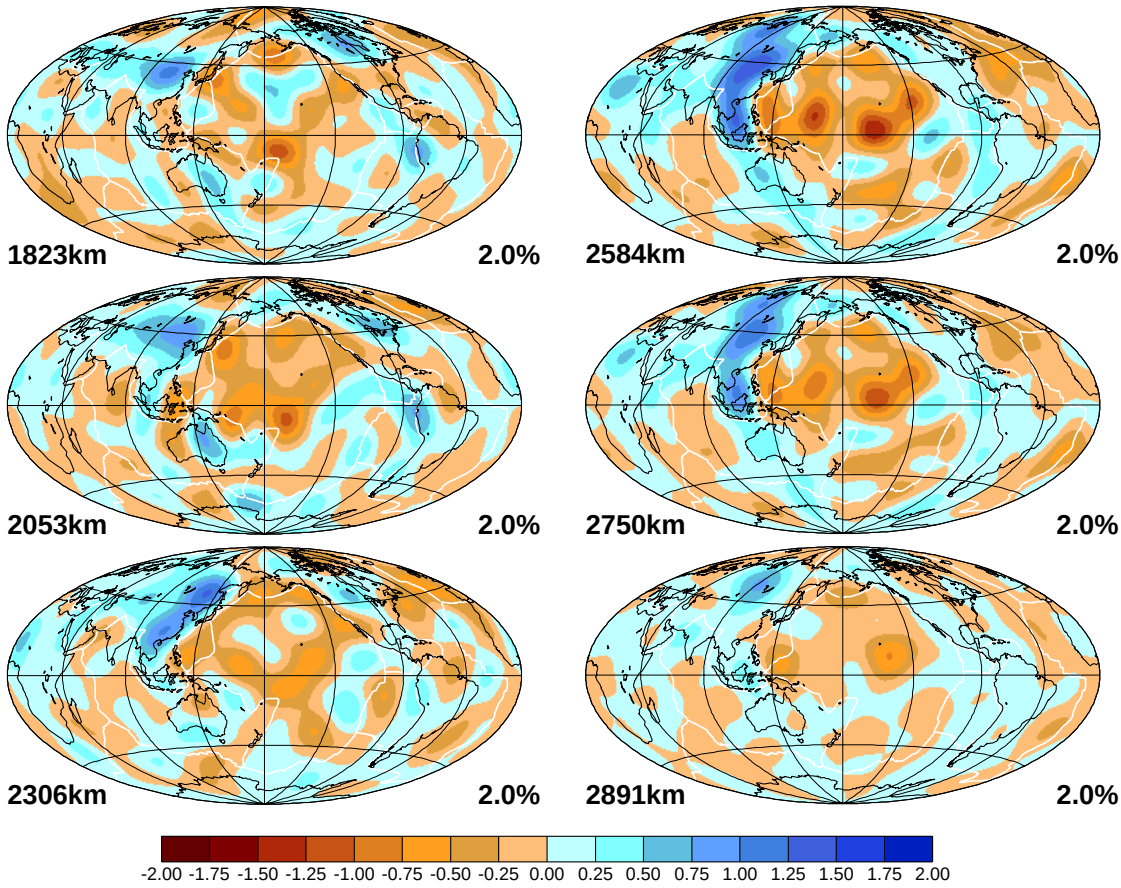


Figure 8.6: Model MVBS for depths 1823 - 2891 km, displayed for degrees 1-12 only.

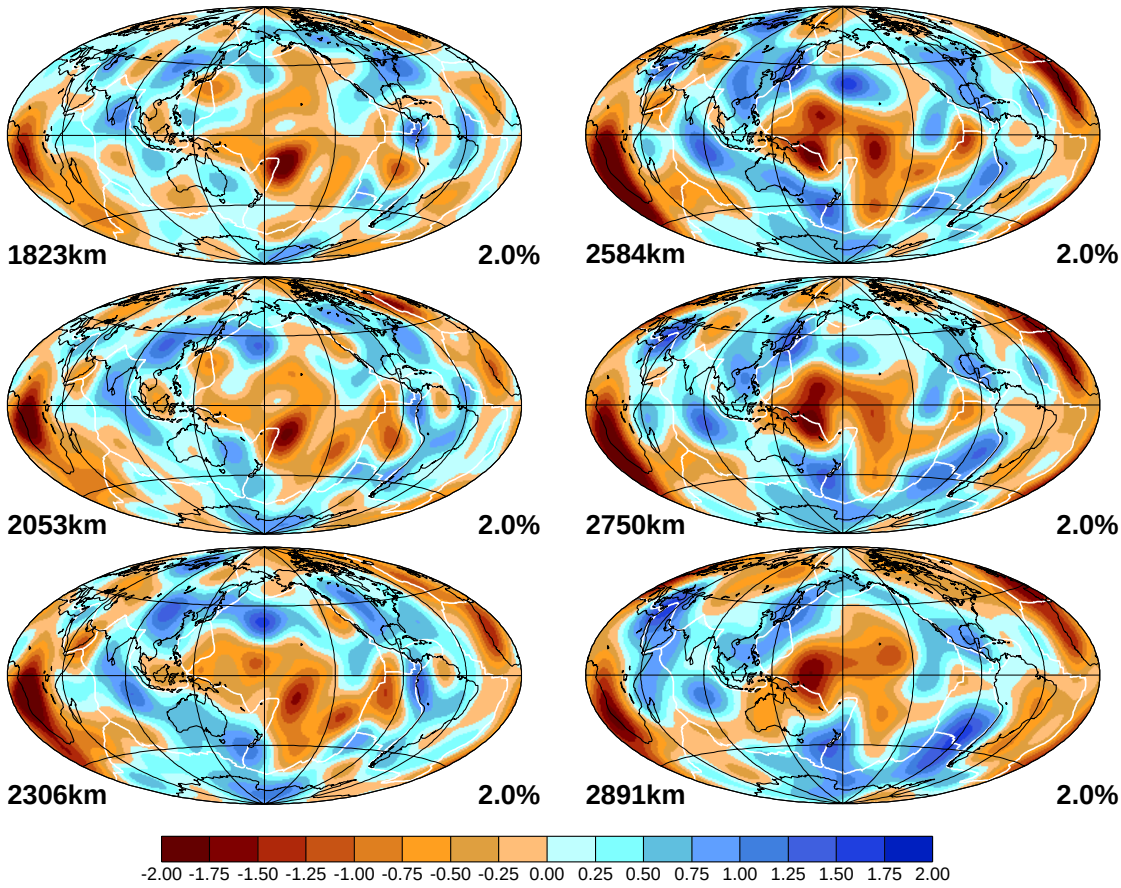


Figure 8.7: Model S12_WM13 for depths 1823 - 2891 km, displayed for degrees 1-12 only.

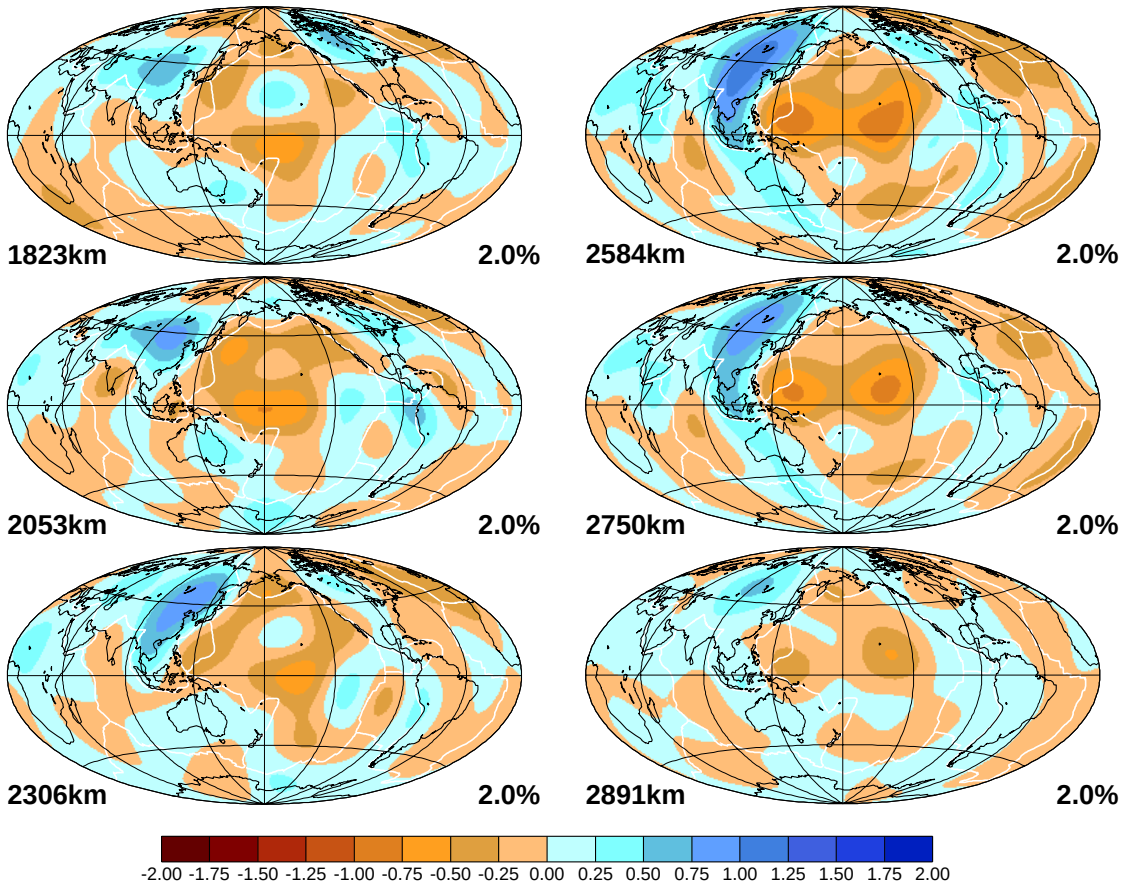


Figure 8.8: Model MVBS for depths 1823 - 2891 km, displayed for degrees 1-8 only.

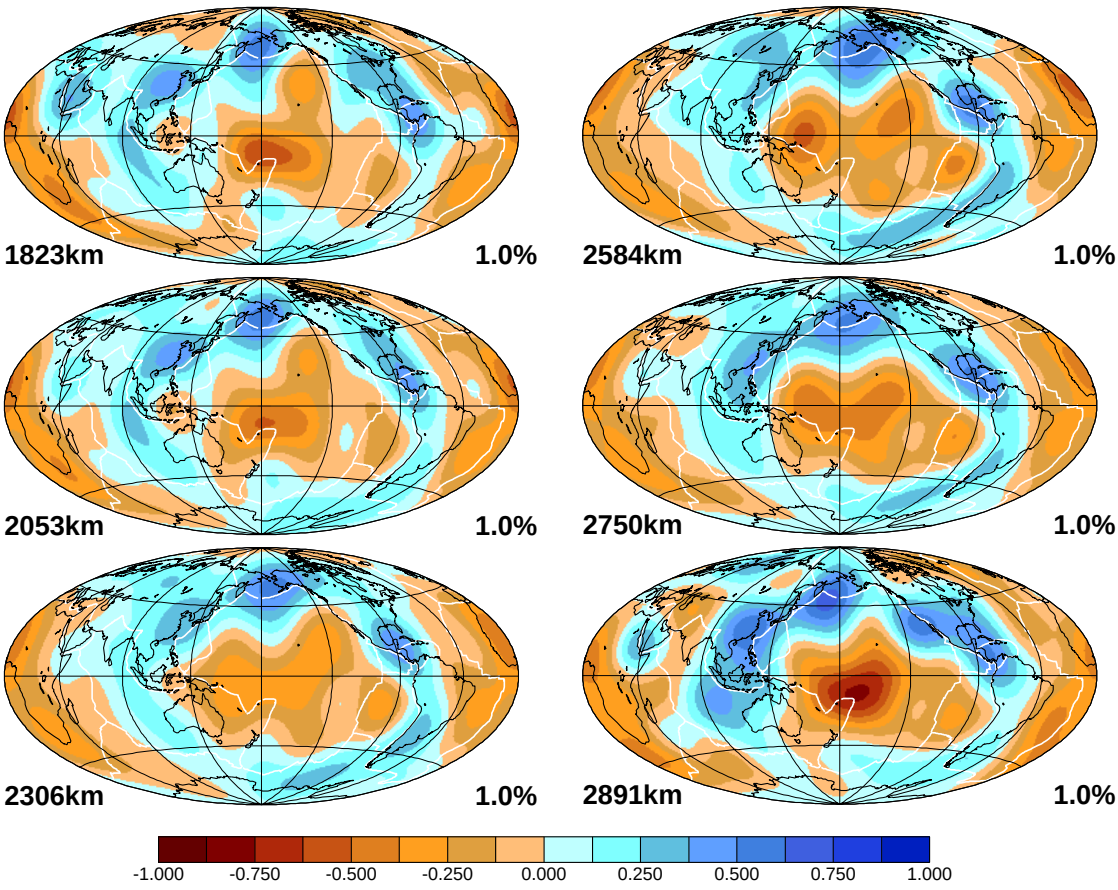


Figure 8.9: Model U84L85/SH for depths 1823 - 2891 km, displayed for degrees 1-8 only.

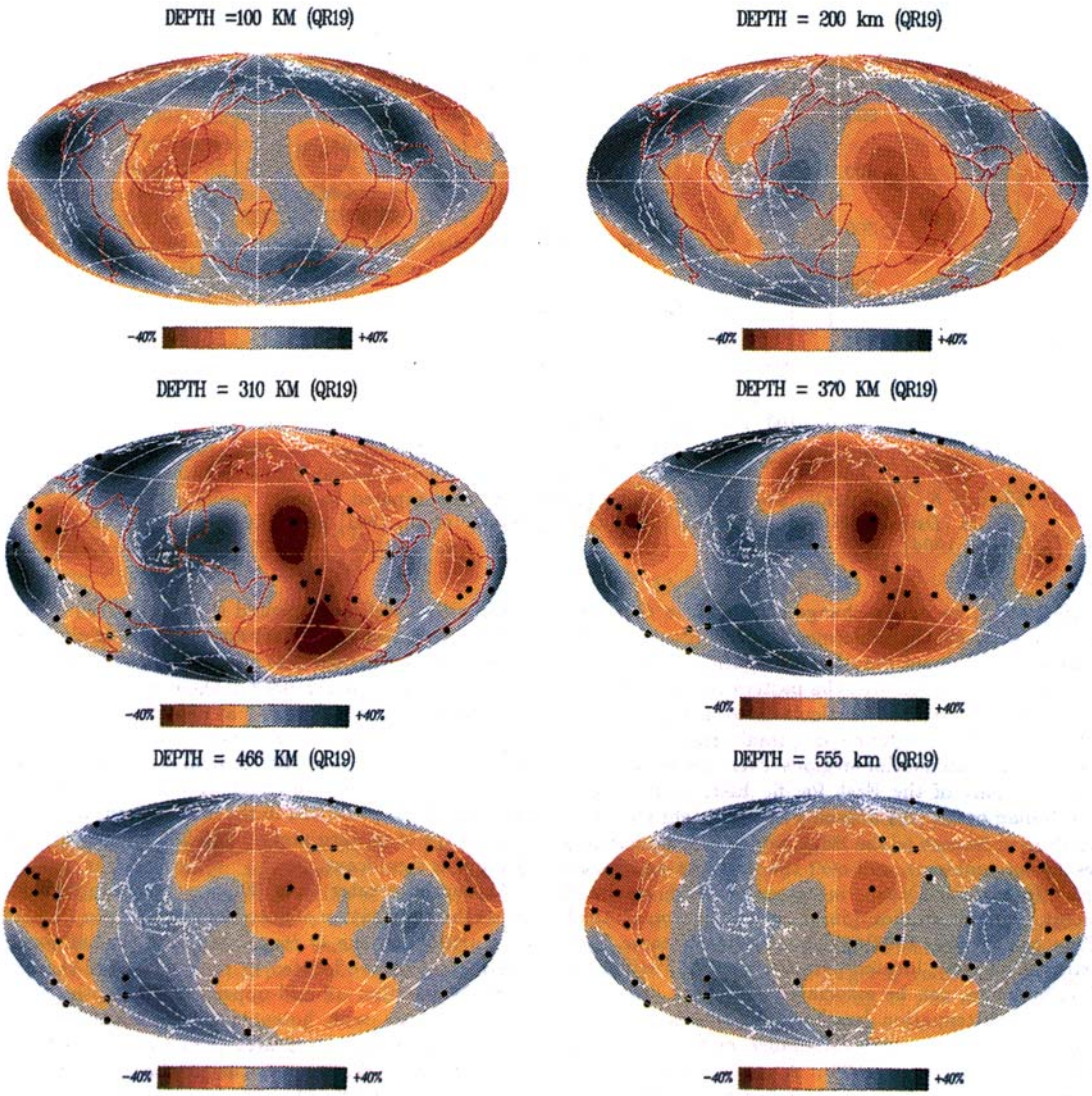


Figure 8.10: Q model, QR19, from Romanowicz (1995).

The figure originally located here has been removed from this version of the thesis for copyright reasons.

Figure 8.11: Model QMU3b from Selby (1998).

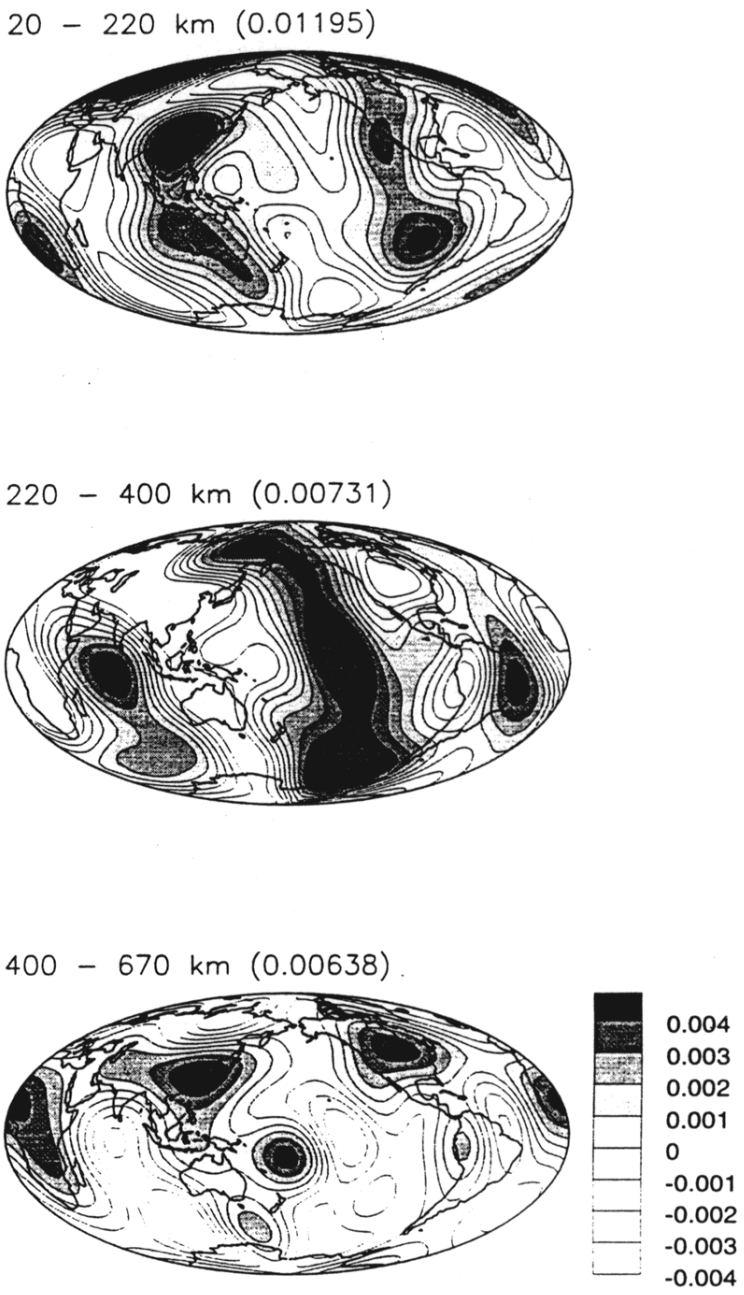


Figure 8.12: Upper mantle combined body wave and surface wave q_μ model from Bhattacharyya (1996).

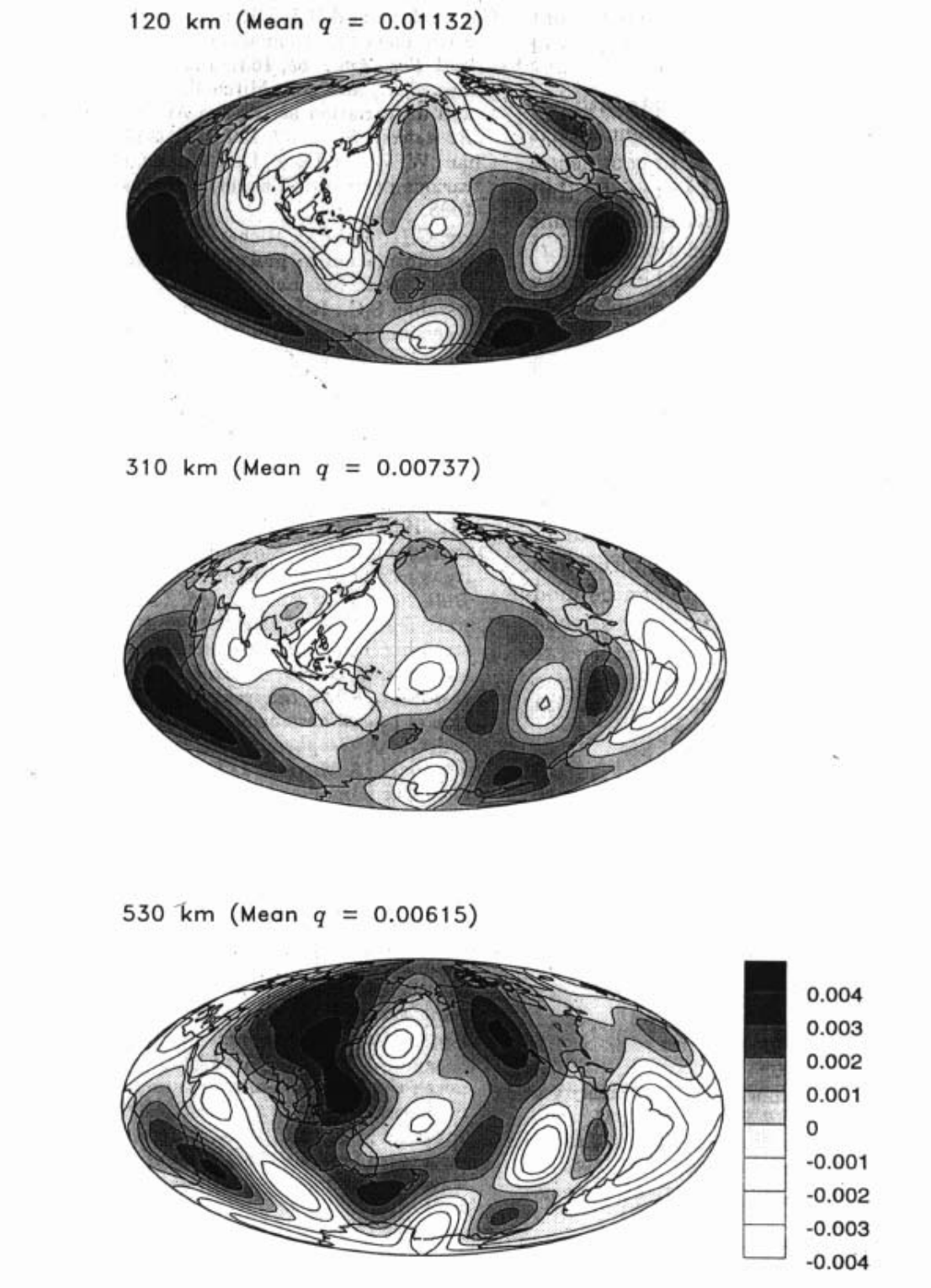


Figure 8.13: q_μ model from Bhattacharyya *et al.* (1996).

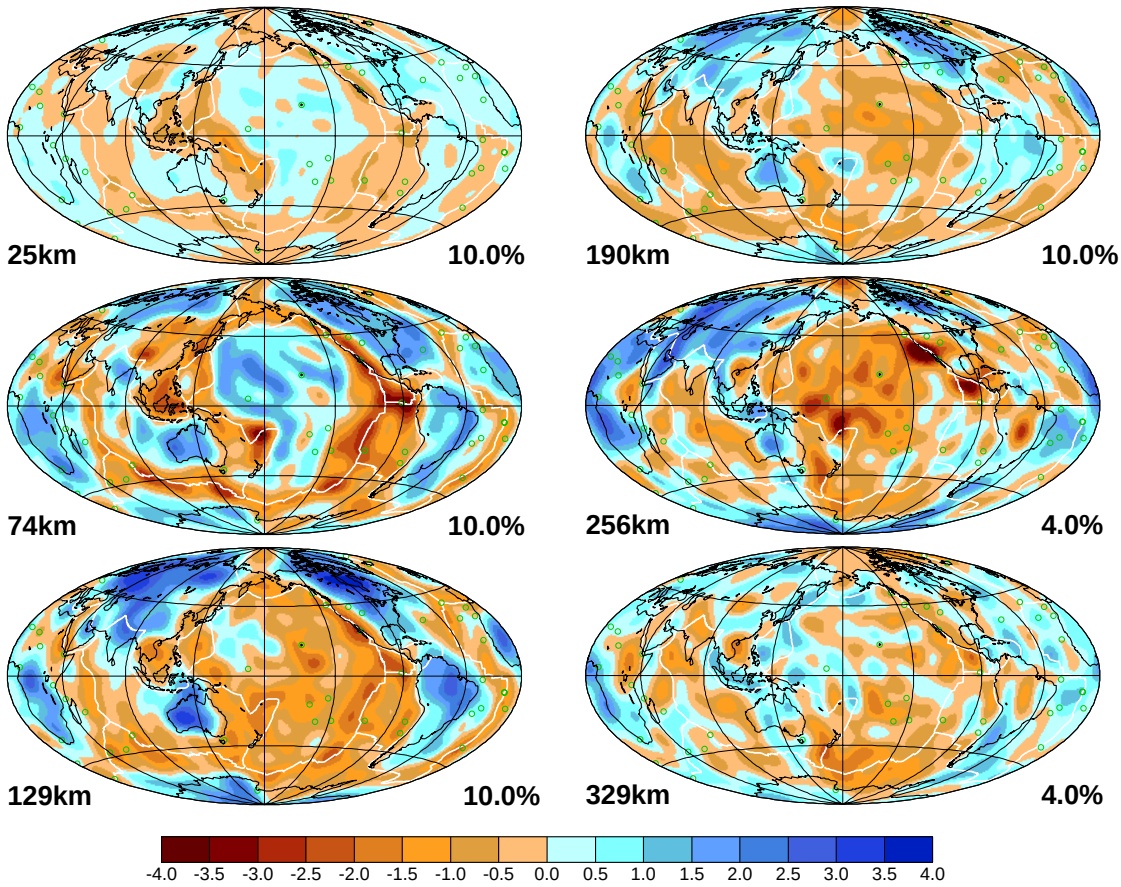


Figure 8.14: Model MVBS for depths 25-329 km showing the hotspot distribution. Hotspots are plotted as green circles.

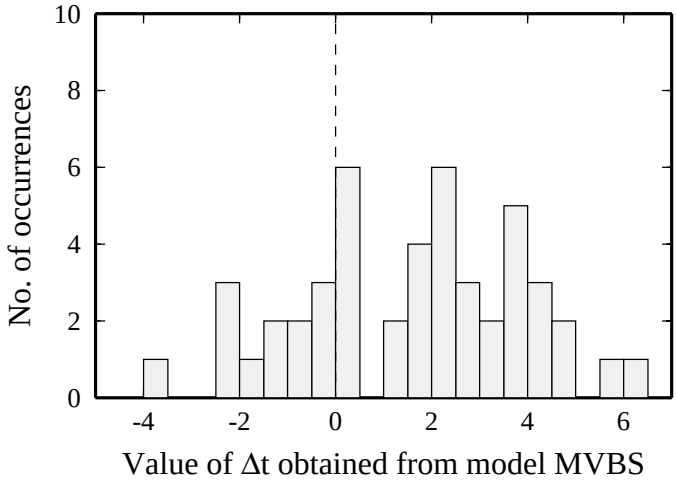


Figure 8.15: Values of Δt calculated at the hotspot locations for model MVBS at a depth of 129 km. 12 hotspots correspond to regions of high velocity and 35 correspond to regions of low velocity.

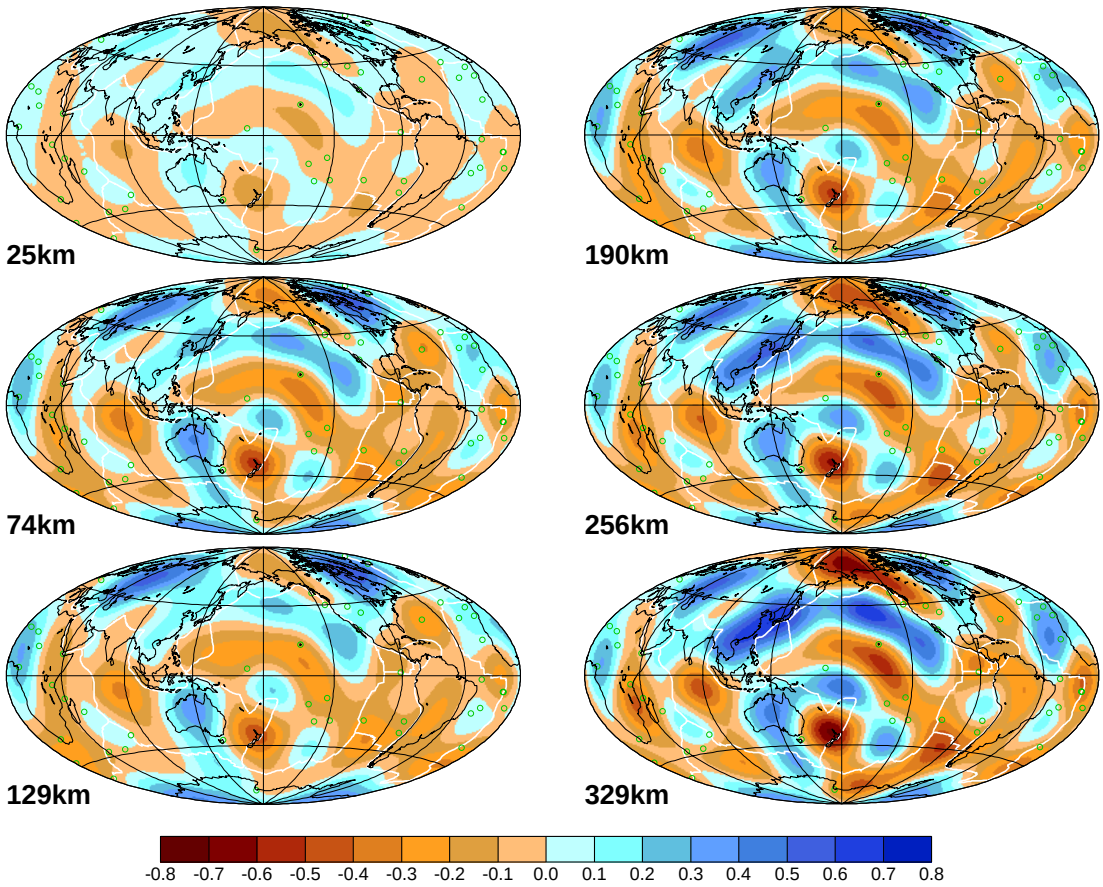


Figure 8.16: Model MQBS showing the hotspot distribution. Hotspots are plotted as green circles.

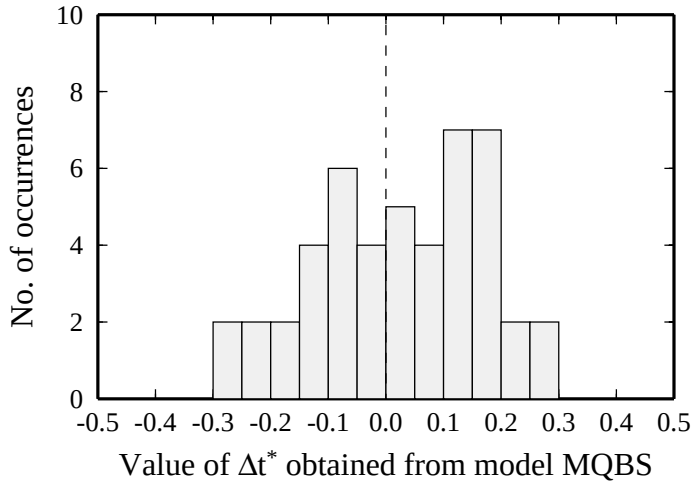


Figure 8.17: Values of Δt^* calculated at the hotspot locations for model MQBS at a depth of 129 km. 27 hotspots correspond to regions of high attenuation and 20 correspond to regions of low attenuation.

Chapter 9

Conclusions

In this study, two new methods for measuring the differential properties of multiple S phases are presented. The "waveform fitting method" enables measurements of both $SS - S$ and $SSS - SS$ differential travel time and attenuation to be made. The "spectral ratio method" enables only measurements of $SS - S$ and $SSS - SS$ differential attenuation to be made. Of the two methods, the waveform fitting method appears to be more suitable for measuring differential attenuation than the spectral ratio method. Using the results from the waveform fitting method, models of the lateral variations of upper mantle shear velocity and intrinsic attenuation are calculated.

Velocity models

Model MVCOMB2 is the first model of upper mantle shear velocity perturbations to include differential $SSS - SS$ measurements. Despite the small number of measurements, the $SSS - SS$ measurements show a great deal of promise. They provide very good sampling of the upper mantle as there are three bounce points for each source and receiver pair: one arising from the SS ray and two arising from the SSS ray. Although the depth resolution of model MVCOMB2 is limited, the features observed are consistent with the expectations of plate tectonics: low velocities are observed underlying mid oceanic ridges and convergent margins with high velocities underlying continental regions. Comparisons with existing models of shear velocity heterogeneity show many similarities.

The body wave datasets of this study are successfully combined with surface wave and overtone data of Van Heijst (1997) to obtain the combined body wave and surface wave model, MVBS. Model MVBS yields a very low variance ratio, (≈ 0.13), meaning that the body wave dataset fits model MVBS extremely well. This is encouraging as the addition of other types of data to a model serves to give confidence to the model. The resulting model has good depth resolution due to the surface wave data and also has sensitivity to the lower mantle from the turning of the deepest body wave S rays. In this region there is excellent agreement with existing studies.

Attenuation models

Model MQCOMB2 is the fourth truly three dimensional model of upper mantle intrinsic attenuation after the models of Romanowicz (1995), Bhattacharyya *et al.* (1996) and Selby (1998). Model MQCOMB2 is constructed using differential t^* measurements made from broadband data. Since the broadband data contain more high frequency information a more accurate estimation of body wave attenuation should be possible. Certainly, model MQCOMB2 shows significant improvement on the one other global body wave study of shear attenuation i.e. Bhattacharyya *et al.* (1996). The fact that the body wave data of this study can be combined successfully with surface wave data gives added confidence to model MQCOMB2. The size degree zero term provides, we believe evidence of the frequency dependence of q_μ in the frequency range of this study ($\approx$ 15 s) and that of the the mantle wave data of previous global studies ($\approx$ 150 s). This is a significant finding which should be further explained in future work.

The body wave datasets of this study are successfully combined with the surface wave dataset of Selby (1998) to obtain model MQBS. This model is the third attempt to combine body wave and surface wave datasets to obtain a model for lateral variations in q_μ after the studies of Bhattacharyya (1996) and Selby (1998). In constructing this model, it is demonstrated that the body wave and surface wave datasets are compatible and that models of lateral variations in q_μ can be obtained from the combination of body wave and surface wave data. Model MQBS shows a pattern of attenuation which is correlated with the ocean-continent pattern and with tectonic features. The main conclusions are summarised as follows:

Conclusions from the different methods:

- The waveform fitting method is capable of making measurements of differential travel time and attenuation.
- Despite using a broader frequency band than in previous studies, the spectral ratio method has achieved limited success in making measurements of differential attenuation. This casts serious doubt on the validity of earlier studies which have relied on spectral methods.

General points

- The $SSS-SS$ measurements are new: these have not been used in previous studies. The results from the $SSS-SS$ dataset show a great deal promise. Use of $SSS-SS$ measurements provide additional constraints to the shear velocity structure of the upper mantle.
- The three dimensional models of velocity and attenuation structure of the Earth have limited depth resolution.
- Areas of high velocity correlate with areas of low attenuation and regions of low velocity are observed to correlate with areas of high attenuation.

Velocity structure of the Earth

- Model MVCOMB2 shows good correlation with surface tectonics: low velocities are observed underlying mid ocean ridges and convergent margins, high velocities are observed under continental areas.
- For model MVCOMB2, the perturbations in shear velocity relative to PREM do not exceed $\pm 8\%$ with the majority of variations within $\pm 5\%$.
- Model MVCOMB2 is in good agreement with existing three dimensional studies, however the depth resolution is limited.
- The body wave travel time measurements show excellent compatibility with the surface wave dataset of Van Heijst (1997).
- Model MVBS shows good agreement with existing studies of mantle shear velocity. In particular, the maps of the lowermost mantle show excellent agreement with the models of Woodhouse & Dziewonski (1989) and Su *et al.* (1994).
- It could be argued that MVBS provides the most detailed model of three dimensional velocity structure of the mantle to date.

q_μ structure of the Earth

- Model MQCOMB2: Regions of low attenuation are observed to correlate with continental areas. Regions of high attenuation are observed to correlate with mid oceanic ridges and convergent margins.
- Lateral variations in q_μ can be as high as ± 0.02
- The amplitude of the q_μ anomalies leads to the conclusion that the source of intrinsic attenuation must be in the low Q i.e. high attenuation, region of the mantle corresponding approximately to the low velocity zone (80-220 km).
- A significant degree zero term is observed in the q_μ models, providing evidence for the frequency dependence of q_μ.
- The q_μ model MQCOMB2 agrees well with the study of Selby (1998); the agreement with other studies is limited.
- The attenuation model, MQCOMB2, is not in good agreement with that of Bhattacharyya *et al.* (1996). We conclude that Bhattacharyya *et al*'s model is flawed.
- Combining body wave and surface wave data leads to a model of lateral variations in q_μ which is capable of explaining both the body wave and surface wave datasets, MQBS.

- Model MQBS provides confidence that the observations are largely due to variations of intrinsic attenuation and not to other factors. For example it is unlikely the elastic focusing and defocusing can effect both datasets in similar ways. One of the main results of this thesis, it is argued that this model provides the best representation to date of the 3D variation of q_μ in the upper mantle.

Some suggestions for further work on this study are:

1. Expansion of the $SSS - SS$ dataset. This is the first time such data have been used and the results obtained seem very promising. By examining data from the last 2.5 years it should be possible to at least triple the size of the $SSS - SS$ dataset.

2. The combined body wave and surface wave models MVBS and MQBS are very promising. Further work should be carried out in this area as it will lead to further constraints on the velocity and attenuation structure of the mantle.

3. Addition of more $SS - S$ measurements for epicentral distances greater than 100° to model MVBS will give improved data coverage in the lowermost mantle.

4. Investigation of the degree zero term in the q_μ models. We believe that this provides evidence for the frequency dependence of Q_μ in the frequency range of this study ($\approx$ 15 s) to ($\approx$ 150s). This requires further investigation as, if confirmed, the frequency dependence has implications for future studies of body wave attenuation.

5. Investigation as to why the spectral ratio method did not provide reliable measurements of differential t^*. What else is interfering with the signal ?

6. Automation of the picking process: It should be possible to implement some sort of automated picking. This could make is possible to assemble much larger datasets than in the current study.

7. Experimentation with different data filtering: In this study the same filters are applied to all the seismograms so that any bias introduced will be constant. It is possible that adjusting the filters may result in more data suitable for processing using the waveform method.

Bibliography

Aki, K., & Richards, P.G. 1980a. *Quantitative Seismology.* Vol. 1. San Francisco: W.H. Freeman and Company.

Aki, K., & Richards, P.G. 1980b. *Quantitative Seismology.* Vol. 2. San Francisco: W.H. Freeman and Company.

Anderson, D.L. 1967. The Anelasticity of the Mantle. *Geophys. J. R. Astron. Soc.*, **14**, 135–164.

Anderson, D.L. 1989. *Theory of the Earth.* Oxford: Blackwell Scientific Publications.

Anderson, D.L., & Dziewonski, A.M. 1984. Seismic Tomography. *Am. Sci.*, **251**(October), 58–66.

Anderson, D.L., & Given, J.W. 1982. Absorption Band Q Model for the Earth. *J. Geophys. Res.*, **87**(B5), 3893–3904.

Anderson, D.L., & Hart, R.S. 1978. Q of the Earth. *J. Geophys. Res.*, **83**(B12), 5869–5882.

Anderson, D.L., Kanamori, H., Hart, R.S., & Lui, H.P. 1977. The Earth as a Seismic Absorption Band. *Science*, **196**(June), 1104–1106.

Bath, M. 1974. *Spectral Analysis in Geophysics.* Amsterdam: Elsevier.

Bercovici, D., Schubert, G., & Glatzmaier, G. A. 1989. Three-Dimensional Spherical Models of Convection in the Earth's Mantle. *Science*, **244**(May), 950–955.

Bevington, P. R. 1969. *Data Reduction and Error Analysis for the Physical Sciences.* 1st edn. New York: McGraw-Hill.

Bhattacharyya, J. 1996. *Three-Dimensional Anelastic Structure of Earth.* Ph.D. thesis, University of California, San Diego, U.S.A.

Bhattacharyya, J., Masters, G., & Shearer, P. 1996. Global Lateral Variations of Shear Wave Attenuation in the Upper Mantle. *J. Geophys. Res.*, **101**(B10), 22,273–22,289.

Bulter, R. 1987. A Seismic Absorption Band in the Western Pacific Lithosphere. *Bull. Seismol. Soc. Am.*, **77**(1), 266–269.

Chan, W.W., & Der, Z.A. 1988. Attenuation of Multiple *ScS* in Various parts of the World. *Geophys. J. Int.*, **92**, 303–314.

Choy, G.L., & Richards, P.G. 1975. Pulse Distortion and Hilbert Transformation in Multiply Reflected and Refracted Body Waves. *Bull. Seismol. Soc. Am.*, **65**(1), 55–70.

Cormier, V.F. 1989. Seismic Attenuation: Observation and Measurement. *Pages 1006–1018 of:* James, D.E. (ed), *The Encyclopedia of Solid Earth Geophysics*. Van Nostrand Reinhold.

Der, Z.A., & Lees, A.C. 1985. Methodologies for estimating $t^*(f)$ from Short-Period Body Waves and Regional Variations of $t^*(f)$ in the United States. *Geophys. J. R. Astron. Soc.*, **82**, 125–140.

Der, Z.A., McElfresh, T.W., & O'Donnell, A. 1982. An Investigation of the Regional Variation and Frequency Dependence of Anelastic Attenuation in the Mantle Under the United States in the 0.5-4Hz Band. *Geophys. J. R. Astron. Soc.*, **69**, 67–99.

Der, Z.A., Lees, A.C., & Cormier, V.F. 1986. Frequency Dependence of Q in the Mantle Underlying the Shield Areas of Eurasia, Part III: The Q Model. *Geophys. J. R. Astron. Soc.*, **87**, 1103–1112.

Durek, J.J., & Ekström, G. 1996. A Radial Model of Anelasticity Consistent with Long-Period Surface-Wave Attenuation. *Bull. Seismol. Soc. Am.*, **86**(1A), 144–158.

Durek, J.J., Ritzwoller, M.H., & Woodhouse, J.H. 1993. Constraining Upper Mantle Anelasticity Using Surface Wave Amplitudes. *Geophys. J. Int.*, **114**, 249–272.

Dziewonski, A.M. 1984. Mapping the Lower Mantle: Determination of Lateral Heterogeneity in P Velocity Up To Degree and Order 6. *J. Geophys. Res.*, **89**(B7), 5929–5952.

Dziewonski, A.M., & Anderson, D.L. 1981. Preliminary Earth Reference Model. *Phys. Earth Planet. Inter.*, **25**, 297–356.

Dziewonski, A.M., & Gilbert, F. 1976. The Effect of Small, Aspherical Perturbations on Travel Times and a Re-examination of the Corrections for Ellipticity. *Geophys. J. R. Astron. Soc.*, **44**, 7–17.

Dziewonski, A.M., & Woodhouse, J. H. 1987. Global Images of the Earth's Interior. *Science*, **236**(April), 37–48.

Dziewonski, A.M., Hales, A.L., & Lapwood, E.R. 1975. Parametrically Simple Earth Models Consistent with Geophysical Data. *Phys. Earth Planet. Inter.*, **10**, 12–48.

Dziewonski, A.M., Hager, B. H., & O'Connell, R. J. 1977. Large-Scale Heterogeneities in the Lower Mantle. *J. Geophys. Res.*, **82**(2), 239–255.

Ekström, G., Tromp, J., & Larson, E. W. F. 1997. Measurements and Global Models of Surface Wave Propagation. *J. Geophys. Res.*, **102**(B4), 8137–8157.

Flanagan, M. P., & Wiens, D. A. 1990. Attenuation Structure Beneath the Lau Back Arc Spreading Center from Teleseismic *S* Phases. *Geophys. Res. Lett.*, **17**(12), 2117–2120.

Flanagan, M. P., & Wiens, D. A. 1994. Radial Upper Mantle Attenuation Structure of Inactive Back Arc Basins from Differential Shear Wave Measurements. *J. Geophys. Res.*, **99**(B8), 15,469–15,485.

Giardini, D., Li, X-D., & Woodhouse, J. H. 1987. Three-Dimensional Structure of the Earth from Splitting in Free-Oscillation Spectra. *Nature*, **325**, 405–411.

Gilbert, F., & Dziewonski, A.M. 1975. An Application of Normal Mode Theory to the Retrieval of Structural Parameters and Source Mechanisms from Seismic Spectra. *Philos. Trans. Roy. Soc*, **278A**, 187–269.

Grand, S. P. 1994. Mantle Shear Structure Beneath the Americas and Surrounding Oceans. *J. Geophys. Res.*, **99**(B6), 11,591–11,621.

Grand, S. P., van der Hilst, R. D., & Widiyantoro, S. 1997. Global Seismic Tomography: A Snapshot of Convection in the Earth. *GSA Today*, **7**(4), 1–7.

Gutenberg, B. 1958. Attenuation of Seismic Waves in the Earth's Mantle. *Bull. Seismol. Soc. Am.*, **48**, 269–282.

Inoue, H., Fukao, Y., Tunabe, K., & Ogata, Y. 1990. Whole Mantle P-wave Travel Time Tomography. *Phys. Earth Planet. Inter.*, **59**, 294–328.

Jeffreys, H., & Bullen, K. E. 1940. *Seismological Tables.* London: British Association for the Advancement of Science.

Kanamori, H., & Anderson, D.L. 1977. Importance of Physical Dispersion in Surface Wave and Free Oscillation Problems: Review. *Rev. Geophys. Space. Phys.*, **15**(1), 105–112.

Kellogg, L. H., Hager, B. H., & van der Hilst, R. D. 1999. Compositional Stratification in the Deep Mantle. *Science*, **283**(March), 1881–1884.

Kennett, B. L. N., & Engdahl, E. R. 1991. Travel Times for Global Earthquake Location and Phase Identification. *Geophys. J. Int.*, **105**, 429–465.

Kennett, B. L. N., & Gudmundsson, O. 1996. Ellipticity Corrections for Seismic Phases. *Geophys. J. Int.*, **127**, 40–48.

Lay, T., & Wallace, T.C. 1983. Multiple *ScS* Travel Times and Attenuation Beneath Mexico and Central America. *Geophys. Res. Lett.*, **10**(4), 301–304.

Lay, T., & Wallace, T.C. 1988. Multiple *ScS* Attenuation and Travel Times Beneath Western North America. *Bull. Seismol. Soc. Am.*, **178**(6), 2041–2061.

Li, X-D., & Romanowicz, B. 1996. Global Mantle Shear Velocity Model Developed Using Nonlinear Asymptotic Coupling Theory. *J. Geophys. Res.*, **101**(B10), 22,245–22,272.

Masters, G., Jordan, T. H., Silver, P. G., & Gilbert, F. 1982. Aspherical Earth Structure from Fundamental Spheroidal-Mode Data. *Nature*, **298**(August), 609–613.

Masters, G., Johnson, S., Laske, G., & Bolton, H. 1996. A Shear-Velocity Model of the Mantle. *Phil. Trans. R. Soc. Lond.A*, **354**, 1385–1411.

Matheney, M. P., & Nowack, R. L. 1995. Seismic Attenuation Values Obtained From Instantaneous-Frequency Matching and Spectral Ratios. *Geophys. J. Int.*, **123**, 1–15.

Menke, W. 1989. *Geophysical Data Analysis: Discrete Inverse Theory.* San Diego: Academic Press.

Mooney, W.D., Laske, G., & Masters, G. 1998. Crust 5.1: A Global Crustal Model at $5^\circ \times 5^\circ$. *J. Geophys. Res.*, **103**(B1), 727–747.

Morelli, A., & Dziewonski, A. M. 1991. Joint determination of lateral heterogeneity and earthquake location. *Pages 515–534 of:* Sabadini, R., Lambeck, K., & Boschi, E. (eds), *Glacial Isostasy, Sea-Level and Mantle Rheology.* NATO ASI Series. Kluwer, Dordrecht.

O'Nions, R. K., & Tolstikhin, I. N. 1996. Limits on the Mass Flux Between the Lower and Upper Mantle and Stability of Layering. *Earth and Planetary Science Letters*, **139**, 213–222.

Press, W.H., Flannery, B.P., Teukolsky, S.A., & Vetterling, W.T. 1986. *Numerical Recipes, The Art of Scientific Computing.* Cambridge: Cambridge University Press.

Resovsky, J. S., & Ritzwoller, M. H. 1998. New and Refined Constraints on Three-Dimensional Earth Structure from Normal Modes Below 3 mHz. *J. Geophys. Res.*, **103**(B1), 783–810.

Ritzwoller, M. H., & Lavely, E. M. 1995. Three-Dimensional Seismic Models of the Earth's Mantle. *Rev. Geophys.*, **33**(February), 1–66.

Ritzwoller, M. H., Masters, G., & Gilbert, F. 1988. Constraining Aspherical Structure With Low-Degree Interaction Coefficients: Application to Uncoupled Multiplets. *J. Geophys. Res.*, **93**(B6), 6369–6396.

Robertson, G. S., & Woodhouse, J. H. 1995. Evidence for Proportionality of P and S Heterogeneity in the Lower Mantle. *Geophys. J. Int.*, **123**, 85–116.

Romanowicz, B. 1990. The Upper Mantle Degree 2: Constraints and Measurements from Global Mantle Wave Attenuation Measurements. *J. Geophys. Res.*, **95**, 11,051–11,071.

ROMANOWICZ, B. 1994. On the Measurement of Anelastic Attenuation Using Amplitudes of Low-Frequency Surface Waves. *Phys. Earth Planet. Inter.*, **84**, 179–191.

ROMANOWICZ, B. 1995. A Global Tomographic Model of Shear Attenuation in the Upper Mantle. *J. Geophys. Res.*, **100**(B7), 12,375–12,394.

ROULT, G., ROMANOWICZ, B., & MONTAGNER, J.P. 1990. 3-D Upper Mantle Shear Velocity and Attenuation from Fundamental Mode Free Oscillation Data. *Geophys. J. Int.*, **101**, 61–80.

SAILOR, R.V., & DZIEWONSKI, A.M. 1978. Measurements and Interpretation of Normal Mode Attenuation. *Geophys. J. R. Astron. Soc.*, **53**, 59–581.

SELBY, N. D. 1998. *Rayleigh Wave Amplitudes and the Attenuation Structure of the Earth.* D.Phil. thesis, University of Oxford, Oxford, UK.

SHARROCK, D.S., MAIN, I.G., & DOUGLAS, A. 1995. A Two-Layer Attenuation Model for the Upper Mantle at Short Periods. *Geophys. Res. Lett.*, **22**(19), 2561–2564.

SIPKIN, S.A., & JORDAN, T.H. 1980. Regional Variation of Q_{ScS}. *Bull. Seismol. Soc. Am.*, **70**(4), 1071–1102.

SIPKIN, S.A., & REVENAUGH, J. 1994. Regional Variation of Attenuation and Travel Time in China from Analysis of Multiple-*ScS* Phases. *J. Geophys. Res.*, **99**(B2), 2687–2699.

SMITH, M.F., & MASTERS, G. 1989. Aspherical Structure Constraints from Free Oscillation Frequency and Attenuation Measurements. *J. Geophys. Res.*, **94**(B2), 1953–1976.

SU, W. J., WOODWARD, R. L., & DZIEWONSKI, A. M. 1992. Deep Origin of Mid-Ocean Ridge Seismic Velocity Anomalies. *Nature*, **360**, 149–152.

SU, W. J., WOODWARD, R. L., & DZIEWONSKI, A. M. 1994. Degree 12 Model of Shear Velocity Heterogeneity in the Mantle. *J. Geophys. Res.*, **99**(B4), 6945–6980.

SUDA, N., SHIBATA, N., & FUKAO, Y. 1991. Dergee-2 Pattern of Attenuation Structure in the Upper Mantle from Apparent Complex Frequency Measurements of Fundamental Spheroidal Modes. *Geophys. Res. Lett.*, **18**, 1119–1122.

TANIMOTO, T. 1990. Long-wavelength S-wave Velocity Structure Throughout the Mantle. *Geophys. J. Int.*, **100**, 327–336.

TARANTOLA, A. 1988. *Inverse Problem Theory.* 1st edn. Amsterdam: Elsevier.

TRAMPERT, J., & WOODHOUSE, J. H. 1995. Global Phase Velocity Maps of Love and Rayleigh Waves Between 40 and 150 Seconds. *Geophys. J. Int.*, **122**, 675–690.

TRAMPERT, J., & WOODHOUSE, J. H. 1996. High Resolution Global Phase Velocity Distributions. *Geophys. Res. Lett.*, **23**(January), 21–24.

VAN DER HILST, R. D., & KÁRASON, H. 1999. Compositional Heterogeneity in the Bottom 1000 Kilometers of the Earth's Mantle: Toward a Hybrid Convection Model. *Science*, **283**(March), 1885–1888.

VAN DER HILST, R. D., WIDIYANTORO, S., & ENGDAHL, E. R. 1997. Evidence for Deep Mantle Circulation from Global Tomography. *Nature*, **386**(April), 578–584.

VAN HEIJST, H. J. 1997. *New Constraints on the Seismic Structure of the Earth from Surface Wave Overtone Phase Velocity Measurements*. D.Phil. thesis, University of Oxford, Oxford, UK.

VAN HEIJST, H. J., WOODHOUSE, J. H., & REID, F. J. L. 1998. The Shear Velocity Structure of the Transition Zone Determined From Surface Overtone Dispersion and Body Wave Travel Times. *EOS, Trans. Am. Geophys. Un.*, **79**(45), F656.

WESSEL, P., & SMITH, W.H.F. 1991. Free Software Helps Map and Display Data. *EOS, Trans. Am. Geophys. Un.*, **72**, 441–446.

WESSEL, P., & SMITH, W.H.F. 1995. New Version of the Generic Mapping Tools Released. *EOS, Trans. Am. Geophys. Un.*, **76**, 329.

WIDMER, R., MASTERS, G., & GILBERT, F. 1991. Spherically Symmetric Attenuation Within the Earth from Normal Mode Data. *Geophys. J. Int.*, **104**, 541–552.

WOODHOUSE, J. H., & DZIEWONSKI, A.M. 1984. Mapping the Upper Mantle: Three-Dimensional Modelling of Earth Structure by Inversion of Seismic Waveforms. *J. Geophys. Res.*, **89**(B7), 5953–5986.

WOODHOUSE, J. H., & DZIEWONSKI, A.M. 1986. Three Dimensional Mantle Models Based on Mantle Wave and Long Period Body Waves. *EOS, Trans. Am. Geophys. Un.*, **67**(16), 307.

WOODHOUSE, J. H., & DZIEWONSKI, A.M. 1989. Seismic Modelling of the Earth's Large-Scale Three-Dimensional Structure. *Phil. Trans. R. Soc. Lond.A*, **328**, 291–308.

WOODWARD, R.L., & MASTERS, G. 1991a. Global Upper Mantle Structure from Long-period Differential Travel Times. *J. Geophys. Res.*, **96**(B4), 6351–6377.

WOODWARD, R.L., & MASTERS, G. 1991b. Lower Mantle Structure from $ScS - S$ Differential Travel Times. *Nature*, **352**, 231–233.

WOODWARD, R.L., & MASTERS, G. 1991c. Upper Mantle Structure from Long-period Differential Travel Times and Free Oscillation Data. *Geophys. J. Int.*, **109**, 275–293.

Wu, R.S. 1989. Seismic Wave Scattering. *Pages 1166–1186 of:* James, D.E. (ed), *The Encyclopedia of Solid Earth Geophysics*. Van Nostrand Reinhold.

Appendix A

Inverse Theory

A.1 The spherical harmonics

The spherical harmonics are a set of basis functions which are commonly used to parameterise Earth models. Taking the real part of the spherical harmonics produces real functions which can be used to describe a spherical surface. The spherical harmonics, $Y_l^m(\theta, \phi)$, are defined by:

$$Y_l^m(\theta,\phi) = \begin{cases} \sqrt{2} X_l^{|m|}(\theta) \cos m\phi & -l \leq m < 0 \\ X_l^0(\theta) & m = 0 \\ \sqrt{2} X_l^m(\theta) \sin m\phi & 0 < m \leq l \end{cases}$$

where

$$X_l^m(\theta) = (-1)^m \sqrt{\frac{(2l+1)(l-m)!}{4\pi(l+m)!}} P_l^m(\cos\theta) \tag{A.1}$$

and P_l^m are the associated Legendre Polynomials.

A.2 Inverse theory: some further details

A.2.1 Introduction

In this Section a brief overview of the theory of weighted damped least squares is presented. For further details the reader is referred to any of the following Menke (1989), Tarantola (1988), or Van Heijst (1997) It should be noted that for many of the models presented in this thesis all the weights are set equal to 1.0 and the problem reduces to that of damped least squares.

A.2.2 Weighted damped least squares

Consider the case of an over-determined system of linear equations:

$$\boldsymbol{A}\boldsymbol{m} = \boldsymbol{d} \tag{A.2}$$

where $\boldsymbol{d}$ is the data vector, $\boldsymbol{m}$ is the model vector and $\boldsymbol{A}$ is the matrix of derivatives relating $\boldsymbol{d}$ and $\boldsymbol{m}$. The data vector, $\boldsymbol{d}$ is an $N \times 1$ matrix (i.e. a column vector of length N) where N is the total number of data points. The derivative matrix, $\boldsymbol{A}$ is an $N \times n$ matrix where n is equal to the the total number of basis functions (equal to the number of possible spherical harmonic functions multiplied by the number of possible radial functions). For example, a model parameterised up to degree 8 using 6 depth splines has a value of n equal to $(8+1)^2 * 6 = 486$. The model vector, $\boldsymbol{m}$, is an $n \times 1$ matrix (i.e. a column vector of length n) containing the model parameters.

Now we seek to find a solution which minimises both the residual vector

$$(\boldsymbol{d} - \boldsymbol{A}\boldsymbol{m})^T(\boldsymbol{d} - \boldsymbol{A}\boldsymbol{m}) \tag{A.3}$$

and the norm of the model vector

$$\boldsymbol{m}^T\boldsymbol{m} \tag{A.4}$$

In weighted least squares we seek to minimise

$$(\boldsymbol{d} - \boldsymbol{A}\boldsymbol{m})^T\boldsymbol{D}^T\boldsymbol{D}(\boldsymbol{d} - \boldsymbol{A}\boldsymbol{m}) \tag{A.5}$$

and

$$\boldsymbol{m}^T\boldsymbol{M}^T\boldsymbol{M}\boldsymbol{m} \tag{A.6}$$

where $\boldsymbol{D}$ represents the data weighting and $\boldsymbol{M}$ represents an *a priori* model weighting. Usually we would like

$$\boldsymbol{D}^T\boldsymbol{D} = \mathrm{cov}\boldsymbol{d}^{-1} \tag{A.7}$$

where $\mathrm{cov}\boldsymbol{d}^{-1}$ is the data covariance matrix.

The solution of A.2 is given by:

$$\boldsymbol{m} = \boldsymbol{M}^{-1}(\boldsymbol{A}'^T\boldsymbol{A}')^{-1}\boldsymbol{A}'^T\boldsymbol{D}\boldsymbol{d} \tag{A.8}$$

where $\boldsymbol{A}'$ is defined as $\boldsymbol{A}' = \boldsymbol{D}\boldsymbol{A}\boldsymbol{M}'$.

It is possible to decompose the matrix $\boldsymbol{A}'^T\boldsymbol{A}'$ into its eigenvectors and eigenvalues as follows:

$$\boldsymbol{A}'^T\boldsymbol{A}'\boldsymbol{U} \equiv \boldsymbol{U}\boldsymbol{\Lambda} \tag{A.9}$$

Where $\boldsymbol{U}$ is a an $n \times n$ matrix whose columns are the eigenvectors of $\boldsymbol{A'}^T\boldsymbol{A'}$, e.g.

$$\boldsymbol{U} = \begin{pmatrix} \boldsymbol{U_1} & \boldsymbol{U_2} & \boldsymbol{U_3} & \cdots & \boldsymbol{U_n} \\ \vdots & \vdots & \vdots & \vdots & \vdots \\ \vdots & \vdots & \vdots & \vdots & \vdots \end{pmatrix} \tag{A.10}$$

and $\boldsymbol{\Lambda}$ is an $n \times n$ diagonal matrix containing the eigenvalues, λ_i of $\boldsymbol{A'}^T\boldsymbol{A'}$ along the diagonal, e.g.

$$\boldsymbol{\Lambda} = \begin{pmatrix} \lambda_1 & & & & \\ & \lambda_2 & & 0 & \\ & & \lambda_3 & & \\ & 0 & & \ddots & \\ & & & & \lambda_n \end{pmatrix} \tag{A.11}$$

Recall that the eigenvectors of a real symmetric matrix are orthogonal and therefore since $\boldsymbol{A'}^T\boldsymbol{A'}$ is a real symmetric matrix it is possible to write:

$$\boldsymbol{U}^T\boldsymbol{U} = \boldsymbol{I} \tag{A.12}$$

where $\boldsymbol{I}$ is the identity matrix. Now A.12 can be re-written as:

$$\boldsymbol{U}^T = \boldsymbol{U}^{-1} \tag{A.13}$$

Now multiplying A.9 through by $\boldsymbol{U}^{-1}$ we obtain:

$$\boldsymbol{A'}^T\boldsymbol{A'} = \boldsymbol{U}\boldsymbol{\Lambda}\boldsymbol{U}^{-1} = \boldsymbol{U}\boldsymbol{\Lambda}\boldsymbol{U}^T \tag{A.14}$$

Now taking the inverse of both sides to obtain

$$(\boldsymbol{A'}^T\boldsymbol{A'})^{-1} = (\boldsymbol{U}\boldsymbol{\Lambda}\boldsymbol{U}^T)^{-1} = (\boldsymbol{U}^T)^{-1}\boldsymbol{\Lambda}^{-1}\boldsymbol{U}^{-1} \tag{A.15}$$

Thus

$$(\boldsymbol{A'}^T\boldsymbol{A'})^{-1} = \boldsymbol{U}\boldsymbol{\Lambda}^{-1}\boldsymbol{U}^T \tag{A.16}$$

This expression for $(\boldsymbol{A'}^T\boldsymbol{A'})^{-1}$ is now substituted back into A.8 to obtain an expression for $\boldsymbol{m}$:

$$\boldsymbol{m} = \boldsymbol{M}^{-1}\boldsymbol{U}\boldsymbol{\Lambda}^{-1}\boldsymbol{U}^T\boldsymbol{A'}^T\boldsymbol{D}\boldsymbol{d} \tag{A.17}$$

A.17 gives the exact solution for $\boldsymbol{m}$ in which all n eigenvalues of $\boldsymbol{A'}^T\boldsymbol{A'}$ are used. In the ideal situation, with an even distribution of sources and receivers it should be possible to use all the eigenvalues and

eigenvectors to find the model parameters. However the distribution of sources and receivers on the Earth is far from uniform and it is often not possible to use all n eigenvectors and eigenvalues when constructing the model. As a result, we may choose to damp the solution (consider the trade off between the variance ratio and the model size shown by Figures 6.5 and 6.6). Damping is achieved by selecting a point at which to cut-off the eigenvalues. Beyond this cut-off value the remaining eigenvalues are tapered off. Such damping can be achieved by setting:

$$(\boldsymbol{A'}^T\boldsymbol{A'})^{-1} = \boldsymbol{U}\hat{\boldsymbol{\Lambda}}^{-1}\boldsymbol{U}^T \tag{A.18}$$

where

$$\hat{\boldsymbol{\Lambda}}^{-1} = (\boldsymbol{\Lambda} + \lambda_i\boldsymbol{I})^{-1} \tag{A.19}$$

and λ_i is the i^{th} eigenvalue of $\boldsymbol{A'}^T\boldsymbol{A'}$ in ordering of increasing size. If λ_i is chosen as the eigenvalue cut-off then:

$$\frac{\lambda}{\lambda + \lambda_i} \approx \begin{cases} 1 & \text{for } \lambda \gg \lambda_i \\ 0 & \text{for } \lambda \ll \lambda_i \end{cases}$$

This form of damping ensures that all the eigenvalues are used in construction of the model. However eigenvalues with $\lambda \ll \lambda_i$ are damped effectively to zero. The value of λ_i is determined by choosing a value of η such that:

$$\lambda_i = \eta\lambda_{max} \tag{A.20}$$

where λ_{max} is the largest eigenvalue and $\lambda_{max} = \lambda_1$.

Now the damped weighted least squares solution of A.2 is given by:

$$\boldsymbol{m} = \boldsymbol{M}^{-1}\boldsymbol{U}\hat{\boldsymbol{\Lambda}}^{-1}\boldsymbol{U}^T\boldsymbol{A'}^T\boldsymbol{D}\boldsymbol{d} \tag{A.21}$$

A.3 Resolution

The application of damping to the least squares problem means that the solution provided by A.21 will only be approximate. This means that the best resolved parts of the model (e.g. the parts with the best coverage) are retrieved with most detail and the less well resolved or sampled data are retrieved with less detail. Clearly this is desirable as we don't want our model to be inventing structure in parts of the model where there is little or no data. The resolution matrix $\boldsymbol{R}$ can be used as an indication of the amount of detail that can be solved for in different parts of the model, e.g.

$$\boldsymbol{m} = \boldsymbol{R}\boldsymbol{m}_t \tag{A.22}$$

$\boldsymbol{m}_t$ represents the *true* model which is the model that would be obtained with no damping. Therefore for an undamped model $\boldsymbol{R} = \boldsymbol{I}$. For an undamped model $\boldsymbol{m}_t$ is given by A.17. Substituting A.17 and

A.21 into A.22 and re-arranging it follows that

$$\boldsymbol{R} = \boldsymbol{M}^{-1}\boldsymbol{U}\boldsymbol{\Lambda}^{-1}\boldsymbol{U}^{T}\boldsymbol{U}\boldsymbol{\Lambda}\boldsymbol{U}^{T}\boldsymbol{M} \tag{A.23}$$

Recall that since $\boldsymbol{U}$ is an orthogonal matrix, $\boldsymbol{U}^{T}\boldsymbol{U} = \boldsymbol{I}$. Now the trace of the resolution matrix, denoted $tr(\boldsymbol{R})$, gives the effective number of unknowns in the solution - this should be equivalent to the effective number of eigenvalues used.

A.4 Variance Ratio

The variance ratio is used to measure how well a given model fits the input data. The unweighted variance ratio is defined as:

$$v = \frac{|\boldsymbol{d} - \boldsymbol{A}\boldsymbol{m}|^{2}}{\boldsymbol{d}^{T}\boldsymbol{d}} \tag{A.24}$$

which is equivalent to:

$$v = \sum_{i=1}^{N} \frac{(d_i - p_i)^2}{d_i^2} \tag{A.25}$$

where N is the total number of data points used to create the model, d_i is the value of data point i and p_i is the model prediction of data point i. The smaller the value of v is the better the fit between the model and the input data.

We can also define the weighted variance ratio, v_w:

$$v_w = \frac{|\boldsymbol{D}\boldsymbol{d} - \boldsymbol{D}\boldsymbol{A}\boldsymbol{m}|^{2}}{\boldsymbol{d}^{T}\boldsymbol{D}^{T}\boldsymbol{D}\boldsymbol{d}} = \frac{|\boldsymbol{D}\boldsymbol{d} - \boldsymbol{A}'\boldsymbol{M}\boldsymbol{m}|^{2}}{\boldsymbol{d}^{T}\boldsymbol{D}^{T}\boldsymbol{D}\boldsymbol{d}} \tag{A.26}$$

which again is equivalent to:

$$v_w = \sum_{i=1}^{N} \frac{(w_i d_i - w_i p_i)^2}{(w_i d_i)^2} \tag{A.27}$$

where w_i is the data weighting for the i^{th} data point. Typically the v_w ranges between 0 and 1. The lower v_w is, the better the fit between the model and the data.

Appendix B

Additional figures

This appendix provides some additional figures that the reader may find informative. Figures B.1(a) and B.1(b) show the shear velocity model, S20RMC18 of Van Heijst (1997).

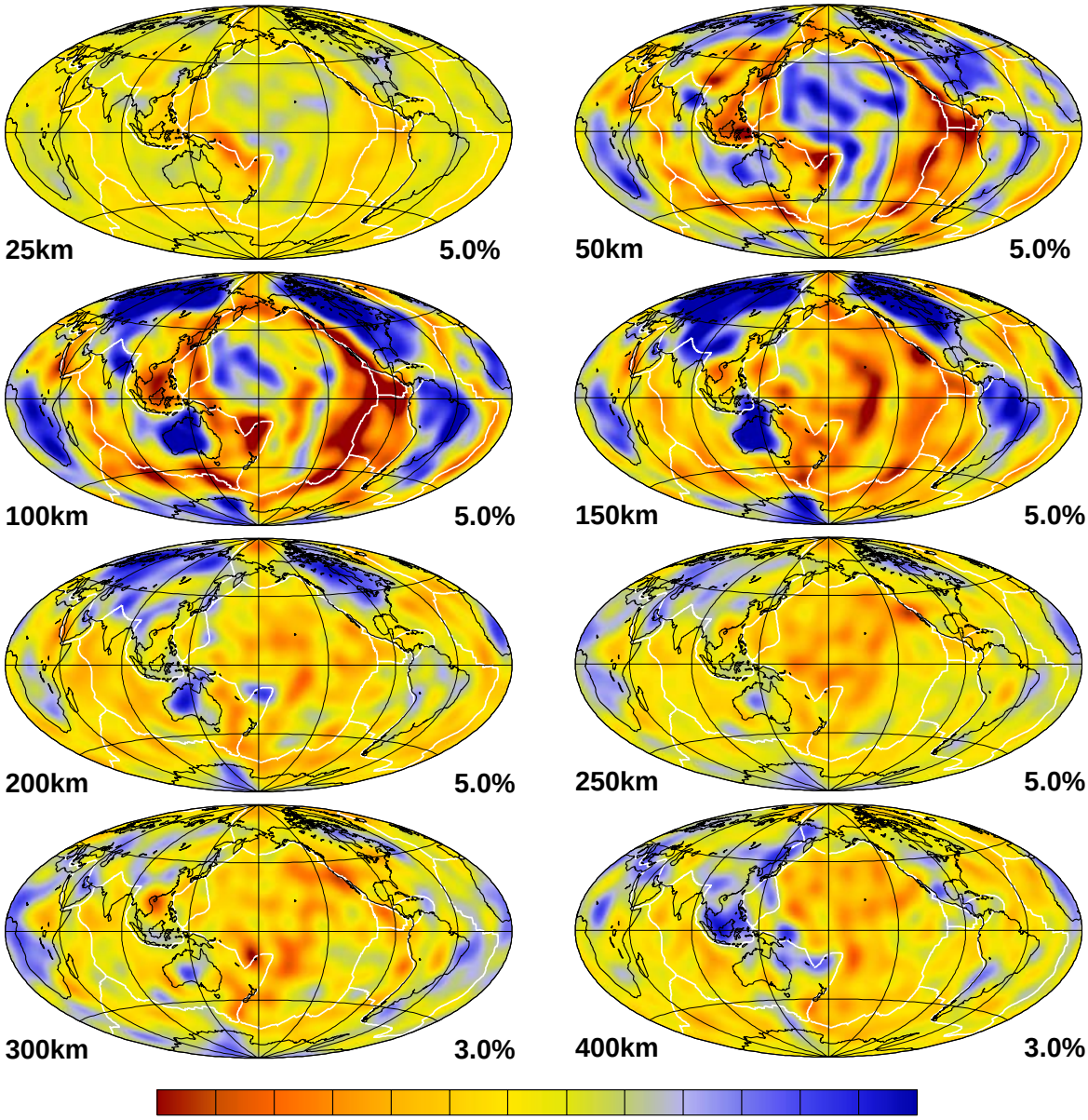


Figure B.1(a): Model S20RMC18 of Van Heijst (1997) for depths 50-400 km

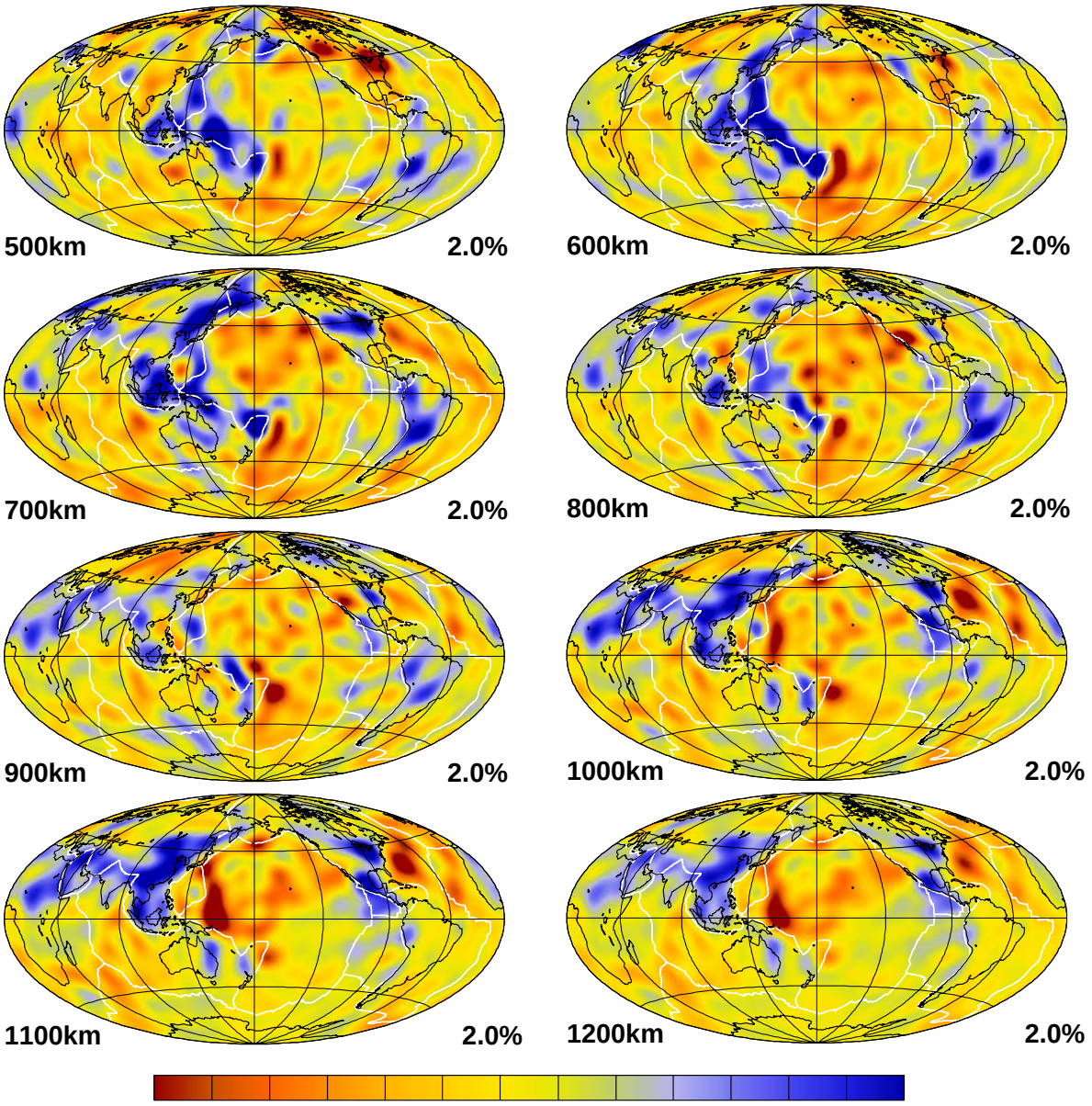


Figure B.1(b): Model S20RMC18 of Van Heijst (1997) for depths 500-1200 km

Appendix C

Testing the methodologies employed in this study

In this appendix synthetic tests are presented for both the waveform fitting (Section C.1) and spectral ratio (Section C.2) methods. The methodology employed is identical to that described in Chapters 3 and 4 except that synthetic data are used in place of real data in each case.

C.1 Synthetic testing of the waveform fitting method

In this section we use synthetic data to test the validity of the waveform fitting method. The methodology is described in detail by Chapter 3. The synthetic testing of the waveform fitting method is applied as follows:

- Choose a selection of synthetic traces for the same source station pairs selected for processing in Section 3.4.
- For these traces apply a t^* filter of 3.0 seconds.
- Apply the waveform fitting method to the synthetic S and SS traces without any t^* filter applied.
- Apply the method again this time using the synthetic S and the t^* filtered SS.
- Measure the difference in Δt^* between the two applications of the method. The expected result is 3.0 seconds.

Figure C.1 shows a selection of synthetic seismograms from event 950712B. The seismograms have been filtered using the filters as mentioned in Section 2.2. The top trace for each station pair shows the seismogram without any additional filtering applied. The bottom trace shows the seismogram after the application of an additional t^* filter of 3.0 seconds. The results obtained from application of the waveform fitting method to event 950712B are summarised in Table C.1.

Station	Δ (degrees)	Δt^* (seconds)	$\sigma_{\Delta t^*}$	Fit parameter
BAR	88.72	3.14	0.25	0.04
CALB	88.01	3.16	0.29	0.05
CMB	88.74	3.12	0.24	0.03
GSC	89.88	3.09	0.19	0.02
KMI	81.63	3.02	0.16	0.01
LZH	86.48	3.08	0.36	0.07
PLCA	94.58	2.94	0.50	0.13
TATO	67.71	3.13	0.19	0.02
TUC	92.98	2.99	0.14	0.01
WMQ	101.01	3.01	0.16	0.02
XAN	81.88	2.95	0.20	0.03

Table C.1: Results of synthetic testing of the waveform fitting method for event 950712B. The value of Δt^* corresponds to the difference between the differential t^* values obtained with and without the additional t^* filter of 3 seconds applied. Δ is the epicentral distance in degrees, $\sigma_{\Delta t^*}$ is the error in Δt^* as obtained from the waveform fitting method, the fit parameter is also given for reference.

The values of Δt^* are all obtained to be 3.0 seconds within the experimental error. Thus, we have proved that the waveform fitting method can successfully retrieve a known value of Δt^* using synthetic data, and therefore validated the methodology of the waveform fitting method.

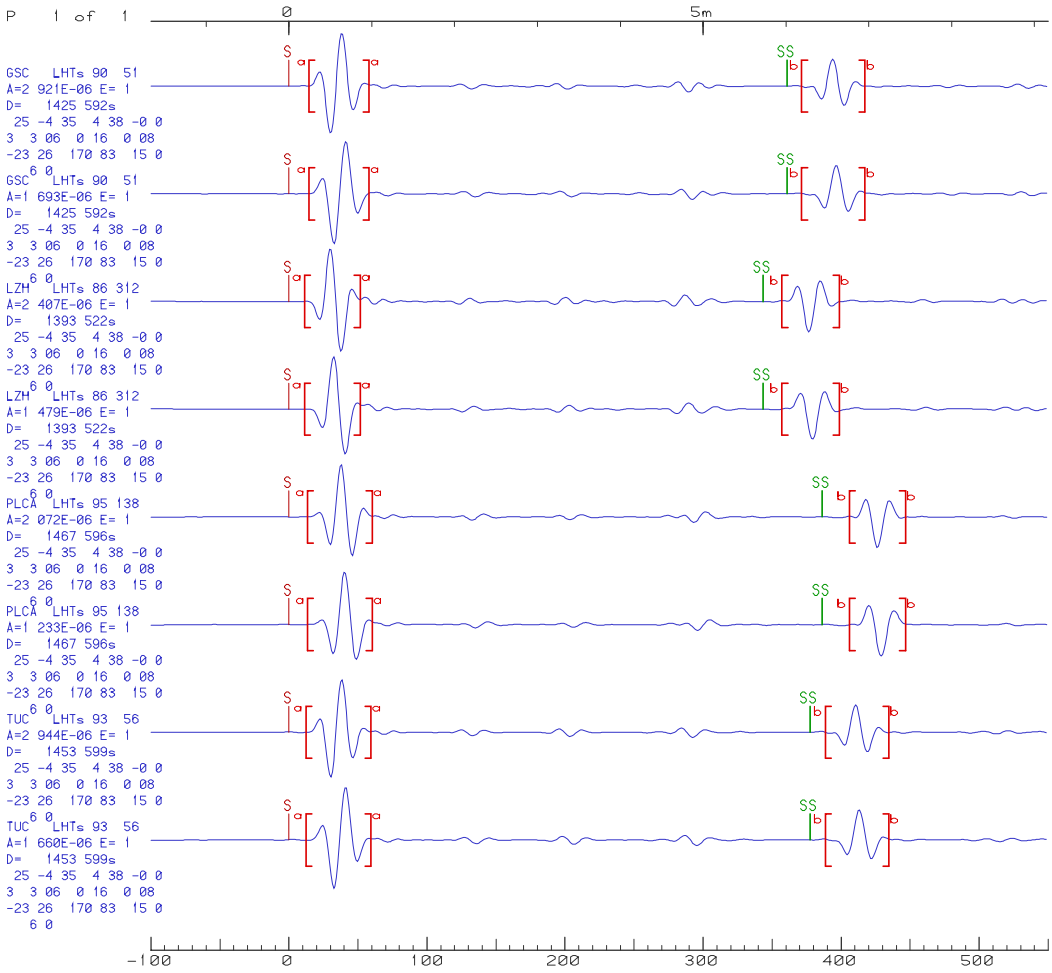


Figure C.1: Synthetic traces for 4 stations from event 950712B. For each station pair, the top trace shows the synthetic seismogram with the usual filters applied (see Section 2.2). The lower trace shows the synthetic seismogram with an additional t^* filter of 3.0 seconds applied. The "a" and "b" intervals show the windows selected for the S and SS phases respectively. The S and SS ticks mark the PREM travel times for the S and SS phases.

C.2 Testing of the spectral ratio method

In this section we use real data to test the spectral ratio method. Chapter 4 provides a detailed description of the spectral ratio method. The procedure for the testing of the spectral ratio method is similar to that described in Section C.1 except that real data are used. The outline is as follows:

1. Choose a selection of seismograms from the dataset used with the spectral ratio method.
2. Apply a t^* filter of 3.0 seconds to the raw seismogram and store the result.
3. Apply the spectral ratio method to the S and SS traces which have not had the t^* filter applied.
4. Apply the spectral ratio method to the S phase without the t^* filter and the SS phase which has had the additional t^* filter applied.
5. If the test is successful then the difference in Δt^* between steps 3 and 4 should be 3.0 seconds.

Table C.2 shows an example of the results obtained from the testing of the spectral ratio method for event 950629D. The column labelled Δt^* is the difference in Δt^* obtained with and without the t^* filter at 3.0 seconds. If test the is successful then we expect to obtain a value of 3.0 seconds. Indeed the value of Δt^* obtained for each station is close to 3.0 seconds. We have applied a t^* filter of 3.0 seconds to the data and successfully retrieved a differential t^* of approximately 3.0 seconds. Effectively this validates the spectral ratio method.

Station	Δ (degrees)	Δt^* (seconds)	$\sigma_{\Delta t^*}$
ADK	72.10	3.58	0.28
CHTO	78.44	3.30	0.46
CMB	87.48	2.97	0.16
ERM	65.61	3.47	0.80
GLA	89.46	3.37	0.34
GSC	88.88	2.89	0.16
HIA	81.13	3.04	0.25
MLAC	88.40	3.18	0.21
SNCC	85.97	2.75	0.35
SVD	88.16	2.87	0.28
TUC	92.33	2.74	0.24
XAN	78.03	2.95	0.17
YSS	70.16	2.74	0.27

Table C.2: Results from testing of the spectral ratio method for event 950629D using real seismograms. The value of Δt^* corresponds to the difference between the differential t^* values obtained with and without the additional t^* filter of 3 seconds applied. Δ is the epicentral distance in degrees, $\sigma_{\Delta t^*}$ is the error in the differential value of Δt^* as obtained from the spectral ratio method.

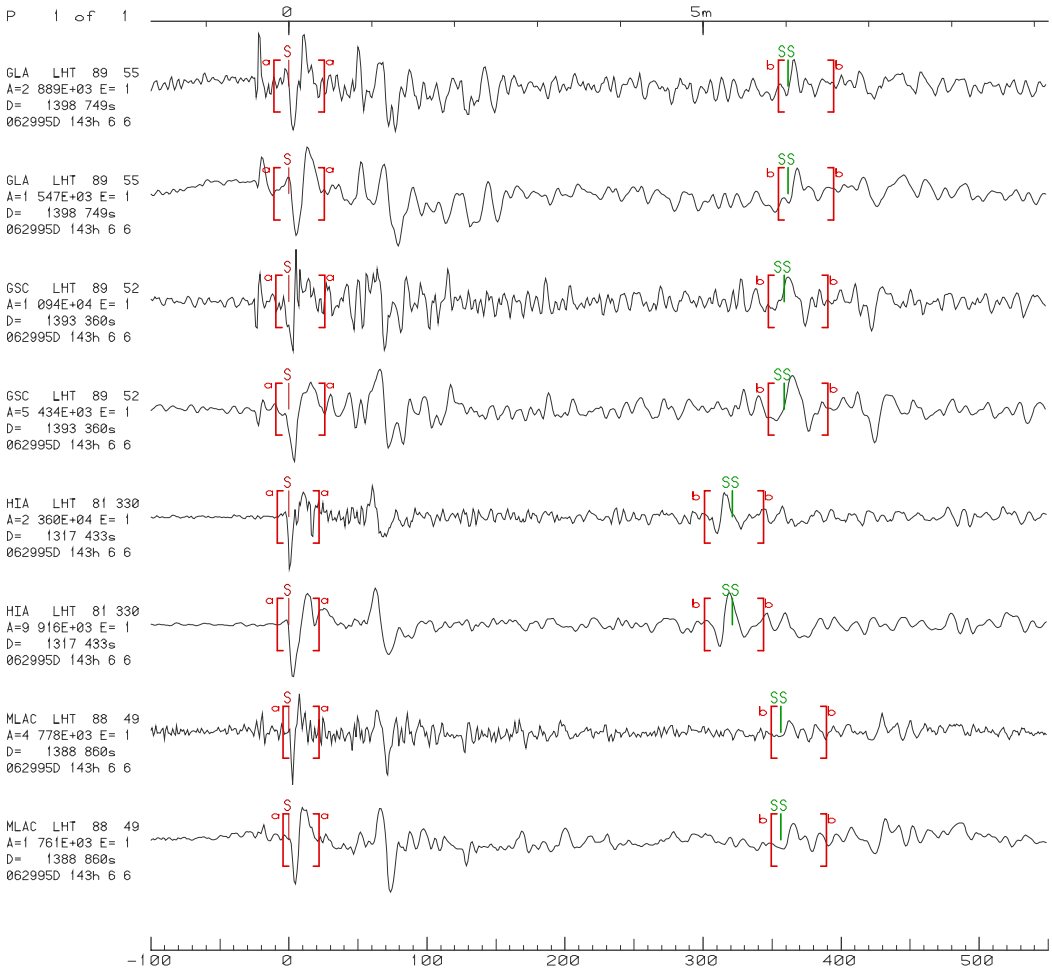


Figure C.2: Seismograms for 4 stations from event 950629D. For each station pair, the top trace shows the raw unfiltered seismogram, the lower trace shows the same seismogram with an additional t^* filter of 3.0 seconds applied. The "a" and "b" intervals show the windows selected for the S and SS phases respectively. The S and SS ticks mark the PREM travel times for the S and SS phases.